

· ROMA TRE UNIVERSITY OF ROME ·

DEPARTMENT of PHYSICS
Doctorate in Physics - XIX Cycle

Doctorate Thesis

ROMA TRE University - LPCE/CNRS Orléans University *Co-Tutorship* Agreement
"Vinci" Programme of the Italian-French University

DEMETER Satellite Data Analysis of Seismo-Electromagnetic Signals

by

AURORA BUZZI

Supervisors:

Prof. Vittorio Sgrigna

ROMA TRE University, Department of Physics, Rome, Italy

Prof. Michel Parrot

LPCE/CNRS, Orléans, France

*To my grandmother Rosa, my uncles,
my mother, and my boyfriend
who have given me the smile for the life*

Acknowledgements

I am deeply grateful to my supervisors Prof. Vittorio Sgrigna and Prof. Michel Parrot for their guidance, and kind support in the course of this research work.

I also express my gratefulness to many members of LPCE at Orléans and Department of Physics at Roma Tre University, within which the help and suggestions of Jean-Louis Pinçon, Jean-Yves Brochot, and Livio Conti, are particularly acknowledged.

Finally, I wish to thank the ESPERIA and DEMETER teams, which created a friendly and productive human and scientific atmosphere in both Rome and Orléans laboratories.

Abstract

This thesis work has been carried out within the Co-Tutorship Agreement between University of Orleans and University of Roma Tre, which has been signed according to "Vinci" Programme of the French-Italian University. The research work is based on the study of electromagnetic (EM) and particle data collected by the DEMETER satellite mission, which is still flying (end of the mission is scheduled for 2008). In particular, the study is focused to check possible time and space correlations of earthquakes with anomalous whistler-waves and particle bursts detected by DEMETER. In recent times, ionospheric and magnetospheric perturbations constituted by radiation belt particle precipitations, variations of temperature and density of ionic and electronic components of ionospheric plasma, as well as electric and magnetic field fluctuations, were detected on board of Low-Earth-Orbit (LEO) satellites. Observations aim at reconciling these phenomena not only with solar or atmospheric effects but also with Earth natural and anthropogenic activities. The latter are constituted by power line harmonic radiation (PLHR), VLF transmitters, and HF broadcasting stations. Physical mechanisms underlying all these phenomena are not yet well known, but one of the most fascinating applications is the so-called seismo-electromagnetic emissions (SEME). It consists of EM emissions (EME) in a large frequency band (from DC to a few tens of MHz), which cause ionospheric perturbations as a consequence of the earthquake preparation and occurrence. The idea is that EM fields generated by seismic sources in the

seismogenic layer of the upper lithosphere, are transmitted into the near Earth's space, before, during, and after an earthquake. These emissions can be detected on board of LEO satellites together with EME-waves produced by human activities. The privileged zone for investigating these phenomena appears to be the ionosphere-magnetosphere transition zone (topside ionosphere). What is lacking is the demonstration of a causal relationship with explained physical processes and looking for a correlation between data gathered simultaneously and continuously by space observations and ground-based measurements. In contrast to ground experiments, satellite missions cover most seismic zones of the Earth, and statistical studies become meaningful because of the much larger number of recorded events. DEMETER is the first satellite devoted and optimized to study the correlation between seismo- electromagnetic phenomena and iono-magnetospheric perturbations. The scientific payload of DEMETER is composed of several sensors: - three electric and three magnetic sensors (6 components of the electromagnetic field to investigate from a frequency range DC up to 3.5 MHz). A Langmuir probe, an ion spectrometer, and, an energetic particle analyzer. There are two modes of operation: (i) a survey mode to record low bit rate data, and (ii) a burst mode to record high bit rate data above seismic regions. DEMETER has been launched by CNES (French National Space Agency), 29th June 2004. DEMETER is a micro-satellite with a low-altitude (~ 700 km) and a nearly polar orbit. The data processing center is located in LPCE, Orléans. To carry out this thesis work the candidate has worked for 1 year at the LPCE laboratory. Aim of this thesis is to study the influence of seismo-electromagnetic emissions in the near Earth-space. At this purpose, after a recognition of the state of art of the literature on this field, three different studies have been carried out. First it has been analyzed the effect of seismicity on the propagation of whistlers. Following a previous work (Hayakawa et al., 1993) based on whistler data detected by ground based observatories, that has suggested the influence of seismic activity on the occurrence of anomalous whistlers of high dispersion parameter, in this thesis the spatial and temporal correlation between earthquakes and whistlers phenomena has also been investigated but using the DEMETER space data. This is the first study of such a correlation based on satellite whistler observations. At this purpose a special software (WHIMAP) has been developed to construct the DEMETER whistler database

including time, position, whistler data and geomagnetic activity indices information. Starting from the USGS data of earthquakes with medium and strong magnitude, an ad hoc catalogue has been built including epicenters, magnetic field line data, McIlwain L-parameter and conjugate coordinates of the geomagnetic point. Whistler waves and earthquake events to be correlated have been selected with an original method of analysis applying several cuts. Two correlation estimators have been identified and the significance of their spatial and temporal distributions have been investigated, as a function of distance, time, geomagnetic condition, whistler dispersion, earthquake magnitude and latitude, spatial distribution and local time dependence, to verify the stability of results. Although some aspects of DEMETER whistler dispersion classes distribution have to be clarified, it has been observed that for high whistler coefficient dispersion values, number of whistlers close to earthquakes and conjugated points exhibits a greater increase than those detected in average in the same zone. On the contrary, this result does not allow to distinguish and classify anomalous signals between pre-seismic, co-seismic, and post-seismic ones. Results must be validated by extending the time window used in the analysis and refining selection criteria. The second study carried out in this thesis is an attempt to look for a possible statistical correlation between anomalous bursts of particles precipitating from the inner Van Allen radiation belt and selected earthquakes of moderate and large magnitude, according to a previous work based on particle data collected by SAMPEX/PET mission (Sgrigna et al., 2005). For this analysis, a special software (PARMAP) has been developed to construct a database on the basis of original data from the DEMETER particle counter IDP. Data collected during burst mode and survey mode have been merged and telemetry information interpolated to build a common particle database with sampling rate of 4 seconds. Contrary to positive correlation obtained with SAMPEX/PET data, results obtained up to now in this thesis do not show any significant correlation between earthquakes and particle burst occurrence detected by IDP. Several reasons can be at the basis of such results. In fact, energy range of particles detected by IDP is significantly lower than that of the SAMPEX/PET detector, and this will surely cause a non efficient particle longitudinal drift, which is necessary for a good detection of particle fluxes in precipitation from the inner radiation belt. Moreover, due to the orientation of IDP,

data collected by this detector are mainly constituted by trapped particles, that are not easy to precipitate into the lower topside ionospheric region. This part of the study is in progress and will be continued after the end of this thesis work. As an outlook, there are aspects of the IDP detector that must be better investigated, for instance, its capability in discriminating low-, medium-, and high-energy particles, or its behavior during the burst mode-survey mode transition. Therefore, the analysis is still in progress and in this preliminary step of the study the main goal has been to try to better understand the IDP behavior and, then, the physical mechanisms of the phenomenology.

The third analysis developed in this thesis has been to study the effects of magnetic storms on radiation belt particles. Geomagnetic activity is one of the main sources of particle precipitation. Therefore it generates a large background with respect to possible precipitations induced by seismo-electromagnetic perturbations. According to a model proposed by a few authors, in this thesis has been verified that during most great magnetic storms, precipitation of fluxes of charged particles was mainly caused by the cyclotron-resonance mechanism. In fact, particle energy spikes observed by the DEMETER IDP during several orbits revealed to be consistent with those expected for a cyclotron-resonance coupling mechanism between waves and particles moving parallel to the magnetic field lines. Results pointed out by this thesis work on whistler, particle and magnetic storms seem to be interesting and promising for further applications. The study of particle precipitation induced by geomagnetic storms has been already published. The analysis is still in progress in order to confirm and improve quality of results obtained up to now.

Riassunto

Questo lavoro di tesi è stato effettuato in co-tutela tra le Università di Roma Tre ed Orleans, nell'ambito del programma "Vinci" dell'Università Italo-Francese. La ricerca ha riguardato lo studio di dati di campo elettromagnetico (EM) e di particelle rivelati dal satellite DEMETER, tutt'ora in volo (la fine della missione è prevista per dicembre 2008), al fine di evidenziare perturbazioni iono-magnetosferiche e relative sorgenti. In particolare sono state studiate le correlazioni spazio-temporali tra whistlers anomali ed attività sismica, la precipitazione di particelle dalle fasce di radiazione indotta da emissioni sismo-elettromagnetiche e gli effetti di tempeste magnetiche sulle fasce di Van Allen. I risultati ottenuti sono interessanti e passibili di ulteriori sviluppi. Per quanto attiene i whistlers, utilizzando i dati originali ottenuti dalla rete neurale RNF di DEMETER, è stato inizialmente sviluppato un software speciale, denominato WHIMAP, per costruire il database dei whistlers da utilizzare nello studio. Quindi si è costruito il database dei terremoti, i quali successivamente sono stati correlati con i whistlers. Dall'analisi dei dati di campo elettrico e magnetico ottenuti a bordo del satellite, è stato sviluppato un metodo ad hoc per studiare l'influenza dell'attività sismica sulla propagazione di onde whistlers. Applicando questo metodo ai dati, si è visto che il numero di whistlers in zone prossime ai terremoti ed ai loro punti geomagneticamente coniugati, è sensibilmente perturbato rispetto a quello registrato mediamente nelle stesse zone. Il risultato è particolarmente evidente per alti valori del coefficiente di

dispersione dei whistlers. Allo stato delle conoscenze attuali non è stato ancora possibile discriminare se le fluttuazioni anomale di whistlers abbiano carattere pre-sismico, co-sismico o post-sismico, essendo possibile soltanto rilevare tali perturbazioni in intervalli temporali che includono l'avvento di terremoti. Si tratta del primo studio in assoluto della correlazione tra perturbazioni elettromagnetiche indotte dall'attività sismica e la propagazione di whistlers basato su dati satellitari. Nella seconda parte della tesi è stato condotto uno studio sui flussi di particelle magnetosferiche che ha fornito ulteriori informazioni. Per questa analisi è stato sviluppato il software PARMAP col quale è stato possibile costruire il database delle particelle a partire dai dati originali ottenuti dal contatore IDP montato a bordo del satellite DEMETER. PARMAP consente di leggere i dati rivelati da IDP sia in "burst" mode ad 1 Hz sia in "survey" mode a 0.25 Hz, evitando il problema della differente frequenza di campionamento. In questa parte del lavoro si è studiato l'effetto delle emissioni sismo-elettromagnetiche sulla precipitazione di particelle intrappolate nella fascia di radiazione interna. Lo studio, ancora preliminare, della correlazione tra la precipitazione di flussi anomali di particelle misurati da DEMETER e l'avvento di terremoti (effettuato secondo una metodologia messa a punto in un precedente studio di Sgrigna et al., 2005, riguardante la missione SAMPEX-PET della NASA) non ha mostrato l'esistenza di alcuna correlazione spazio-temporale. Ciò è probabilmente da addebitarsi ad alcune caratteristiche del contatore IDP e del suo programma di puntamento che sono risultati essere assai diversi dal contatore PET (energia delle particelle rivelabili notevolmente inferiore, un puntamento del contatore che favorisce principalmente la rivelazione di particelle intrappolate anziché di quelle nel cono di perdita). Lo studio è ancora in corso in quanto si sta cercando di approfondire alcuni aspetti del funzionamento del contatore IDP quali la risoluzione in energia (capacità di discriminazione tra particelle di energia bassa, media ed alta) e il comportamento nel passaggio tra una frequenza di campionamento e l'altra (burst mode e survey mode). I risultati così ottenuti confermano quelli della precedente analisi dei dati di SAMPEX a bassa energia. Infine nell'ultima parte del lavoro di tesi è stato studiato l'effetto delle tempeste magnetiche sulla precipitazione di particelle magnetosferiche. È stato osservato che durante intense tempeste magnetiche la precipitazione delle particelle avviene principalmente con il meccanismo di riso-

nanza ciclotronica. In particolare le misure a bordo del satellite DEMETER in concomitanza con grandi tempeste magnetiche, hanno evidenziato picchi di flussi di particelle che sono risultati essere consistenti con quelli attesi dal meccanismo di accoppiamento di risonanza ciclotronica tra onde e particelle in girazione lungo le linee di forza del campo geomagnetico. Questo risultato è stato presentato a due congressi internazionali (Buzzi et al., 2006; Parrot et al., 2006) e pubblicato su una rivista internazionale con referee (Parrot et al., 2006) con la dottoranda quale co-autore in entrambe le occasioni. Più in generale, durante il suo lavoro di tesi la candidata ha prodotto, come co-autore, cinque articoli e partecipato a dieci congressi internazionali e workshops specifici della tematica in questione. In sintesi, i risultati ottenuti in questa ricerca sembrano assai interessanti e promettenti per futuri sviluppi ed applicazioni. Il lavoro è ancora in corso per confermare e migliorare la qualità dei risultati ottenuti. In particolare, per ciò che concerne la correlazione tra whistlers e EQs è stata prevista una estensione fino ad alcuni giorni della finestra temporale centrata sugli EQs, si è deciso di ripetere l'analisi statistica utilizzando EQs con distribuzione random e l'intera analisi all'intero periodo di misure di DEMETER, fino a novembre 2006 (i dati degli indici geomagnetici Ap e Dst non sono purtroppo stati ancora resi disponibili dal NOAA).

Résumé

Le travail principal de cette thèse concerne l'étude des corrélations entre l'activité sismique et divers paramètres mesurés par le satellite DEMETER : les sifflements ayant une dispersion anormale d'une part et les précipitations de particules contenues dans les ceintures de radiation d'autre part. Les sifflements sont des ondes électromagnétiques engendrées par les éclairs atmosphériques lors des orages et qui peuvent se propager d'un hémisphère à l'autre dans la magnétosphère. Ils sont enregistrés par l'expérience RNF à bord de DEMETER qui comporte un réseau de neurones pour les détecter et les trier suivant leur dispersion. La principale caractéristique qui concerne la propagation des sifflements est la dispersion en fréquence de ces ondes au cours du temps qui est due au fait que la vitesse de propagation d'un hémisphère à l'autre varie en fonction de la fréquence et en fonction des paramètres du milieu parcouru. Un logiciel spécial WHIMAP a été développé pour construire la base de données qui est utilisée dans cette étude. En plus des informations sur les sifflements, la base comporte des informations sur l'orbitographie du satellite (y compris sur les coordonnées liées au champ magnétique terrestre) et sur les paramètres caractérisant l'activité magnétique. Puis une base de données sur les tremblements de Terre a été créée pour la corréler avec les sifflements. A partir des données électromagnétiques relatives aux sifflements une méthode appropriée a été développée pour chercher si l'activité sismique pouvait avoir une influence sur la propagation de ces sifflements dans la magnétosphère.

En appliquant notre méthode d'analyse on montre que le nombre de sifflements ayant une grande dispersion est plus important près des séismes ou de leurs points conjugués magnétiques que le long de la ligne de champ magnétique. Ce résultat est d'autant plus évident pour les classes de sifflements qui ont des dispersions comprises entre 30 et 100 $s^{1/2}$. Par contre cette analyse ne montre pas de dépendance en fonction du temps ce qui indique que l'on ne peut pas distinguer si cet accroissement anormal du nombre de sifflements est du à un effet pré-, co-, ou post séismique. Ceci est la première étude de corrélation entre l'activité séismique et les sifflements recueillis par un satellite. Un article est en préparation pour être soumis à un journal scientifique international. Dans la seconde partie de cette thèse nous avons étudié les flux de particules détectés par DEMETER. Pour cette analyse un logiciel spécial (PARMAP) a aussi été développé pour construire une base de données à partir des données originales de l'instrument compteur de particules IDP. PARMAP permet de lire les données particules détectées par IDP dans le mode burst comme dans le survey en homogénéisant les données qui sont acquises avec des vitesses différentes dans ces deux modes. Cette étude a été menée pour rechercher des corrélations entre les précipitations anormales des particules contenues dans les ceintures de radiation de Van Allen et des tremblements de Terre ayant des magnitudes modérées et fortes. La méthode utilisée est similaire aux travaux précédents sur les données particules recueillies par la mission SAMPEX-PET (Sgrigna et al., 2005). Mais contrairement aux résultats obtenus par cette analyse les données IDP ne montrent pas de corrélation significative entre les deux bases. Plusieurs raisons peuvent expliquer cette discordance. En fait la gamme d'énergie des particules détectées par IDP est beaucoup plus basse que celle du détecteur de SAMPEX-PET, et à cause de l'orientation de IDP, les données qu'il collecte sont principalement constituées de particules piégées. Des investigations supplémentaires sont aussi nécessaires pour étudier l'aptitude de IDP pour discriminer les particules de basse, moyenne, et haute énergie et aussi il faut analyser les problèmes potentiels qui peuvent survenir lors de la transition entre mode burst et mode survey. Donc cette analyse se poursuit pour mieux comprendre le comportement de l'analyseur IDP. La troisième partie de la thèse est dédiée à l'analyse de l'effet des orages magnétiques sur les particules qui sont dans les ceintures de radiation. En

accord avec un modèle déjà proposé par quelques auteurs, une application a été faite pendant des orages magnétiques très intenses qui montre que les précipitations de particules sont induites par le mécanisme de résonance cyclotronique. En particulier, des bouffées de particules énergétiques ont été observées par IDP pendant plusieurs orbites qui sont consistantes avec le mécanisme de couplage de résonance cyclotronique entre des ondes électromagnétiques de type cyclotronique ionique à une certaine fréquence et les particules à une énergie donnée qui se déplacent sur les lignes de force du champ magnétique. Ce résultat a été présenté dans deux congrès internationaux (Buzzi et al., 2006; Parrot et al., 2006). Il a été publié dans un journal international (Parrot et al., 2006), et un autre article est en préparation. Pendant cette thèse quatre autres papiers ont été produits et neuf participations à des congrès ont été faites (voir la liste de références). Tous les résultats présentés ci-dessus montrent que le travail produit est intéressant et prometteur pour de nouvelles applications. Ce travail continue pour confirmer et améliorer la qualité des résultats avec de nouvelles données collectées par le satellite DEMETER qui est toujours en activité.

Contents

1	Science Background	21
1.1	The ionosphere-magnetosphere “privileged” transition region.	21
1.1.1	The magnetic cavity	22
1.1.2	The geomagnetic field	24
1.1.3	Solar wind	25
1.1.4	The external magnetic field and electric current systems	25
1.1.5	The Van Allen radiation belts	27
1.1.6	The atmosphere of the Earth	33
1.1.7	Location of the ionosphere-magnetosphere transition zone	36
1.2	Main phenomena inside the magnetic cavity: Geomagnetic Substorms .	37
1.3	Atmosphere-ionosphere coupling during thunderstorm activity	38
1.3.1	Whistlers	38
1.3.2	ELF/VLF magnetospheric emissions: hiss, chorus, discrete emissions	40
1.4	The seismic activity. Is the earthquake a natural predictable disaster? . .	43
1.4.1	Earthquake phenomenology	44
1.4.2	Energy budget	45
1.4.3	Earthquake space distribution	47
2	Pre-earthquake Phenomena: observations and modeling	50
2.1	Earthquake generation mechanisms: dilatancy models	50
2.2	Seismo-associated phenomena and earthquake precursors	55
2.3	Earthquake precursors. Space and ground-based investigations.	57
2.4	Observations of lithospheric and ionospheric pre-seismic perturbations .	58
2.4.1	Local ground-based measurements.	59
2.4.2	Space observations	63

2.4.3	Longitudinal size of ionospheric perturbations from seismo-associated phenomena	66
2.5	Some theoretical approaches	69
2.5.1	ElectroKinetic effect (EKE)	71
2.5.2	Piezoelectric effect	74
2.5.3	Magnetostriction of ferromagnetic materials	75
2.5.4	Piezomagnetism and magnetoelectric effects in anti-ferromagnetic materials	75
2.5.5	Exoelectron emission and charge generation and propagation in igneous rocks	77
2.5.6	Fracturing as an underlying mechanism of seismo-electric signals (SES)	78
2.5.7	EMEs generation due to Moving Charged Dislocations (MCD)	79
2.5.8	ULF EMEs generated by Magnetic Pulses (MP)	80
2.5.9	Generation of ULF seismogenic electromagnetic emission	80
2.5.10	Attenuation of EME waves in the lithosphere and their penetration into the near Earth's space	81
2.6	The state of scientific knowledge relevant for the study: gaps and issues	83
2.7	A qualitative representation of the phenomenology	86
3	Demeter satellite	88
3.1	Demeter mission	88
3.2	Introduction to Neural network background	94
3.3	Application of neural network on continuous sets of Demeter data	97
3.4	IDP spectrometer	105
4	Study of the possible correlation between earthquakes and whistlers recorded by DEMETER	110
4.1	Ground-based observations of the influence of seismic activity on the whistlers propagation	110
4.2	Study of the EQ-whistler correlation using DEMETER observations	111
4.3	EQs database	112
4.4	WHIMAP whistler database	117
4.5	Space and time whistler distribution	119
4.6	Construction of the EQ-whistler correlation estimators: Δw_σ and $hcum_{ratio}$	126
4.7	Selection of whistler data using EQ magnetic field line	128

4.8	Stability of the correlation estimators	131
4.9	Analysis of EQ-whistler correlation	148
4.10	Analysis of EQ-whistler correlation using normalized magnetic field line distance	163
5	Testing temporal correlations between earthquakes and IDP anomalous particle bursts	185
5.1	Seismo induced particle precipitation	185
5.2	IDP-PARMAP database	186
5.3	Anomalous counting-rate events: PBs selection	199
5.4	Earthquake database	200
5.5	Analysis of temporal correlation between PBs and EQs	201
5.6	Results of the EQ-PB analysis	203
6	A comparative study of particle measurements by Demeter and model of wave-particle interaction during a magnetic storm .	205
6.1	Magnetospheric plasma interactions through waves	205
6.1.1	EMIC Waves	206
6.1.2	Whistler mode wave	207
6.1.3	Plasmaspheric hiss	208
6.2	Wave-particle interaction	209
6.2.1	L-dependent peaks in the energy spectra of electron precipitating from the inner belt	210
6.2.2	Physics of nonrelativistic and relativistic wave-particle interaction	212
6.3	New observations of ELF emissions by the Demeter satellite during large magnetic storms and interaction with the electron populations	216
	Conclusions and Outlook	227
	References	233

List of Figures

1.1	Schematic of the Earth's magnetosphere, with principal particle regions (adapted from T. W. Hill). The direction to the Sun is to the left. The interplanetary magnetic field (IMF), imbedded in the solar wind, impinges upon the magnetopause. If southward, as here, it connects to the Earth's magnetic field at the X-line (shown as circle with X inside), resulting in a region of field lines connecting from the Earth to deep space. Plasma from the solar wind enters via the cusp, becomes trapped in the plasma sheets, and eventually precipitates to Earth or is lost down the magnetotail, [http://space.rice.edu/IMAGE/livefrom/sunearth.html].	22
1.2	View of the magnetosphere showing wind currents, fields, and plasma regions.	23
1.3	Earth's radiation belts. The panels show the counters of the omni-directional flux of protons with energies greater than 10 MeV (top panel) and electrons with energies greater than 0.5 MeV (bottom panel), [M.G. Kivelson and C.T. Russell, 1995].	27
1.4	A graphical depiction of the Earth's radiation belts, showing the inner and outer radiation belts to scale, [http://www.nasa.gov/vision/universe/solarsystem/killer-electrons.html].	28
1.5	Trajectory of trapped electrons and protons experiencing magnetic mirroring and gradient and curvature drifts in the geomagnetic field.	29
1.6	Characteristic motions of a particle trapped in the Van Allen radiation belt, [http://www-spc.igpp.ucla.edu/ssc/tutorial/msphere07.thumb.gif].	29
1.7	Longitude drift caused by a gradient in geomagnetic field intensity, (Hargreaves, 1992).	31
1.8	Typical pitch-angle distribution at three latitudes on the $L = 3$ field line (Walt, 1994).	32
1.9	The upper neutral atmosphere. Nomenclature based on temperature, composition, mixing and ionization. (Hargreaves, 1992)	34
1.10	Electron density of the Earth's ionosphere as a function of altitude.	35

1.11	Whistler waves propagation in the magnetosphere, [http://www-star.stanford.edu/vlf/Science/Science.html].	39
1.12	Spectrogram of whistler and sferic from North America received at Palmer station, Antarctica. The vertical axis denotes frequencies from 0 to 10 kHz, and the horizontal axis covers 5 s. Intensities are labelled by colour, red being greatest. Labelled by the arrow is the sferic from the lightning flash that launched the whistler. From the Stanford VLF group website (http://wwwstar.stanford.edu/vlf/Science/Science.html).	40
1.13	Schematic representation of the complex interactions between whistler waves and electrons in the magnetosphere and consequent formation of <i>chorus</i> , <i>discrete emissions</i> , and <i>hiss</i> (black space region A).	41
1.14	Chorus emission frequency time spectra observed on board of the DE1 satellite (Poulsen and Inan, 1988).	42
1.15	Characteristic frequency-time spectrum of discrete emissions detected on board DE1, ISEE1, and ISIS2 satellites (Poulsen and Inan, 1988).	43
1.16	Three types of seismic events. (a) ordinary earthquake; (b) slow earthquake; (c) silent earthquake	45
1.17	Earthquake events organized according to depth (yellow(shallow)=surface to 25 km below the surface, red(intermediate)=26 to 75 km below the surface, and black(deep) \leq 76 km below the surface	48
1.18	Typical earthquake hypocentral distribution obtained for earthquakes with magnitude > 3.0 observed over the world in the period 1990 – 2000. (Sgrigna, V., 2001)	48
1.19	Epicentral distribution of the earthquakes reported in the previous figure 1.18. (Sgrigna, V., 2001)	49
2.1	Evolution of a seismic deformation process from the fault seismic slippage to coalescence and fracture. Fault asperities and final seismic fracture are shown. During the deformation process dilatancy is reported as to occur at the third step of the cracking evolution (boldfaced rectangle).	52
2.2	Different rock behaviours (stages I-IV) prior to an earthquake (seismic rupture) represented by the elastic potential energy W as a function of time.	53

2.3	[a] Seismic events occurred in the central Apennines of Italy (points) and the four PES, AQU, GRS, and STI tilt sites (stars) used for the study (left panel). [b] the four upper lines of the central panel indicate GRS, AQU, and PES residual preseismic tilt anomalies over the 3σ (standard deviation) level, and the STI residual (normal) tilt signal. Earthquakes of the Umbria-Marche sequence and related cumulative energy release are reported in the two bottom lines of the same panel. [c] best tilt anomaly fitting by using creep curves from Kelvin-Voigt model (upper right panel) and theoretical 2D crust block modeling (bottom right panel).	61
2.4	ULF magnetic variations before the Loma Prieta earthquake (Fraser-Smith et al., 1990) on the left. Variation of the H-component amplitude of the ULF EME before the Spitak earthquake (Kopytenko et al., 1993) on the right.	62
2.5	Preseismic VLF EME anomaly from a narrow band receiver centered at 81 kHz (Gokhberg et al., 1982).	62
2.6	Preseismic variation of the hourly number of LF EME.	62
2.7	(a) Orbit of AUREOL-3 satellite. (b) and (c) Time variations of the electric component signal in filters centered around 72 Hz and 150 Hz, respectively, [Parrot and Mogilevsky, 1989].	64
2.8	Result from statistical study using AUREOL 3 satellite, [Parrot, 1994].	65
2.9	A double measurement of seismic EMEs (AUREOL-3 and ITK-1300), in two different frequency band ($40 \div 100$ Hz and $100 \div 200$ Hz), observed above Spitak seismic areas ~ 4 h before a terrible and strong aftershock (January, 21, 1989) (Galperin, 1992).	66
2.10	Histograms of the time difference between time differences $\Delta T = T_{EQ} - T_{PB}$, between the universal times of origin of selected earthquake (T_{EQ}) and PB (T_{PB}) events for four space missions. A positive and significant peak in the histogram (that is a peak in the $\Delta T > 0$ region) indicates that PBs statistically precede in time the earthquake occurrence (Aleksandrin et al., 2003; Sgrigna et al., 2005).	68
2.11	Diagram of an electric double layer and profiles of the electric potential and liquid velocity in a rock pore.	72
2.12	Transfer coefficient of the energy of the magnetic field, between the source and the magnetosphere, as a function of the frequency. Different conditions (curves) are explained in the text.	83
2.13	Qualitative representation of the phenomenology, [Sgrigna, V., 2001].	86

3.1	Summary of statistical studies performed making use of satellite data, [Parrot <i>et al.</i> , 2006].	88
3.2	Myriade platform performances and DEMETER Measured Parameters, [Cussac <i>et al.</i> , 2006].	90
3.3	Picture of the Demeter satellite in flight with its deployed booms and sensors, [Cussac <i>et al.</i> , 2006].	90
3.4	Layout of the Demeter satellite, [Cussac <i>et al.</i> , 2006].	91
3.5	Burst and Survey mode of Demeter satellite.	93
3.6	Neural Network unit or neuron. The neuron sums N weighted inputs and passes the result through a non-linearity process. Here, a sigmoid function is used. The threshold value of sigmoid can be adjusted by using an additional weighted connection to a constant input, [J-L.Pinçon, Demeter Guest Investigator Workshop, 2-4 May 2005].	95
3.7	The neural network architecture used for whistler detection onboard Demeter, [J-L.Pinçon, Demeter Guest Investigator Workshop, 2-4 May 2005].	96
3.8	Example of waveform, spectrogram and input pattern used for whistler detection onboard Demeter, [J-L.Pinçon, Demeter Guest Investigator Workshop, 2-4 May 2005].	98
3.9	Description of neural network output: identification and classification of whistlers [J-L.Pinçon, Demeter Guest Investigator Workshop, 2-4 May 2005].	99
3.10	Level-1 data block types.	100
3.11	Common block 1: general header.	101
3.12	Common block 2: orbital and geomagnetic parameters.	101
3.13	Common block 3: attitude parameters.	102
3.14	Block 4: RNF detection results.	102
3.15	Top panel: spectrogram of data to be analyzed. Bottom panel: corresponding dispersion parameters given by neural networks system, [J-L.Pinçon, Demeter Guest Investigator Workshop, 2-4 May 2005].	103
3.16	Application of neural network to a continuous set of Demeter data.(a) Spectrogram of ICE data to be analyzed and obtained during August 2 2005, orbit 5759 – 1 in the night time; (b) Dispersion time obtain from RNF analysis, [J-L.Pinçon, Demeter Guest Investigator Workshop, 2-4 May 2005].	104
3.17	Principal characteristics of IDP detector, [Sauvaud <i>et al.</i> , 2006].	105
3.18	Cross-sectional view of IDP, showing the collimator in aluminum (green), the Al foil aimed to stop UV photons and protons with energies lower than 500 keV, and the silicon detector (red), [Sauvaud <i>et al.</i> , 2006].	105

3.19	The IDP spectrometer installed on the Demeter satellite, [Sauvaud <i>et al.</i> , 2006]. .	106
3.20	(a) Distribution of the energy deposited inside the detector for wide incident mono-energetic beams, (b) Variation of the geometry factor of IDP as a function of energy, [Sauvaud <i>et al.</i> , 2006].	108
3.21	Block 4: IDP Burst results.	108
3.22	Block 4: IDP Survey results.	109
4.1	Statistical results of comparison between the annual number of local EQs with $M > 6$ and number of days with anomalous whistlers observed at Sugadaira and Moshiri observatory during 1970-1978. Location (left panel) of Sugadaira, Sakushima and Moshiri whistler observatories and their conjugate points, together with those of earthquakes. The full lines indicate the ground projection of the magnetic field line connecting Sugadaira and its conjugate point.	112
4.2	Locations of earthquake epicenters from 2005/05/25 to 2006/04/30 used in the statistical study. Black crosses indicate the EQ epicenters.	113
4.3	Distributions of earthquakes (EQs) and their geomagnetic conjugate points (CPs). Histograms of the CP geocentric latitude (a), CP geocentric longitude (b), EQ magnitude (c), EQ depth (d), EQ magnetic longitude (e), EQ geocentric latitude, EQ geomagnetic latitude and difference of the geocentric latitude between CP and EQ (f).	114
4.4	Schematic illustration EQ magnetic field line, up the EQ conjugate point CP. Also the intersection points between the EQ field line and Demeter orbit are shown.	115
4.5	Selected EQs occurred in the period July, August and September 2005. Black crosses indicate EQ epicenters and blue lines the associated magnetic field lines (see text).	116
4.6	The WHIMAP database.	118
4.7	Geographic distributions of number of whistlers during August 2005. Data are reported separately for Day-times and Night-times and for classes 1-5. The $\langle w(lat, long, 1month) \rangle_{cell}$ data have been integrated over cells of $4^\circ \times 4^\circ$ latitude and longitude intervals.	120
4.8	Geographic distributions of number of whistlers during August 2005. Data are reported separately for Day-times and Night-times and for classes 6-10. The $\langle w(lat, long, 1month) \rangle_{cell}$ data have been integrated over cells of $4^\circ \times 4^\circ$ latitude and longitude intervals.	121

4.9	Geographic distributions of number of whistlers during August 2005. Data are reported separately for Day-times and Night-times and for classes 11-15. The $\langle w(lat, long, 1month) \rangle_{cell}$ data have been integrated over cells of $4^\circ \times 4^\circ$ latitude and longitude intervals.	122
4.10	Geographic distributions of number of whistlers during August 2005. Data are reported separately for Day-times and Night-times and for classes 16-19. The $\langle w(lat, long, 1month) \rangle_{cell}$ data have been integrated over cells of $4^\circ \times 4^\circ$ latitude and longitude intervals.	123
4.11	Geographic distributions of number of Demeter observations during a)Daytime and b)Nighttime in the month of August 2005.	124
4.12	Geographic distribution of number of whistler normalized to the number of Demeter tracks in each cell for the 19^{th} class of dispersion coefficient during a)Daytime and b)Nighttime in the month of August 2005. Red crosses indicate, the positions of VLF Russian transmitters and their geomagnetic conjugate points, [J-L.Pinçon, Demeter International Symposium, Toulouse (France), June 14-16, 2006].	125
4.13	Geographic coordinate of VLF Russian transmitters reported in figure 4.12 and their conjugate points, [J-L.Pinçon, Demeter International Symposium, Toulouse (France), June 14-16, 2006].	126
4.14	Example of the projection at the Earth surface of the magnetic field line which footprint is the epicenter of EQ (2006/04/01 with M=4.8).The crosses indicate the latitude, longitude range around the field line inside which Demeter data are accepted for the study.	126
4.15	An example of probability distribution of number of whistlers for dispersion coefficient class 2^{th} related to 15 geographic cells of $20 \text{ degrees} \times 10 \text{ degrees}$	128
4.16	From top to bottom, distribution of number of whistlers , total number of measurements collected, normalized number of whistlers $w(lat, long, 1month)$ during August 2005 in Day-time (left panels) and Night-time (right panels) for dispersion class 1.	129
4.17	Geographic distribution of Demeter observation that satisfy the cut $T_D - T_{EQ} \leq \pm 48 \text{ h}$ and occurring along the EQ magnetic field line for the analyzed time interval.	131

4.18	Distribution of number of whistlers selected for the correlation with EQs averaged over all latitude and longitude ranges, v.s. dispersion classes and Demeter U.T. (a) v.s. dispersion values and Demeter UT (b). In panel (c) is shown the standard score of number of whistlers selected for correlation with EQs. Data are related to the whole time interval.	133
4.19	Geographic distribution of estimator Δw_σ selected for correlation with EQ for whistler dispersion coefficient classes from 00 to 09 during Daytime. Data have been averaged over the whole time interval.	135
4.20	Geographic distribution of estimator Δw_σ selected for correlation with EQ for whistler dispersion coefficient classes from 10 to 18 during Daytime. Data have been averaged over the whole time interval.	136
4.21	Geographic distribution of estimator Δw_σ selected for correlation with EQ for whistler dispersion coefficient classes from 00 to 09 during Nighttime. Data have been averaged over the whole time interval.	137
4.22	Geographic distribution of estimator Δw_σ selected for correlation with EQ for whistler dispersion coefficient classes from 10 to 18 during Nighttime. Data have been averaged over the whole time interval analyzed June 2005-April 2006.	138
4.23	Geographic distribution of estimator Δw_σ selected for correlation with EQ for whistler dispersion coefficient classes from 00 to 09 during Nighttime+Daytime. Data have been averaged over the whole time interval.	139
4.24	Geographic distribution of estimator Δw_σ selected for correlation with EQ for whistler dispersion coefficient classes from 10 to 18 during Nighttime+Daytime. Data have been averaged over the whole time interval.	140
4.25	Geographic distribution of estimator $hcum_{ratio}$ selected for correlation with EQ for whistler dispersion coefficient classes from 00 to 09 during Daytime. Data have been averaged over the whole time interval.	141
4.26	Geographic distribution of estimator $hcum_{ratio}$ selected for correlation with EQ for whistler dispersion coefficient classes from 10 to 18 during Daytime. Data have been averaged over the whole time interval.	142
4.27	Geographic distribution of estimator $hcum_{ratio}$ selected for correlation with EQ for whistler dispersion coefficient classes from 00 to 09 during Nighttime. Data have been averaged over the whole time interval.	143
4.28	Geographic distribution of estimator $hcum_{ratio}$ selected for correlation with EQ for whistler dispersion coefficient classes from 10 to 18 during Nighttime. Data have been averaged over the whole time interval.	144

4.29	Geographic distribution of estimator $hcum_{ratio}$ selected for correlation with EQ for whistler dispersion coefficient classes from 00 to 09 during Nighttime+Daytime. Data have been averaged over the whole time interval.	145
4.30	Geographic distribution of estimator $hcum_{ratio}$ selected for correlation with EQ for whistler dispersion coefficient classes from 10 to 18 during Nighttime+Daytime. Data have been averaged over the whole time interval.	146
4.31	Geographic distribution of Δw_{σ} selected for correlation with EQ (a) and $hcum_{ratio}$ (b) averaged over whistler dispersion classes from 00 to 18, during Daytime(top), Nighttime (center), Nighttime+Daytime (bottom). Data have been averaged over the whole time interval.	147
4.32	Geographic distribution of EQs after cuts have been applied on $\Delta t, \Delta latmag$ and Ap index for the period May 25, 2005-April 30, 2006.	148
4.33	Δw_{σ} distributions from 2005/05/25 to 2006/04/30 for whistler dispersion classes from 00 to 04 v.s. a)($\Delta latmag, \Delta t$) b) $abs(\Delta latmag, \Delta t)$ and c) Δt after an averaging over $\Delta latmag$	153
4.34	Δw_{σ} distributions from 2005/05/25 to 2006/04/30 for whistler dispersion classes from 05 to 09 a)($\Delta latmag, \Delta t$) b) $abs(\Delta latmag, \Delta t)$ and c) Δt after an averaging over $\Delta latmag$	154
4.35	Δw_{σ} distributions from 2005/05/25 to 2006/04/30 for whistler dispersion classes from 10 to 14 a)($\Delta latmag, \Delta t$) b) $abs(\Delta latmag, \Delta t)$ and c) Δt after an averaging over $\Delta latmag$	155
4.36	Δw_{σ} distributions from 2005/05/25 to 2006/04/30 for whistler dispersion classes from 15 to 18 a)($\Delta latmag, \Delta t$) b) $abs(\Delta latmag, \Delta t)$ and c) Δt after an averaging over $\Delta latmag$	156
4.37	$hcum_{ratio}$ distributions from 2005/05/25 to 2006/04/30 for whistler dispersion classes from 00 to 04 a)($\Delta latmag, \Delta t$) b) $abs(\Delta latmag, \Delta t)$ and c) Δt after an averaging over $\Delta latmag$	157
4.38	$hcum_{ratio}$ distributions from 2005/05/25 to 2006/04/30 for whistler dispersion classes from 05 to 09 a)($\Delta latmag, \Delta t$) b) $abs(\Delta latmag, \Delta t)$ and c) Δt after an averaging over $\Delta latmag$	158
4.39	$hcum_{ratio}$ distributions from 2005/05/25 to 2006/04/30 for whistler dispersion classes from 10 to 14 a)($\Delta latmag, \Delta t$) b) $abs(\Delta latmag, \Delta t)$ and c) Δt after an averaging over $\Delta latmag$	159
4.40	$hcum_{ratio}$ distributions from 2005/05/25 to 2006/04/30 for whistler dispersion classes from 15 to 18 a)($\Delta latmag, \Delta t$) b) $abs(\Delta latmag, \Delta t)$ and c) Δt after an averaging over $\Delta latmag$	160

4.41	Δw_σ averaged over all whistler classes (1-19) (according to eq.(4.11)) vs. $abs(\Delta latmag)$ and Δt (left panel) and vs. Δt (after an averaging over $\Delta latmag$) (right panel). Time interval is from 2005/05/25 to 2006/04/30.	161
4.42	Distribution of Demeter whistler observations as a function $\Delta latmag$ and Δt , satisfying cuts applied to the whistler–EQ analysis.	162
4.43	Δw_σ v.s $nml d$ and Δt for whistler dispersion classes from 00 to 09 during Daytime.	165
4.44	Δw_σ $nml d$ and Δt for whistler dispersion classes from 10 to 18 during Daytime.	166
4.45	Δw_σ $nml d$ and Δt for whistler dispersion classes from 00 to 09 during Nighttime.	167
4.46	Δw_σ $nml d$ and Δt for whistler dispersion classes from 10 to 18 during Nighttime.	168
4.47	Δw_σ $nml d$ and Δt for whistler dispersion classes from 00 to 09 during Nighttime+Daytime.	169
4.48	Δw_σ $nml d$ and Δt for whistler dispersion classes from 10 to 18 during Nighttime+Daytime.	170
4.49	$hcum_{ratio}$ v.s $nml d$ and Δt for whistler dispersion classes from 00 to 09 during Daytime.	171
4.50	$hcum_{ratio}$ v.s $nml d$ and Δt for whistler dispersion classes from 10 to 18 during Daytime.	172
4.51	$hcum_{ratio}$ v.s. $nml d$ and Δt for whistler dispersion classes from 00 to 09 during Nighttime.	173
4.52	$hcum_{ratio}$ v.s. $nml d$ and Δt for whistler dispersion classes from 10 to 18 during Nighttime.. . . .	174
4.53	$hcum_{ratio}$ v.s. $nml d$ and Δt for whistler dispersion classes from 00 to 09 during Nighttime+Daytime.	175
4.54	$hcum_{ratio}$ for v.s $nml d$ and Δt for whistler dispersion classes from 10 to 18 during Nighttime+Daytime.	176
4.55	Δw_σ v.s $nml d$ and Δt averaged over dispersion classes from 00 to 06 a), from 07 to 12 b), from 13 to 18 c) during Daytime (top), Nighttime(center), Nighttime+Daytime (bottom).	178
4.56	$hcum_{ratio}$ v.s $nml d$ and Δt averaged over dispersion classes from 00 to 06 a), from 07 to 12 b), from 13 to 18 c) during Daytime (top), Nighttime(center), Nighttime+Daytime (bottom).	179

4.57	Δw_σ v.s n_{mld} and Δt averaged over dispersion classes from classes 00+02+04+06 a), 08+10+12 b), 14+16+18 c) during Daytime (top), Nighttime(center), Night-time+Daytime(bottom).	181
4.58	Δw_σ v.s n_{mld} and Δt averaged over dispersion classes from classes 01+03+05 a), 07+09+11 b), 13+15+17 c) during Daytime (top), Nighttime(center), Night-time+Daytime(bottom).	182
4.59	$hcum_{ratio}$ v.s n_{mld} and Δt averaged over dispersion classes from classes 00+02+04+06 a), 08+10+12 b), 14+16+18 c) during Daytime (top), Nighttime(center), Night-time+Daytime(bottom).	183
4.60	$hcum_{ratio}$ v.s n_{mld} and Δt averaged over dispersion classes from classes 01+03+05 a), 07+09+11 b), 13+15+17 c) during Daytime (top), Nighttime(center), Night-time+Daytime(bottom).	184
5.1	PARMAP database.	188
5.2	Geographic distribution of the survey (red) and burst (blue).	189
5.3	Geographic distribution (a) and histogram (b) of the IDP pitch angle during January 2005 . Observations are centered near 90° with a narrow range from $\sim 55^\circ$ up to $\sim 120^\circ$	189
5.4	Geographic distribution (a) and histogram (b) of DEMETER L-shell values in 1 month of observations (January 2005).	190
5.5	Distributions of IDP particle fluxes for 8 of the 128 PARMAP energy channels, as a function of α_{IDP} pitch angle (degrees) and L-shell. As an example, data collected in 1 month are reported. Energy channel increases from the top left panel to the bottom right one.	192
5.6	Distributions of IDP particle fluxes for 8 of the 128 PARMAP energy channels, as a function of α_{IDP} pitch angle (degrees) and L-shell. As an example, data collected in 1 month are reported. Energy channel increases from the top left panel to the bottom right one.	193
5.7	Geographic distributions of IDP-PARMAP particle fluxes for 8 of the 128 PARMAP energy channels. As an example, are reported data collected from July to December 2004 . Energy channel increases from the top left panel to the bottom right one.	194
5.8	Geographic distributions of IDP-PARMAP particle fluxes for 8 of the 128 PARMAP energy channels. As an example, are reported data collected from July to December 2004. Energy channel increases from the top left panel to the bottom right one.	195

5.9	(a) geographic distribution of the IDP total particle flux, (b) geographic distribution of the IDP total flux and contour plot of the regions where IDP data have been collected in the burst mode. The spurious little shift of the whole burst mode contour plot on the right is due to graphical reasons. In both (a) and (b) panels, all 128 PARMAP energy channels have been added during time until July 2004 to December 2004.	196
5.10	Geographic distribution of low (channels 0-42) (a), medium (channels 43-85) (b) and high (channels 86-127) (c) energy IDP particle fluxes.	198
5.11	Example of background $\{L, \alpha_{IDP}\}$ matrix analysis. Total IDP flux (black line) and poissonian fit (red line) for $1.7 < L < 1.8$ and $60^\circ < \alpha_{IDP} < 75^\circ$ cell. Cyan line is the cumulative number of DEMETER measurements in the given $\{L, \alpha_{IDP}\}$ cell normalized to the total number of days with observations. This acquisition rate (scale on the right) is plotted as a function of number of days (scale on the top) for 4 months of data.	200
5.12	Histogram of temporal correlations between PBs and EQs versus ΔT_{EQ-PB} . The bin step is 1 hour, the temporal window is 18 hours. There are no significant peak at any ΔT values neither positive nor negative.	203
6.1	Example of a nighttime pass of orbit 1891 on 9 November 2004, provides an overview of typical night time ELF and VLF electric fields measurements. Plasmaspheric hiss is clearly visible in the low latitude part of the orbit with a sharp cut-off which follows the H^+ gyrofrequency. At higher latitudes, structured VLF emissions dominate in two frequency ranges, from 2 to 3 kHz and above 6 kHz, extending above 20 kHz, the frequency limit of the VLF channel. At mid-latitudes the most intense and regular sources are the lightning generated whistler emissions clearly visible on the figure in particular around 12 : 38 UT at a latitude of $\sim 30^\circ$	208
6.2	The electron energies calculated for first-order cyclotron resonant interactions near the equator for waves traveling parallel to the magnetic field lines. The central energies of observed peaks are plotted for selected cases identified as being due to waves associated with VLF transmitters, or lightning or plasmaspheric hiss [Imhof <i>et al.</i> , 1996].	211
6.3	Schematic diagram showing spatial distribution of whistler mode waves and EMIC waves during magnetic storms. This map is taken from [Summers <i>et al.</i> , 1998]; the regions of wave activity are determined empirically from published data.	213
6.4	Dst for the magnetic storm of November 2004.	217

6.5	Dst for the magnetic storm of January 2005.	217
6.6	Dst for the magnetic storm of May 2005.	217
6.7	Electric, magnetic and particle data, recorded during a complete half-orbit on November 8, 2004 between 06:53:30 and 07:02:30 UT (night time).	218
6.8	Electric, magnetic and particle data, recorded during a complete half-orbit on November 9, 2004 between 20:25:30 and 20:59:30 UT (night time).	219
6.9	Electric, magnetic and particle data, recorded during a complete half-orbit on November 9, 2004 between 21:40:00 and 21:48:00 UT (night time).	219
6.10	Electric, magnetic and particle data, recorded during a complete half-orbit on January 21, 2004 between 22:36:00 and 23:09:28 UT (night time).	220
6.11	Electric, magnetic and particle data, recorded during a complete half-orbit on May 15, 2004 between 09:43:30 and 10:22:30 UT (day time).	220
6.12	Curves resonant energy for different frequencies v.s. L calculated resonant energies for different frequencies. The square represents experimental value energy from Demeter data along the for orbit 1873 – 1.	223
6.13	Curves resonant energy for different frequencies v.s. L calculated resonant energies for different frequencies. The square represents experimental value energy from Demeter data along the for orbit 1896 – 1.	223
6.14	Curves resonant energy for different frequencies v.s. L calculated resonant energies for different frequencies. The square represents experimental value energy from Demeter data along the for orbit 1897 – 0.	224
6.15	Curves resonant energy for different frequencies v.s. L calculated resonant energies for different frequencies. The square represents experimental value energy from Demeter data along the for orbit 2959 – 1.	224
6.16	Curves resonant energy for different frequencies v.s. L calculated resonant energies for different frequencies. The square represents experimental value energy from Demeter data along the for orbit 2959 – 1.	225
6.17	Curves resonant energy for different frequencies v.s. L calculated resonant energies for different frequencies. The square represents experimental value energy from Demeter data along the for orbit 2959 – 1.	225
6.18	Curves resonant energy for different frequencies v.s. L calculated resonant energies for different frequencies. The square represents experimental value energy from Demeter data along the for orbit 4611 – 0.	226

List of Tables

2.1	Dimensions of a preseismic spherical “dilatant” source (r) at depth and related Earth’s surface precursory area (R_P) for different values of the earthquake magnitude (M).	55
3.1	Class and dispersion values of whistlers.	100
4.1	EQ database defined by software MAGLIB.	116
4.2	$\Delta w_\sigma, hcum_{ratio}$ estimators of whistler–EQ correlation introduced in the analysis, together with their representation and cuts applied to data for selecting EQ and whistler populations to be correlated. Symbol $\langle \dots \rangle$ indicate the average on diverse whistler dispersion classes.	149
5.1	IDP characteristics	187
6.1	Parameters used to calculate energy kinetic in the relativistic case.	216
6.2	Parameters used to calculate the energy kinetic in the relativistic case	222
6.3	Orbit, UT, values of L frequency, electron kinetic energy calculated in the relativistic case and electron energy spectra measured on board of Demeter along selected orbits.	222

Chapter 1

Science Background

In this chapter I will remind basic concepts, which I consider to be important for the present study.

1.1 The ionosphere-magnetosphere “privileged” transition region.

The ionosphere-magnetosphere transition zone, at several hundred kilometres of altitude, is a particular, very important, and not well-known region of the near-Earth space, whose structure and dynamical behavior are regulated by natural Earth’s interior processes, and other sources (sun and cosmic rays) external to the magnetic cavity. External and internal sources play an important role in defining the particle and electromagnetic field character of the zone, both in steady-state and perturbed-state conditions. So, a suitable monitoring of this transition region, allowed by a space mission like the French microsatellite Demeter (see chapter 3) may give an help in understanding physical mechanisms of many largely unknown Earth’s interior processes and solar activity phenomena as well as in studying propagation effects of radiation (EM and acoustic waves) and stream of matter (solar wind) through layered media with or without a dispersive character.

The importance in investigating ionospheric perturbations caused by ground electro-

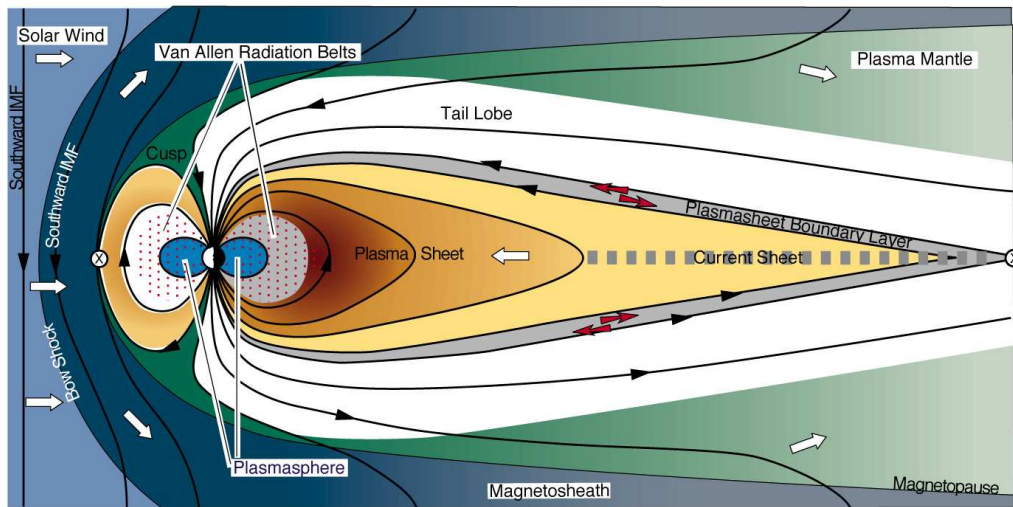


Figure 1.1: Schematic of the Earth's magnetosphere, with principal particle regions (adapted from T. W. Hill). The direction to the Sun is to the left. The interplanetary magnetic field (IMF), imbedded in the solar wind, impinges upon the magnetopause. If southward, as here, it connects to the Earth's magnetic field at the X-line (shown as circle with X inside), resulting in a region of field lines connecting from the Earth to deep space. Plasma from the solar wind enters via the cusp, becomes trapped in the plasma sheets, and eventually precipitates to Earth or is lost down the magnetotail, [<http://space.rice.edu/IMAGE/livefrom/sunearth.html>].

magnetic emissions (EME) generated by natural phenomena or human activities, lies in the possibility to attempt for prediction approaches in order to defend society from natural disasters, as earthquakes. To better introduce concepts underlying the study performed in this thesis work, the location and main features of the above-mentioned ionosphere-magnetosphere transition zone will shortly be focused in the following sections.

1.1.1 The magnetic cavity

Our Planet is a source of electric and magnetic fields, acoustic and electromagnetic emissions, and gas exhalation. Some of them are generated at the ground surface also by human activities. All these fields, wave-radiation, and gases propagate from the Earth's interior (where their sources are located in) through the stratified lithosphere and penetrate into the neutral and ionized atmosphere, up to the magnetosphere, giv-

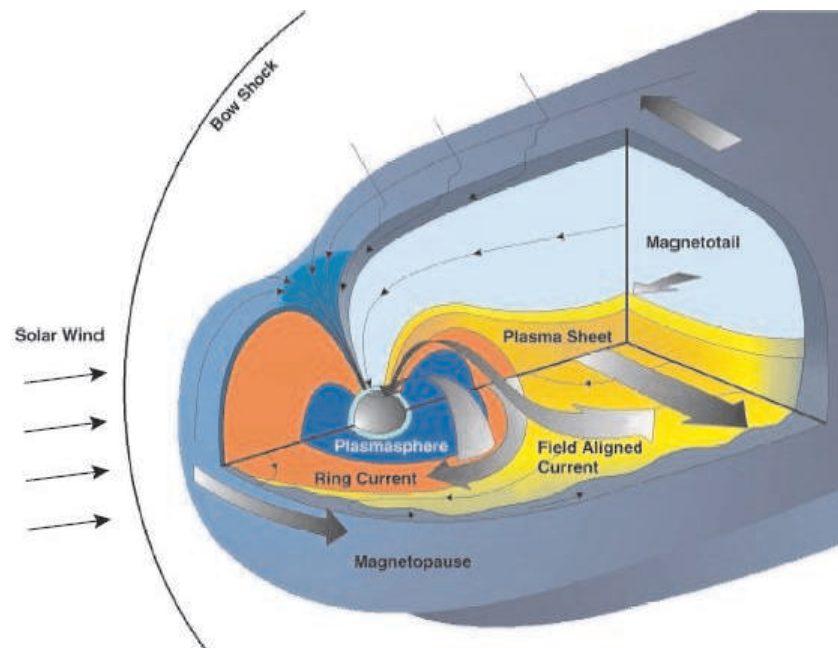


Figure 1.2: View of the magnetosphere showing wind currents, fields, and plasma regions.

ing rise to very important lithosphere-atmosphere-ionosphere-magnetosphere coupling interaction processes.

When taking into account external contributions to the ionosphere-magnetosphere transition zone, we have to consider the fact that the Earth is immersed in the solar *electromagnetic radiation*, in the rapidly expanding solar atmosphere consisting of a stream of matter (*solar wind*), and in the sporadic particle and electromagnetic solar emissions constituted by intense and localized outbursts (*solar flares*).

As a result of the supersonic expansion of the *solar corona*, the highly conducting plasma consisting of charged particles (electrons, protons and helium ions) of the solar wind interacts with the *geomagnetic field*. The balance between the dynamic pressure of the solar wind and the magnetic pressure of the Earth's magnetic field (which acts as a barrier) produces a distortion of the outer part of the geomagnetic field. This gives rise (fig. 1.2) to the *magnetosphere*, a *geomagnetic cavity* bounded by the *magnetopause* that separates the *external* plasma and magnetic field of solar origin from the *internal* plasma and magnetic field associated with the Earth (Parks, 1991).

1.1.2 The geomagnetic field

In the inner magnetosphere the main contribution to the geomagnetic field comes from the Earth's interior, a less important contribution coming from external currents. The expressions Ψ^i and Ψ^e of the potential field $\Psi(\vec{R})$ of these two components are:

$$\Psi^i = R_E \sum_{n=1}^{\infty} \left(\frac{R_E}{R} \right)^{n+1} \sum_{m=0}^{\infty} (C_n^m \sin m\phi + D_n^m \cos m\phi) P_n^m(\cos \vartheta)$$

$$\Psi^e = R_E \sum_{n=1}^{\infty} \left(\frac{R}{R_E} \right)^n \sum_{m=0}^{\infty} (\bar{C}_n^m \sin m\phi + \bar{D}_n^m \cos m\phi) P_n^m(\cos \vartheta)$$

where R_E is the Earth's radius, ϕ and ϑ are geomagnetic longitude and colatitude, respectively, P_n^m Legendre functions, quantities C, D, \bar{C}, \bar{D} are constants of integration, and n and m are separation constants.

Above the Earth's surface, within distances of several Earth radii from the Earth center, the geometrical pattern of the field is approximately a dipole, defined as follows:

$$B_R = 2 \frac{M}{R^3} \cos \vartheta$$

$$B_{\vartheta} = \frac{M}{R^3} \sin \vartheta$$

$$B_{\phi} = 0$$

where $M = B_0 R_E^3$ is the magnetic moment, and B_0 is the field intensity at the magnetic equator. The field intensity in a point near the Earth is given by:

$$B = \frac{M}{R^3} (1 + 3 \cos^2 \vartheta)^{1/2}$$

The geomagnetic field line equation, in Earth's radii units, is given by:

$$R = L \sin^2 \vartheta$$

where L is the McIlwain coordinate. On the Earth's surface the field assumes values ranging from about 0.3 G, at equatorial latitudes, to about 0.6 G in polar regions.

Since the geomagnetic field is not dipolar one, a more precise representation of such

a field is needed. The most important deviation with respect to the dipolar configuration is given by the South Atlantic Anomaly (SAA) where the intensity of the magnetic field assumes the lowest values. The International Geophysical Reference Field model (IGRF) is periodically updated and gives the most realistic description of the geomagnetic field.

1.1.3 Solar wind

Solar wind is mainly constituted by electrons, protons and an admixture of 5% helium ions, emitted by the Sun at supersonic speeds (about 500 km/s) into the interplanetary space as a result of the supersonic expansion of the solar corona.

When the solar wind hits the Earth’s dipolar magnetic field, it is slowed down generating a *bow shock* wave and, to a large extent, deflected around it. The region of thermalized subsonic plasma behind the bow shock is called the *magnetosheath*.

Plasma inside the magnetosphere is grouped into different regions with quite different densities and temperatures.

In midnightward the magnetic field lines are stretched in the *magnetotail* and field lines of opposite senses along the center of the tail (*neutral sheet*) are very close to each other. The low magnetic field in this region allows some penetration of the solar wind into the magnetosphere, causing a kink in the magnetopause (Kivelson and Russel, 1995). It is commonly argued that the magnetosphere is probably open (Stern, 1977) in the sense that some of the geomagnetic field lines connect with those of the interplanetary magnetic field.

1.1.4 The external magnetic field and electric current systems

The not complete separation of the internal geomagnetic field from the external one of solar origin requires boundary electric current systems and is believed to be important for the dynamics of the magnetosphere. In other words, the distortion of the terrestrial magnetic field into the typical shape of the magnetosphere is accompanied by electrical currents (fig. 1.2).

Large-scale currents in space are produced by the charged particles of the solar wind,

magnetosphere, and ionosphere. They are sources of magnetic fields and can be classified as boundary (or magnetopause) currents, ring currents, cross-tail currents, ionospheric currents (S_q , S_D , auroral and equatorial electrojets), and field-aligned currents. Magnetopause currents justify the separation between internal terrestrial magnetic field and external solar magnetic field. Ionospheric currents are generated by atmospheric winds and tidal oscillations of the atmosphere. Magnetotail currents are responsible for the long geomagnetic tail. Field-aligned currents are driven by the parallel electric field component. They connect the magnetospheric currents to those flowing in the polar ionosphere and that are essential for the exchange of energy and momentum between ionosphere and magnetosphere (Kivelson, 1995).

Although the electrical currents flowing inside the Earth are the most important currents in the production of the geomagnetic field, the external currents flowing in the magnetosphere also influence the field. These external currents are important at distances beyond about $4R_E$ and become dominant near the magnetopause or deep in the tail region. As stated earlier the primary magnetospheric current systems are the magnetopause currents, the ring current, the tail current sheet and the field-aligned currents. Although trapped particles rely on the properties of the core field for containment, the distortion of the core field by the external current systems is also relevant, and it is frequently necessary to include these systems in models of the geomagnetic field (Lagnel et al., 1996).

Also because the short-term time variations of the geomagnetic field in the trapping region are caused by changes in these external currents, modeling the field fluctuations requires modeling the external field produced by these currents.

Since the solar wind is highly variable in time, its pressure on the geomagnetic field will vary with time and will cause the magnetopause to change shape. This leads to changes in the magnetic field at the Earth's surface. However, tracing the sources of disturbance of the magnetic field at the Earth's surface is very difficult (Kan et al., 1990). This is because processes that occur in distant regions can induce other major disturbances within the ionosphere. Conversely, changes in ionospheric currents could lead to changes far above the ionosphere.

The ionosphere is electrically conducting and can support strong electric currents. The

ionized medium also affects radio waves, and as a plasma it can support and generate a variety of waves, interactions and instabilities that are not found in the neutral gas of the atmosphere.

1.1.5 The Van Allen radiation belts

The Earth’s magnetosphere is not in a steady-state. The overall size varies with solar wind velocity and density and internal instabilities cause changes in the tail structures. Also the direction of the interplanetary magnetic field carried by the solar wind affects the character of the connections between solar and terrestrial field lines (Brautigam et al., 1991).

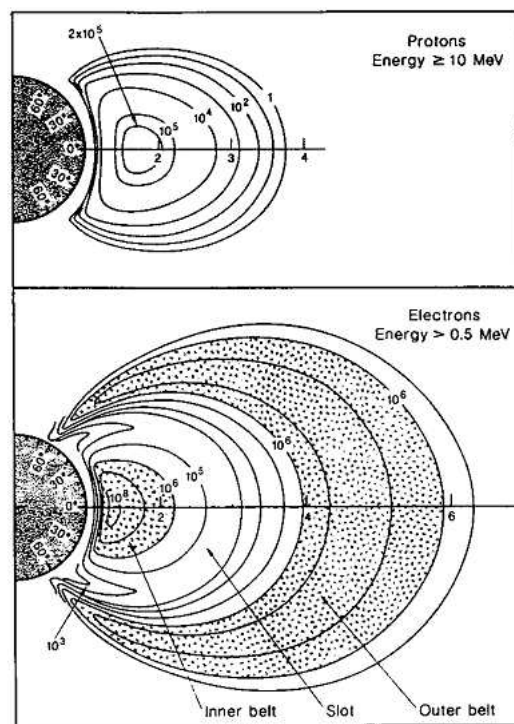


Figure 1.3: Earth’s radiation belts. The panels show the counters of the omni-directional flux of protons with energies greater than 10 MeV (top panel) and electrons with energies greater than 0.5 MeV (bottom panel), [M.G. Kivelson and C.T. Russell, 1995].

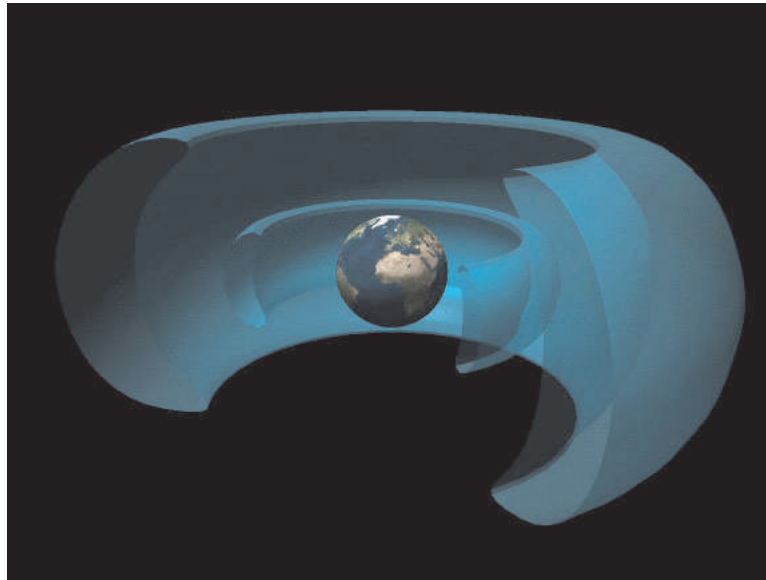


Figure 1.4: A graphical depiction of the Earth's radiation belts, showing the inner and outer radiation belts to scale, [<http://www.nasa.gov/vision/universe/solarsystem/killer-electrons.html>].

Well inside the magnetosphere the Earth's inhomogeneous magnetic field gives rise to particle trapping which create the *Van Allen radiation belts*, regions occupied by energetic ions and electrons which experience long-term geomagnetic trapping. The radiation belt lies on dipolar field lines between about 2 and 6 Earth's radii fig. 1.3. It consists of energetic electrons ($\approx 1 \text{ eV} \div 50 \text{ MeV}$) and ions ($\approx 10 \text{ eV} \div 1 \text{ GeV}$) which move along the field lines and oscillate back and forth between the two hemispheres.

For purposes of introduction it is sufficient to say that a large population of trapped electrons form structures as shown in (fig. 1.4) which depicts an inner belt, an outer belt, and an intermediate region with depleted energetic fluxes known as the 'slot-region'.

The trapping mechanism arises from the interaction between the moving energetic charged particles and the static geomagnetic field. The motion of particles is defined on the basis of *adiabatic invariants*. Adiabatic invariants are associated with each type of motion the particle can perform (gyration, longitudinal motion along the geomagnetic field, perpendicular drift).

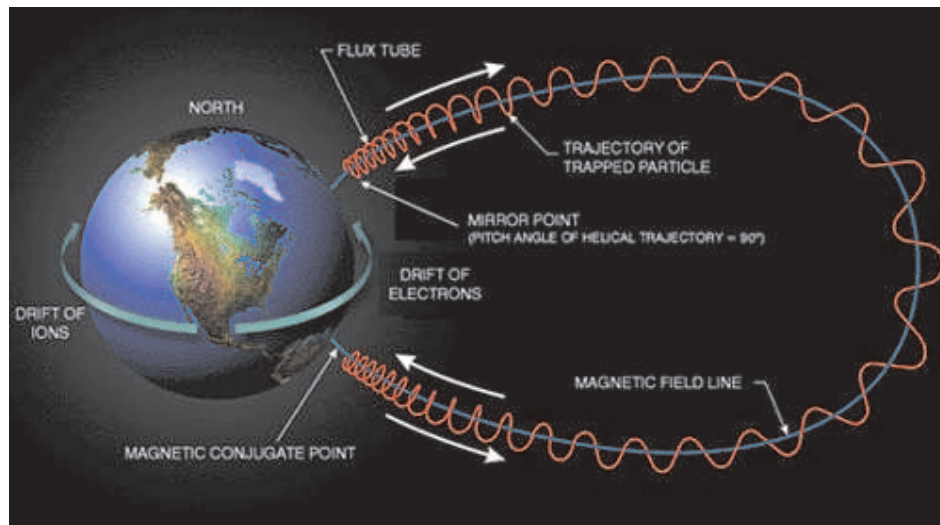


Figure 1.5: Trajectory of trapped electrons and protons experiencing magnetic mirroring and gradient and curvature drifts in the geomagnetic field.

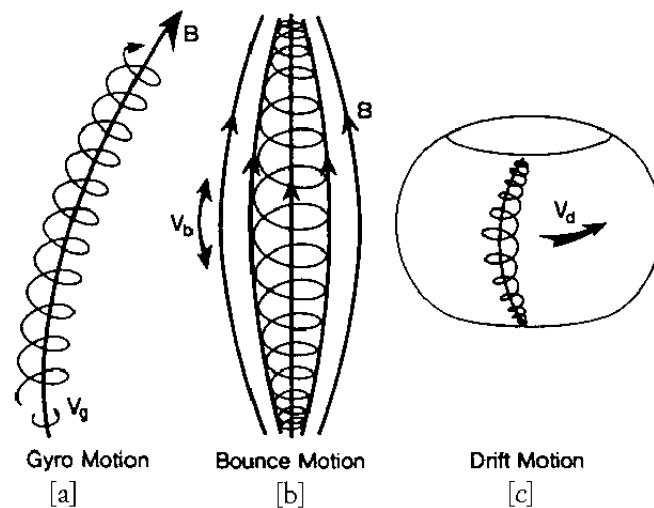


Figure 1.6: Characteristic motions of a particle trapped in the Van Allen radiation belt, [<http://www-spc.igpp.ucla.edu/ssc/tutorial/msphere07.thumb.gif>].

The *first adiabatic invariant* J_1 is the magnetic moment μ . It is associated with the *cyclotron motion* or *gyration* of particles around the geomagnetic field (fig. 1.6[a]). The *gyrofrequency* or *cyclotron frequency* ω_B of a particle q with mass m in a magnetic flux density B and the corresponding radius of gyration (*gyroradius*) r_B are defined as:

$$\omega_B = \frac{qB}{m}; \quad r_B = \frac{mv}{qB}$$

where v is the particle velocity normal to the field line.

The *second adiabatic invariant* J_2 , also called *longitudinal* or *integral invariant*, is associated with the oscillation (*bouncing motion* at a certain *bounce frequency* ω_b) of particles between mirror points along the magnetic field direction (fig. 1.6[b]) due to the presence of the force $\vec{F} = -\mu \nabla B$. The force is always exerted along the field and away from the direction of increasing field. This means that v_{\parallel} decreases to zero at some maximum field strength (B_M) and then changes sign. The longitudinal invariant J_2 is defined through the constant action integral J_i :

$$J_i = \oint p_i dq_i$$

where variables (q_i, p_i) are the generalized momentum and coordinate of Hamilton mechanics, and the integration has to be done over one full cycle of q_i . In our case:

$$J_2 = 2ml \langle v_{\parallel} \rangle$$

where v_{\parallel} is the parallel particle velocity and l is the distance between the mirror points. For a given particle the position of the mirror point is determined by the *equatorial pitch angle* α_{eq} ($\alpha = \tan^{-1} v_{\perp}/v_{\parallel}$) as the particle crosses the equator, since $\sin \alpha_{eq} = B_{eq}/B_M$. Where B_{eq} is the flux density at the equator. The *loss cone* contains the equatorial pitch angles of particles which will be lost, since they encounter the atmosphere before the mirror point.

The *third adiabatic invariant* is the *gradient-curvature drift invariant*. It is a compound

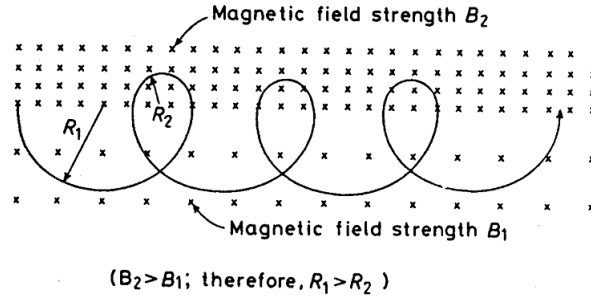


Figure 1.7: Longitude drift caused by a gradient in geomagnetic field intensity, (Hargreaves, 1992).

mechanism. The first is a gradient drift caused by a gradient in the geomagnetic field intensity which provoke a change in the radius of gyration (fig. 1.7) giving rise to a lateral shift of the orbit (fig. 1.6[c]). The second is due to the curvature of the field line, which cause a centrifugal force to which the particle reacts by drifting sideways. The drift velocity V_{GC} given by the two combined effects is:

$$V_{GC} = \frac{m}{qB^2} \nabla B \left(\frac{1}{2} v_{\perp}^2 + v_{\parallel}^2 \right)$$

the Gradient-Curvature Drift depends on the sign of charge q . The primary sources of magnetospheric particles are the solar wind and the ionosphere. The most energetic particles are cosmic rays and the decay products of neutrons produced by the interactions of cosmic rays with the atmosphere (*Cosmic Ray Albedo Neutron Decay*). The presence of electric and magnetic fields, their time variations and inhomogeneities regulate the gyration, bouncing, and longitudinal drift motions of the trapped particles (Baumjohann and Treumann, 1997).

The trapped particles also produce electric currents (see 1.1.4) that in turn generate magnetic fields. Trapped particle populations are described in terms of distribution functions and fluxes. We are interested in the flux direction which is given by the particle pitch angle. The pitch angle distribution of trapped radiation provides clues as to the origin of the particles and their loss mechanisms. A typical pitch-angle distribution of protons in the stable radiation belt is shown in figure 1.8.

The directional flux is maximum at 90° and falls symmetrically to zero at the loss cone

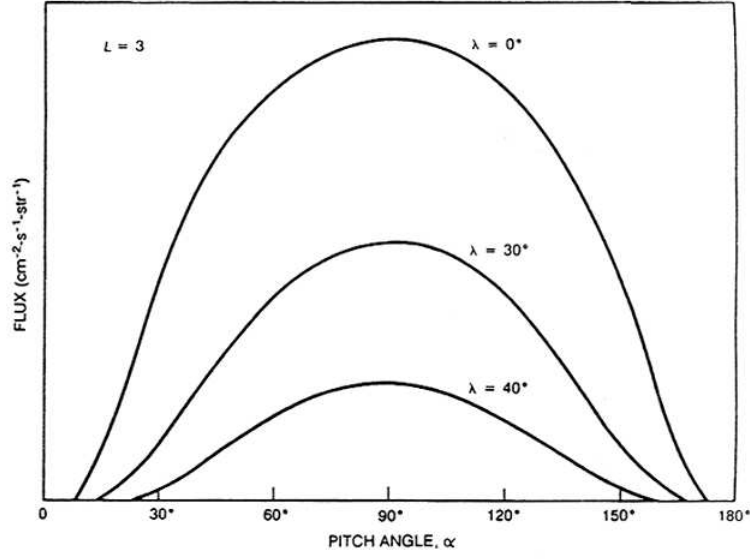


Figure 1.8: Typical pitch-angle distribution at three latitudes on the $L = 3$ field line (Walt, 1994).

angles. On a given field line the distribution will vary with the latitude since the loss cone increases as the observer moves from the equator towards the poles.

The diffusion theory gives a valid description of the time evolution of a distribution of particles whose motions are disturbed by small, random changes. We are interested in the pitch angle diffusion which is an important redistribution and loss mechanism and affects mainly electron population. The two most important causes of particle diffusion are coulomb scattering with neutral components and resonant interaction with EM waves.

In the inner magnetosphere ($L < 3$), scattering rates for electrons exceed the radial diffusion rates.

Calculation of the electron diffusion in this region can be greatly simplified by neglecting radial diffusion and calculating the distribution function $f_0(E, L, \alpha)$. The diffusion equation for pure pitch angle scattering can be written:

$$\frac{\partial f_0}{\partial t} = \frac{1}{\sin(2\alpha_0)T(\alpha_0)} \frac{\partial}{\partial \alpha_0} \left(\sin(2\alpha_0)T(\alpha_0)D_{\alpha\alpha}(\alpha_0) \frac{\partial f_0}{\partial \alpha_0} \right) - \frac{f_0}{\tau_L}$$

where E = energy of particles, α_0 = equatorial pitch angle, $D_{\alpha\alpha}(\alpha_0) = \langle \Delta\alpha \rangle^2 / 2$ pitch angle scattering due to Coulomb collision and wave-particle interactions, f_0/τ_L = loss term, $\tau_L(E, L, \alpha_0)$ = bounce-averaged electron loss timescale, and $T(\alpha_0) \cong$ variation of electron bouncing period vs equatorial pitch angle assuming a dipole magnetic field $T(\alpha_0) = 1.3802 - 0.3198 (\sin \alpha_0 + \sqrt{\sin \alpha_0})$.

1.1.6 The atmosphere of the Earth

Between the magnetosphere and the Earth’s surface there is an *ionized* and *neutral atmosphere*. The lower neutral atmosphere is described mainly by thermodynamic, chemical, and other physical parameters (pressure, density, temperature and composition). With increasing altitude the pressure and density decline. With the exception of thunderstorms, the region from the Earth’s surface up to about 50 km can be considered that EM waves propagate as in vacuum. This gives the possibility to consider the geomagnetic field as a conservative one and then to apply the potential field theory to study its behavior. Into the rarified upper level penetrate the ultra-violet and X-ray emissions from the Sun, photons which are sufficiently energetic to dissociate and to ionize the atmospheric species, altering the atmosphere’s composition and heating it.

An atmosphere supports both neutral and ionized components. Ionization is primarily produced by the solar ultra violet (UV) radiation, and ionized constituents populate the ionosphere and the magnetosphere.

The neutral atmosphere is a relatively dense gas, mainly constituted by molecular nitrogen and oxygen with smaller amounts of carbon dioxide, water and various trace gases.

The atmospheric vertical structure is schematically represented in figure 1.9.

One of the most important properties of an atmosphere is the exponential decrease of the density (ρ) and pressure (p) with height (z). The equation that describes this decrease, examining the fluid equation of motion for an atmosphere that is in hydrostatic equilibrium, is:

$$p(z) = p(z_0) \exp\left(-\frac{z - z_0}{H}\right)$$

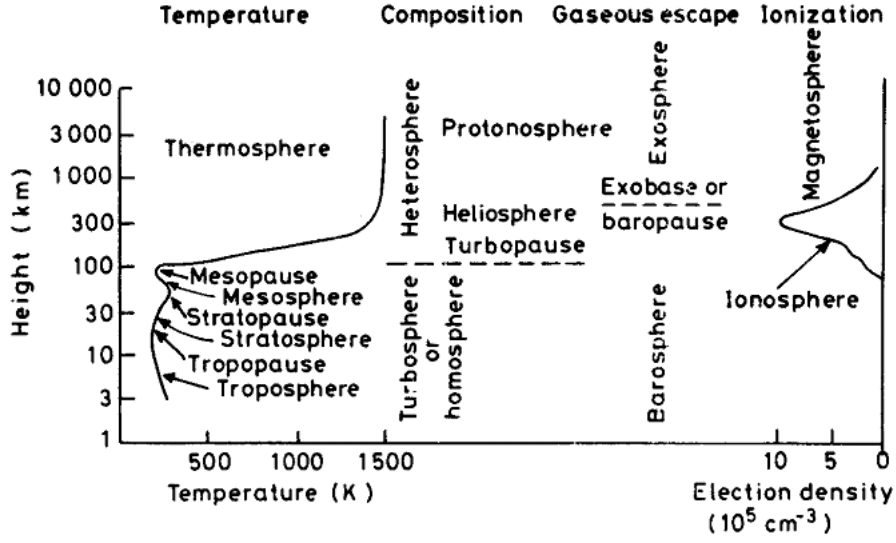


Figure 1.9: The upper neutral atmosphere. Nomenclature based on temperature, composition, mixing and ionization.(Hargreaves, 1992)

where $H = kT/mg$, the scale height, is independent of z . The constancy of the scale height implies that the atmosphere is approximately isothermal and since for isothermal atmosphere $T(z)/T(z_0) = 1$, yields:

$$\rho(z) = \rho(z_0) \exp\left(-\frac{z - z_0}{H}\right)$$

$$n(z) = n(z_0) \exp\left(-\frac{z - z_0}{H}\right)$$

where $\rho = nm$.

Because of the low pressure, above about 100 km ionized species do not necessarily recombine quickly, and there is a permanent population of ions and free electrons. Since photoionization is the dominant production mechanism below about 600 km, this region is often referred to as the *ionosphere*.

The ionosphere forms the base of the magnetospheric plasma environment of the Earth. It is the transition region from the fully ionized magnetospheric plasma to the neutral atmosphere. It consists of a mixture of plasma and neutral particles and will therefore have an electrical conductivity to which electrostatic and neutral collisions may con-

tribute.

Ionization is produced primarily by solar UV radiation, which photoionizes and photodissociates the neutrals.

A vertical profile of the ionosphere distinguishes different layers: D, E, F1, F2 (fig. 1.10). The D-region is a very weakly ionized layer between 60 and 90 km with mean density of about $10^2 - 10^4 \text{ cm}^{-3}$. It is due to high collision frequencies mostly dominated by neutral gas dynamics and chemistry and cannot be considered as a plasma. The E-region is approximately located between 105 and 160 km, has density of several 10^5 cm^{-3} and is formed by the absorption of longer wavelength ultraviolet radiation (about 90 nm). The F-region splits into two layers: the F1-region at about 160-180 km (density of several 10^5 - 10^6 cm^{-3}) and the F2-region around 300 km (density up to several 10^6 cm^{-3}). The more important layer is the F2-region. Its formation is basically defined by the height variation of the neutral densities and the recombination and attachment rates for the different atmospheric constituents. In the lower F2-region ionization of atomic oxygen and recombination play the key role. The D and F1 regions vanish at night, and the E region becomes much weaker. Only the F2 region tends to persist even if at reduced intensity.

In the steady-state, the production rate q of ionized constituents is exactly balanced by recombination process that remove ionization. Sydney Chapman considered a simple theoretical model to show how q could be calculated. His model assumes a flat geometry, one-dimensional in height, with a constant temperature, and a monochromatic input solar spectrum.

The Chapman production function is usually written in a normalized form as:

$$q = q_{m0} \exp(1 - z - \sec\chi \exp(-z)) \quad (1.1)$$

Here z is the reduced height for the neutral gas, $z = \frac{h-h_{m0}}{H}$, H being the scale height. χ is the solar zenith angle, h_{m0} is the height of the maximum rate of production when the Sun is overhead (i.e. h_m when $\chi = 0$), and q_{m0} is the production rate at this altitude, also when the Sun is overhead.

In the ionosphere, the competition between the magnetic field and collisions for control of the ion motion is particularly important in problems requiring an evaluation

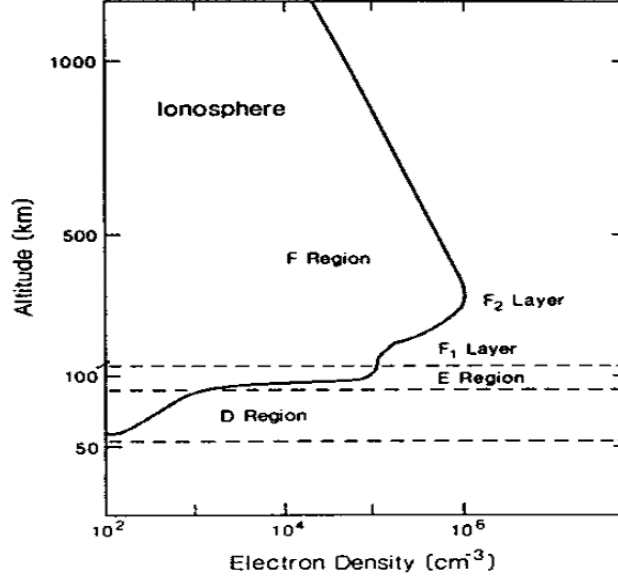


Figure 1.10: Electron density of the Earth's ionosphere as a function of altitude.

of electrical conductivity. In this medium the current density \vec{j} is related to the electric field by the generalized Ohm's law:

$$\vec{j} = \sigma_{//} \vec{E}_{//} + \sigma_p \vec{E}_{\perp} - \sigma_H \left(\frac{\vec{E} \wedge \vec{B}}{B} \right)$$

where $\sigma_{//}$, σ_p , σ_H are the component of the conductivity tensor. σ_p is the *Pedersen conductivity*, and governs the current in the direction of that part of the electric field which is transverse to the magnetic field. σ_H is the *Hall conductivity*, and governs the current in the direction perpendicular to both the electric and magnetic field. $\sigma_{//}$ is the *longitudinal conductivity*, and governs the magnetic field aligned current driven by the parallel electric field component.

1.1.7 Location of the ionosphere-magnetosphere transition zone

Above 600 km altitude the ionospheric plasma is produced both by photoionization and by transport from other regions. Above 1500 km the ionized constituents are dominant over the neutrals and the region is termed the *magnetosphere*, because the local

magnetic field controls the particles' motion (Hargreaves, 1992).

Moreover, the atmosphere limits the radiation belt particles to regions above 200-1000 km within a volume of stable magnetic field. This volume extends above ≈ 200 km and below $\approx 7 R_E$ in altitude and to latitudes equatorward of $\approx 65^\circ$.

So, the *ionosphere-magnetosphere transition zone* of prime interest to us is the relatively small region surrounding the Earth at altitudes ranging between around 600÷1000 km. It constitutes a privileged zone for mapping the geomagnetic field of both internal and external origin as well as for studying many relevant and largely unknown phenomena. They include solar-terrestrial interaction effects, Earth's interior dynamics, terrestrial natural and artificial emission effects (perturbations and instabilities), and some important physical climate phenomena. It is interesting to note that Demeter data, which are studied in this thesis work, are collected in this transition zone, the Demeter orbit altitude being of 715 km.

1.2 Main phenomena inside the magnetic cavity: Geomagnetic Substorms

The magnetospheric substorm [Akasofu, 1964] is considered to be a major building block in understanding the processes of geomagnetic activity in the Earth's magnetosphere, and as such it has been studied intensively through the last four decades based on measurements made in every region from the ground throughout the magnetosphere to the solar wind. Much knowledge has been gathered, but many major and minor issues are still being debated heatedly [Akasofu, 2004]. The magnetospheric substorm can be understood as a process where energy from the solar wind is temporarily stored and subsequently released from the Earth's magnetosphere. The energy is mainly provided from the solar wind through dayside magnetic reconnection and stored as magnetic energy in the magnetotail [Baker *et al.*, 1997]. A substorm is described to go through a series of three phases, where the phase of energy storing is known as the substorm growth phase, followed by the onset and expansion phase where energy rapidly is being dissipated from the magnetic field. Storm onset can most precisely be recognized by an intensification of the aurora, typically the most equator-

ward arc, known as breakup, while other indicators include Pi-2 pulsations, ground magnetic bays, magnetic field dipolarization and particle injections [Meng and Liou, 2004]. The expansion phase is characterized by signatures in auroral emissions where the active aurora of the breakup arc may expand rapidly in all directions, but typically expands most rapidly westward and poleward. The substorm is typically observed to last for a few hours, where the last hours when the activity decrease can be considered as a return to a quiet state and is known as the recovery phase.

1.3 Atmosphere-ionosphere coupling during thunderstorm activity

Several effects are produced in the neutral and ionized atmosphere by lightning discharges. In the following *sub-sections* we will examine the electromagnetic signatures of lightning.

1.3.1 Whistlers

The RF noise generated by lightning has a power density that peaks at a frequency near 10 kHz, in the VLF radio spectrum, but which extends from the ELF (<1 kHz) end of the radio spectrum to the VHF (~100 MHz) end. The ELF and VLF components of this radio noise are confined to the Earth by the ionosphere and are called 'atmospherics', or more commonly, *sferics*.

Lightning-generated electromagnetic waves at frequencies in the VLF or audible range (tens of Hz to tens of kHz) can penetrate the ionosphere over a range of directions of propagation centred on the magnetic field direction, by coupling to the magnetic field. Since these waves travel most quickly at the higher frequencies and more slowly at lower frequencies, the signals produce a characteristic gliding tone when run through a speaker, so that these waves are known as whistlers (fig 1.11). Electromagnetic waves propagating along the magnetic field can be right or left handedly circularly polarized. The electric field vector of right-handed waves rotates clockwise (as viewed along the magnetic field) as the wave propagates. Historically, whistler wave research started with passive ground observations of low-frequency radio waves

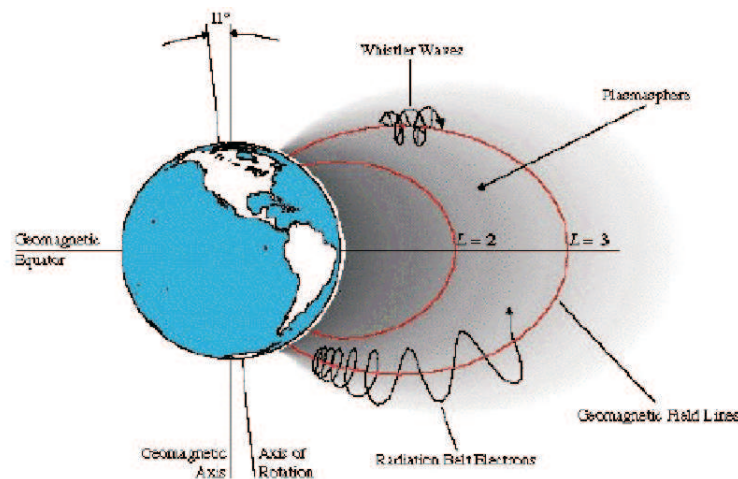


Figure 1.11: Whistler waves propagation in the magnetosphere, [http://www-star.stanford.edu/vlf/Science/Science.html].

from ionosphere. Space plasma research blossomed in era of spacecraft exploration. A wealth of whistler wave phenomena has been collected. The earliest and common observations of whistlers are performed with long-wire antennas, amplifiers, and conversion to sound. The signals may be recorded and displayed as spectrograms such as the one show in figure 1.12.

The thunderstorm activity is a very common atmospheric phenomenon (100 lightning/second on the Earth).

The observed whistlers are excited by natural lightning, couple through the Earth-ionospheric waveguide into an ionospheric duct, and undergo single or multiple reflections at conjugate points [Smith, 1961]. Whistlers are readily detected with electric and magnetic antennas on spacecraft. As on ground, only frequency spectra are recorded while wave vectors are inferred [Sakamoto *et al.*, 1995], radiation sources are extrapolated from direction-finding techniques [Hayakawa *et al.*, 1990].

A spectral analysis of VLF radio signals reveals that whistlers are usually present, but in addition there is a variety of noises that can only be explained by attributing to the magnetospheric medium some active role. Such noises are generally known as *emissions*. The principal emissions will be examined here.

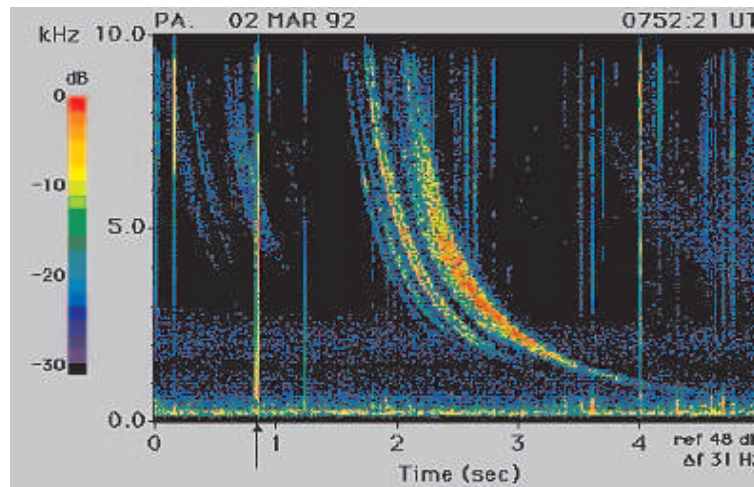


Figure 1.12: Spectrogram of whistler and sferic from North America received at Palmer station, Antarctica. The vertical axis denotes frequencies from 0 to 10 kHz, and the horizontal axis covers 5 s. Intensities are labelled by colour, red being greatest. Labelled by the arrow is the sferic from the lightning flash that launched the whistler. From the Stanford VLF group website (<http://wwwstar.stanford.edu/vlf/Science/Science.html>).

1.3.2 ELF/VLF magnetospheric emissions: hiss, chorus, discrete emissions

When a lightning discharge emits impulsive radiation in the frequency range 100 Hz to tens of kHz, some of this radiation will end up propagating along nearby magnetic field lines. Once it does, this radio wave can travel along a geomagnetic field line and through to the Earth's magnetosphere. Spacecraft detect these whistler waves if it is located at along the path of the waves through the magnetosphere. In the magnetosphere, energetic radiation belt electrons can amplify whistler waves by as much as 30 dB through wave-particle interactions. The complex interactions between whistler waves and electrons in the magnetosphere may also account for *chorus*, *discrete emissions*, and *hiss*. The space region where they are formed is reported in figure 1.13.

Chorus, named for its characteristic sequence of continually repeating, usually rising ($df/dt > 0$), and often overlapping whistler mode ($f < f_H$, where f_H is the local electron gyrofrequency) coherent ELF/VLF tones (300 Hz - 12.5 kHz), ranks among the most intense of all naturally occurring ELF/VLF plasma wave emissions generated within the Earth's magnetosphere (Gurnett and O'Brien, 1964). Chorus occurs regularly in association with disturbed magnetospheric conditions and is believed to be a

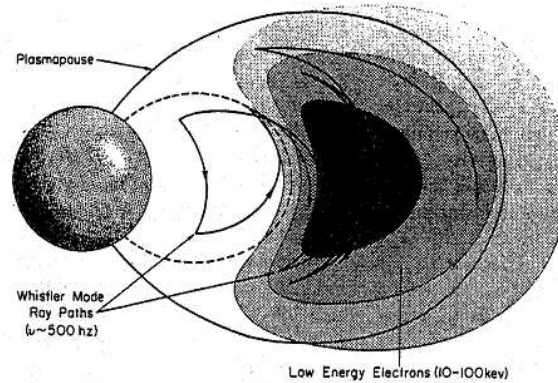


Figure 1.13: Schematic representation of the complex interactions between whistler waves and electrons in the magnetosphere and consequent formation of *chorus*, *discrete emissions*, and *hiss* (black space region A).

driver of energetic electron precipitation on closed field lines in subauroral regions (Salvati et al., 2000), including microbursts, pulsating aurorae, and possibly morningside diffuse aurorae. Chorus is observed both by spacecraft and at high-latitude ground stations. The source of chorus is thought to be anisotropic energetic electrons (10-100 keV) in the equatorial magnetosphere beyond the plasmasphere which interact with whistler-mode plasma waves via the electron cyclotron instability (Sazhin and Hayakawa, 1992).

Plasmaspheric hiss is a broad diffuse band of electromagnetic radiation in the hundreds of hertz to 4 kHz frequency range that is confined to the plasmasphere [Taylor and Gurnett, 1968]. Sonwalkar and Inan [1989] were the first to observe lightning-generated whistlers triggering hiss emissions. VLF hiss activity observed at ground stations spread in latitude and longitude varies from station to station. Satellite observations indicate that broad band hiss is present almost continuously in plasmasphere (Thorne et al., 1973). Global distribution of hiss is characterized by three principal zone of intense activity of which the first zone is located around invariant latitudes above

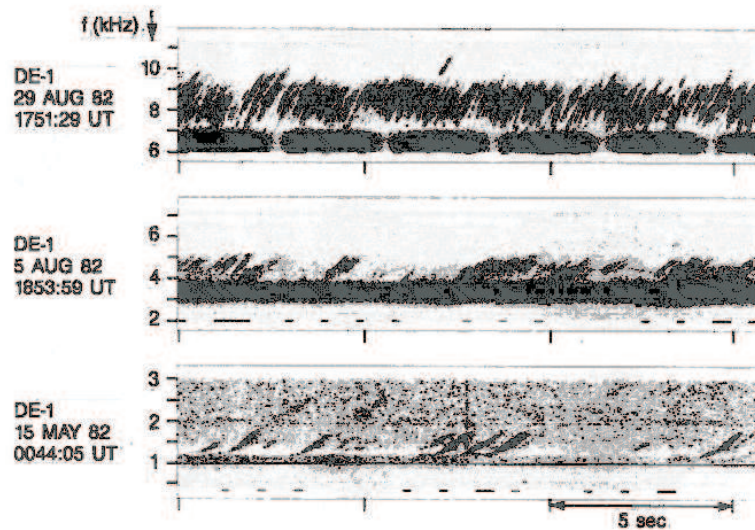


Figure 1.14: Chorus emission frequency time spectra observed on board of the DE1 satellite (Poulsen and Inan, 1988).

70° (auroral hiss), the second near 50° (mid-latitude) and the third below 30° latitude (equatorial hiss). Ground-based observations revealed that the low-latitude hiss are less intense than those observed at middle and high latitudes. A number of generation mechanism (Doppler-shifted cyclotron radiation, Cerenkov instability, cyclotron instability) have been proposed from time to time to explain the observed hiss emission intensity at ground stations as well as on-board rockets and satellites (Church and Thorne, 1983). In addition to the noise-like chorus and hiss signals, many emissions of discrete form are observed in the frequency-time spectra. These discrete emissions are attributed to limited interaction regions in the magnetosphere, in which groups of particles transfer energy into particular wave frequencies. It has been supposed that the particle population in some region is close to instability, so that waves passing through it are readily amplified and a small injection of wave energy is all that is needed to stimulate the emission. As an example, a discrete emission frequency-time spectrum is reported in figure 1.15. A difference appears evident when comparing the slope of the elementary emissions of this spectrum with those concerning the other whistler-modes (see fig. 1.14) (Poulsen and Inan 1988).

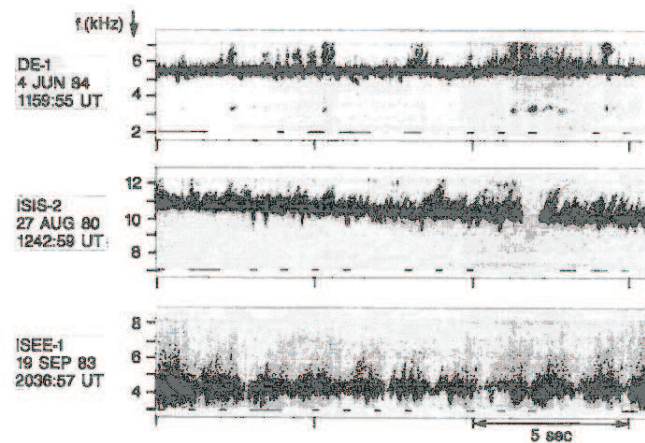


Figure 1.15: Characteristic frequency-time spectrum of discrete emissions detected on board DE1, ISEE1, and ISIS2 satellites (Poulsen and Inan, 1988).

1.4 The seismic activity. Is the earthquake a natural predictable disaster?

The earthquake is one of the most dangerous of the natural disasters. Very strong earthquakes happen approximately 20 times a year over the globe. When they occur in the densely populated areas, they destroy cities and cause the drastic loss of lives and material damages. The energy released by such earthquakes in several minutes is comparable with the energy produced by a big nuclear explosion or by the greatest electric power plants during a year.

The latest example is the earthquake which occurred in the northern India on January 26, 2001. About 20,000 people lost their lives, more than 160,000 were injured, and about 600,000 became homeless due to the quake. But if the earthquake could be predicted, the lives of people would be saved. This is illustrated by the well-known (though the only one!) prediction of the Haicheng earthquake in northern China in 1975, when about one million of peoples were evacuated from their houses several hours before the shock with magnitude 7.3. Therefore the earthquake prediction is the most important societal goal of seismologists. Hence, the studies of the physics of earthquake related phenomena are not only of fundamental but also of practical importance since earthquake prediction is an extremely important and urgent problem.

To predict earthquakes a wide network of seismic stations and earthquake prediction sites has been set up throughout the world and they are very expensive. Nevertheless, the efficiency of the network is now extremely low since it is not uniformly and properly distributed over the globe.

Obviously, new non traditional approaches to the problem are required and satellite monitoring is one of them. The feasibility of such an approach relies upon recent achievements of space science and technology.

Recently, a great attention has been given to the problem of ionospheric and magnetospheric plasma perturbations caused by the seismic activity and a few interesting results have been obtained. Some of them are reported in chapter 2.

It is evident that global satellite monitoring should be combined with ground-based measurements to form a unified system for observing seismic activity and related precursory phenomena.

1.4.1 Earthquake phenomenology

An earthquake is a deformation, fracture, structure and phase transformation event which releases suddenly a large amount of the elastic energy stored in the medium (Earth's lithosphere) and is accompanied by a substantial fraction of energy radiated as elastic (seismic) waves.

Following definitions given by Jordan (1990), episodic deformations of the lithosphere are constituted by fast *seismic ruptures*, *slow earthquakes* and *sub-seismic events* (fig. 1.16).

The most familiar lithospheric deformation events are defined as *ordinary earthquakes*. They are deformation events that occur in the upper thin brittle layer of the Earth's crust and consist of elastodynamic cracks propagating in this brittle material at a significant fraction of the shear elastic wave velocity (i.e., at speeds of kilometers per second). The brittle character of the seismogenic crustal layer allows big changes of shear stress ($\sigma_0 = 100\text{-}200$ MPa) and has a thickness of about 15-20 km.

At this depth there is a brittle-ductile transition layer, below of which a plastic layer (fig.1.16) allows creep phenomena to occur. In this bottom viscous part, stresses are distributed more smoothly and earthquakes exhibit a great, fast release of elastic energy (with a stress drop $\Delta\sigma \approx 0.5\text{-}5$ MPa).

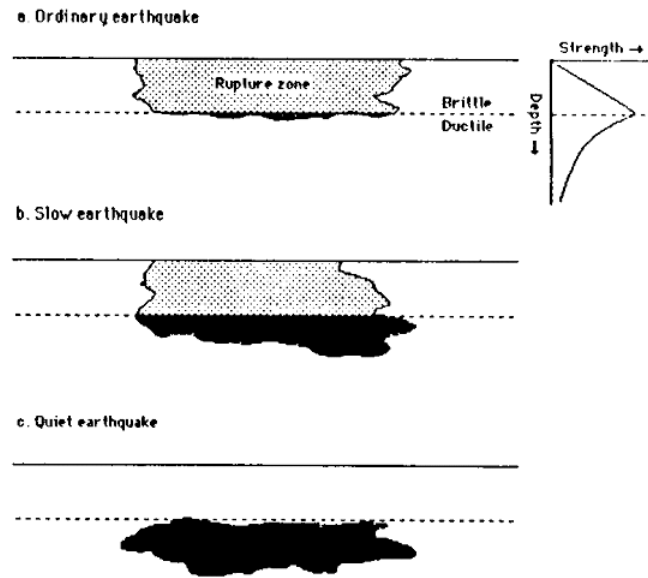


Figure 1.16: Three types of seismic events. (a) ordinary earthquake; (b) slow earthquake; (c) silent earthquake

1.4.2 Energy budget

Much of the strain energy of the medium is transformed into heating and fracturing of the rocks, and a portion is converted into seismic waves that propagate in the elastic medium and are recorded at remote seismic stations. Part of the accumulated preseismic elastic energy is also converted to electromagnetic energy and this conversion is probably the same as the conversion to seismic energy (Molchanov,1995).

For estimating the gross energy budget we need to consider the potential energy E_P , which is the sum of the strain energy W and the gravitational energy E_G . That is:

$$E_P = W + E_G$$

An earthquake process transfers the potential energy E_P to wave energy E_R (energy radiated as seismic body and surface waves) and nonradiated energy E_{NR} :

$$\Delta E_P = E_R + E_{NR}$$

E_{NR} is given by the sum of frictional energy loss E_T (thermal energy caused by frictional stress on the fault plane during slippage) and fracture energy E_F (energy required to cause fracture near the end of the fault during fracture):

$$E_{NR} = E_T + E_F$$

Only E_R can be measured directly with seismological methods. The others need to be either inferred or estimated from other data.

So, from seismograms we can estimate the energy of seismic waves radiated from the source. Since the seismic wave energy is a certain part of total energy (from 1 to 10%) it is usually assumed as an estimate of the total energy of the earthquake. For strong earthquakes, which occur approximately once a year, it is of the order of 10^{25} erg (10^{18} J). To quantify the *size* of the earthquake seismologists use the concepts of *magnitude* (M), *seismic moment* (M_0) and energy release (E). The relationship between the magnitude M_S , determined from seismic surface waves, and the energy (in erg) was given by Gutenberg and Richter:

$$\log E = 1.56M_S + 11.8$$

According to this relationship, the magnitude corresponding to the energy value of 10^{25} erg is ~ 8.5 . For comparison the Chile 1960 and Alaska 1964 earthquakes had magnitudes 8.4.

There exist different magnitude scales, which estimate the energy of different waves and in different frequency bands.

The scalar seismic moment is equal to the product of the fault surface area (A), the rigidity of the rock (μ), and the average displacement on the fault (\bar{D}). That is:

$$M_0 = \mu \bar{D} A$$

Kostrov (1974) showed that the radiated seismic energy is proportional to the stress drop $\Delta\sigma$ as follows:

$$E \approx \frac{1}{2} \Delta\sigma \bar{D} A$$

This relationship allows to relate M_0 to magnitude M_S . For stress drop values constant and equal to 30 bar (3MPa), we obtain:

$$\log M_0 = 1.5M_S + 16.1$$

Strong earthquakes occur much rarer than weak. Richter and Gutenberg first proposed the relation between earthquake size and frequency of occurrence:

$$\log N = a - bM_S$$

where N is the number of earthquakes with magnitudes in a fixed range around magnitude M_S , and a and b (so-called *b-value*) are constants. For different regions the b -value varies from 0.7 to 1.2, but in general it is close to 1.0. For seismic swarms b value can be as large as 2.5. In the following we will consider only lithospheric earthquakes (seismic events which occur in the elastic lithosphere), because the EM precursors are presumably connected with them.

1.4.3 Earthquake space distribution

On the global scale the earthquakes occur not uniformly but are concentrated within narrow belts (fig. 1.17), but on the regional scale potentially dangerous seismic areas are sufficiently extended. The overwhelming majority of the earthquakes occurs at low and middle latitudes (between 50° S and 50° N) and a great part of them at equatorial latitudes.

Earthquake hypocentral distribution

Generally shallow earthquakes are observed and concentrated at two different depths around 10 km and 30 km respectively (fig. 1.18). This seems to confirm the existence of a ductile layer in the crust which divides the two above-mentioned brittle (seismic)

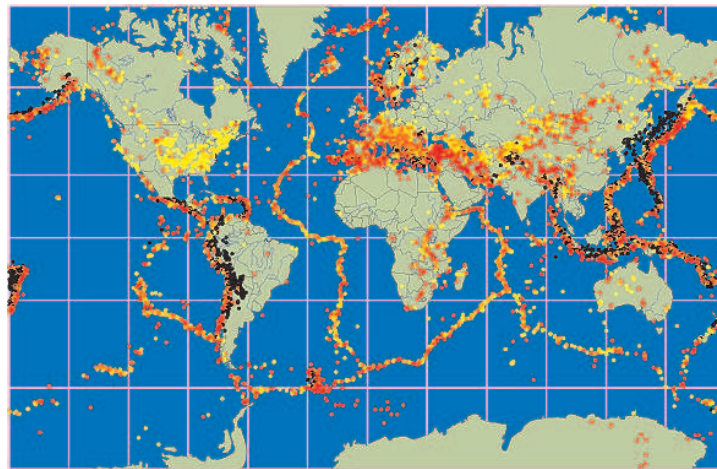


Figure 1.17: Earthquake events organized according to depth (yellow(shallow)=surface to 25 km below the surface, red(intermediate)=26 to 75 km below the surface, and black(deep) ≤ 76 km below the surface)

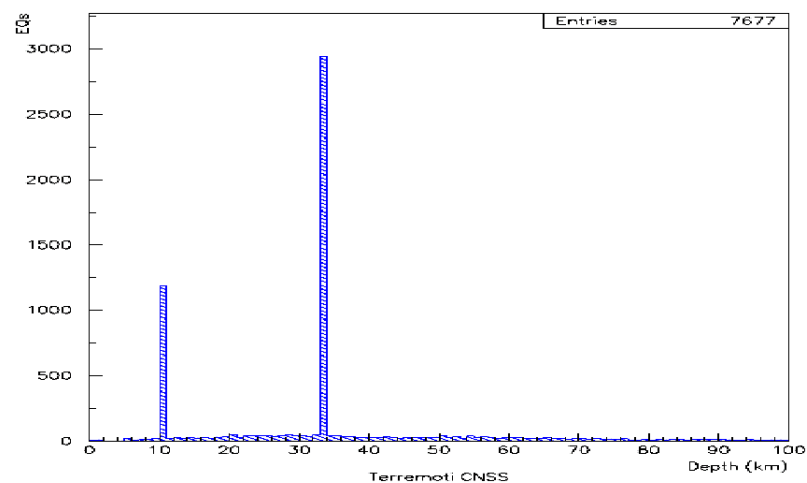


Figure 1.18: Typical earthquake hypocentral distribution obtained for earthquakes with magnitude > 3.0 observed over the world in the period 1990 – 2000. (Sgrigna, V., 2001)

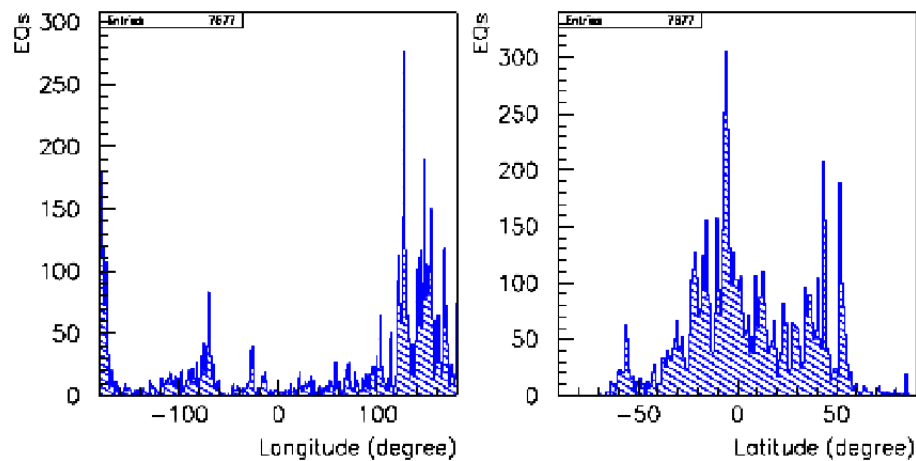


Figure 1.19: Epicentral distribution of the earthquakes reported in the previous figure 1.18. (Sgrigna, V., 2001)

layers. In constructing our model we will take into account of this rheological behavior.

Also the distribution of epicenters on the Earth's surface indicate that earthquakes are mainly distributed along the equatorial zone (fig. 1.19).

Chapter 2

Pre-earthquake Phenomena: observations and modeling

In this chapter will be described the dilatancy models of earthquake preparation and occurrence. Results of ground-based and space observations together with theoretical models proposed to justify the observations will also be reported.

2.1 Earthquake generation mechanisms: dilatancy models

The lithosphere of the Earth is not a continuous layer. It is broken into a number of huge plate-like pieces called lithospheric plates. The plates have horizontal dimensions of the order of $10^3 - 10^4$ km. The Earth's internal thermal convection is always moving the lithospheric plates and changing the Earth's surface. Such motions involve complicated events, all of which are embraced by the term tectonics, the study of the movement and deformation of the lithosphere. The special branch of tectonics that deals with the processes by which the lithosphere is moved laterally over the viscous material of the asthenosphere is called plate tectonics.

Due to relative motion of the lithospheric plates stresses are accumulated at their boundaries and are released by earthquakes. The seismic belts coincide with the plate boundaries. These seismic events are called interplate earthquakes.

The basic mechanism responsible for relative motions of the plates must provide the energy for the earthquakes, volcanism, and mountain building, since these phenomena are largely associated with plate interactions at plate margins. The only source of energy of sufficient magnitude is heat from the interior of the Earth. This heat is the result of the radioactive decay of the uranium isotopes ^{238}U and ^{235}U , the thorium isotope ^{232}Th , and the potassium isotope ^{40}K as well as the cooling of the Earth. The energy associated with seismicity, volcanism, and mountain building is about 1% of the heat flow to the surface.

Many interpretations have been given on the problem of how an earthquake takes place. The main ones are the *dilatancy-diffusion (DD)* and *avalanche-unstable fracturing (AUF)* or *crack-avalanche models* (Myachkin et al., 1975).

The non elastic behavior in which volumetric strain increases relative to what would be expected from elasticity is known as *dilatancy* and has been extensively studied. It is commonly accepted that dilatancy is connected with microfracture process. It was verified from observations of acoustic emissions (AE), originated from the creation of systems of cracks.

Tiny cracks are present in any body, but the development in their number and length begins when the stress reaches a value about half of the failure value. At this stage rocks dilate or expand. The microcracks are oriented along the axis of maximum stress and opened in perpendicular direction. Finally, these microcracks coalesce, leading to the formation of the fault (fig. 2.1).

The behavior of rocks during dilatancy depends strongly on whether the cracks are dry or wet. In a wet model the diffusional water plays an important role. The water penetrates into the cracks, the porous pressure increases, decreasing the effective pressure in the rock. Correspondingly the fracture stress decreases. Water within the cracks acts as a lubricant and decreases friction between the edges of the cracks. These factors facilitate the occurrence of fracture. Dilatancy and diffusion are the key features of this model, that is why it is called as *DD model*.

This model explains most of the precursors. Behavior of the precursors allows us to recognize three different stages prior to the earthquake (fig. 2.2). The stage I corresponds to elastic behavior of the material, and all physical characteristics have their normal

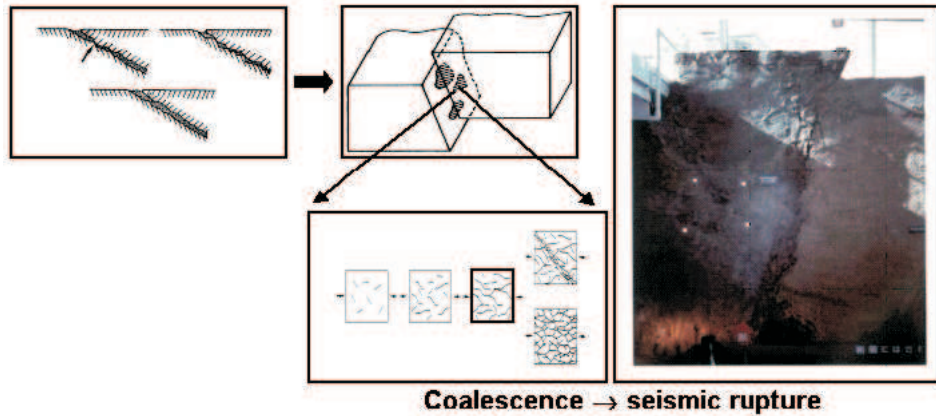


Figure 2.1: Evolution of a seismic deformation process from the fault seismic slippage to coalescence and fracture. Fault asperities and final seismic fracture are shown. During the deformation process dilatancy is reported as to occur at the third step of the cracking evolution (boldfaced rectangle).

values. At the stage II the dilatancy is developed, but the cracks are still not filled with water. At this stage the elastic modulus and seismic velocities are changed, this leads to decrease of the v_P/v_S ratio between seismic P- and S-waves. During this stage land uplift and strong change in ground tilt are also expected. At the stage III water penetrates to the cracks. Due to water saturation S-wave velocity decreases, and the same ratio returns to its initial value. Moreover, due to development of the cracks at the stage II the total surface of the cracks increases strongly, and this leads to increase of radon emission from rocks. Dissolution and alternation of the wet rocks surfaces increase the ion concentration and change the composition in the ground water. Water saturation of the rocks causes decrease of electrical resistivity. In dry rocks, on the contrary, the resistivity increases due to appearance of cracks.

In 1970s Russian seismologists (Myachkin et al., 1975) proposed an alternative model based on the interaction of cracks (AUF model). The main principles of the model are illustrated as follows:

1. in statistically homogeneous medium fracturing is quasi-uniform; there is no predominant orientation of cracks (stage I).
2. When a critical density of the cracks is achieved in some part of the medium,

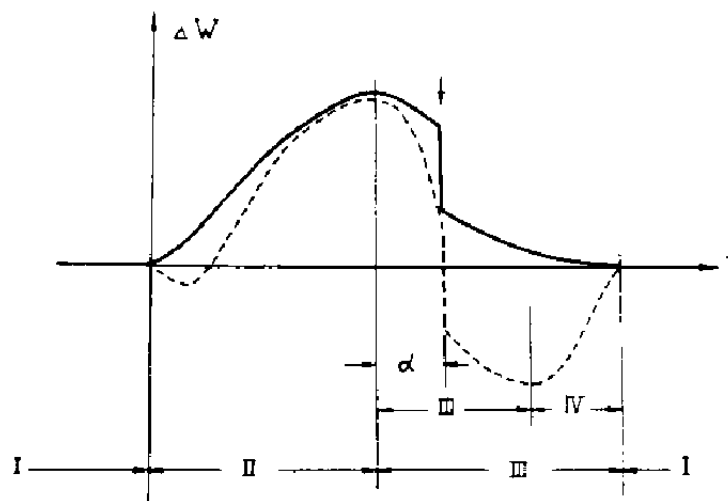


Figure 2.2: Different rock behaviours (stages I-IV) prior to an earthquake (seismic rupture) represented by the elastic potential energy W as a function of time.

the fractures are developed in an avalanche: the cracks acquire a dominant orientation, some small cracks are consolidated and form larger cracks leading to re-distribution of the stress field (stage II).

3. Further increase of deformation causes a decrease of stress. Due to heterogeneity of the medium properties the unstable deformation is concentrated within a narrow zone, where few main cracks are formed, and the other cracks are healing due to decrease of the stress (stage III). The narrow zone of the unstable deformation with high density of cracks represents a surface of the future fracture.
4. The earthquake (stage IV) occurs by means of ripping the barriers between the individual cracks.

This model also explains the precursors at the II and III stages prior to the earthquake. Dobrovolsky (1989) called the state of the medium when no seismicity is recorded as the regular state or phase I. The arising inhomogeneity, or soft inclusion, constituted by the dilatancy volume initiates phase II (of consolidation or of preparation proper). During phase II the inclusion of microfractured rock grows in size and the amount of stored elastic potential energy increases slowly. Precursors in phase II are classified as

long-term ones, the duration T of this phase being practically identical with the total earthquake preparation time. Zubkov (1987) estimated that:

$$T = 10^{0.5M-2.1} \text{ yr}$$

Final phase III corresponds to the failure of the soft inclusion which also involves ductile displacements, foreshocks, main rupture, and aftershocks. At the end of stage III the medium returns to its original regular state. The interval from the onset of phase III to the main rupture constitutes the so-called α -stage or foreshock stage. During this stage, the process “changes sign”; a similar “change of sign” is not infrequently observed during the precursory period. During α -stage precursors are short-term ones (from a few tens of minutes to a few days). This scenario may vary as indicated by dotted line in figure 2.2.

Dimensions of the preparing hypocentral focal source at depth in the lithosphere

The “dilatant” volume of cracked rock at depth in the lithosphere, as defined by the preseismic anelastic volumetric increase (dilatancy), may be considered as a soft inclusion.

Volume V of this preseismic source has been defined by Dobrovolsky et al. (1989) as a function of the magnitude M of the forthcoming earthquake, as follows:

$$V_{max} = 10^{(1.24M-4.47)} \text{ km}^3$$

For a spherical shape, the radius r of such a source becomes:

$$r = 10^{(0.41M-9.18)} \text{ km}$$

Dimensions of the earthquake precursory area at the Earth's surface

The Earth's surface area where preseismic strain exceed tidal strains ($\approx 10^{-8}$) is defined as “precursory area” (Dobrovolsky et al., 1989). It is the region where earthquake precursors can be observed. The radius R_P of such a region is defined as a function of

M	r (km)	R_P (km)
4.0	~ 0.1	~ 52.5
5.0	~ 2.5	~ 141
6.0	~ 6	~ 380
7.0	~ 41.3	~ 1023

Table 2.1: Dimensions of a preseismic spherical “dilatant” source (r) at depth and related Earth’s surface precursory area (R_P) for different values of the earthquake magnitude (M).

the magnitude M of the forthcoming earthquake, as follows:

$$R_P = 10^{0.43M} \text{ for } 10^{-4} \leq \epsilon \leq 10^{-8}$$

where ϵ is strain, given by:

$$\epsilon = \frac{10^{1.5M-9.18}}{R_P^3} \text{ for } M < 5.0$$

and

$$\epsilon = \frac{10^{1.3M-8.19}}{R_P^3} \text{ for } M \geq 5.0$$

Values of r and R_P for earthquakes with magnitude $4.0 \leq M \leq 7.0$ are given in table 2.1.

2.2 Seismo-associated phenomena and earthquake precursors

Despite of a few differences, all the above-mentioned models suppose that the abrupt fracturing of the rock is preceded by accumulation of deformation in the fault zone. The strain increase is accompanied by variations in different physical fields and by other natural phenomena in the vicinity of the preparing fracture which give rise to the so-called earthquake precursors.

Thus, the microfracturing process is related not only with seismic events, but also with other natural *seismo-associated* (SA) phenomena that are important for the development of earthquake forecasting and methods of seismic vulnerability.

SA phenomena like seismogenic EME are demonstrated to be the most significant

earthquake precursors. The most reliable interpretative models concerned with EMEs generation mechanisms are reported in chapter ???. We stress that the study of SA phenomena is necessary to understand the physics of the earthquake (earthquake triggering, post-seismic relaxation, lithosphere-atmosphere-ionosphere-magnetosphere coupling).

The main SA phenomena, anthropogenic EME, and effects produced by local preseismic stress-strain fields are listed in the following.

Main seismo-associated phenomena

- Tectonic deformation, rock microfracturing, fluid diffusion and gas emissions;
- Electrokinetic, piezomagnetic, and piezoelectric effects:
- Exoelectron emissions;
- Charged particles motion;
- EM-waves propagation through the lithosphere up to the magnetosphere;
- Plasma instabilities and magnetospheric particle precipitation.

Effects of local preseismic stress-strain fields

- Ground tilt and strain changes;
- Ground acoustic, gas, and EM emissions (in the DC-10 MHz frequency band)
- Ionospheric and magnetospheric perturbations caused by these emissions
- Ionospheric perturbations also are caused by the above-mentioned anthropogenic emissions

2.3 Earthquake precursors. Space and ground-based investigations.

As mentioned in chapter 1, coordinated simultaneous and continuous ground-based and space measurements are ways by which it is possible to explore and investigate the properties of the Earth's interior, and in particular the dynamic processes in the core, mantle and crust (Bell et al., 1982; Bell, 1985), as well as to probe the electromagnetic and acoustic emissions of anthropogenic origin and related perturbations in the near Earth space (Parrot and Zaslavski, 1996). It has also been mentioned that the geomagnetic field and its variations, together with natural electromagnetic, acoustic and gas emissions from the Earth surface generated by seismic ruptures, geothermal activity, volcanic eruptions, as well as artificial acoustic and electromagnetic emissions of anthropogenic origin (Power line Harmonic Radiation, VLF transmitters, HF broadcasting stations, underground nuclear explosions), demonstrated to affect strongly the dynamics, structure and composition of the medium in the ionosphere-magnetosphere region (Parrot, 1995; Parrot and Zaslavski, 1996).

Taking into account the efficiency and reliable character needed for preseismic phenomena (also called earthquake precursors or SA effects), ground-based measurements of local deformation fields, and EME-waves should be carried out in selected test areas of the Earth's surface. At the same time a space monitoring of ionospheric and magnetospheric perturbations caused by the above-mentioned ground preseismic EME-waves should be performed.

Ground SA phenomena, and in particular changes of local deformation and EM fields, are frequently observed at the Earth's seismic areas prior-to, during and after an earthquake. The main mechanical and EM earthquake precursors include aseismic fault creep events and EME-waves over a wide frequency band, respectively.

First promising results have also been obtained from rare observations carried out in the ionosphere-magnetosphere region. They include an accurate knowledge of the internal and external components of the geomagnetic field, as well as measurements of the electric field, EM-waves, ionospheric plasma temperature and density, and fluxes of charged particles.

Although several theoretical models have been proposed on the subject, the physical mechanisms of these ground and space observations are yet largely unknown. In particular, it remains to be explained the generation of the EME radiation in the preparation focal area, at depth in the lithosphere, its propagation through the lithospheric layers with an assigned vertical conductivity profile, and the successive penetration of this radiation into the neutral and ionized atmosphere, up to the magnetosphere. For the EME-wave propagation through the last two regions a dispersive character of the medium must also to be taken into account.

In the following sections we give a short overview of the main ground-based and space observations obtained up to now and the first physical explanations proposed to justify these results. At the end of this chapter a qualitative representation of the phenomenology will be also reported as a baseline for constructing our model.

2.4 Observations of lithospheric and ionospheric pre-seismic perturbations

Ground-based measurements revealed slow electrotelluric and magnetic field variations (Johnston and Mueller, 1987; Varotsos et al., 1993) and preseismic ground potentials. The latter are generated as streaming potentials when saline water moving through porous rocks entrains ionic charges (Bernabé, 1998; Draganov et al., 1991), or through stress applied to rocks containing or not piezoelectric minerals as quartz (Bishop, 1981; Varotsos et al., 1997; Freund, 2002). The transmission of substantial stress over large distances has been debated (Geller, 1996; Sgrigna et al., 2002a; Sgrigna and Malvezzi, 2003).

Ground low-frequency (ULF/ELF) electromagnetic emission (EME) signals have also been documented in connection with relevant earthquakes (Kopytenko et al., 1993; Fraser-Smith et al., 1990; Ohta et al., 2001; Ismaguilov et al., 2001) and preliminary, even if not exhaustive, explanations have been reported on the subject (Park et al., 1993; Merzer and Klemperer, 1997; Molchanov and Hayakawa, 1998; Surkov, 1999; Hayakawa et al., 2000).

More in general, results of local ground-based SEME observations have been obtained

on a larger (ULF HF) frequency band (see, in addition to the above-mentioned authors, also Warwick et al., 1982; Oike and Ogawa, 1986; Johnston, 1997; Bella et al., 1998; Uyeda et al., 1999; Eftaxias et al., 2003).

Space observations of ionospheric perturbations over seismic regions have been reported and discussed on the occasion of several strong earthquakes (Gokhberg et al., 1989; Larkina et al., 1989; Parrot and Mogilevsky, 1989; Bilichenko et al., 1990; Serebriakova et al., 1992; Parrot et al., 1993; Chmyrev et al., 1997; Rodger et al., 1999; Lee et al., 2000).

In the following sections we will report a few main significant results obtained from ground-based and space observations together with some theoretical explanations.

2.4.1 Local ground-based measurements.

Preseismic creep strain observations

Aseismic fault creep strains have been observed prior to earthquakes in seismic areas. We report here an example of such an intermediate-term precursor obtained from ground tilt measurements on the occasion of the 1997 Umbria-Marche seismic sequence (Sgrigna and Malvezzi, 2003).

Daily averaged tilt component data from four sites of the Central Apennines (Italy) revealed intermediate-term tilts of a few months as possible precursors of the seismic sequence occurred in the Umbria-Marche region during 1997 (fig 2.3). The observed intermediate-term preseismic tilts are considered as the manifestation of aseismic creep episodes in the fault materials close to the tilt sites. The mechanism refers to a strain field slowly propagating from the dilatancy (focal) area to the tiltmeters, through rigid crustal blocks separated by weak transition zones with viscoelastic rheology. This propagation is thought to be the cause of the local aseismic fault slip recorded by tiltmeters. The existence of a propagating strain field is confirmed by the different onset time delays in the preseismic tilt signals recorded at different distances from the same earthquake. In particular, the onset time delay observed at each one of the PES, AQU, and GRS tilt sites appears to increase with increasing distance of such a site from the epicentral area. At greatest distances (STI site), where the preseismic strain becomes

negligible, the characteristic intermediate-term ground tilts vanish completely.

A 1-D and 2-D models have been proposed for slow crustal movements caused by subhorizontal forces applied to a system of rigid blocks separated by transition zones (faults) filled with viscoelastic material (Bella et al., 1990; Sgrigna et al, 2002a; Malvezzi et al., 2002).

The slow movements of crustal blocks cause the accumulation of deformation in the weakened fault zones, which is released either through a creep yielding process, or by an abrupt fracture, i.e. by an earthquake. Figure 2.3 shows the good agreement between the shape, amplitude and phase shift of creep curves predicted by the model with those from observations.

Electric and magnetic observations

As mentioned above, the literature shows that seismic EMEs are short-term precursors phenomena ($\sim 3 \div 12$ h), in fact they are observed in seismic active regions prior to earthquakes while they are not detected in seismic quiet regions. In particular, ULF EME are believed to be a direct emission from earthquake preparation zone whereas VLF emission are considered as a consequence of pre-seismic ionospheric perturbations that affect VLF transmissions. The intensity and the attenuation of the seismic EMEs depends on the geological conformation of the ground (ferromagnetic minerals give large static fields, sedimentary rocks strongly attenuate an EM emission).

We stress the fact that it is difficult to obtain general and uniform results from observations made in many different parts of the globe. Now, an estimation of the coverage of the world by EME networks is of about 10 % of globe's seismic areas.

Some main preseismic EME observations are reported in the following.

Figure 2.4 shows ULF anomalous variations of the geomagnetic field recorded before the Loma Prieta earthquake of October 18, 1989 ($M=7.1$; left) and the Spitak earthquake of December 7, 1988 ($M=6.9$, right).

Figure 2.5 shows the EME anomaly at 81 kHz detected before some earthquakes which occurred in Japan. Figure 2.6 illustrates a preseismic EME noise at 1.5 kHz before an earthquake of $M=6.2$.

Caputo (2003) and Nardi et al. (2003) presented the results of experiments made

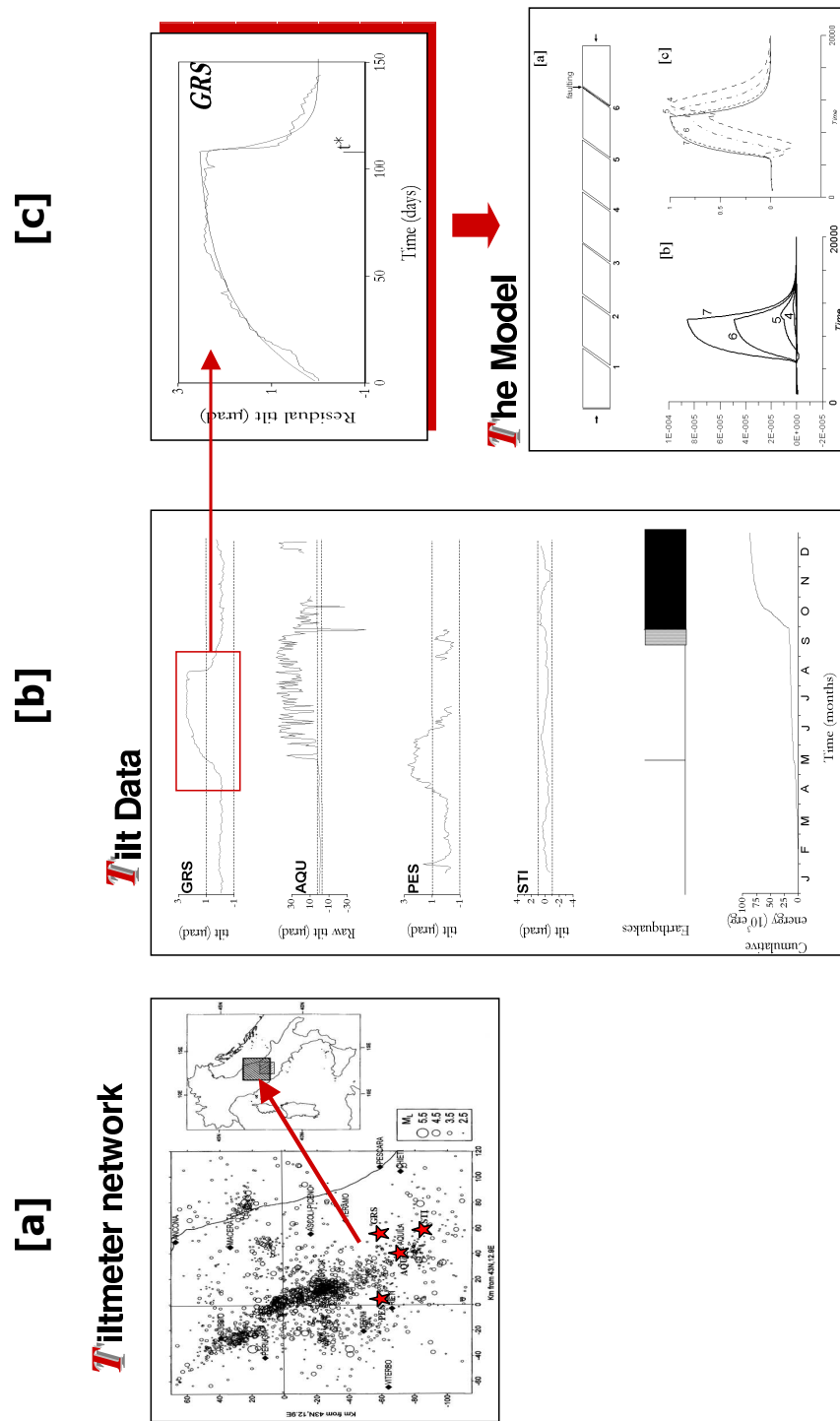


Figure 2.3: [a] Seismic events occurred in the central Apennines of Italy (points) and the four PES, AQU, GRS, and STI tilt sites (stars) used for the study (left panel). [b] the four upper lines of the central panel indicate GRS, AQU, and PES residual preseismic tilt anomalies over the 3σ (standard deviation) level, and the STI residual (normal) tilt signal. Earthquakes of the Umbria-Marche sequence and related cumulative energy release are reported in the two bottom lines of the same panel. [c] best tilt anomaly fitting by using creep curves from Kelvin-Voigt model (upper right panel) and theoretical 2D crust block modeling (bottom right panel).

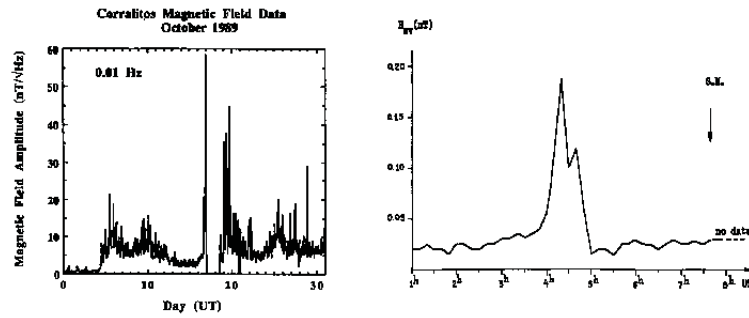


Figure 2.4: ULF magnetic variations before the Loma Prieta earthquake (Fraser-Smith et al., 1990) on the left. Variation of the H-component amplitude of the ULF EME before the Spitak earthquake (Kopytenko et al., 1993) on the right.

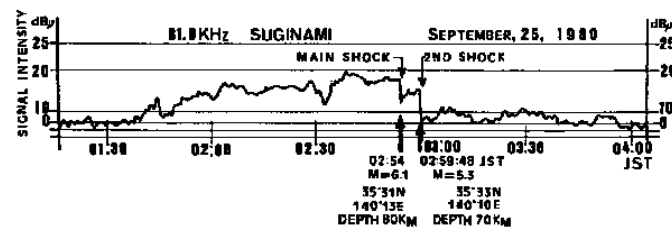


Figure 2.5: Preseismic VLF EME anomaly from a narrow band receiver centered at 81 kHz (Gokhberg et al., 1982).

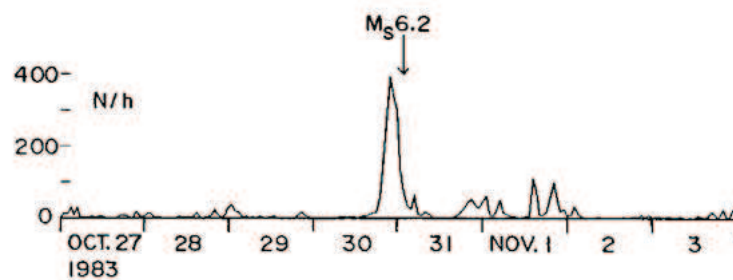


Figure 2.6: Preseismic variation of the hourly number of LF EME.

on rock samples in the laboratory and in the field which show the very low frequency (ELF, VF (voice frequency), VLF) radio emission associated to mechanical deformation and fracture of the rocks.

The method is based on the monitoring of the electromagnetic emission in the acoustic band (20 Hz - 20 kHz). The phenomenon at the origin of these emission has not yet been determined with certainty. They refer to two hypotheses both based on the micro-fracturing implied by dilatancy.

The field experiments have been made in a quarry of *Calcare Massiccio* during and after the explosions used to produce the rock material. The laboratory experiments has been made on samples of different rocks (*Calcare Massiccio*, *Calcare a Rudiste*, *Scaglia Variegata*, *Porphyry*, *Corniola*) subject to uniaxial compression.

In the bands ELF-VLF the premonitory signals of the fracture have been systematically observed. These emissions have a maximum intensity in the radio-acoustic band, decreasing with increasing frequency and therefore very low in the radio band of major use. The emission mechanism seems independent from the type of rock and from the type of perturbations used which lead to the fracture. Concerning the type of rock the signals seem more correlated to the structural homogeneity rather than to the mineralogical composition.

2.4.2 Space observations

EME observations

A reliable technique to observe preseismic EMEs and perturbations they produce in the near-earth's space is to use suitable satellite missions with a maximum ground tracks density over selected seismic regions and short-term revisit time for an high-accuracy Earth's surface monitoring. Moreover, simultaneous and continuous measurements of ULF-HF EME-waves, ionospheric plasma temperature and density, and particle fluxes are requested as well as coordinated, continuous and simultaneous ground-based and space observations.

On the contrary, the majority of the rare results obtained up to now are concerned with observations that are not specifically devoted to the study of preseismic phenomena.

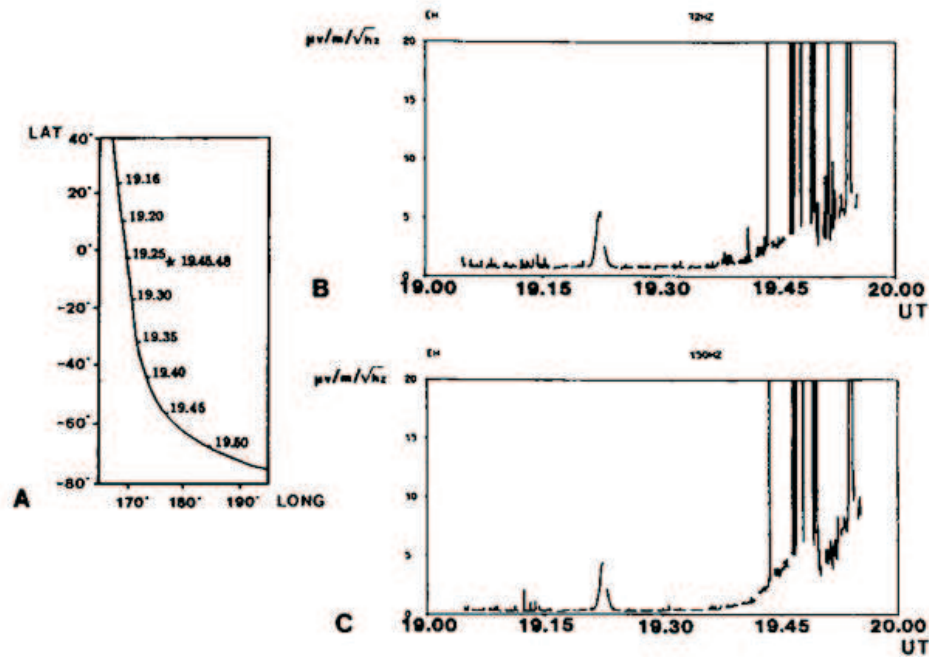


Figure 2.7: (a) Orbit of AUREOL-3 satellite. (b) and (c) Time variations of the electric component signal in filters centered around 72 Hz and 150 Hz, respectively, [Parrot and Mogilevsky, 1989].

Space observations of seismic ULF and ELF/VLF EME on board satellites whose orbit cross the upper ionosphere and low magnetosphere have been reported in literature in the last decade (Park et al., 1993). In particular, electric and magnetic data in the frequency range $10 \text{ Hz} \div 15 \text{ kHz}$ has been obtained by satellite AUREOL-3 (Parrot and Mogilevsky, 1989). The electric signals at the outputs of two filters centered around 72 Hz and 150 Hz are reported in figure 2.7. They can be considered short-term precursors (about 20 minutes) of an earthquake of magnitude 5.1.

Perturbations in the ULF EME has been detected before an earthquake of $M = 5.2$ with ITK-1300 satellite. ELF-VLF EME associated with earthquakes were observed as bursts above the epicentral zone by the Intercosmos-24 satellite 12-24 hours before the main shock (Molchanov et al., 1993).

ELF waves and increasing fluxes of energetic electrons and protons has been observed together before earthquakes by Galperin et al., (1992). A more detailed analysis on the

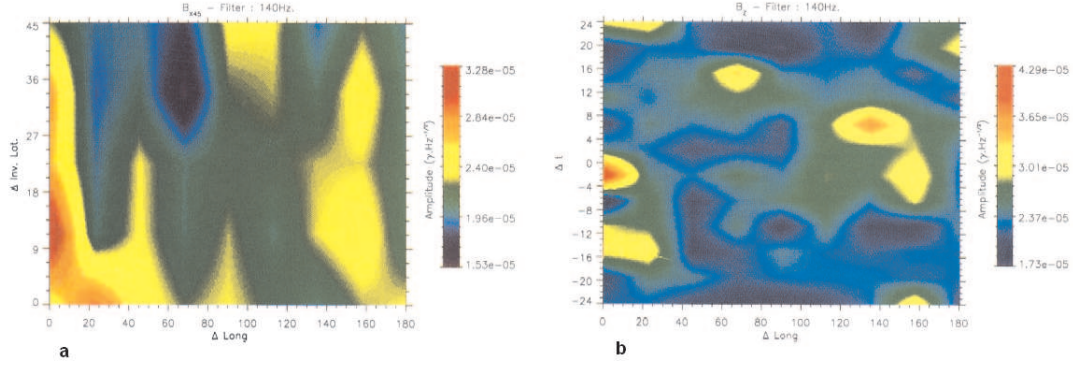


Figure 2.8: Result from statistical study using AUREOL 3 satellite, [Parrot, 1994].

influences of seismic ULF/ELF EMEs on the earth inner radiation belt is reported in the following sections. In figure 2.9 is reported a double measurement of seismic EMEs (AUREOL-3 and ITK-1300), in two different frequency band ($40 \div 100$ Hz and $100 \div 200$ Hz), observed above Spitak seismic areas ~ 4 h before a terrible and strong after-shock (January, 21, 1989).

The EM intensity spectrum decreasing with increasing frequencies is noted in most of the cited works. Ionospheric perturbations caused by acoustic waves during earthquakes were revealed through TEC measurements on board the TOPEX-POSEIDON satellite and carried out with GPS technique. A dissipative instability of acoustic-gravity waves was also obtained from the increased injection of active material, as radon (radioactive gas exhalation) into the atmosphere by the IC-B 1300 satellite 15 minutes before an earthquake with $M = 4.8$ (Sorokin and Chmyrev, 1999).

Only a statistical study can show the general behavior of wave emissions. Such statistical work was carried out by Henderson et al., (1993), using data from the low-altitude satellite DE 2, but this work indicates no evident correlation between seismic activity and wave emissions. Molchanov et al., (1993) however, have observed electromagnetic emissions associated with many earthquakes when they studied the Intercosmos 24 satellite data. Another statistical study with data from the low-altitude satellite Aureol 3 is reported by Parrot, (1994).

Plate 2.8 a) shows the average amplitude of signal recorded by magnetic component B_{x45} at 140 Hz as function of $\Delta inv.$ Lat and $\Delta long$. An increase of the wave intensity

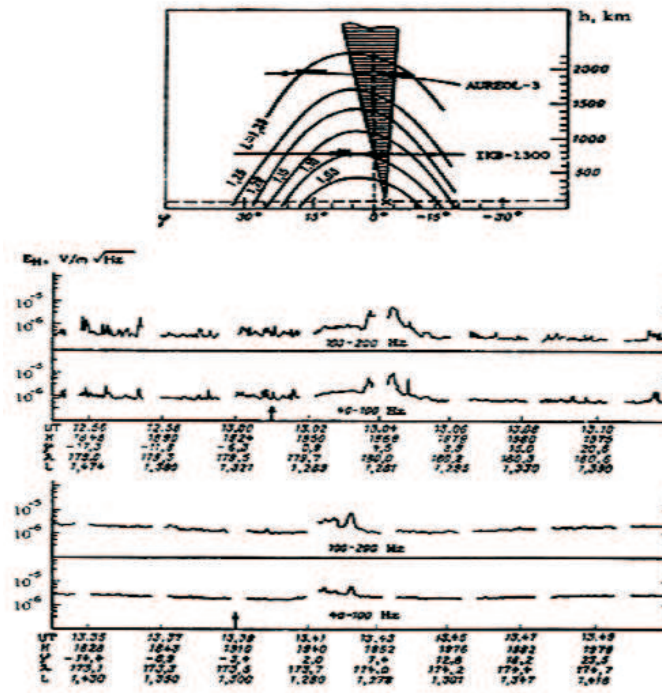


Figure 2.9: A double measurement of seismic EMEs (AUREOL-3 and ITK-1300), in two different frequency band ($40 \div 100$ Hz and $100 \div 200$ Hz), observed above Spitsk seismic areas ~ 4 h before a terrible and strong aftershock (January, 21, 1989) (Galperin, 1992).

is observed for $\Delta long$ between 0 and 20 degrees. Plate 2.8 b) shows the average wave amplitude at 140 Hz recorded by B_z as a function of dt and $\Delta long$, we can see a peak for $\Delta long < 20$ and for dt between 0 and -4 hours, which seems to indicate that it is a precursor emission. A correlation between two phenomena does not necessarily relate to a causative link, it is shown that wave intensity is enhanced at frequencies lower than 800 Hz close the epicenters.

2.4.3 Longitudinal size of ionospheric perturbations from seismo-associated phenomena

Concerning the ionosphere, the phenomenology of seismo-induced perturbations in the ionosphere is very complex. Several kind of perturbations exist from EMEs to anomalies of the ionospheric plasma parameters. Moreover, it is difficult to trace back an observed perturbation to its source because measurements come from non-dedicated

missions. Despite, we can build a general scheme on the basis of the experimental results we have briefly shown above. The longitudinal extension of the ionospheric perturbed region is the fundamental parameter used to distinguish the four different zones.

1. *Small extension zone ($\pm 5^\circ$ of longitude around the epicentral zone)*: ULF seismic EMEs are observed (Molchanov et al., 1993) both over the epicentral zone and in the magnetically conjugated zone. A reliable hypothesis is that seismic EMEs begin to propagate along geomagnetic field lines at a certain altitude (from about 200 km to about 800 km) so that can be observed also in magnetically conjugated region that can be located far from epicentral zone.
2. *Medium extension zone ($\pm 10^\circ$ of longitude around the epicentral zone)*: ULF and ELF seismic EMEs are observed together with the formation of small irregularities of plasma density and associated geomagnetic ULF micropulsations (Sorokin and Chmyrev, 1999). All perturbations are observed in the magnetic flux tube magnetically conjugated with the epicentral zone.
3. *Large extension zone ($\pm 30^\circ$ of longitude around the epicentral zone)*: there can be found perturbations in electronic profile and in ionic composition of the plasma, enhanced fluxes of energetic trapped electrons with $E_{e-} < 1$ MeV (Galperin et al., 1992) and anomalies in VLF waves propagation.
4. *Global extension zone (about all longitudes)*: high energy electrons and ions ($E_{e-} > 5$ MeV, $E_{p+} < 50$ MeV) whose trajectories are perturbed by seismic EMEs can propagate along their drift paths and are observed as bursts by detectors on board space missions (Aleshina et al., 1992). This particular model together with an original analysis about it is critically discussed in section 2.7.

Charged particle bursts

Concerning the magnetosphere, in the last two decades a very interesting and new phenomenon has been observed in the ionosphere-magnetosphere transition region. It

Correlations between Earthquakes & Particle Bursts: ΔT_{EQ-PB} distributions

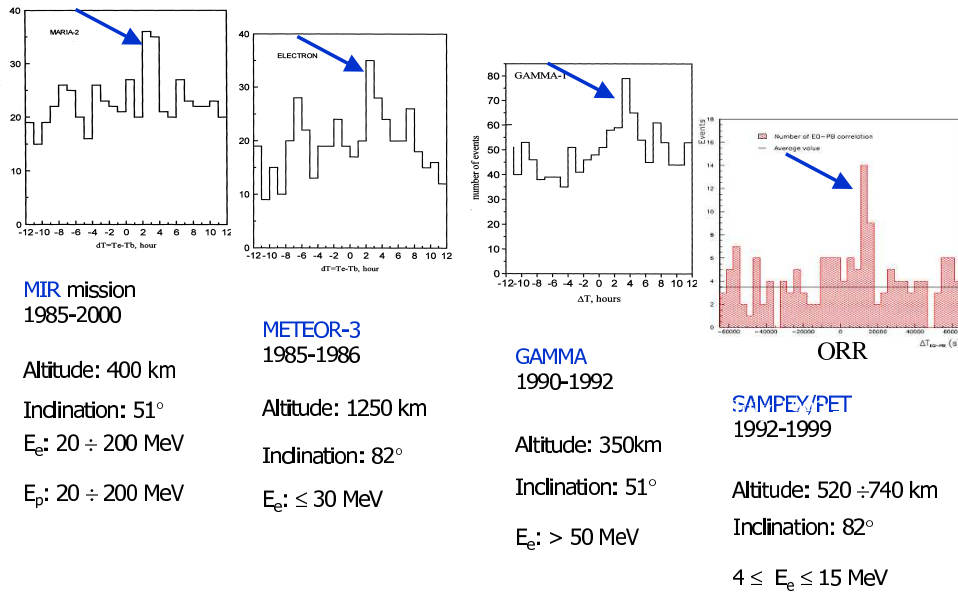


Figure 2.10: Histograms of the time difference between time differences $\Delta T = T_{EQ} - T_{PB}$, between the universal times of origin of selected earthquake (T_{EQ}) and PB (T_{PB}) events for four space missions. A positive and significant peak in the histogram (that is a peak in the $\Delta T > 0$ region) indicates that PBs statistically precede in time the earthquake occurrence (Aleksandrin et al., 2003; Sgrigna et al., 2005).

consists of anomalous particle fluxes detected by several space experiments and reconciled with the EQs occurrence (Galper et al., 1989; Voronov et al., 1990; Aleshina et al., 1992; Pustovetov and Malyshev, 1993). These particle fluxes are characterized by an anomalous short-term and sharp increase of high-energy particle counting rates (CRs). In the following they are referred to as “particle bursts” (PBs). Most of PBs have been collected near the South Atlantic Anomaly (SAA) at altitudes generally between around 400 km and 1200 km, by several satellites (Pustovetov and Malyshev, 1993; Ginzburg et al., 1994; Galper et al., 1995).

Larkina et al. (1989), and, more recently, Sgrigna et al. (2002b; 2003a, 2005) and Alexandrin et al. (2003) also confirmed the preseismic character of these PBs, based on PBs-EQs statistical correlations, and under the hypothesis that preseismic ULF/ELF EME wave-trapped particle interaction may cause the precipitation of radiation belt electrons and protons.

The preseismic character of PBs detected on board of MIR, METEOR-3, GAMMA, and SAMPEX/PET space missions is shown in figure 2.10.

2.5 Some theoretical approaches

The above ground-based measurements, space-observations, and related theoretical speculations, together with laboratory experiments (Nitsan, 1977; Yoshida et al., 1997; Freund, 2003) suggest a possible scenario for the generation and propagation mechanisms of the broad-band preseismic EME-waves (see also Dobrovolsky et al., 1989; Guo et al., 1994; Fenoglio et al., 1995; Molchanov et al., 1995; Teisseyre, 1997; Grimalsky et al., 1999; Sorokin et al., 2001; Gershenzon and Bambakidis, 2001; Fujinawa et al., 2002; Freund, 2003).

On the basis of standard dilatancy-diffusion and crack-avalanche models (Myachkin et al., 1975), most of investigators considers reasonable to assume the increasing and concentrating stress at depth in the fault asperity (preparation focal area) as a cause of the anelastic volumetric increase (“dilatancy”) of a relatively small portion of rock, and consequent rock dislocation and microfracturing. It has been shown (Areshidze et al., 1992; Bella et al., 1995; Guo et al., 1994; Molchanov and Hayakawa, 1998) that rock mi-

crofracturing releases gas (radon, helium) and causes electrical conductivity changes as a function of microcracks number and dimension and of pore fluids redistribution (saline pore fluids motion may cause the formation of intergranular water film). Recently, it has been proposed that also dry rocks can become a source of highly mobile electronic charge carriers, which increase the electric conductivity and may propagate through the rock as a charge cloud (Freund, 2002).

From all the above-reported results, local deformation field, rock dislocation and microfracturing, gas emission, fluid diffusion, charge particle generation and motion, electrokinetic, piezomagnetic and piezoelectric effects are to be considered as the main sources of preseismic EME-waves at depth in the Earth's crust, in the "dilatant" focal volume.

As a result of these preseismic phenomena at depth, ground tilt and strain changes and electric and EM field variations are observed at the Earth's surface as a consequence of the field propagation from the hypocentral source, through the relatively highly elastic and conductive thin upper crust layer. During this propagation the higher frequency content of the ULF HF EME-waves is attenuated and only ULF/ELF EME-waves are supposed to reach the Earth's surface and enter into the near-Earth space, where they cause perturbations (TEC changes, ionospheric motions, joule heating, etc.) in the atmosphere and ionosphere (Molchanov et al., 1995; Ohta et al., 2001).

LEO (Low-Earth-Orbit) satellite observations seem to confirm the above-illustrated scenario. Indeed, preseismic changes of electric and magnetic fields (Molchanov et al. 1993; Parrot, 1994) and of ionospheric plasma temperature and density (Parrot and Mogilevsky, 1989; Parrot et al., 1993; Chmyrev et al., 1997) have been observed from a few minutes to several hours prior to EQs of moderate or strong magnitude (generally, greater than 4.0).

But, preseismic EME-waves produced in the earthquake focal area with the above-described mechanism, are thought to propagate not only through the lithosphere, atmosphere, and ionosphere, but also to reach the inner Van Allen radiation belt, where they may interact with trapped particles (Galperin et al., 1992). In confirmation of this hypothesis, in the last two decades a very interesting and new phenomenon has been observed in the ionosphere-magnetosphere transition region as mentioned in sub-

section 1.1.7 . It consists of anomalous particle fluxes detected by several space experiments and reconciled with the EQs occurrence (Galper et al., 1989; Voronov et al., 1990; Aleshina et al., 1992; Pustovetov and Malyshev, 1993). These particle fluxes are characterized by an anomalous short-term and sharp increase of high-energy particle counting rates (CRs). In the following they are referred to as “particle bursts” (PBs). Most of PBs have been collected near the South Atlantic Anomaly (SAA) at altitudes generally between around 400 km and 1200 km, by several satellites (Pustovetov and Malyshev, 1993; Ginzburg et al., 1994; Galper et al., 1995).

At this purpose, several authors (Aleshina et al., 1992; Galperin et al., 1992; Galper et al., 1995; Krechetov, 1996) propose that in a certain portion of the ionosphere-magnetosphere transition zone such a low frequency content of the SEME radiation (from \sim DC to some hundred Hz) can propagate as Alfvén waves along the geomagnetic field lines. Near the radiation belt boundary, the waves may resonantly interact with trapped particles (electrons and protons from a few MeV to several tens of MeV) causing particle precipitation as a result of pitch-angle diffusion. The lower limit of the above-mentioned portion of the ionosphere-magnetosphere transition zone (that is, the altitude where preseismic ULF/ELF EME-waves are captured in the geomagnetic field lines and, then, propagate as Alfvén waves along these lines up to the inner radiation belt), has been estimated from PBs space observations and resulted to be around 300÷500 km (Aleksandrin et al., 2003).

In the following we will describe some main seismo-associated effects and principal models in order to give an idea of the theoretical concepts of EMEs generation and propagation. Models described in subsection 2.5.5 ÷ 2.5.10 are based on experimental results and try to fit them.

2.5.1 ElectroKinetic effect (EKE)

Electric and magnetic fields can appear near inhomogeneities of conductivity, permeability or, generally, of the streaming potential Φ . The value of Φ depends significantly on temperature, salt content and pH. A complete calculation of EKE arising during earthquake preparation periods consists of solutions to three interrelated problems:

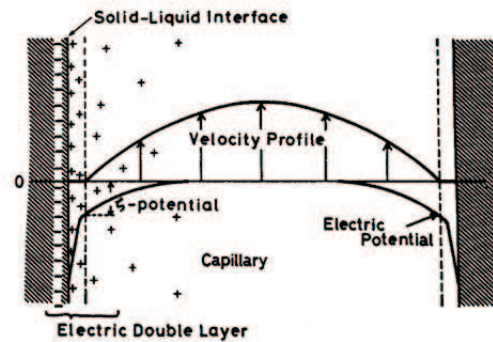


Figure 2.11: Diagram of an electric double layer and profiles of the electric potential and liquid velocity in a rock pore.

1. the description of crustal deformation processes;
2. the calculation of fluid motion in a porous medium;
3. calculation of the electric and magnetic fields of electrokinetic origin.

In the earthquake preparation periods crustal deformation and fracturing processes occur, causing a change of porosity, which, in turn, causes a change of fluid motion and of the associated electric current.

A non-zero gradient of pore fluid pressure will set the fluid in motion and hence will cause an electric current according to the electrokinetic theory.

Electrokinetic phenomena owe their existence to an electric double layer formed at a solid-liquid interface. The double layer is made up of a layer of ions which are firmly held to the solid, and a more diffuse mobile layer extending into the liquid (fig. 2.11). Because of the electrical charges, there is a difference of the electrical potential between the solid-liquid interface and the bulk of the liquid. This is called the electrokinetic potential or zeta potential ζ .

When an electromagnetic field is applied to the electric double layer, there will be a displacement of the oppositely charged layers relative to one another. If the solid cannot move, the fixed part of the double layer also is unable to move; the application of an electromagnetic field will result in movement of diffuse layer ions and liquid.

This is the basis of electro-osmosis. From a balance equation of electric force and vis-

cous force, we derive:

$$\vec{j} = \frac{\varepsilon\zeta}{\eta} \nabla\Phi$$

where \vec{j} is the fluid flow flux through a capillary per unit time and area, ζ is the zeta potential, η is the viscosity of the fluid, and ε is the dielectric constant of fluid. The streaming potential is just the reverse of electro-osmosis; the streaming potential is the production of potential difference when a liquid is forced through a porous medium. From a similar treatment to that in the previous equation, the streaming potential Φ is given by:

$$\nabla\Phi = \frac{-\varepsilon}{\eta\sigma} \nabla p$$

where σ and p are the electric conductivity and the pressure of the fluid, respectively. The most general relations between the electric current \vec{i} and the fluid flow \vec{j} , and the forces of $\nabla\Phi$ and ∇p are:

$$-\vec{i} = L_{11} \nabla\Phi + L_{12} \nabla p$$

$$-\vec{j} = L_{21} \nabla\Phi + L_{22} \nabla p$$

where L_{ij} are constants. The first term in the right hand of first equation represents Ohm's law, and the second term in the second equation represents Darcy's law. The terms with L_{12} and L_{21} correspond to the electrokinetic effect. Explicit expression of the last two equations in a porous medium are:

$$-\vec{i} = m\sigma \nabla\Phi + \frac{-\varepsilon m\zeta}{\eta} \nabla p$$

$$-\vec{j} = \frac{-\varepsilon m\zeta}{\eta} \nabla\Phi + \frac{k}{\eta} \nabla p$$

where k is the permeability, and m is the porosity. We are interested to the first of the

previous two equations.

The effect of electro-osmosis can be neglected in such problem, assuming p to be independent of the electric field. So, the problem of finding the electric field is then described by the equation $\vec{\nabla} \cdot \vec{i} = 0$, or: $\nabla[\sigma(\nabla\Phi + C\nabla p)] = 0$ in which we have both the electric field and pressure variation.

2.5.2 Piezoelectric effect

Piezoelectricity is a property that arises from the crystal anisotropy of substances. A piezoelectric substance shows an electromagnetic response against mechanical stimulations on electric polarization caused by deformation of the crystal lattices. In piezoelectric materials stresses σ_{ij} caused by an electric field E depend linearly on the same field. If we take into account only this linear contribution, we have:

$$\sigma_{ik} = \tilde{F}\delta_{ik} + \left(\frac{\partial \tilde{F}}{\partial u_{ik}} \right)_{T,E}$$

where \tilde{F} is the free energy, u_{ik} is the strain tensor, δ_{ik} is the Kronecker-delta.

The thermodynamic equation for the free energy is given by:

$$d\tilde{F} = -SdT + \sigma_{ik}du_{ik} - \frac{1}{4\pi}\vec{D} \cdot d\vec{E}$$

where T is temperature, S the entropy, D the electric induction.

By introducing the thermodynamic potential $\tilde{\Psi} = \tilde{F} - u_{ik}\sigma_{ik}$ we may write:

$$d\tilde{\Psi} = -SdT + u_{ik}d\sigma_{ik} - \frac{1}{4\pi}\vec{D} \cdot d\vec{E}$$

Then:

$$u_{ik} = - \left(\frac{\partial \tilde{\Psi}}{\partial \sigma_{ik}} \right)_{T,E}$$

It is possible to define the potential $\tilde{\Psi}$ by which we may write the following relation between σ_{ik} and \vec{E} :

$$u_{ik} = \mu_{iklm}\sigma_{lm} + \gamma_{l,ik}E_l$$

where $\gamma_{l,ik}$ is the piezoelectric tensor and μ_{iklm} is a 4-rank tensor in the linear relationship between stress and strain.

2.5.3 Magnetostriction of ferromagnetic materials

This phenomenon consists of a deformation in ferromagnetic materials caused by a change in the magnetization state of the material when it is inside a magnetic field.

The energy variation of relativistic interactions in a strained body is described by introducing magnetoelastic terms in the thermodynamic potential which depend on stress tensor components and on the direction of the magnetization \vec{M} . A general expression for the magnetoelastic energy U_{ME} is given by:

$$U_{ME} = -a_{iklm}\sigma_{ik}m_l m_m$$

where a_{iklm} is an dimensionless tensor of rank 4, symmetric with respect to indices ik and lm , and \vec{m} defines the direction of vector \vec{M} .

2.5.4 Piezomagnetism and magnetoelectric effects in anti-ferromagnetic materials

Similarly to piezoelectricity, this effect consists of the magnetization of a material obtained by applying a stress to the crystal. It is described by a linear term in the thermodynamic potential with respect to both the field and the elastic stress tensor:

$$\tilde{\Psi}_{PM} = -\lambda_{i,kl}H_i\sigma_{kl}$$

where $\lambda_{i,kl}$ is a symmetric tensor with respect to indices kl . It is known as piezomagnetic tensor. This allows to introduce in the relation which defines the magnetic field vector $B_i = -4\pi\partial\tilde{\Psi}/\partial H_i$ the term $4\pi\lambda_{i,kl}\sigma_{kl}$. In other words, for $\vec{H} = 0$:

$$M_i = \lambda_{i,kl}\sigma_{kl}$$

The same property appears when:

$$u_{kl} = -\frac{\partial\tilde{\Psi}_{PM}}{\partial\sigma_{kl}} = \lambda_{i,kl}H_i$$

The piezomagnetic tensor $\lambda_{i,kl}$ changes sign by inverting the sign of time. Then, piezomagnetism may occur only in magnetic bodies. In other cases, material properties are invariant with respect to the time inversion and then $\lambda_{i,kl} = -\lambda_{i,kl} = 0$. Therefore, piezomagnetic effects are possible in antiferromagnetic bodies belonging to particular classes of materials having a magnetic symmetry that contain or not the R transformation (for which all currents change their direction in the opposite one) in combination with rotations or reflections.

The magnetoelectric effect consists of a linear relationship between electric and magnetic fields in the body. This effect is described as follows:

$$\tilde{\Psi}_{ME} = -\alpha_{ik}E_iH_k$$

where α_{ik} is an antisymmetric tensor. For $\vec{H} = 0$ the electric field creates the magnetization M in the body:

$$M_k = \alpha_{ik}E_i$$

and for $\vec{E} = 0$ the magnetic field generates the electric polarization as follows:

$$P_i = \alpha_{ik}H_k$$

As for piezomagnetism, the magnetoelectric effect is possible only for specific classes having magnetic symmetry: the magnetoelectric tensor α_{ik} is an odd number with respect to the time inversion and is nil in non magnetic bodies.

2.5.5 Exoelectron emission and charge generation and propagation in igneous rocks

When the electron subsystem of rock materials which exhibit a dielectric behavior are excited by mechanical deformation, most of the generated nonequilibrium electrons and holes are captured by traps. The ionization energy of the filled traps is lower than that of the states in the unexcited material. Therefore, subsequent excitation results in electron emission from the preliminarily filled traps. This phenomenon is called exoelectron emission (Grunberg, 1958). Various mechanisms of the exoelectron emission effect differ by the way in which the energy required for the ionization of the filled traps is transferred to the localized electrons. Thermal ionization is the most investigated mechanism, in which thermo stimulated exoelectron emission is a result of thermal excitation. The Auger mechanism is a widespread one for thermo stimulated exoelectron emission when the ionization of electron traps is accomplished due to the energy released during recombination of nonequilibrium electrons and holes.

Freund (2002, 2003), proposed a model based on evidence that dry rocks, in particular dry igneous rocks, can become a source of highly mobile electronic charge carriers. These charge carriers not only cause an increase in the electrical conductivity, but they also appear to be capable of propagating through the rocks as a charge cloud.

Electronic charge carriers can be electrons or defect electrons, the latter known as holes. Both electrons and holes can be associated with transition metal cations that change their oxidation states. What is recognized is the fact that oxygen can also exist in two oxidation states: as O^{2-} in the common 2- oxidation state and as O^- in the somewhat uncommon 1- oxidation state. Given special local lattice conditions to be outlined, O^{2-} can convert to O^- . An O^- in an O^{2-} matrix represents an electronic charge carrier, a hole, but it is different from the holes that reside on the cation sublattice. To underscore this difference an O^- in the O^{2-} sublattice is designated as a positive hole. It has been shown (Freund 2002) that positive holes can also be activated by low-energy rock microfracturing. Before activation, the positive holes lay dormant in the form of electrically inactive positive hole pairs, chemically equivalent to peroxy links. Depending on where in the stressed rock volume the charge carriers are activated, they will form rapidly moving or fluctuating charge clouds that may account for earthquake-related

electric signals and EME. Wherever such charge clouds intersect the surface, high fields are expected, causing electric discharges.

2.5.6 Fracturing as an underlying mechanism of seismo-electric signals (SES)

In this model (Molchanov, 1999), SES are believed to be a cumulative quasi-electrostatic field due to electrokinetic effect. The fundamental feature of static solution is its dependence on source current configuration. Experimental data show that the signal is not accompanied by magnetic field variations, but is a pure electrostatic field. The condition to obtain a pure electrostatic field is $\vec{\nabla} \wedge \vec{j}_s = 0$, where \vec{j}_s is the source current density. The best candidate to describe such type of source is EK mechanism, in which an induced current density is connected with a variation in water pressure p as follows:

$$\vec{j}_{se} = \Phi \nabla p$$

where $\Phi = \varepsilon \zeta m / \eta$ is streaming potential coefficient, ζ is zeta potential, η is viscosity and m is porosity. If Φ is constant $\vec{\nabla} \wedge \vec{j}_s = 0$. In these conditions, the electric fields generated during microfracture process by EKE can be estimated:

$$\vec{E}_1 = \hat{e}_x \left(\frac{\Phi \Delta p_0}{2\sigma L_s} \right) (\hat{e}_x \cdot \hat{e}_r) \frac{L_s^3}{r^3} (1 + t/\tau)^{-1}$$

where L_s is the earthquake preparation zone dimension, r is the distance from the observation point, Δp_0 is the stress drop, σ is the medium conductivity, τ is the rupture duration and \hat{e}_x, \hat{e}_r are the \vec{E} field versors.

For many fractures, occurring before an earthquake of magnitude M we suppose that the fields from each fracture has same polarity. We calculate the overlap of a number of electric pulse E_n using the Gutenberg-Richter distribution for the earthquake occurrence rate \dot{N} :

$$E_n \approx E_1 (\dot{N}^{1/2}) \approx E_1 L_s^{-d/2}$$

where d is the fractal parameter ($d \leq 3$). We finally obtain:

$$E_n \approx (L_s)^{2-d/2}; \quad \log E_n = (2 - d/2) \log L_s + C_1$$

where C_1 is a constant value, E_n is the electric field due to the overlap of n electric pulses. Calculation results agree with experimental ones.

2.5.7 EMEs generation due to Moving Charged Dislocations (MCD)

This model is proposed by Vallianatos and Tzanis (1999) to explain the generation of precursory electric and magnetic fields associated with the deformation rate of the earthquake focus. The model describes the generation of an electric current in rocks under stress. The intensity and the behaviour of the electric signal depend drastically on the strain rate ($\dot{\epsilon}$).

In a crystalline structure, dislocation may be formed by an excess or absence of half-plane of atoms. In an ionic structure there will be an excess or absence of a line row of ions along the dislocation line, with consequence that the dislocation becomes charged. In a thermal equilibrium, the dislocation line would be surrounded by a cloud of point defects of the opposite sign to maintain electric neutrality. But, in dynamic processes, when dislocations move, the electric neutrality can no longer be maintained.

Let assume an uniaxial compression (or tension). The motion of charged dislocation produces a transverse polarization:

$$P = (\Lambda^+ - \Lambda^-)q_l \frac{\delta x}{\sqrt{2}} = \delta \Lambda q_l \frac{\delta x}{\sqrt{2}}$$

where Λ^+ and Λ^- are the densities of positive and negative edge dislocations, respectively, q_l is the charge per unit length on the dislocation, and δx is the distance through which the dislocations are moved. A time dependent polarization produces a current in the medium that can be written as:

$$J_p = \frac{\partial P}{\partial t}$$

Since J_p depends on $\dot{\epsilon}$ ($J_p = \frac{\sqrt{2}}{\beta} \frac{q_l}{b} \dot{\epsilon}_p$), then it is possible to write a relation for the horizontal component of the electric field, measured at a point on a surface:

$$E(x, t_k) \approx sf\rho \sum \dot{\epsilon}_i \frac{x - x_i(t_k)}{R_i^n(t_k)}$$

where x is the source position, t_k is the time of occurrence of the dislocation, R_i is the distance of the observation point from the dislocation located at x_i , $n = 2$ for a linear source, ρ is the specific resistivity of material, s is a sensitivity coefficient at the location of the receiver and f is a coefficient dependent on geometry of the source. Calculation results give estimation for the intensity of magnetic anomaly of about 5 nT.

2.5.8 ULF EMEs generated by Magnetic Pulses (MP)

A generation model for ULF electromagnetic perturbations resulting from the fracture and dilatancy in the earthquake preparation zone is proposed by Surkov (1999).

The model explains the presence of intrinsic currents in the medium induced by elastic waves and due to the seismomagnetic effect. Moreover, the associated magnetic moment changes induce currents in the same medium. The resulting electromagnetic field is precursor of the main seismic rupture in the medium. During the opening of a crack an acoustic wave is generated. The consequent velocity in the medium and the presence of the geomagnetic field B_0 induce a density current $\vec{j} \propto \sigma(\vec{v} \wedge \vec{B}_0)$. The total magnetic moment generated during the opening of the crack (p_m) give rises to the magnetic field components:

$$B_r = -\frac{p_m}{C\sigma\lambda} \frac{\cos\theta}{r^3} \left(1 + \frac{\lambda}{r}\right) \exp\left(-\frac{r-Ct}{\lambda}\right)$$

$$B_\theta = -\frac{p_m}{C\sigma\lambda^2} \frac{\sin\theta}{2r^2} \left(1 + \frac{\lambda}{r} + \frac{\lambda^2}{r^2}\right) \exp\left(-\frac{r-Ct}{\lambda}\right)$$

where λ and C are the wave length and speed of the acoustic wave, respectively, and skin effect was taken into account. The two component are related by the condition $\vec{\nabla} \wedge \vec{B} = 0$ which derives from the assumption $\vec{\nabla} \cdot \vec{j}_s = 0$. An estimation of the calculated electric and magnetic fields gives $1 \div 10$ nT e $1 \div 10$ μ V/m, respectively, in agreement with observations.

2.5.9 Generation of ULF seismogenic electromagnetic emission

This model (Molchanov and Hayakawa, 1998) is based on the basic idea that we can describe resultant magnetic field variation $\vec{B}(\vec{r}, t)$ through equivalent system of currents

with volume density distribution $\vec{j}(\vec{r}, t)$, related with microcurrents $i_c(\vec{r}_c, t)$, originated in each opening crack α (number of cracks $N_c \gg 1$). We assume that the process of generation is quasi-stationary. Then we can introduce the spectrum density $\vec{j}(\vec{\omega}, t)$ and:

$$\langle j^2(\vec{r}, t) \rangle = \frac{1}{2T} \int_{-T}^T |j^2(\vec{r}, t')| dt' = \frac{1}{\pi} \int_0^\infty j^2(\vec{r}, \omega) d\omega$$

The assumption of a quasi-steady-state condition is reasonable because the emission observed is noise-like and temporal duration of observations is $T_e \approx 1$ h, then where $T_e \gg \tau \approx 10^{-7}$ is the microcrack opening time.

It is usually supposed that we can expect an opening of a crack with some velocity V and during the opening same charges Q are created. Simultaneously with the charge generation on the surface its disappearance due to the medium conductivity σ_s . Taking into account that a crack can be expanded only up to the length l , we have the following relations for a single microcurrent:

$$i(t) = \frac{dQ}{dt} = \begin{cases} i_m \left(\frac{\tau_d}{\tau_c} \right) (1 - e^{-t/\tau_d}) & t \leq \tau_c \\ -i_m \frac{\Phi(\tau_c)}{\tau_c} e^{-(t-\tau_c)/\tau_d} & t > \tau_c \end{cases}$$

where $i_m = 2\pi q_0 V^2 \tau_c = 2\pi q_0 l^2 / \tau_c$, $q_0 = dQ/dS$, $\tau_c = l/V$, $\tau_d = \epsilon_s / \sigma_s$. Averaging over an ensemble of N microcracks, an expression for the current density spectrum $j(\omega)$ can be derived. An estimation $j(\omega)$ is $j(\omega) = 10^{-6} A m^{-2} H z^{-1/2}$ that gives values of B and E in agreement with previous results and experimental observations.

We stress that all described models, that give reliable results, are related with microfracturing process. Then, it can be supposed that observed EMEs are caused by all the mechanisms together.

2.5.10 Attenuation of EME waves in the lithosphere and their penetration into the near Earth's space

The problem of generation and propagation of preseismic EME-waves in different media (lithosphere, atmosphere, ionosphere, magnetosphere) has been investigated by Molchanov et al.(1995) and Molchanov and Hayakawa (1994) in the case of a ground current source with cylindric symmetry situated in the preparation zone of an earth-

quake (that is in the forthcoming hypocenter).

These authors, considered the attenuation of the EME-waves in the upper lithosphere to be proportional to $e^{-(\pi\omega\mu\sigma)^{1/2}z}$, where z is the distance from the source region, ω the wave frequency, μ the magnetic permeability, and σ the electric conductivity. This calculation for surface rock common values of σ ($\cong 10^{-2} \div 10^{-5} Sm^{-1}$) indicates that beyond a depth of 10 km from the ground surface, only ULF waves ($\omega \leq 10Hz$) can reach the Earth's surface with an attenuation less than 10 dB.

Concerning the penetration of preseismic EME-waves from the Earth into the near Earth's space, Molchanov et al., (1995) considered the ULF/ELF EM radiation ($\omega \cong 10^{-2} \div 10^2$ Hz) under the assumption that the density of EM energy is small compared with seismic energy in the ground or the kinetic energy of the particles in the ionosphere and magnetosphere. In this way they divided the total current into the source current (J_s) and current induced by the EM field, that is: $J = \sigma E + J_s$ with E , electric field. By introducing an *effective spectrum density* $J(\omega, R)$ of the source current, Molchanov and Hayakawa (1994) defined a relation for spectrum amplitudes between $J(\omega, R)$ and $E(\omega, R)$ by using Maxwell equations and assuming all values to vary as $e^{-i\omega t}$:

$$\nabla \wedge H = \sigma'(\omega)E + J_s; \quad \nabla \wedge E = i\omega\mu H; \quad \sigma' = \sigma - i\omega\epsilon I$$

where $\sigma'(\omega)$ is the tensor of conductivity, I is the unit matrix, and ϵ the electrical permittivity of the medium.

By assuming a one-dimensional dependence of the conductivity tensor on vertical direction and a cylindrical symmetry of the source current distribution and resulting fields, the above mentioned authors proposed a model for the propagation of ULF/ELF EME waves, from the hypocentral depth to the near Earth's space.

Using the continuity of the solutions of wave equations at the edges of the different layers encountered ($z = 0$; $z = z_i$; $z = z_m$), one can calculate the coefficient of the energy transmission. Figure 2.12 gives the total transfer coefficient of the energy of the magnetic field from the ground source up to the magnetosphere, as a function of the frequency. Several cases are considered:

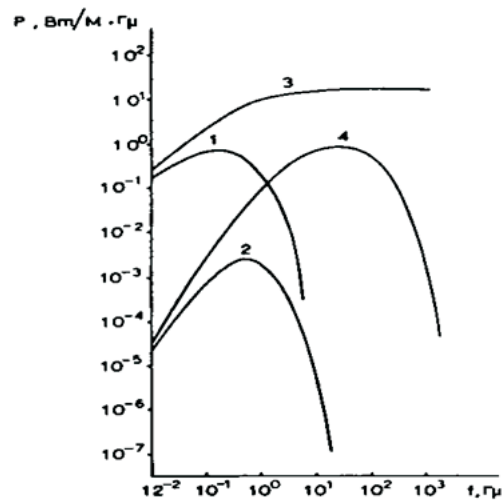


Figure 2.12: Transfer coefficient of the energy of the magnetic field, between the source and the magnetosphere, as a function of the frequency. Different conditions (curves) are explained in the text.

1. observations on the ground ($z = 0$ km) and source at depth in the Earth's crust ($z_0 = 30$ km);
2. observations in the ionosphere ($z = 500$ km) and source at depth in the Earth's crust ($z_0 = 30$ km);
3. observations on the ground ($z = 0$ km) and source at the Earth's surface ($z_0 = 0$ km);
4. observations at ionospheric altitude ($z = 500$ km) and source at the Earth's surface.

2.6 The state of scientific knowledge relevant for the study: gaps and issues

Virtually all regions of the Earth's magnetosphere have been explored. The various populations of trapped particles have been observed, their compositions and energy

spectra measured, and a long history of changes in particle distributions caused by natural variations in the Earth's magnetic and electric fields has been recorded (Abel and Thorne, 1998). The motion of individual particles in static magnetic and electric fields is completely understood (Baumjohann and Treumann, 1997). The interaction of the solar wind and the geomagnetic field is complex and the processes that control many of the characteristics are not yet understood. The complexity of the processes experienced by charged particles in the geomagnetic field is truly bewildering, such that, important phenomena are still only dimly perceived. In many ways, some only vaguely understood, the trapped population acts as a coupling agent transferring energy, momentum and mass between the interplanetary medium and the Earth's atmosphere. This transfer is many-faceted, sometimes occurring by the direct transport of particles, and sometimes through the intermediary of stresses in the geomagnetic field, electric currents, and plasma waves. Unraveling these dynamic interactions is one of the principal immediate goal of magnetospheric research. Many features that have been observed repeatedly still lack a quantitative explanation, and new discoveries will, no doubt, continue to be made. These features are distinguished by magnetic field topologies, by the characteristics of the plasma found there, by the presence of electric currents and fields, or by the presence of certain types of plasma waves. The effects of changes in the large-scale magnetic and electric fields and the resulting diffusion and acceleration of particles (Pustovetov et al., 1993; Aleshina et al., 1992) retain some of their mystery in that the time variations of the fields have not been measured sufficiently to support a complete verification of the theoretical formulations. Also, much of the theoretical foundations rest on approximations that are not always valid. In spacecraft technology the energetic trapped particles have always been an important, sometimes dominant, concern. Satellite components may be degraded by an increased background resulting from the passage of charged particles through the electrically active volume. Trapped particles may also deposit unequal charges on satellite surface leading to differences in the electric potential of various satellite segments. The resulting electric discharges can damage electronic components or produce spurious signals which can modify the instrumental monitoring of electric field or give false instructions to spacecraft computers. The effects of the radiation belts on satellites remains a major factor in satellite

lifetimes. The origin of the great part of intermediate- and low-energy particles which occupy the outer magnetosphere is not well known. Knowledge of the influence of various types of waves on trapped particles is in a less satisfactory state, although there is no controversy over the general principles by which waves and particles interact. Various approximations have been applied successfully when the wave amplitudes are small. However, these simplifications cannot be used for strong waves. The general case where the waves and particles exchange appreciable energy has not been fully investigated within magnetospheric geometry and is an active area of current research. This case is of particular relevance for one of the aspects of the scientific objectives of the proposal concerned with the study of the Earth's surface activity through the observation of the interactions with trapped particles, of low-frequency electromagnetic waves, emitted from the ground. These interactions demonstrated to cause the precipitation of high-energy charged particles from the inner radiation belt and a relatively long-term longitudinal drift of these particles makes them detectable by satellite measurements. Electromagnetic waves around $\approx \text{DC} \div 10 \text{ MHz}$ and acoustic emissions emitted from the Earth's surface are known since a long time, even if their generation mechanisms and propagation up to the magnetosphere, as well as their interaction processes with neutrals and charged particles is not yet completely understood. A specific study based on many events is required in order to support investigations on the generation and propagation mechanisms of such emissions, as well as on the ionospheric and magnetospheric perturbations they produce. As a complementary approach to ground-based investigations (carried out by local or global networks), satellite observations may cover most of the active Earth's surface areas and offer the possibility to increase statistics useful for the study of such natural ground effects. It is correct to say that the exploratory phase of radiation belt is ending, and we are now entering an area of detailed investigation in which theory will be confronted by more comprehensive and precise data. The data most needed now are simultaneous observations made from key locations throughout the magnetosphere. On the basis of what above-mentioned, we think the ionosphere-magnetosphere transition zone around 600 - 1000 km, selected for the study, is one of the most important region of investigation, since its behavior is largely unknown and it is very sensitive to many phenomena and effects

produced by the solar-terrestrial interactions and Earth-near-Earth environment. Measurements need to involve multispacecraft observations as well as multi-instrument measurements of particle fluxes, electric and magnetic fields, and wave characteristics over a broad frequency range. Only when such data are available and have been explained by a specific physical model can one be confident that many of the important physical processes in the ionosphere-magnetosphere transition zone have been identified. This aim at to the understanding of many phenomena included in the scientific objectives of the DEMETER mission .

2.7 A qualitative representation of the phenomenology

Our qualitative representation of the phenomenology, is reported in figure 2.13.

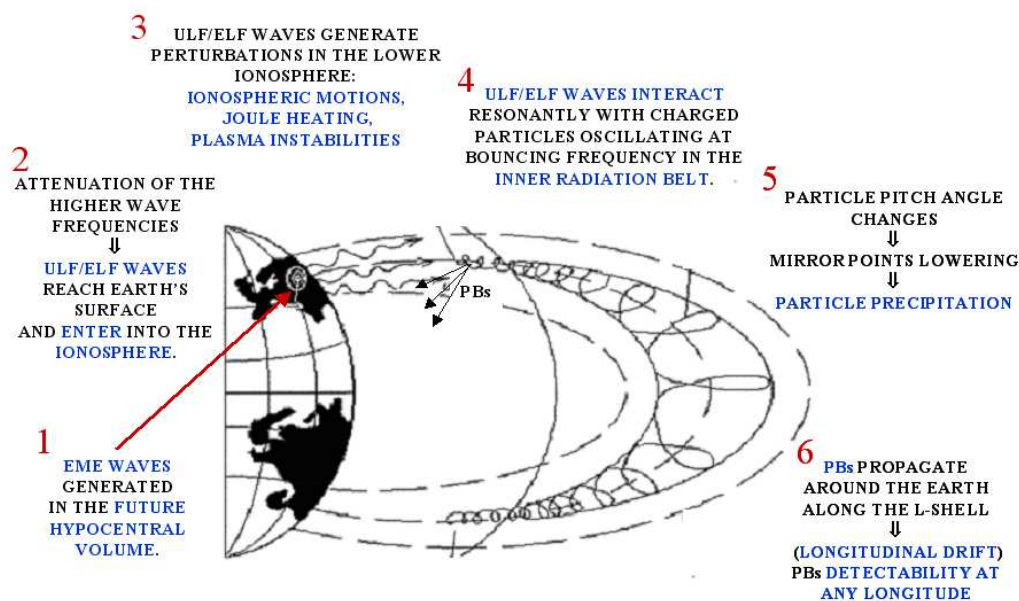


Figure 2.13: Qualitative representation of the phenomenology, [Sgrigna, V., 2001].

Local preseismic deformation field changes are better observed on the ground. Pre-seismic acoustic emissions are detectable on the ground. Such a radiation seem to be enough efficient to be detected in space only as a co-seismic effect, that is when it is gen-

erated by seismic waves. Preseismic gas exhalations seem to be more efficient on the ground than in the ionosphere-magnetosphere transition region. On the contrary pre-seismic EME are observed both in space and on the ground (see section 2.4). Therefore, EM waves appears to be as the primary phenomenon to be investigated simultaneously in space and on the Earth's surface. This justifies and demands for both experimental and theoretical specific studies on the subject. From the experimental point of view the DEMETER satellite (which is flying now), as well as other experiments like ARINA (M. Boezio, et al., 2004) and EGLE (Sgrigna et al., 2006) are valid attempts for investigating the earthquake preparation. The study of space whistler and particle data collected by the Demeter microsatellite is the bulk of this thesis work.

Chapter 3

Demeter satellite

The aim of the present chapter is to introduce the DEMETER satellite mission, and in particular to describe the RNF and IDP experiments used in this thesis work.

3.1 Demeter mission

In the last decades, EM observations have been progressively improved by increasing the number of ground-based networks and developing space investigations by appropriate satellite missions.

Authors	Satellites	Number of events	Location	Frequency range	Methods	Results
Larkina et al. (1983)	IK-19 600–1000 km	39 $M > 5.5$	$D < 60$ km, $\text{InvLat} < 45^\circ$	Filters 140 Hz–15 kHz	Visual	Positive low freq.
Parrot and Lefeuvre (1985)	GEOS-2	296 $M > 4.7$	$D_{\text{long}} < 20^\circ$	Filters 300 Hz–10 kHz	Comparison with random data	Positive $f < 1$ kHz
Matthews and Lebreton (1985)	GEOS-2	65 $M < 5$		0.3–11 Hz	Visual	Negative
Henderson et al. (1993)	DE2 300–1300 km	63 $M > 5$	$\text{InvLat} < 45^\circ$	Filters 4 Hz–512 kHz	Control orbit and threshold	Negative
Molchanov et al. (1993)	IK-24 500–2500 km	28 $M > 5.2$	$\text{InvLat} < 45^\circ$	Filters 140 Hz–15 kHz	Visual	Positive $f < 1$ kHz, $f > 10$ kHz
Parrot (1994b)	Aureol 3 400–2000 km	325 $M > 5$	$\text{InvLat} < 45^\circ$	Filters 140 Hz–15 kHz	Distance	Positive
Rodger et al. (1996)	ISIS 2 1350–1420 km	37 $M > 5$	New Zealand, Alaska	Wideband spectra 50 Hz–10 kHz	Control orbit and visual	Negative

Figure 3.1: Summary of statistical studies performed making use of satellite data, [Parrot et al., 2006].

But at present, these simultaneous ground and space observations are not yet suitable for an exhaustive explanation of the physical mechanisms underlying electric and magnetic signals associated with volcanic or seismic activity. Therefore, research with this aim continues with a critical view and with new ideas and deep investigations. Results obtained from e.m. wave experiments are summarized in fig. 3.1. This table resumes statistical studies performed on satellite data. A positive result indicates that authors have found a correlation with seismic activity.

The DEMETER (Detection of Electro Magnetic Emissions Transmitted from Earthquake Regions) mission has the objective to fill gap mentioned above (Parrot et al., 2006). On 29 June 2004, the French Space Agency (CNES) launched a micro-satellite called Demeter, specifically devoted to EM and particle studies. Objectives were to search signals related to natural disasters and anthropogenic activity. In particular, Demeter aims at studying ionospheric disturbances: i) due to the seismo-electromagnetic effects and ii) due to anthropogenic activities (Power Line Harmonic Radiation, VLF transmitters, HF broadcasting stations). Demeter is then entirely dedicated to these observations, through i) continuous data collection, ii) in the appropriate frequency ranges, and iii) in the different components of the electro magnetic field. The satellite, located on a Low Earth Orbit (LEO) (715 km height), works continuously in two modes: a survey mode in which EM data are recorded at a low bit-rate (spectrograms are computed), and a burst mode during which waveforms are recorded at several kHz. The time and space locations of one or the other of the two modes are determined as function of the ground volcanic and seismic targets.

In fig. 3.2 are reported Myriade platform performances and a list of the parameters measured by Demeter.

A three-axis magnetic search-coil instrument (IMSC), four electrical sensors (ICE), two Langmuir probes (ISL), a plasma analyzer (IAP), an energetic particle detector (IDP) and an electronic unit (BANT) constitute the Demeter scientific payload. To avoid electromagnetic disturbances to the sensors caused by the satellite, the IMSC captor is set at the end of a 1.9m long boom, while the ICE captors are set at the extremity of four booms of 4m long each. One can see this boom configuration in fig. 3.3.

The general layout of the satellite is given in the Fig. 3.4.

Orbit	<ul style="list-style-type: none"> Low earth orbit DEMETER : 710 km, SSO
Pointing	<ul style="list-style-type: none"> Earth pointing (DEMETER) Sun or inertial pointing
Stabilisation	<ul style="list-style-type: none"> 3 axis. Typical accuracy: Coarse mode < 5° Fine mode < 0,1 ° Stability: < 3'/s.
Telemetry Telecommand	<ul style="list-style-type: none"> CCSDS, convolutionnal & R- S coding. S -Band Transmission. Useful TM rate: 400 kbits/s. Useful TC rate: 20 kbit/s.
Localisation	<ul style="list-style-type: none"> Doppler measurement Accuracy: 1 km (LEO), 10 km (GTO).
Date	<ul style="list-style-type: none"> Ground synchronization. On board accuracy: < 0,5 s.
Power	<ul style="list-style-type: none"> Steerable sun generator AsGa solar cells(200 W EOL) Li Ion battery: 14 Ah Payload: around 70 W permanent.
Weight	<ul style="list-style-type: none"> Total: 130 kg. Payload weight: 50 kg.
Propulsion	<ul style="list-style-type: none"> Hydrazine, Δv : 80 m/s 4 thrusters 1 N
High rate TM	<ul style="list-style-type: none"> X-Band emitter 16,8 Mbits/s Memory : 8 Gbits (Flash)
GPS	<ul style="list-style-type: none"> Topstar 3000

Frequency range, B	10 Hz - 17 kHz
Frequency range, E	DC – 3,5 MHz
Sensibility B :	$2 \cdot 10^{-5} \text{ nT Hz}^{-1/2}$ at 1 kHz
Sensibility E :	$0.2 \text{ } \mu\text{V Hz}^{-1/2}$ at 500 kHz
Particles: Electrons :	30 keV - 10 MeV
Ionic density:	$5 \cdot 10^2 - 5 \cdot 10^6 \text{ ions/cm}^3$
Ionic temperature:	1000 K - 5000 K
Ionic composition:	H ⁺ , He ⁺ , O ⁺ , NO ⁺
Electron density:	$10^2 - 5 \cdot 10^6 \text{ cm}^{-3}$
Electron temperature:	500 K - 3000 K

Figure 3.2: Myriade platform performances and DEMETER Measured Parameters, [Cussac et al, 2006].



Figure 3.3: Picture of the Demeter satellite in flight with its deployed booms and sensors, [Cussac et al, 2006].

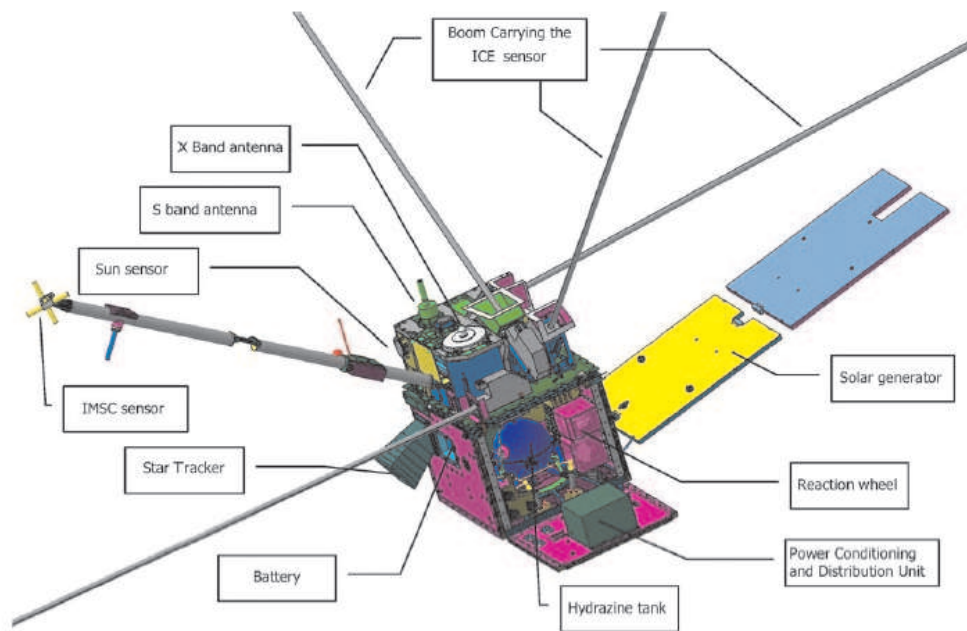


Figure 3.4: Layout of the Demeter satellite, [Cussac et al, 2006].

IMSC is composed of three orthogonal magnetic antennae (search coil type) linked to a pre-amplifier unit with a shielded cable of 80 cm. The search coil magnetometer consists of a core in permalloy (high permeability material) on which are wound a main coil with several thousand turns (12,000) of copper wire and a secondary coil with a few turns. The flat frequency response of the VLF frequency band is going from 100 Hz up to 17.4 kHz [Parrot et al., 2006].

The main objective of the ICE (Instrument Champ Electrique) experiment on board Demeter is to provide a nearly continuous survey of the electromagnetic and/or electrostatic waves that may arise from the coupling of seismic activity with the upper atmosphere and ionosphere. To this aim it makes use of 4 spherical electrodes with embedded preamplifiers that, as mentioned above, are deployed by stacer booms at approximately 4m from the satellite. Measurements are made over a wide frequency range from DC to 3.175 MHz, subdivided by the signal processing unit in four frequency channels DC/ULF, ELF, VLF and HF. Three axis measurements are available

in the DC/ULF range for all modes of operation of DEMETER and in the ELF range in the DEMETER Burst modes. In the VLF and HF ranges and in ELF during DEMETER Survey modes only one axis of measurement is available that can be selected by telecommand [Berthelier *et al.*, 2006a].

The Demeter Langmuir probe experiment, called Instrument Sonde de Langmuir (ISL), has been designed for in situ measurements of the bulk parameters of the ionospheric thermal plasma. The ISL instrument includes two sensors: (i) a classical cylindrical sensor and (ii) a spherical sensor with surface divided in seven segments: six spherical caps electrically isolated and the rest of the sphere which is used as a guard electrode. The two main parameters measured by ISL are the electron density and temperature; they are obtained with a 1 s time-resolution. In addition, the ion density and its variation can be derived from the current-voltage characteristics of the probe, but it requires an a-priori knowledge of the ion composition and a more sophisticated processing than the one currently implemented [Lebreton *et al.*, 2006].

The Instrument d'Analyse du Plasma (IAP) on board Demeter provides a nearly continuous survey of the main parameters of the thermal ion population with two main objectives. The first one is to detect disturbances in the ionosphere that may arise from the coupling between seismic events on the ground and the upper atmosphere and ionosphere. The second objective is to provide with a sufficient time resolution the ionospheric parameters such as the plasma density and the ion composition that are needed to analyze the plasma wave data from the ICE and IMSC experiments. The instrument makes use of two analyzers to measure: (i) the energy distribution of the rammed ions and (ii) the direction of their bulk velocity [Berthelier *et al.*, 2006b].

The IDP detector with a large geometrical factor is aimed to measure trapped electron fluxes in the energy range from 70 keV to about 0.8 MeV and to provide information on the electron fluxes between 0.8 and 2.5 MeV. The energy resolution, better than 10 keV, and the 256 energy channels allow to obtain insights on the radiation belt structure [Sauvaud *et al.*, 2006]. More details about IDP and statistical analysis produced will be reported in the next chapter.

The RNF experiment onboard Demeter allows, for the first time, a continuous survey of whistler phenomena. It consists of a neural network system dedicated to automati-

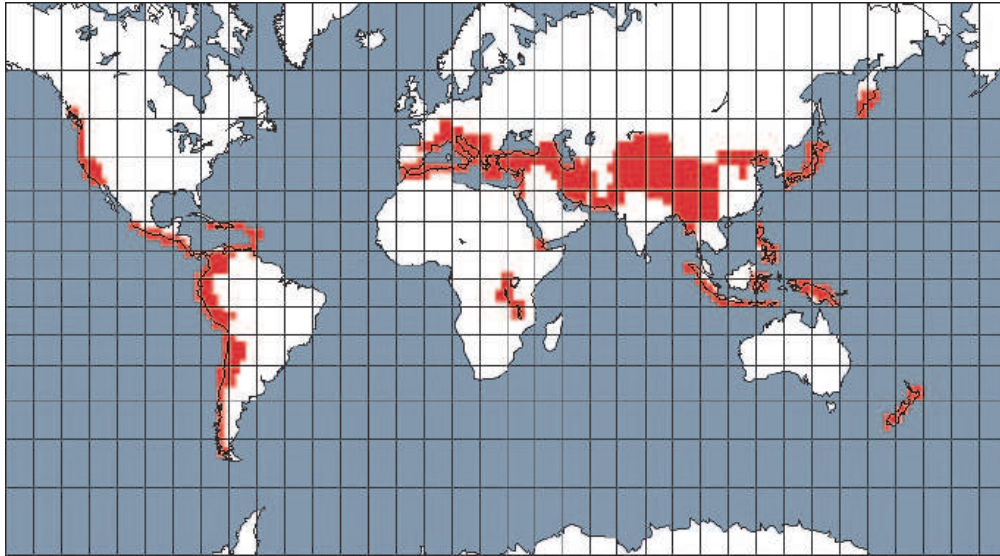


Figure 3.5: Burst and Survey mode of Demeter satellite.

cally identify and classify from ELF-VLF electric field measurements whistlers encountered by the satellite. In this way, each whistler is identified and characterized onboard Demeter by the RNF experiment. In particular using data provided by the neural network, it is possible to obtain the geographic whistler distributions at the altitude of the satellite for different ranges of dispersion parameters and for both night time and day time conditions. More details about RNF and statistical analysis produced will be reported in the next section. Concerning the two main Demeter modes of operation (see fig. 3.5) : (a burst mode which is triggered when the satellite is above given seismic zones, and elsewhere a survey mode), following corresponding recorded data are obtained :

1. in the BURST MODE

- waveforms of the three magnetic and the three electric components in the ELF range up to 1 kHz (sampling frequency 2.5 kHz),
- waveforms of one magnetic and one electric component in the VLF range up to 17 kHz (sampling frequency 40 kHz),
- spectra of one electric component up to 3.3 MHz.

2. in the SURVEY MODE

- spectra of one magnetic and one electric component up to 17 kHz. Three possible combinations of frequency and time resolutions can be selected by telecommand.
- spectra of one electric component up to 3.3 MHz.

In both modes, the three electric components are recorded in the ULF range, and either a magnetic or an electric component in the VLF range is used as input for an onboard neural network which will detect whistlers.

3.2 Introduction to Neural network background

Lightning-related phenomena are currently observed in the ELF/VLF range by magnetospheric satellites, but limitations in telemetry systems prevent continuous observation. There are several open questions on the effect of lightning on global precipitation patterns of energetic particles and also on triggering of steady emissions. The object of this section is to present a new system, based on neural networks, that allows on board real-time identification and classification of whistlers. The main reasons for using a neural-network approach are as follows:

1. huge data-banks exist that allow the constitution of almost exhaustive databases for training, generalization, and validity test;
2. once trained on the ground the neural networks require minimal and constant computing time, which permits real-time analysis;
3. the same architecture may be used for quite different phenomena, e.g. the same neural network can be applied to electron and proton whistlers;
4. neural networks accept large variations within a class of phenomena, which allows us to cope with many geophysical parameters that may affect a whistler: altitude of the point of observation, invariant latitude, local time, geophysical activity.

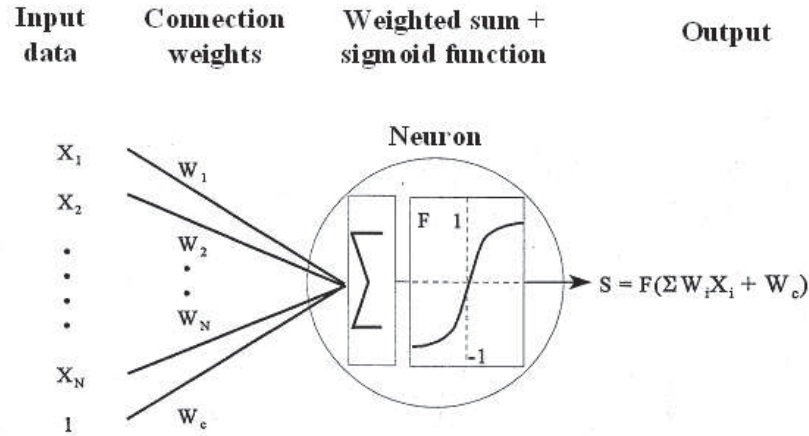


Figure 3.6: Neural Network unit or neuron. The neuron sums N weighted inputs and passes the result through a non-linearity process. Here, a sigmoid function is used. The threshold value of sigmoid can be adjusted by using an additional weighted connection to a constant input, [J-L.Pinçon, Demeter Guest Investigator Workshop, 2-4 May 2005].

The approach adopted is the Time Delay Neural Network (TDNN) described by Waibel *et al.*, [1989] for phenomena recognition. It is very adapted to the structure, in the frequency time domain, of power spectra obtained for whistler. The architecture presented here has been obtained by considering several neural networks, each of which had only two classes to identify. To make this feasible:

- we allowed large variations in each class ;
- we explored several time resolutions when one event was detected;
- we estimated dispersion and amplitude parameters a posteriori, i.e. outside the neural network.

In this section will be presented an introduction and application of whistler phenomena to a neural network. A neural network is a dense interconnection of simple elements called neurons . The basic task fulfilled by a neuron consists of the summation of N weighted inputs and the decision making through a nonlinear operator [Miniere *et al.*, 1996]. A neuron using a sigmoid function is shown in fig 3.6

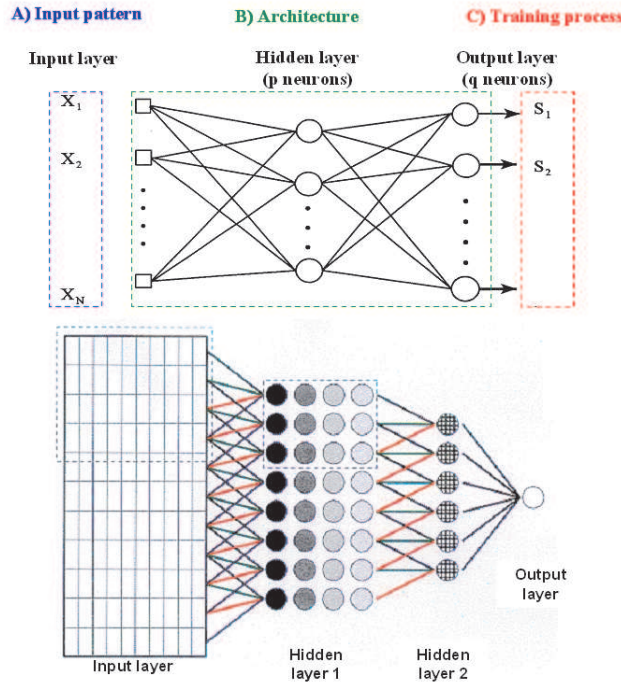


Figure 3.7: The neural network architecture used for whistler detection onboard Demeter, [J.-L. Pinçon, Demeter Guest Investigator Workshop, 2-4 May 2005].

Neural networks are used for a variety of information-processing tasks. For the classification tasks considered here, one generally uses the multilayer perceptron architecture. Topologically, it is a feed-forward network with one input layer, one or more intermediate processing layers (hidden layers), and an output layer containing one node for each pattern class. Each neuron in a layer is connected to all neurons in the layer above. Connections within a layer or from higher to lower layer are not permitted. A multilayer perceptron with two hidden layers is shown in fig. 3.7

In a neural network the knowledge is stored in the connection weights between the neurons. The training or learning algorithm determines the manner in which the weights are fixed. The computation of the weights represents the network's "training" process. Training is accomplished by using a set of input/output pairs. Contrary to expert systems, explicit modelling is not required. The training phase is completed when the difference between the computed and expected outputs is below a given threshold.

As input to network, we used a subset of a normalized spectrogram estimated here from the waveform of electromagnetic component observed by Demeter satellite. A total of ten distinct input patterns are necessary to allow the estimation of dispersion parameters ranging from $0 \text{ s}^{\frac{1}{2}}$ to $282 \text{ s}^{\frac{1}{2}}$. They are built from spectrograms after logarithmic conversion (decibel) with three different time resolutions and four sets Fourier components. The dispersion domain analyzed is splitted into 19 classes.

The objective of whistler analysis aboard Demeter is to detect phenomena with "anomalous" characteristics. Such kind of phenomena were observed by *Hayakawa et al.*, [1993] at longitude of seismic zones prior to earthquakes. We expect the neural network system on board Demeter will help to make a definitive statement on possibility(or not) to use such phenomena as precursors of earthquakes (see 4).

The whistler are characterized by peculiar values of dispersion parameter noted D. The dispersion parameter is defined by the Eckersley law, $D = t_f \cdot f^{\frac{1}{2}}$ where t_f is the time necessary for the Fourier component with frequency f to propagate between the lightning and satellite. Such signals have very distinct signature structured in the frequency /time domain, and are currently observed in the ELF/VLF range by magnetospheric satellites. In order to construct the different database needed we start, as all experimenters do, from spectrograms. Provided the time resolution is small compared with the duration of the structured events, the spectrograms are known to contain all the necessary information. However, to avoid unnecessary neurons, we limit the neural network's input to appropriate frequency bands.

3.3 Application of neural network on continuous sets of Demeter data

In the ELF range, lightning-related phenomena can be separated in two distinct classes: fractional whistlers and whistlers. Each class is characterized by certain values of dispersion parameter D [*Elie et al.*, 1999]. Fractional whistlers correspond to electromagnetic impulses due to lightning observed onboard the satellite in the frequency range from a few Hz to a few MHz, and are characterized by a weak positive dispersion parameter. One generally considers D values between $3 \text{ s}^{\frac{1}{2}}$ and $12 \text{ s}^{\frac{1}{2}}$ for fractional

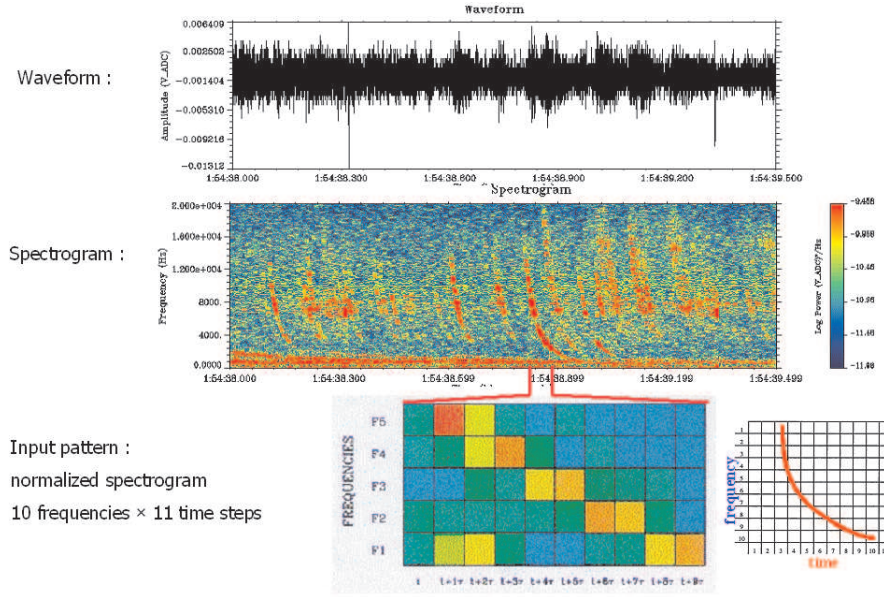


Figure 3.8: Example of waveform, spectrogram and input pattern used for whistler detection onboard Demeter, [J-L.Pinçon, Demeter Guest Investigator Workshop, 2-4 May 2005].

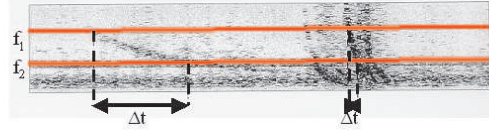
whistlers. This low dispersion value is a consequence of a relatively short propagation path from the ionospheric input point to the satellite.

Whistler have longer propagation times in the ionospheric and magnetospheric plasma (at least one magnetospheric path between conjugate hemispheres). There are observed in the frequency range from a few hundred Hz to a few tens of kHz, and are characterized by large positive values of D , usually ranging from several tens to a few hundred $s^{\frac{1}{2}}$. At low frequency, the D parameter of fractional whistler and whistler tends towards a limit termed Do (for $f < 2$ kHz one usually considers $D \simeq Do$). In this case, these phenomena are characterized by a relationship as follows:

$$\Delta t_{12} = Do \cdot \left(\frac{1}{\sqrt{f_1}} - \frac{1}{\sqrt{f_2}} \right) \quad (3.1)$$

where Δt_{12} is the time interval observed on the satellite between the arrival of the two frequencies f_1 and f_2 . The Do values depend upon the plasma parameters encountered by the phenomenon during its propagation and upon the satellite latitude. Due to the large difference in dispersion parameters for fractional whistler and whistler,

a) Dispersion parameter D_0 : $\Delta t = D_0 [(f_2)^{-1/2} - (f_1)^{-1/2}]$



b) Combining the frequency bands and the time resolutions one may identify 19 whistler classes

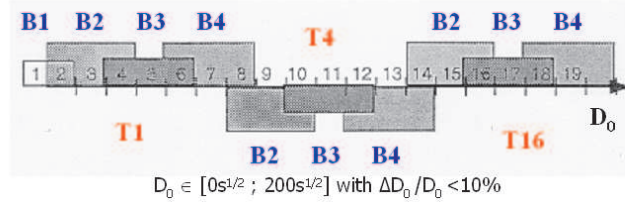
• 3 time resolutions: T_1, T_4, T_{16}

$T_1 = 6.4\text{ms}$; $T_4 = 4 T_1$; $T_{16} = 16 T_1$

• 4 frequency bands: $B1, B2, B3, B4$

$B1 = [3.2\text{kHz} - 11\text{kHz}]$, $B2 = [2.4\text{kHz} - 10.2\text{kHz}]$,

$B3 = [4\text{kHz} - 12\text{kHz}]$, $B4 = [5.5\text{kHz} - 14\text{kHz}]$



$D_0 \in [0s^{1/2} ; 200s^{1/2}]$ with $\Delta D_0 / D_0 < 10\%$

Figure 3.9: Description of neural network output: identification and classification of whistlers [J-L.Pinçon, Demeter Guest Investigator Workshop, 2-4 May 2005].

different time and frequency resolutions are needed. These frequency and time resolutions can be determined from estimates of the minimum and maximum dispersion values expected for Demeter data used. In order to identify fractional whistlers, 100 point FFT are computed on the waveform. They are gathered on a spectrogram whose frequency and time resolutions, respectively, are 50 Hz and 10 ms. The number of selected frequency bands in TDNN input layer should be as small as possible to minimize the number of inputs, and large enough to allow a sufficient frequency description of the phenomena. A good compromise consist of selecting five successive Fourier components, (600Hz, 650Hz, 700Hz, 750Hz, 800Hz), located in the frequency band with the best signal-to-noise ratio. Such a subset of a spectrogram is perfectly consistent with a fractional whistler dispersion $D_0 \geq 3s^{1/2}$. Taking $f_1 = 600\text{Hz}$ and $f_2 = 800\text{Hz}$, and using equation 3.1, has been found a minimum dispersion time of 16.4 ms. Now will be examine the TDNN inputs associated with whistler detection. A rough estimate gives a maximum value of D_0 equal to $70 s^{1/2}$ for Demeter whistlers. Replacing it in equation 3.1 and using the same frequency bands as fractional whistlers, has been found a max-

Block number	Description
1	General header
2	Orbital and geomagnetic parameters
3	Attitude parameters
4	Experiment data

Figure 3.10: Level-1 data block types.

imum dispersion time. An example of waveform, spectrogram and input pattern of RNF are reported in figure 3.8. In figure 3.9 are represented a description of the identification and classification of whistlers used in the neural network output. In the table 3.1 are reported the classes of whistler and whistler dispersion values, respectively.

CLASS	$D(s^{\frac{1}{2}})$
1	0 - 2,5
2	2,5 - 3,2
3	3,2 - 4
4	4 - 5
5	5 - 6,3
6	6,3 - 7,9
7	7,9 - 10
8	10 - 12,6
9	12,6 - 15,9
10	15,9 - 20
11	20 - 25,2
12	25,2 - 31,7
13	31,7 - 40
14	40 - 50,4
15	50,4 - 63,5
16	63,5 - 80
17	80 - 101
18	101 - 127
19	127 -

Table 3.1: Class and dispersion values of whistlers.

The level-1 data files of RNF are organized with a constant time structure as presented in 3.10. It is composed of four successive data blocks, each block containing parameters useful to make science. The size of each block is constant per data type. Four different blocks have been defined, block1, block2, block3 and block4. The detail of block1, block2, block3 are reported in figure 3.11, 3.12, 3.13. The data block 4 of RNF is detailed in Table 3.14. The number of whistler for every class are taken every 0,1 s.

Figure 3.15 present the final set of characteristic dispersion parameters resulting from the analysis of few seconds of Demeter data by ICE. The top panel contains a

Block 1: General Header					
Field number	Type	Array dim.	Size (bytes)	Unit	Description
Standard CCSDS date					
1	I*1	1	1		P field (decimal value = 76)
2	I*3	1	3		Number of days from 01/01/1950
3	I*4	1	4		Number of milliseconds in the day
Time and orbit information					
4	I*2	7	14		UT time of the first point of the data array as: year, month, day, hour, minute, second, millisecond (year as 20xx)
5	I*2	1	2		Orbit number
6	I*2	1	2		Sub-orbit type: 0: downward, 1: upward
7	A8	1	8		Telemetry station: "TOULOUSE"
Code and calibration versions					
8	I*1	1	1		Version (edition number) of the processing software: from 0 to 9
9	I*1	1	1		Sub-version (revision number) of the processing software: from 0 to 9
10	I*1	1	1		Version (edition number) of the calibration file: from 0 to 9
11	I*1	1	1		Sub-version (revision number) of the calibration file: from 0 to 63

Figure 3.11: Common block 1: general header.

Block 2: Orbital and Geomagnetic Parameters					
Field number	Type	Array dim.	Size (bytes)	Unit	Description
Orbital parameters					
1	R*4	1	4	degree	Geocentric latitude (-90°, +90°)
2	R*4	1	4	degree	Geocentric longitude (0°, +360°)
3	R*4	1	4	km	Altitude
4	R*4	1	4	hour	Local time of the first point of the data array (0, 24h)
Geomagnetic parameters					
5	R*4	1	4	degree	Geomagnetic latitude (-90°, +90°)
6	R*4	1	4	degree	Geomagnetic longitude (0°, +360°)
7	R*4	1	4	hour	Magnetic local time of the first point
8	R*4	1	4	degree	Invariant latitude (-90°, +90°)
9	R*4	1	4		Mc Ilwain parameter L (0, 999)
10	R*4	1	4	degree	Geocentric latitude of the conjugate point at the satellite altitude (-90°, +90°)
11	R*4	1	4	degree	Geocentric longitude of the conjugate point at the satellite altitude (0°, +360°)
12	R*4	1	4	degree	Geocentric latitude of North conjugate point at altitude 110 km (-90°, +90°)
13	R*4	1	4	degree	Geocentric longitude of North conjugate point at altitude 110 km (0°, +360°)
14	R*4	1	4	degree	Geocentric latitude of South conjugate point at altitude 110 km (-90°, +90°)
15	R*4	1	4	degree	Geocentric longitude of South conjugate point at altitude 110 km (0°, +360°)
16	R*4	3	12	nT	Components of the magnetic field model at the satellite point (geographic coordinate system)
17	R*4	1	4	Hz	Proton gyrofrequency at satellite point
Solar parameters					
18	R*4	3	12		Solar position, Xs, Ys, Zs in the geographic coordinate system
Code version					
19	I*1	1	1		Version (edition number) of the software component: from 0 to 9
20	I*1	1	1		Sub-version (revision number) of the software component: from 0 to 9

Figure 3.12: Common block 2: orbital and geomagnetic parameters.

Block 3: Attitude Parameters					
Field number	Type	Array dim.	Size (bytes)	Unit	Description
Attitude parameters					
1	R*4	9	36		M_{satgeo} : Matrix from satellite coordinate system to geographic coordinate system
2	R*4	9	36		M_{geo2um} : Matrix from geographic coordinate system to local geomagnetic coordinate system
3	I*2	1	2		Quality index of attitude parameters
Code version					
4	I*1	1	1		Version (edition number) of the software component: from 0 to 9
5	I*1	1	1		Sub-version (revision number) of the software component: from 0 to 9

Figure 3.13: Common block 3: attitude parameters.

RNF results					
Filename: <i>DMT_N1_1138</i> <nnnnns> <start_date> <end_date>.DAT					
Field number	Type	Array dim.	Size (bytes)	Unit	Description
Data header					
1	A21	1	21		Data type: "Neural Network "
2	I*1	32	32		House-Keepings and Status (see DR1)
3	I*1	1	1		Data sub-type: 0 or 1 (0: 3D spectrogram, 1: 2D curves)
4	A20	1	20		Study title: "WHISTLER "
5	A3	1	3		Component name: "Eij" or "Bi "
6	R*4	1	4	s	Time resolution (<i>dt</i>)
7	I*1	1	1		Class number (<i>Nbclasses</i>): from 1 to 20
8	I*1	1	1		Number of spectra (<i>Nbs</i>)when '3D spectrogram' sub-type Number of plot points (<i>Nbp</i>) when '2D curves' sub-type Value from 1 to 128
9	I*1	1	1		0 when '3D spectrogram' sub-type Number of curves <i>Nbc</i> when '2D curves' sub-type, from 0 to 5
Class description					
10	A10	1	10		Unit name for the class ranges
11	R*4	20	80		Minimum ranges for the classes <i>Di</i> (filled by 0 when <i>Nbclasses</i> < 20)
12	R*4	20	80		Maximum ranges for the classes <i>Di</i> (filled by 0 when <i>Nbclasses</i> < 20)
Spectrogram intensity					
13	I*1	128	128		Spectrum validity: 0 = not valid, 1 = valid
14	I*1	128*20	2560		<i>Nbs</i> vectors of <i>Nbclasses</i> elements when '3D spectrogram' sub-type; the vectors are set in the order $V_0, V_1, \dots, V_{Nbs-1}$ <i>Nbc</i> vectors of <i>Nbp</i> elements when '2D curves' sub-type; the vectors are set in the order $C_0, C_1, \dots, C_{Nbc-1}$ The field is completed by 0.
Spectrogram uncertainty (time resolution)					
15	I*1	128*20	2560		<i>Nbs</i> vectors of <i>Nbclasses</i> elements when '3D spectrogram' sub-type; the vectors are set in the order $V_0, V_1, \dots, V_{Nbs-1}$ <i>Nbc</i> vectors of <i>Nbp</i> elements when '2D curves' sub-type; the vectors are set in the order $C_0, C_1, \dots, C_{Nbc-1}$ The field is completed by 0.

Figure 3.14: Block 4: RNF detection results.

spectrogram of data to be analyzed . The bottom panel shows the corresponding dispersion parameters estimated by the wave analyzed as function of time. In figures 3.16 are reported an examples of whistler class selection using the spectrogram of ICE data during Night time.

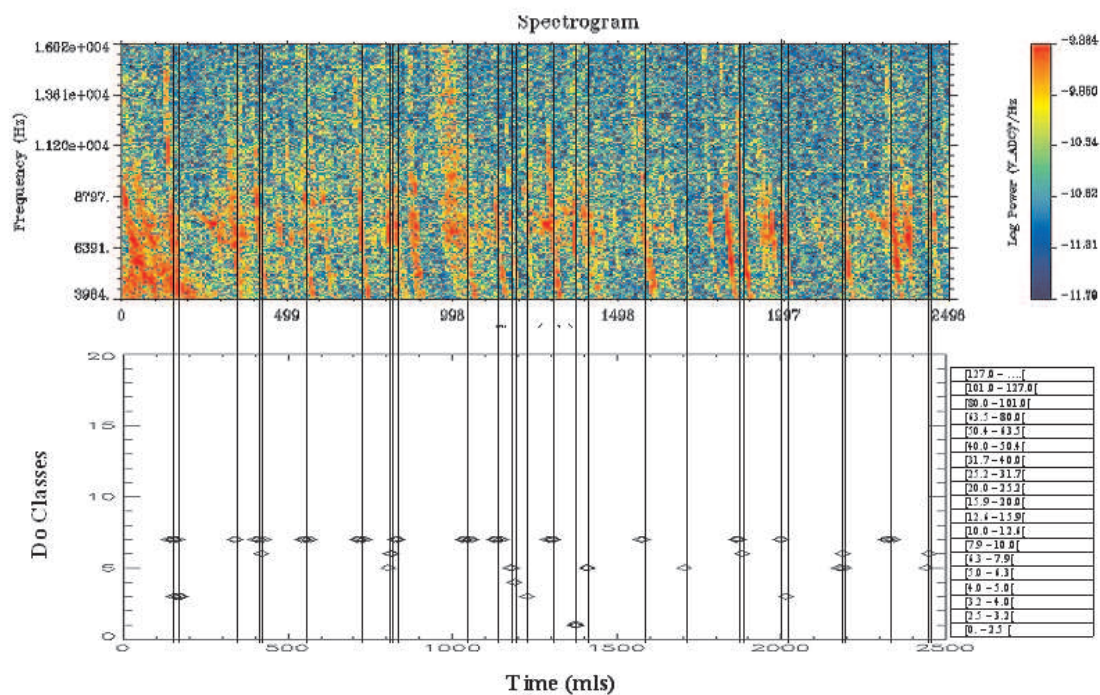


Figure 3.15: Top panel: spectrogram of data to be analyzed. Bottom panel: corresponding dispersion parameters given by neural networks system, [J-L.Pinçon, Demeter Guest Investigator Workshop, 2-4 May 2005].

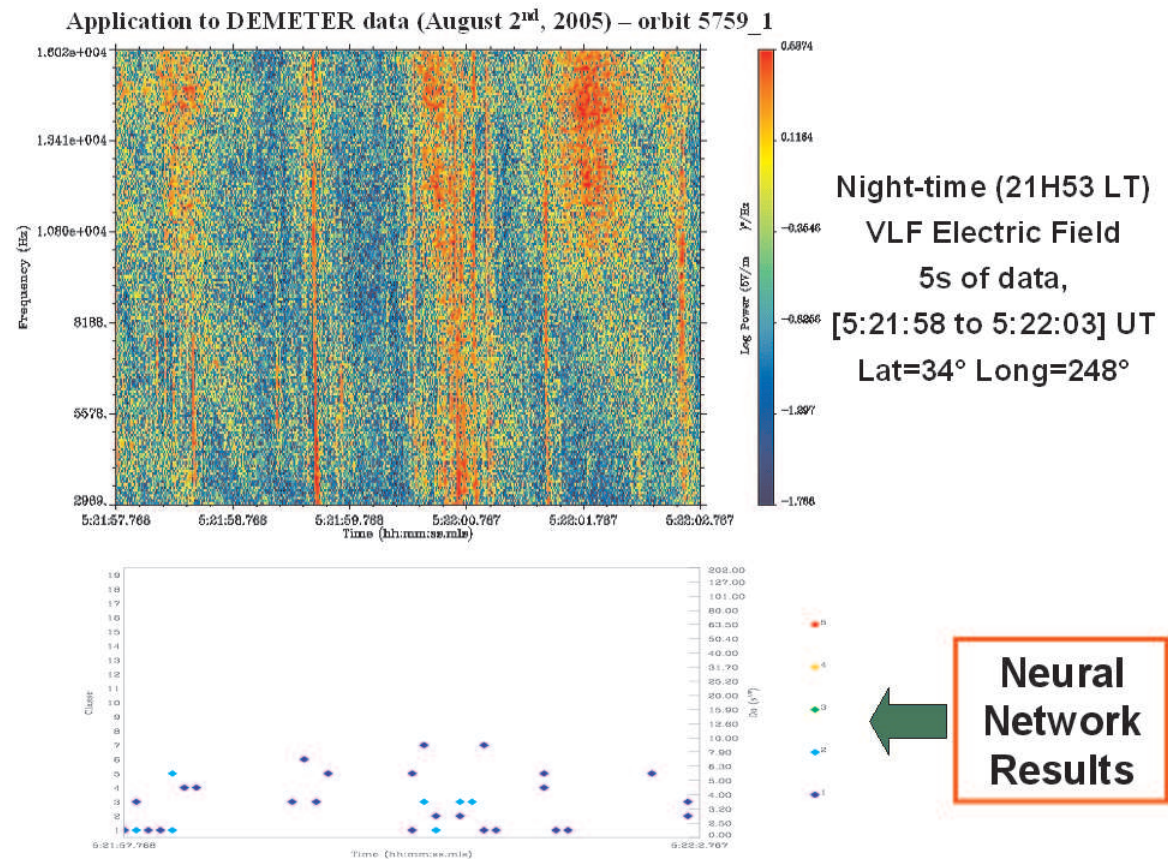


Figure 3.16: Application of neural network to a continuous set of Demeter data.(a) Spectrogram of ICE data to be analyzed and obtained during August 2 2005, orbit 5759 – 1 in the night time; (b) Dispersion time obtain from RNF analysis, [J-L.Pinçon, Demeter Guest Investigator Workshop, 2-4 May 2005].

Detector	Implanted silicon, Thickness: 1 mm Active surface 490 mm ² (Ø 25 mm)
External shielding	2 mm Al
Foil for protons and photons rejection	6 µm Al
Mass	525 gr
Power	895 mW
Energy range, e ⁻	70–1000 (2500) keV, 256 channels
Maximum geometrical factor	1.2 cm ² sr

Figure 3.17: Principal characteristics of IDP detector, [Sauvaud *et al.*, 2006].

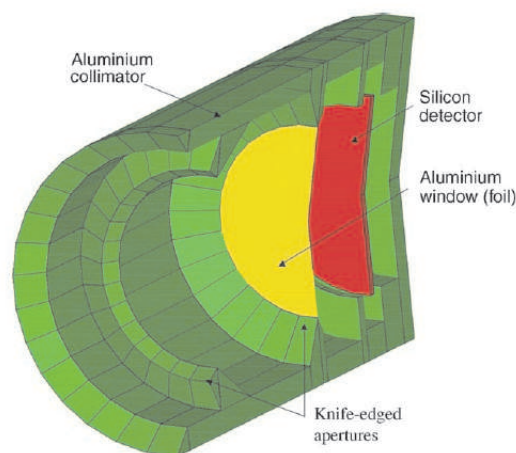


Figure 3.18: Cross-sectional view of IDP, showing the collimator in aluminum (green), the Al foil aimed to stop UV photons and protons with energies lower than 500 keV, and the silicon detector (red), [Sauvaud *et al.*, 2006].

3.4 IDP spectrometer

The IDP spectrometer was designed to allow the detection of weak electron fluxes on the low-latitude part of the Demeter orbit, mainly located below the radiation belts. In order to fulfill this requirement, the maximum geometry factor of IDP was defined as large as $\simeq 1.2 \text{ cm}^2 \text{ sr}$. The calculation of the geometry of the instrument and of its shielding thickness was performed for the complete energy range (i.e., from tens of keV up to the MeV range) using the GEANT-3 code from CERN. Figure 3.17 provides the main characteristics of the instrument and Fig. 3.18 gives a sketch of the sensor head [Sauvaud *et al.*, 2006].

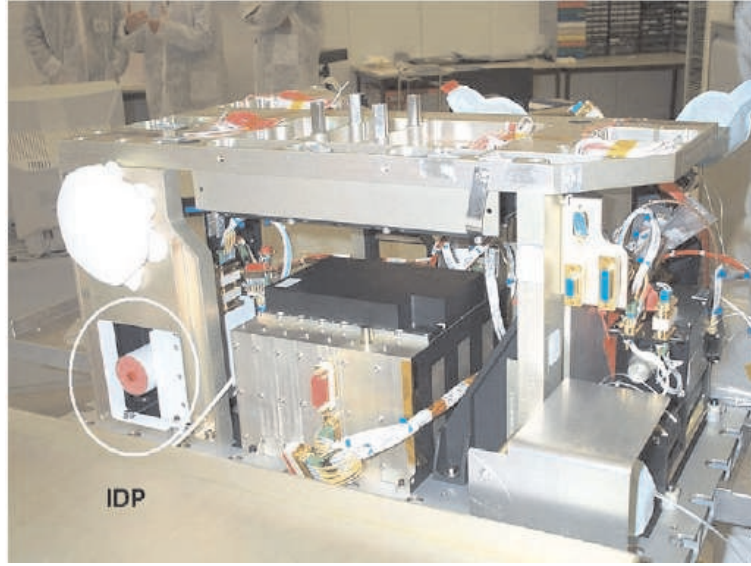


Figure 3.19: The IDP spectrometer installed on the Demeter satellite, [Sauvaud *et al.*, 2006].

The collimator built in aluminum, a light material particularly well adapted to minimize the X-ray production by Bremsstrahlung, is designed to provide a view angle of $\pm 16^\circ$ and to stop secondary particles (electrons and also low-energy photons) created on its internal parts. The optic has also an aluminum foil with a thickness of $6 \mu\text{m}$ to avoid parasitic light and to stop protons with energies lower than $\sim 500 \text{keV}$. The silicon detector is made of completely depleted Silicon of 1mm thickness. The sensor head is located on top of a case containing the associated analog electronics. The detector looks perpendicularly to the orbital plane of the satellite, which is almost polar and circular. The pitch angle of the detected particles is then close to 90° . The sun never directly illuminates the silicon detector whose temperature stays below -5°C in the nightside portion of the orbit and below -1°C during its diurnal part. This allows keeping the intrinsic noise of the detector at low levels. Fig. 3.19 shows the installation of IDP spectrometer in the satellite bus. Numerical simulations together with calibrations performed using a Van de Graaff accelerator at *DESP/ONERA* in Toulouse were used to determine the efficiency of the detector. This was defined as

$$\epsilon(E_0) = \frac{N_{PEAK}}{N_{INC}}$$

where N_{PEAK} is the number of particle in the peak and N_{INC} the number of incident particles. The absolute efficiency of the detector is strongly dependent on the energy of the particles, as can be seen in Fig.3.20a. The energy geometry factor $G(E)$, which allows to compute the flux of particle from the count-rate measured in each energy channel, ($J = \frac{C}{G(E)}$) is defined as

$$G(E) = \epsilon(E) f(\theta) d\Omega dS$$

where dS is the effective entrance aperture, $d\Omega$ is the solid angle of acceptance and $f(E, \theta)$ the detector normalized angular response. This angular response depends only slightly on the energy, so that $G(E)$ can be written as

$$G(E) = 2\pi\epsilon(E)S_{ENTR}f(\theta)\sin(\theta)\cos(\theta)d\theta$$

For IDP, the effective surface, S_{ENTR} , is $12.57cm^2$, and the integration of the angular response over the incident angle gives 0.044 rad. In a first approximation, we use the geometrical factor as displayed in Fig. 3.20b to convert counts/s into differential fluxes. A more precise method taking into account the probability for an energetic electron to loose less energy than its initial one was also used. However, this method, based on assumptions on the shape of the differential fluxes of electrons, gives results almost identical to the simple method given above. The total deposited energy range from 70 keV to 2.34MeV is divided in 255 channels. One more channel is used to code all counts corresponding to an energy loss greater than 2.34 MeV. IDP is working in two main modes. In the burst mode, an electron energy spectra is obtained every second with 256 channels. In the survey mode, the energy channels are grouped by two and the duration of each energy spectra is now 4 s. The sums are made onboard by the DPU. In the burst mode, the energy resolution is better than 10 keV.

The level-1 file structure of "Energetic Electron Spectrum" is given in tables of figure 3.11,3.12,3.13, The data burst block 4 is detailed in the table of figure 3.21, the data survey block 4 is detailed in figure 3.22

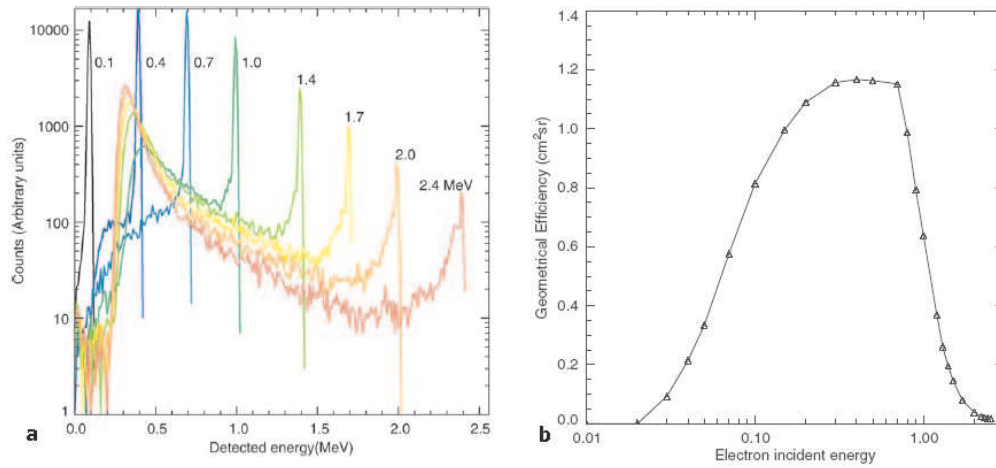


Figure 3.20: (a) Distribution of the energy deposited inside the detector for wide incident mono-energetic beams, (b) Variation of the geometry factor of IDP as a function of energy, [Sauvaud et al., 2006].

Spectrum of energetic electrons					
Filename: <i>DMT_N1_1141</i> <nnnnns> <start_date> <end_date>.DAT					
Field number	Type	Array dim.	Size (bytes)	Unit	Description
Data header					
1	A10	1	10		Data type: "IDP BURST "
2	I*1	32	32		House-Keepings and Status (see DR1)
3	R*4	1	4	s	Time resolution (one spectrum / second)
4	R*4	1	4	V	Polarisation voltage
5	R*4	1	4	keV	Discrimination level
6	A20	1	20		Spectrum data unit: "elec/cm ² /s/ster/keV"
7	A6	1	6		Pitch angle unit: "degree"
Electron spectra					
8	R*4	256	1024	elec/cm ² /s/ster/keV	Data array of spectrum n°1
9	R*4	256	1024	elec/cm ² /s/ster/keV	Data array of spectrum n°2
10	R*4	256	1024	elec/cm ² /s/ster/keV	Data array of spectrum n°3
11	R*4	256	1024	elec/cm ² /s/ster/keV	Data array of spectrum n°4
Energy table					
12	R*4	256	1024	keV	Energy table
Pitch angle data					
13	R*4	1	4	degree	Pitch angle (from 0 to 180°)

Figure 3.21: Block 4: IDP Burst results.

Counters of energetic electrons					
Filename: DMT N1 1142 <nnnnns> <start_date> <end_date>.DAT					
Field number	Type	Array dim.	Size (bytes)	Unit	Description
Data header					
1	A10	1	10		Data type: "IDP SURVEY"
2	I*1	32	32		House-Keepings and Status (see DR1)
3	R*4	1	4	s	Spectrum time resolution
4	R*4	1	4	s	Counters time resolution
5	R*4	1	4	V	Polarisation voltage
6	R*4	1	4	keV	Discrimination level
7	R*4	1	4	keV	Threshold low interval 1
8	R*4	1	4	keV	Threshold low interval 2
9	R*4	1	4	keV	Threshold low interval 3
10	R*4	1	4	keV	Threshold high interval 3
11	A20	1	20		Spectrum data unit: "elec/cm^2/s/ster/keV"
12	A6	1	6		Pitch angle unit: "degree"
Counters and spectrum data					
13	I*4	12	48		4 x [counter #1 value counter #2 value counter #3 value]
14	R*4	128	512	elec/cm^2/s/ster/keV	Data array of spectrum #1
15	I*4	12	48		4 x [counter #1 value counter #2 value counter #3 value]
16	R*4	128	512	elec/cm^2/s/ster/keV	Data array of spectrum #2
17	I*4	12	48		4 x [counter #1 value counter #2 value counter #3 value]
18	R*4	128	512	elec/cm^2/s/ster/keV	Data array of spectrum #3
19	I*4	12	48		4 x [counter #1 value counter #2 value counter #3 value]
20	R*4	128	512	elec/cm^2/s/ster/keV	Data array of spectrum #4
21	I*4	12	48		4 x [counter #1 value counter #2 value counter #3 value]
22	R*4	128	512	elec/cm^2/s/ster/keV	Data array of spectrum #5
23	I*4	12	48		4 x [counter #1 value counter #2 value counter #3 value]
24	R*4	128	512	elec/cm^2/s/ster/keV	Data array of spectrum #6
25	I*4	12	48		4 x [counter #1 value counter #2 value counter #3 value]
26	R*4	128	512	elec/cm^2/s/ster/keV	Data array of spectrum #7
Energy table					
27	R*4	128	512	keV	Energy table
Pitch angle data					
28	R*4	1	4	degree	Pitch angle (from 0 to 180°)

Figure 3.22: Block 4: IDP Survey results.

Chapter 4

Study of the possible correlation between earthquakes and whistlers recorded by DEMETER

This chapter and the following two ones are the bulk of the thesis work. In this chapter, starting from the approach proposed by *Hayakawa et al.*, [1993] I carry out a deeper investigation about the possible influence of seismic activity on the propagation of magnetospheric whistlers. The aim is to give additional, more detailed, and complementary information to the promising results shown by *Hayakawa et al.*, [1993]. At this purpose the statistical analysis of whistlers will be performed making use of Demeter data obtain from the RNF experiment (see chapter 3).

4.1 Ground-based observations of the influence of seismic activity on the whistlers propagation

Studies of whistlers propagation, based on data collected by ground observatories, have indicated that whistlers with anomalous dispersion coefficient values are likely to be closely correlated with earthquakes occurring in the relevant longitude range. *Hayakawa et al.*, [1993] first pointed out a possible seismic influence on the propagation of magnetospheric whistlers at low altitudes on the basis of long-term ground data

detected at Sugadaira observatory (geomagnetic latitude 25° N) during 1970-1978. By a statistical analysis of the Sugadaira data it has been found that number of anomalous whistlers, whose dispersion value is greater than twice the typical value, exhibit a substantial increase in coincidence with earthquakes occurrence in the Japanese geographic longitude sector of $100^{\circ}E - 160^{\circ}E$. Figure 4.1 illustrates the geographical setting of the whistler observing stations with their conjugate points, and the results obtained at Sugadaira during the whole time span of 1970-1978. In particular, the figure shows a correlation (correlation coefficient $r=0.63$) between the number of days with anomalous whistlers detected at Sugadaira and corresponding seismic activity in the Japanese longitude. Moreover, Hayakawa *et al.*, [1993] found an exceedingly high statistical correlation between the summertime anomalous whistlers detected at Sakushima (a second observatory used in the study) and seismic activity. The same authors also found that anomalous whistlers tend to be detected mainly in summer, and never in winter when numerous normal whistlers are generally observed. That is why whistler data collected in the winter season have not been included in the study by Hayakawa *et al.*, [1993]. On the contrary it must be noted that there is no evidence of seasonal variations in the earthquakes occurrence. Results reported in figure 4.1 are obtained making use of data collected in the June-August summertime period.

4.2 Study of the EQ-whistler correlation using DEMETER observations

Result obtained by Hayakawa *et al.*, [1993] is interesting and stimulating but needs to be confirmed by further investigations. The statistical study presented here aims at giving a contribution in the field. It is the first time that correlation between seismic activity and whistler occurrence is investigated using satellite data. At this purpose, EQs from the USGS catalogue with $M \geq 4.8$ and anomalous whistler collected by the RNF experiment have been used in our study. The analysis is critically investigated and presented here. To perform a suitable whistler-EQ correlation, long time series of whistler data are requested together with EQ parameters and information on magnetospheric perturbations caused by non-seismic sources. Unfortunately, contrary to the

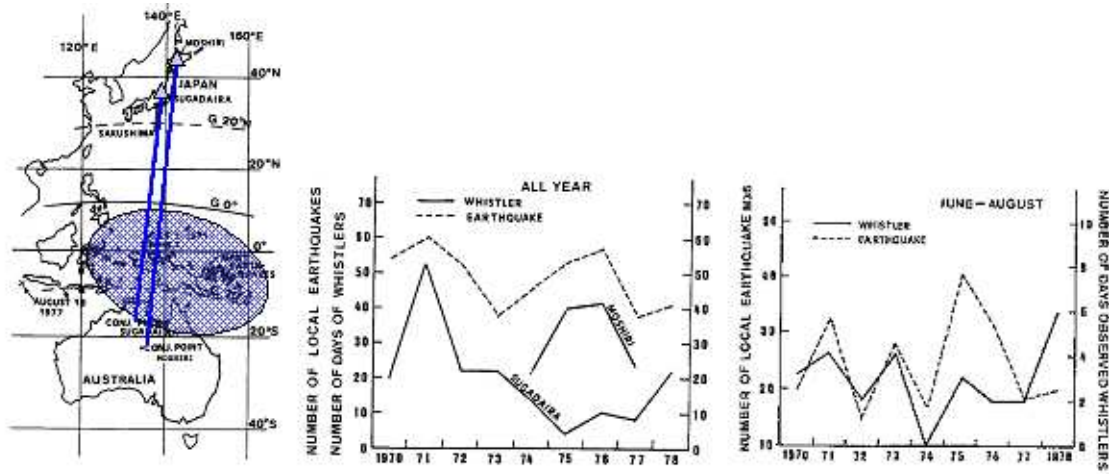


Figure 4.1: Statistical results of comparison between the annual number of local EQs with $M > 6$ and number of days with anomalous whistlers observed at Sugadaira and Moshiri observatory during 1970-1978. Location (left panel) of Sugadaira, Sakushima and Moshiri whistler observatories and their conjugate points, together with those of earthquakes. The full lines indicate the ground projection of the magnetic field line connecting Sugadaira and its conjugate point.

9 year whistlers data of the previous study carried out by Hayakawa *et al.*, [1993], in our case only 11 month data are available from RNF. But, since Demeter mission is still flying for other two years this study will be improved in the future.

In the following, will be detailed and clarified conditions for cuts to be applied to data in order to select EQs and whistler populations to be correlated. In this way two databases of such populations have been available for the study.

4.3 EQs database

Most of observations of seismic EME-waves reported in literature are generally associated with moderate and strong shallow earthquakes. Taking into account of the maximum latitude of Demeter measurements (see chapter 3) and of the EQs geographic distribution (see chapter 1), a total number of 2721 EQs with magnitude $M \geq 4.8$ and magnetic latitude lower than 65 degrees were selected for the study in the period from May 25, 2005 to April 30, 2006. The spatial distribution of selected EQs, is shown in

EQs from 2005/05/25 to 2006/04/30, $M \geq 4.8$, $\text{latmag} < 65$ deg. Total #: 2721

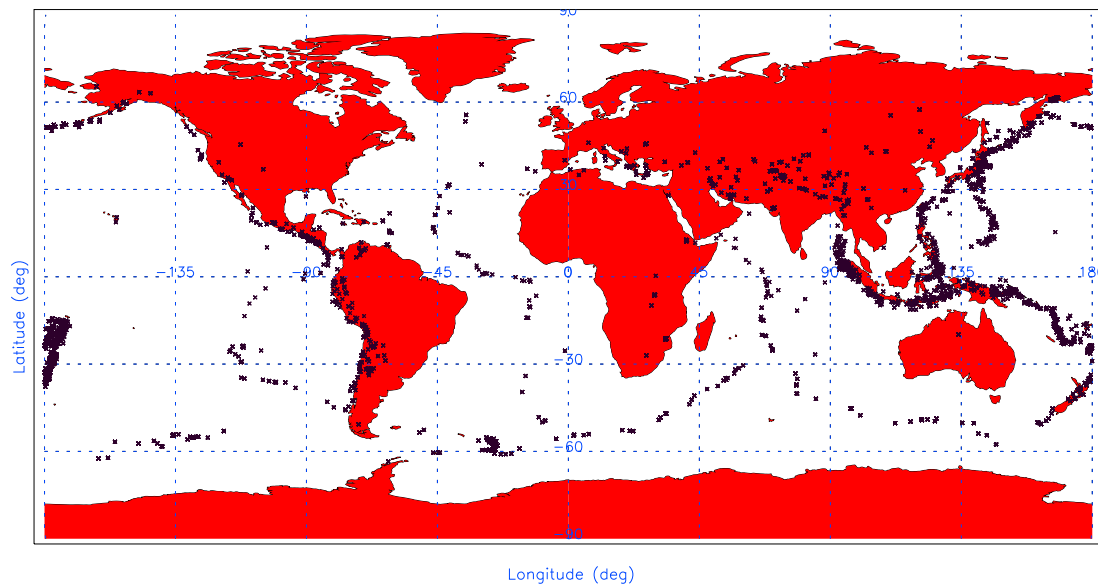


Figure 4.2: Locations of earthquake epicenters from 2005/05/25 to 2006/04/30 used in the statistical study. Black crosses indicate the EQ epicenters.

figure 4.2.

Scope of this work is to investigate the influence of seismic activity on the propagation of anomalous whistlers. At this purpose I have studied how whistlers generated near the EQ magnetic field line, or propagation along the EQ magnetic field line, are perturbed by seismic activity. First, we need to know the coordinates of point belonging to the projection on Earth's surface of each EQ magnetic field line defined as described in the following. Aim of this calculation is to know geographic regions sensitive to seismic activity. Along this magnetic field line narrow region have been selected the Demeter observations to be correlated with seismic phenomena. At this purpose, for each earthquake have been calculated the geographic coordinates of the projection to the Earth surface of the magnetic field line, which footprints are the EQ epicenter and the EQ geomagnetic conjugate point(CP), respectively (see figure 4.4).

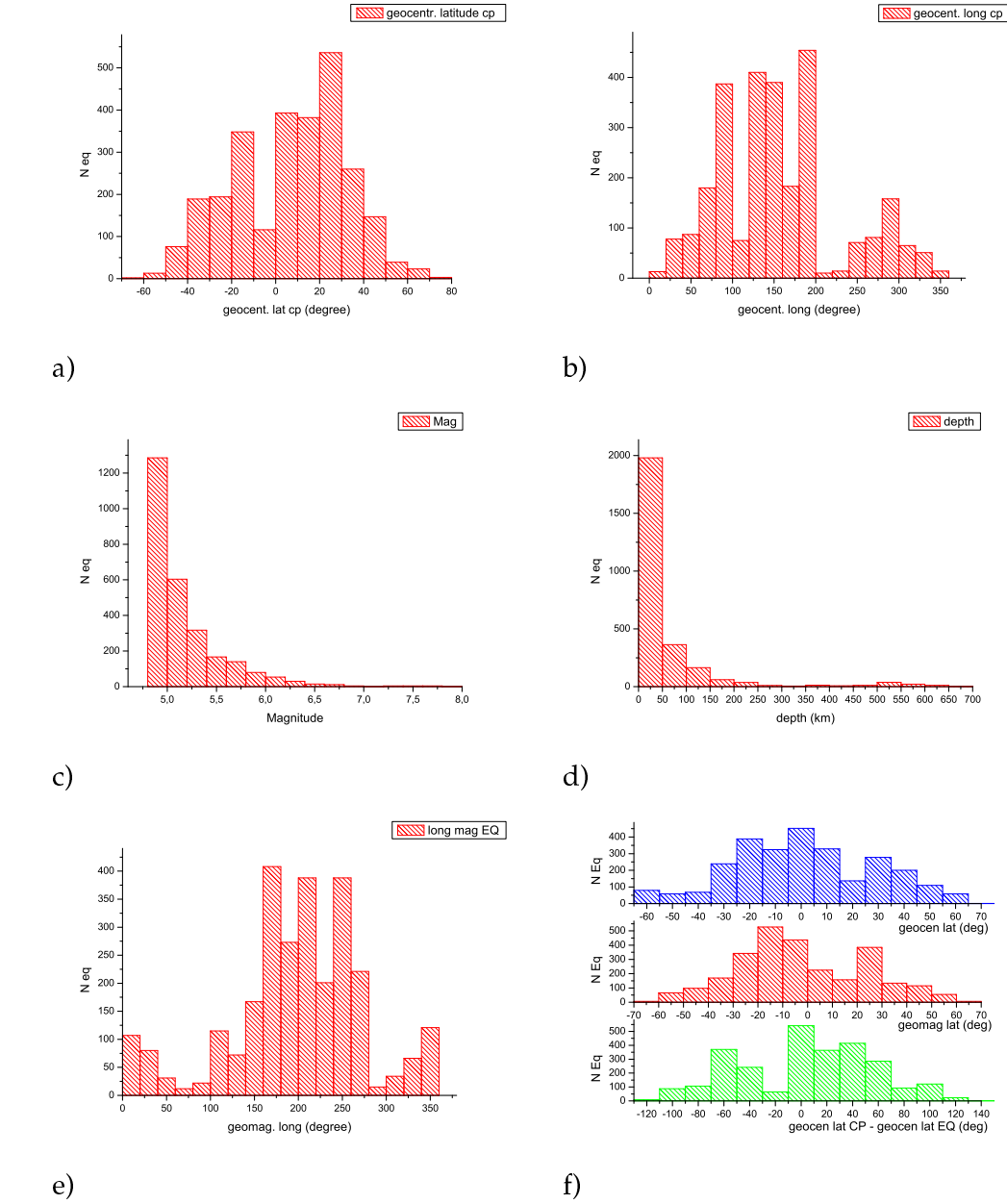


Figure 4.3: Distributions of earthquakes (EQs) and their geomagnetic conjugate points (CPs). Histograms of the CP geocentric latitude (a), CP geocentric longitude (b), EQ magnitude(c), EQ depth (d), EQ magnetic longitude (e), EQ geocentric latitude, EQ geomagnetic latitude and difference of the geocentric latitude between CP and EQ(f).

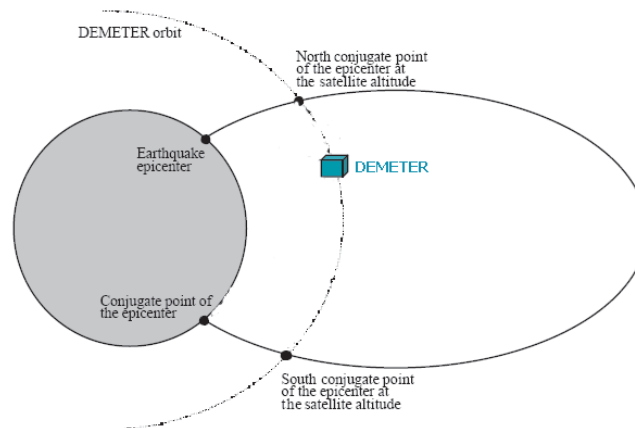


Figure 4.4: Schematic illustration EQ magnetic field line, up the EQ conjugate point CP. Also the intersection points between the EQ field line and Demeter orbit are shown.

Then, have also been calculated the magnetic coordinates of the intersection of the EQ field line defined above with Demeter orbit at altitude of 715 km (from 2004/06/29 to 2005/12/16), and 660 km (from 2005/12/16 to 2006/04/30). For calculating the magnetic field line, which footprint is the geographic position of EQ, has been used an ad hoc software MAGLIB (<http://logiciels.cnes.fr/MAGLIB/en/accept.htm>). In figure 4.3 are reported histograms of the CP geocentric latitude(a) and longitude (b), EQ magnitude(c), depth (d), magnetic longitude (e), EQ geocentric latitude, EQ geomagnetic latitude and difference of the geocentric latitude between CP and EQ(f). Comparing figure 4.3 a)with top panel of 4.3 f) we can observe that EQ geocentric latitudes and CP geocentric latitude are mainly concentrate between 0 and -30 degrees and between 0 and 40 degrees, respectively. Consequently, in our statistical analysis will remain selected a higher number of EQs which occur in the Southern Hemisphere than that of the Northern Hemisphere. A database of earthquakes, including USGS EQ parameters and information of the magnetic field lines that have as footprints the selected EQs, has been developed. All variables included in this EQ database are reported in table 4.1. An example of EQs location with the associated magnetic field lines, for the period July-September 2005, is reported in figure 4.5, where for each EQ event, the blue line represents the magnetic field line calculated by MAGLIB.

Variable	Description
year	EQ year(UT)
m	EQ month(UT)
dd	EQ day(UT)
hh	EQ hour (UT)
mm	EQ minute(UT)
ss	EQ second(UT)
julianday	UT EQ date in number of seconds since 1970/01/01
indexeq	number of EQ
lat	EQ geocentric latitude
long	EQ geocentric longitude
depth	EQ depth
Mag	EQ magnitudo
latmag	EQ magnetic latitude
longmag	EQ magnetic longitude
tgl	EQ MLT
fl	L-shell value using galperin model at altitude 0km altitude
fl4	L-shell value using galperin model at altitude 400km altitude
xlamb	invariant latitude at 0km altitude
xlamb4	invariant latitude at 400km altitude
latcd	geocentric latitude of conjugate point at 0km altitude
longcd	geocentric longitude of conjugate point at 0km altitude
latcd4	geocentric latitude of conjugate point at 400km altitude
longcd4	geocentric longitude of conjugate point at 400km altitude
np	field line interpolation points
tr	(RE+Demeter altitude)/RE
tthetdegl	geocentric latitude of magnetic field line
tphideg	geocentric latitude of magnetic field line
tthetl	latitude of the conjugate point(CP) of EQ at altitude of Demeter

Table 4.1: EQ database defined by software MAGLIB.

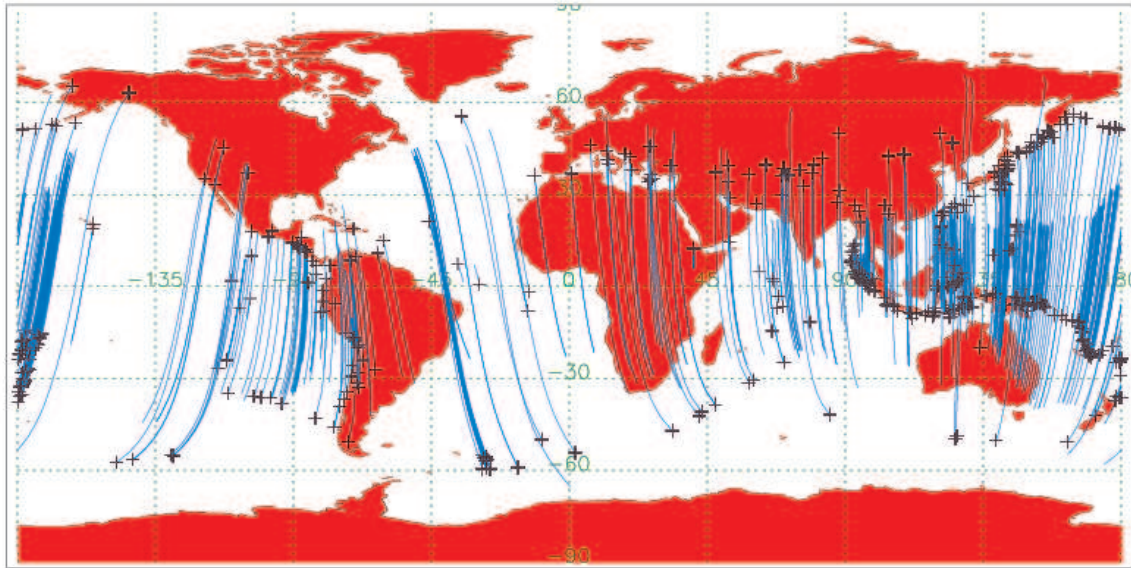


Figure 4.5: Selected EQs occurred in the period July, August and September 2005. Black crosses indicate EQ epicenters and blue lines the associated magnetic field lines (see text).

4.4 WHIMAP whistler database

The RNF Neural Network of DEMETER is fully operational since May 9, 2005¹. For this study a specific software, called WHIMAP, has been developed to merge the information of Demeter time, position, and orientation with the RNF whistler data and geomagnetic conditions during the observations. Then, a specific database with all these informations has been built including the number of whistlers for 19 dispersion coefficient classes, Dst and Ap index values selected by NOAA through the web addresses

<ftp://ftp.ngdc.noaa.gov/STP/GEOMAGNETIC-DATA/INDICES/DST/>, and <http://swdcwww.kugi.kyoto-u.ac.jp/cgi-bin/kp> respectively. The original RNF whistler data sampling rate is $(1/128)s^{-1}$, whereas DEMETER position and altitude control are recorded every 13 seconds. To reduce the amount of data, number of whistlers of each class has separately been integrated over 13 seconds. WHIMAP database constructed on this basis is reported in figure 4.6.

¹J.L. Pinçon Personal Communication

WHIMAP_<halforbit>_<start_date>_<end_date>.DAT					
- <halforbit>: orbit number as "nnnnns"; - <start_date>: date of the first data record as "yyyymmdd_hhmmss"; - <end_date>: date of the last data record + duration as "yyyymmdd_hhmmss".					
Field number	Type	Array dim.	Size (bytes)	Unit	Description
1	I*2	7	14		UT time of the first point of the data array as: year, month, day, hour, minute, second, millisecond (year as 20xx)
2	R*8	1	8	s	Number of seconds since 01/01/1970 00:00:00
3	I*2	1	2		Orbit number
4	I*2	1	2		Sub-orbit number
5	I*1	1	1		Version (edition number) of the processing software: from 0 to 9
6	I*1	1	1		Sub-version (revision number) of the processing software: from 0 to 9
7	R*4	1	4	degree	Geocentric latitude (-90°, +90°)
8	R*4	1	4	degree	Geocentric longitude (0°, +360°)
9	R*4	1	4	km	Altitude
10	R*4	1	4	hour	Local time (0, 24h)
11	R*4	1	4	degree	Geomagnetic latitude (-90°, +90°)
12	R*4	1	4	degree	Geomagnetic longitude (0°, +360°)
13	R*4	1	4	hour	Magnetic local time
14	R*4	1	4	degree	Invariant latitude (-90°, +90°)
15	R*4	1	4		Mc Ilwain parameter L (0, 999)
16	R*4	1	4	degree	Geocentric latitude of the conjugate point at the satellite altitude (-90°, +90°)
17	R*4	1	4	degree	Geocentric longitude of the conjugate point at the satellite altitude (0°, +360°)
18	R*4	1	4	degree	Geocentric latitude of North conjugate point at altitude 110 km (-90°, +90°)
19	R*4	1	4	degree	Geocentric longitude of North conjugate point at altitude 110 km (0°, +360°)
20	R*4	1	4	degree	Geocentric latitude of South conjugate point at altitude 110 km (-90°, +90°)
21	R*4	1	4	degree	Geocentric longitude of South conjugate point at altitude 110 km (0°, +360°)
22	R*4	3	12	nT	Components of the magnetic field model at the satellite point (geographic coordinate system)
23	R*4	1	4	nT	Modulus of the magnetic field model
24	R*4	1	4	Hz	Proton gyrofrequency at satellite point
25	I*1	128	128		Spectrum validity: 0 = not valid, 1 = valid
26	I*1	128 * 19	2432		Number of whistlers detected for each class. 128 vectors of 19 elements; the vectors are set in the order V ₀ , V ₁ , ..., V ₁₂₇
27	I*2	19	38		Total number of whistlers per class
28	R*4	1	4	nT	Dst index
29	R*4	1	4	nT	Ap index
Total			2714		

Figure 4.6: The WHIMAP database.

4.5 Space and time whistler distribution

As it is well known, the occurrence of magnetospheric whistlers is controlled by two factors:

1. source activity (lightning, etc.)
2. propagations condition in the ionosphere and magnetosphere

Starting from the whistlers database I have produced geographic maps of whistlers in order to determine the normal background of space and time whistler distributions. Obviously, the expected value of number of whistlers $w(lat, long, t)$ depends on cells used to determine the whistler mean number time and space distribution. Therefore, for each one of the 19 RNF whistler dispersion coefficient classes (see chapter 3) whistlers maps have been constructed as a function of the:

- geographic position
- monthly whistler data
- local time of the observations (day-time and night-time data, are reported separately)

At this purpose, the Earth surface, included in the latitude interval of ± 66 degrees, has been divided in cells with geographic latitude and longitude width of 4 degrees. For each RNF whistler dispersion coefficient class the integrated number of whistlers collected by Demeter RNF during a month within these geographic cells have been determined, separately for day and night times. As an example, maps of w mean values $\langle w(lat, long, t) \rangle_{cell}$ obtained in this way, using data collected in August 2005, are reported in figures 4.7 - 4.10 for dispersion coefficient classes $0 \div 18$.

As it can be seen in figures 4.7 - 4.10, $\langle w(lat, long, 1month) \rangle_{cell}$ distribution of whistlers is almost irregular in space and time. Note that this result could also be affected by the different number of Demeter measurements in the diverse cells.

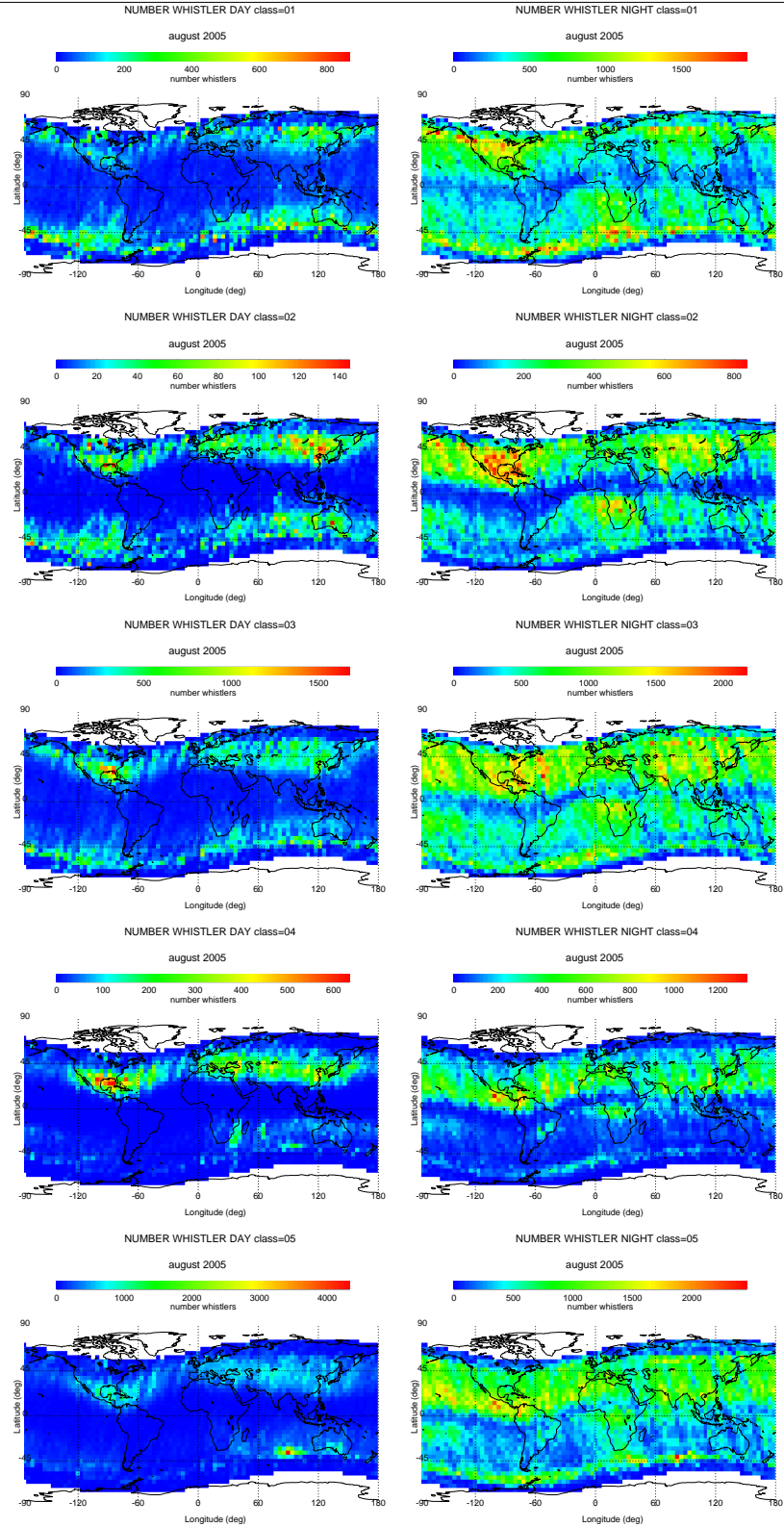


Figure 4.7: Geographic distributions of number of whistlers during August 2005. Data are reported separately for Day-times and Night-times and for classes 1-5. The $\langle w(lat, long, 1month) \rangle_{cell}$ data have been integrated over cells of $4^\circ \times 4^\circ$ latitude and longitude intervals.

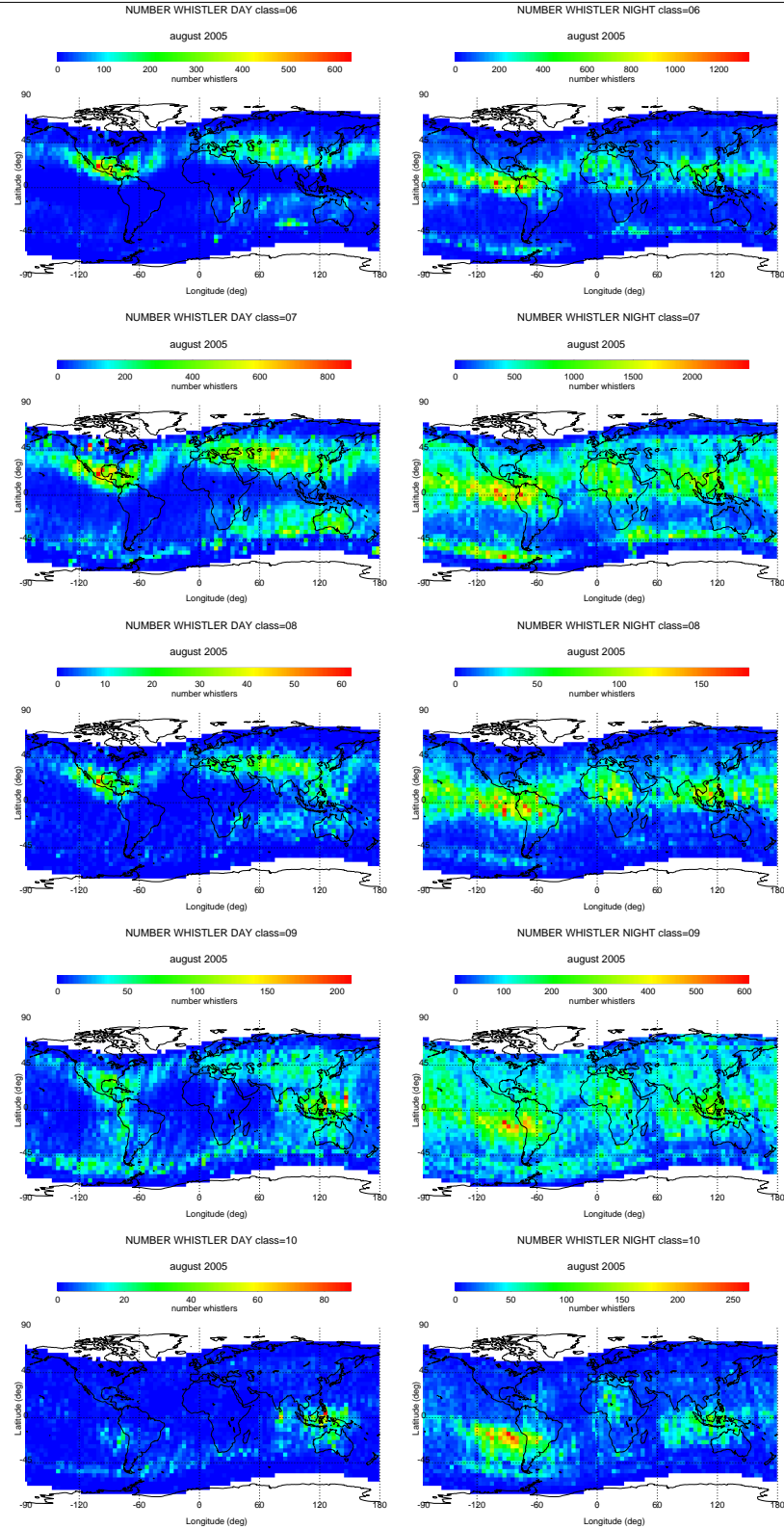


Figure 4.8: Geographic distributions of number of whistlers during August 2005. Data are reported separately for Day-times and Night-times and for classes 6-10. The $\langle w(lat, long, 1month) \rangle_{cell}$ data have been integrated over cells of $4^\circ \times 4^\circ$ latitude and longitude intervals.

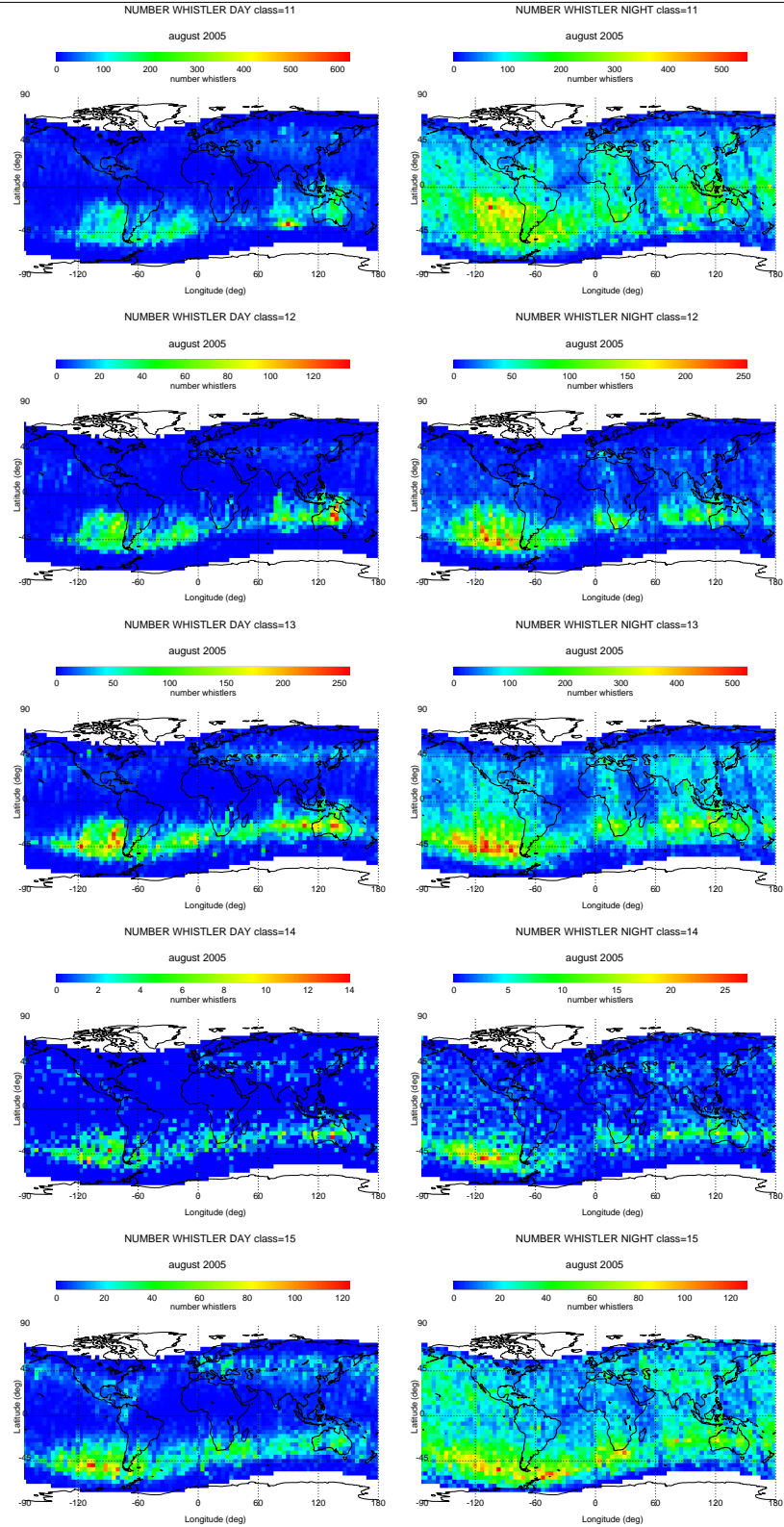


Figure 4.9: Geographic distributions of number of whistlers during August 2005. Data are reported separately for Day-times and Night-times and for classes 11-15. The $\langle w(lat, long, 1month) \rangle_{cell}$ data have been integrated over cells of $4^\circ \times 4^\circ$ latitude and longitude intervals.

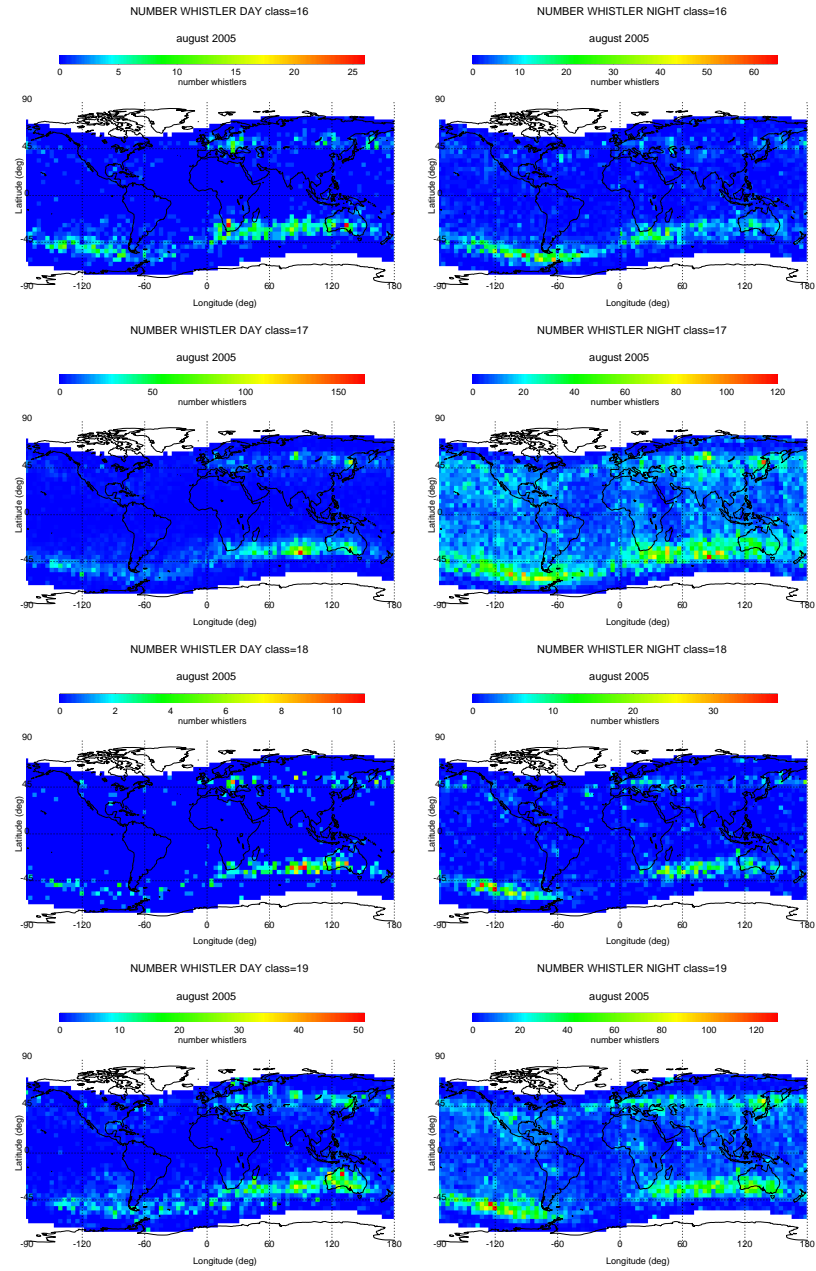


Figure 4.10: Geographic distributions of number of whistlers during August 2005. Data are reported separately for Day-times and Night-times and for classes 16-19. The $\langle w(lat, long, 1month) \rangle_{cell}$ data have been integrated over cells of $4^\circ \times 4^\circ$ latitude and longitude intervals.

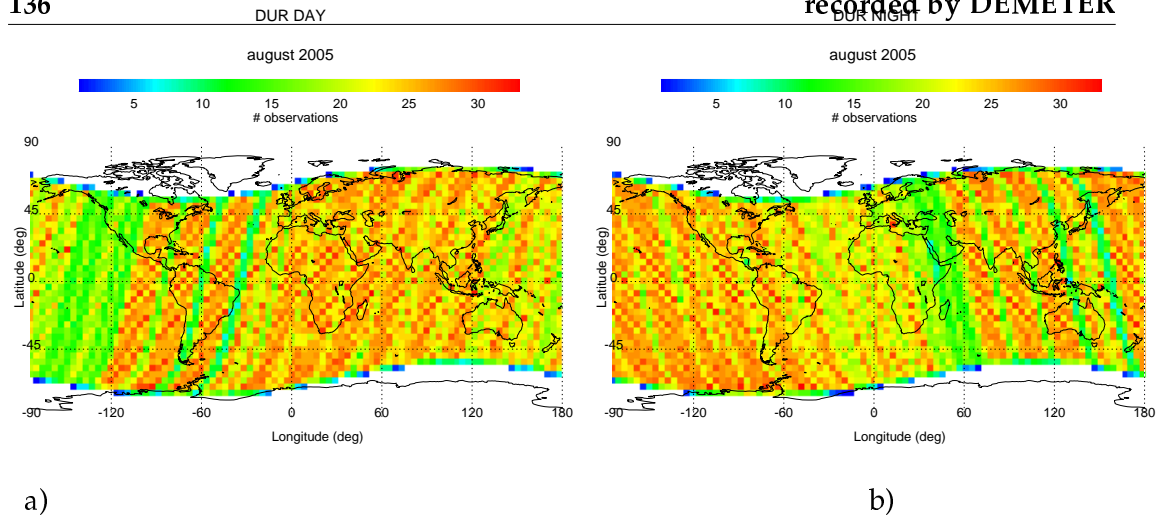


Figure 4.11: Geographic distributions of number of Demeter observations during a) Daytime and b) Nighttime in the month of August 2005.

Figure 4.11 seems to confirm this hypothesis, since it shows a different number of tracks in the diverse cells, and between night and day times. In particular, also a lacking in space and time observations can be noted in both panels of figure 4.11, where a few relatively large longitudinal sectors (from about -90 to -120 degrees in day times and centered around 60 degrees in night time) exhibit long revisit times of Demeter. To try to avoid these irregularities, caused by the method adopted for mapping, we normalized data by dividing the previous integrated number of whistlers (detected in each cell during 1 month of observations) by the number of satellite tracks in the same cell. An example of this normalization for the 19th class of whistler dispersion coefficient is reported in figure 4.12.

As it can be seen in figures 4.7 - 4.10, and 4.12, whistlers geographic distributions strongly depend upon the dispersion coefficient class, and night and day local times. Moreover, the whistlers number also strongly depends on the tropospheric activity. Therefore, maps for each whistler coefficient class have been constructed on a monthly basis, and for the whole period May 25, 2005 - April 30, 2006 at our disposal. Monthly maps constructed in this way pointed out a strong seasonal variation in the number of whistlers, which resulted to be maximum in the winter season (austral summer), and minimum in the summer season (austral winter). This result is in agreement with that obtained by Hayakawa et al. (1971), by ground-based observations, and explained

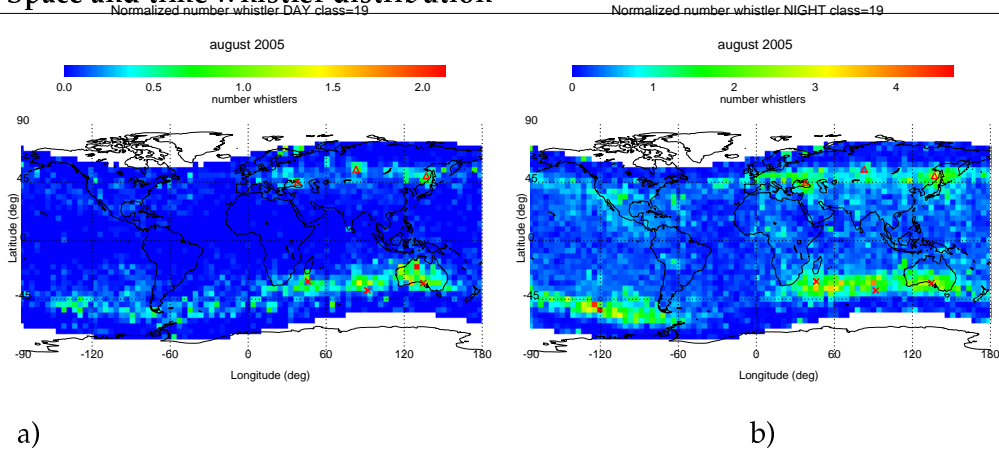


Figure 4.12: Geographic distribution of number of whistler normalized to the number of Demeter tracks in each cell for the 19th class of dispersion coefficient during a) Daytime and b) Nighttime in the month of August 2005. Red crosses indicate, the positions of VLF Russian transmitters and their geomagnetic conjugate points, [J-L.Pinçon, Demeter International Symposium, Toulouse (France), June 14-16, 2006].

in terms of the corresponding seasonal variation of lightning activity in the southern hemisphere.

From figures 4.7 -4.10 it is also possible to note an increase in the number of whistlers in the SAA region. An attempt to justify this results could be the occurrence of the great magnetic storm of 2005/08/23 and/or by stormy area above USA, which could have influenced the ionospheric and magnetospheric conditions in the surrounding area of the whistler occurrence. The same figures also show an increase in the number of whistlers at high magnetic latitude and at conjugate points. A possible explanation of this result could be the presence of active VLF transmitters [J-L.Pinçon, Demeter International Symposium, Toulouse (France), June 14-16, 2006]. An example is illustrated in the maps of the 19th whistler class of normalized number of whistler data reported in figure 4.12. In this figure are also reported the positions of VLF Russian transmitters together with their geomagnetic conjugate points. Geographical coordinates of these VLF transmitters are reported in the table of figure 4.13. The two plots of figure 4.12 show the influence of VLF transmitters on the geographic whistler distribution. In fact, the increase in the number of whistlers close to location of the transmitters and their conjugate points appears evident.

VLF Transmitters	Latitude	Longitude
Krasnodar	45° N	38° E
Conjugate Point of Krasnodar	31° S	46° E
Novosibirsk	55° N	83° E
Conjugate Point of Novosibirsk	38° S	91° E
Konsomolsk	50° N	137° E
Conjugate Point of Konsomolsk	32° S	134° E

Figure 4.13: Geographic coordinate of VLF Russian transmitters reported in figure 4.12 and their conjugate points, [J-L.Pinçon, Demeter International Symposium, Toulouse (France), June 14-16, 2006].

4.6 Construction of the EQ-whistler correlation estimators: Δw_σ and $hcum_{ratio}$

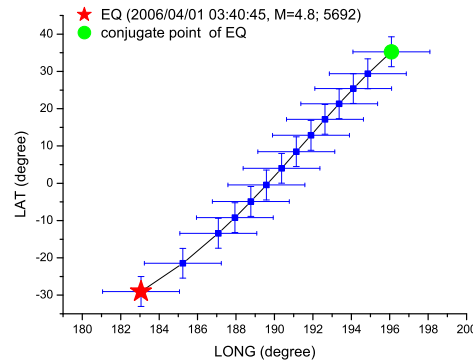


Figure 4.14: Example of the projection at the Earth surface of the magnetic field line which footprint is the epicenter of EQ (2006/04/01 with M=4.8). The crosses indicate the latitude, longitude range around the field line inside which Demeter data are accepted for the study.

In order to study how the seismic activity may influence the whistler propagation I looked for a possible anomalous variation in the number of whistlers in coincidence with the occurrence of selected moderate and strong EQs. Therefore, we need to know the expected distribution of averaging whistler data in a given area under homoge-

neous space and time conditions. This expected distribution $\langle w(lat, long, t) \rangle_{cell}$ of whistlers will be the background reference value to define the possible existence of an anomalous fluctuation in the number of whistlers .

From this information on the normal background of whistlers distributions (see section 4.5) I looked for the possible space and time correlations between whistlers and EQs. At this purpose, two variables have been introduced in the study and defined as follows:

$$\Delta w_\sigma(lat, long, t) = \frac{w(lat, long, t) - \langle w(lat, long, t) \rangle_{cell, 1month}}{\sigma(lat, long, t)|_{cell, 1month}} \quad (4.1)$$

$$hcum_{ratio}(lat, long, t) = \frac{hcum(w(lat, long, t))}{hcum(\langle w(lat, long, t) \rangle_{cell, 1month})} \quad (4.2)$$

First variable represents the standard score number of whistlers as a function of (lat, long, t), where σ is standard deviation. Second variable is the cumulative function of number of whistlers calculated at the observation point normalized to the cumulative function of number of whistlers calculated at mean value. $hcum(w)$ (also called the cumulative density function (CDF)) is related to a discrete probability $P(w)$ by:

$$hcum(w_0) = P(w \leq w_0) = \sum_0^{w_0} P(w) \quad (4.3)$$

Values of these two parameters have been calculated for each class of whistlers. I stress that the value of each variable has been calculated for day or night times comparing the RNF observations with the mean value of observations. Distributions of the above-mentioned variables constructed in this way, for each geographic cell of $4^\circ \times 4^\circ$ and for each month of data have been performed for the whole period May 25, 2005-April 30, 2006. Results indicate that, due to the separation of whistlers data in the 19 dispersion classes and in the 2 time intervals (daytime and nighttime), a scanty pop-

ulation in each geographic cell is obtained. Therefore, a larger dimension for the geographic cells was adopted and, after several attempts, it was found convenient to divide the Earth surface in cells with dimensions of 20 degrees \times 10 degrees of longitude and latitude intervals, respectively (figure 4.15).

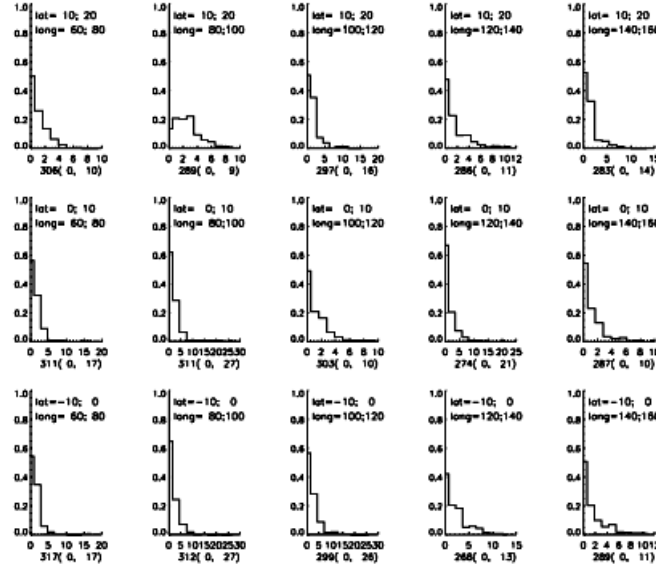


Figure 4.15: An example of probability distribution of number of whistlers for dispersion coefficient class 2^{th} related to 15 geographic cells of 20 degrees \times 10 degrees.

Maps of whistlers produced in this way are reported in figure 4.16. Using the 20 degrees \times 10 degrees geographic cell the increase of the populations of whistlers allow the statistical analysis to be performed. Also seasonal, daily and spatial differences in the whistlers distributions for each class of events remain confirmed. In fact, the same clear differences in the diverse cases (geographic latitude and longitude, month, day-and night times) already pointed out by using smaller cells, can be again observed in the maps of figure 4.16.

4.7 Selection of whistler data using EQ magnetic field line

In this statistical analysis I have only considered the propagation of whistlers which occurs along the EQ magnetic field line. This would imply to include in the study

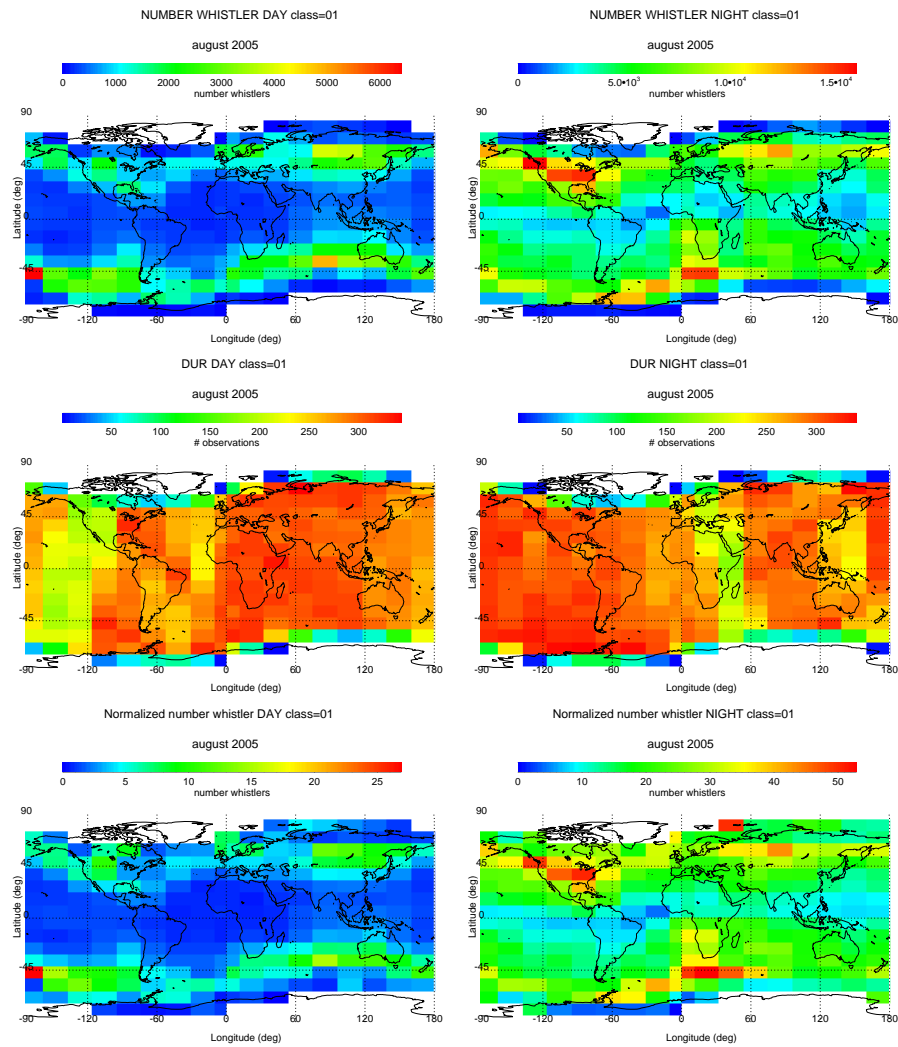


Figure 4.16: From top to bottom, distribution of number of whistlers , total number of measurements collected, normalized number of whistlers $w(lat, long, 1month)$ during August 2005 in Day-time (left panels) and Night-time (right panels) for dispersion class 1.

either the so-called ducted whistlers, which propagate along the selected magnetic line, or non-ducted whistlers but which cross the same field line. For this reason as a first approach in the study, whistlers data have been selected inside a space interval of $\pm 2^\circ$ degrees in geocentric longitude along the EQ magnetic field line. At this purpose, I have calculated the geographic coordinates of several points along the magnetic field line of each selected EQ in order to cover the whole field line. Moreover have opened a box of $\pm 2^\circ$ in longitude and $\pm 4^\circ$ in latitude centered on each one of these points. The $\pm 4^\circ$ width in latitude assures that boxes can overlap one relatively to each other, covering the whole region of $\pm 2^\circ$ in longitude along the field line without any gap in latitude. An example of this construction for a given EQ field line is given in figure 4.14. Therefore, we can accept one WHIMAP observation only if it occurs within almost one box of $\pm 2 \times \pm 4$ in longitude and latitude. Obviously, the WHIMAP observation can occur in the overlapping region of 2 or more adjacent boxes, but in this case we count only one time the WHIMAP observation. I like to stress that for this type of data selection, WHIMAP whistler data are accepted for the analysis only if geocentric latitude of Demeter (λ_D) is within inequality

$$[\lambda_{CP} \leq \lambda_D \leq \lambda_{EQ}]_{along the EQ field line} \quad (4.4)$$

for EQs occurring in the Northern magnetic Hemisphere and

$$[\lambda_{EQ} \leq \lambda_D \leq \lambda_{CP}]_{along the EQ field line} \quad (4.5)$$

for EQs occurring in the Southern geomagnetic Hemisphere. In addition to the above-described selection criterium of whistlers, based on their observation position with respect to the projection of magnetic field line on the Earth's surface for each EQ, a further cut based on time was applied to data. In particular, only whistlers detected in a time window of ± 48 hours, centered on the time of origin of the selected EQs, were taken into account.

Since it has been demonstrated (Tanaka et al., 1973) that geomagnetic disturbances with high values of geomagnetic indices, as Ap, play an important role in the enhancement of the occurrence of whistlers and also of anomalous whistlers, both the whole

WHIMAP database time interval (from May 25, 2005-April 30, 2006) and quiet periods of the magnetosphere have been considered in the study. At this purpose, both whistlers detected disregarding the Ap index value or when Ap was less than 20 (quiet magnetospheric period) were considered and the analysis of correlation with seismicity carried out separately.

4.8 Stability of the correlation estimators

Figure 4.17 shows the geographic distribution of Demeter whistler observations collected along the EQ field lines, which also satisfy the temporal and geographic cuts.

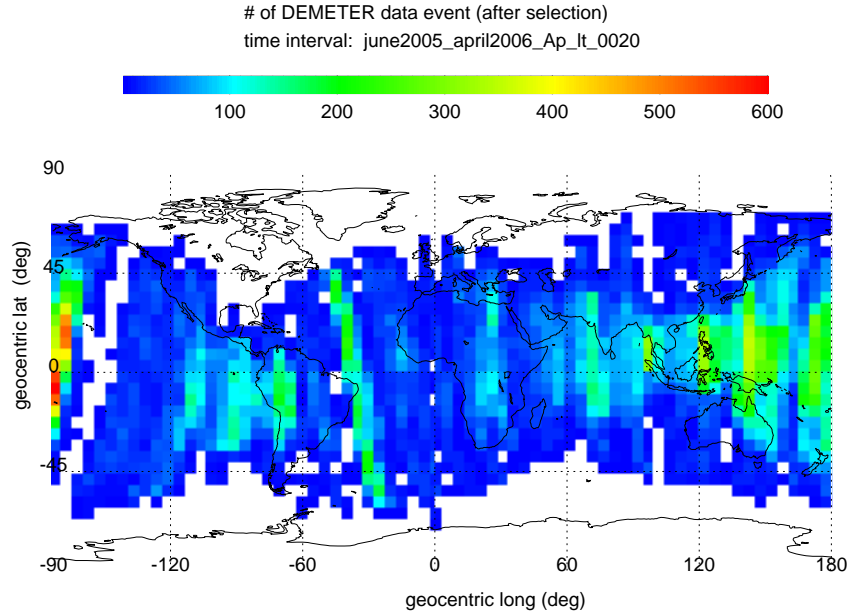


Figure 4.17: Geographic distribution of Demeter observation that satisfy the cut $T_D - T_{EQ} \leq \pm 48$ h and occurring along the EQ magnetic field line for the analyzed time interval.

It is possible to note the existence of large gaps in the space and time coverage of the analyzed period. These "gaps" are more frequent at high latitudes and there are also region not covered at all near longitude -100° . Due to the well-know low-latitude EQ distribution, number of "conjunctions" at low latitude produce an higher number of selected Demeter observations near the western central America region and in

the Indian-Hawaii area. Data are also clearly scattered according with the pattern of Earth magnetic field lines. Although I have analyzed 11 months of Demeter whistler data, the type of EQ field line and $\Delta t (T_D - T_{EQ})$ selection criteria strongly reduces the amount of data useful for searching a possible whistler-EQ correlation. Therefore, to study the stability of correlation estimators (Δw_σ and $hcum_{ratio}$) I have analyzed the dependence of number of whistlers selected for the analysis as a function of dispersion class and Demeter UT for the whole time interval May 25, 2005 - April 30, 2006. Data have been averaged over the whole latitude and longitude ranges.

In figure 4.18(a) is clearly evident:

- the existence of gaps in the WHIMAP data due to the absence of Demeter data
- the decrease in the number of whistlers as function of dispersion parameter
- a clear increase in the number of whistlers, which occurs in June-August 2005
- The existence of three density ranges in the number of whistlers for dispersion coefficient classes 0-6, 7-12, and 13-18 corresponding to $0 \leq D \leq 10s^{-1}$, $10 \leq D \leq 40s^{-1}$, $40 \leq D \leq 202s^{-1}$, respectively
- a systematic fluctuation in the number of whistlers detected in odd and even classes. This behavior unexpected is still under investigation but seems to be caused by an artifact. This is a know effect due to a problem regarding the algorithm used during the postprocessing of the RNF data ².

In figure 4.18(b) is shown the map of number of whistler v.s. true whistler dispersion value. The fluctuation in the number of whistlers versus odd and even classes could systematically influence the analysis. To try avoid this problem we have separately calculated for each class the standard score of number of whistlers (Δw_σ), averaged over the whole latitude and longitude ranges, and plotted as a function of Demeter UT (see figure 4.18(c)). Aim of this plot is to verify if number of whistlers of given class, normalized to the mean number of whistlers in the same class (which in turn is

²J.L. Pinçon Personal Communication

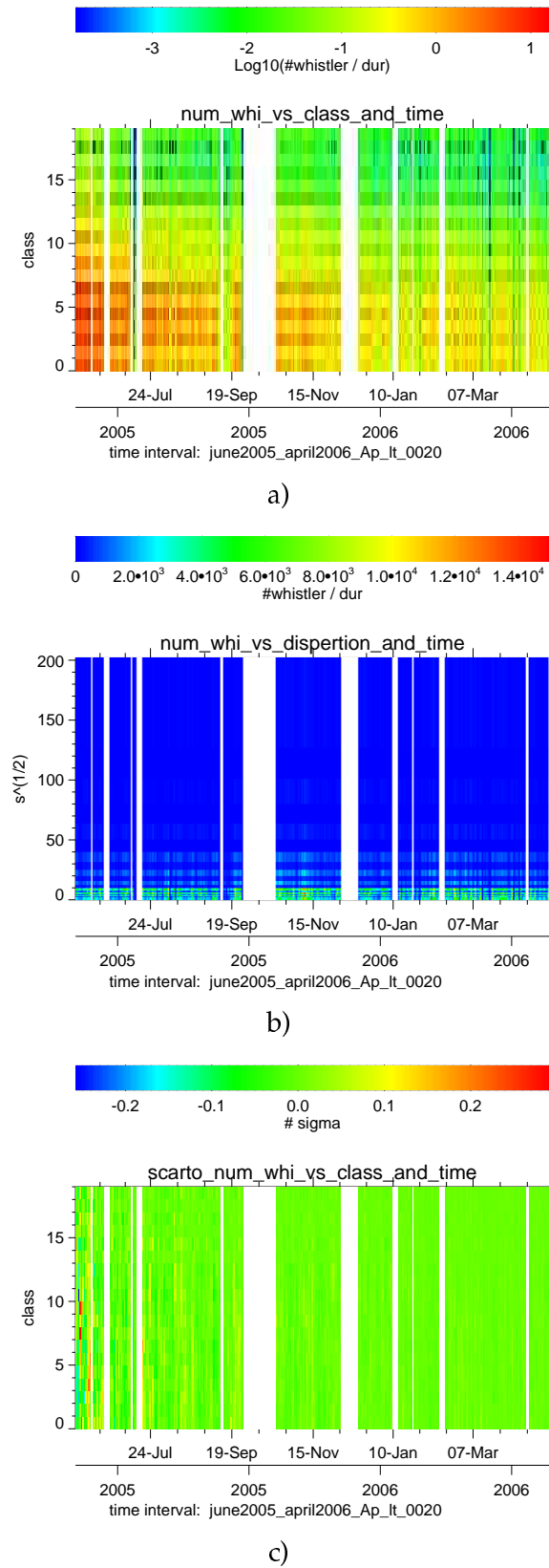


Figure 4.18: Distribution of number of whistlers selected for the correlation with EQs averaged over all latitude and longitude ranges, v.s. dispersion classes and Demeter U.T. (a) v.s. dispersion values and Demeter UT (b). In panel (c) is shown the standard score of number of whistlers selected for correlation with EQs. Data are related to the whole time interval.

averaged over latitude and longitude), still shows the systematic dependence from the odd and even class index. Apparently, as well as can be seen in the June-August period, Δw_σ does not show any dependence from odd and even class indexes but it is always sensitive to large fluctuations of number of whistlers. It means that Δw_σ exhibit a little memory of its systematic dependence from the odd even class index. To better investigate this aspect we have constructed distributions of Δw_σ and $hcum_{ratio}$ as a function at geographic latitude and longitude, for each class (0-18) and for daytime, nighttime, and day+night time, separately (see figures 4.19- 4.30). Maps of Δw_σ and $hcum_{ratio}$ averaged over all the classes for daytime, nighttime, and day+night time are shown in figure 4.31.

It appears evident from the figures that :

- Δw_σ and $hcum_{ratio}$ do not have memory of the geographic distribution of number of whistlers. In particular, remain filtered the effect due to the equatorial belt as well as to the two sub auroral belts, typically present in the geographic distributions of number of whistlers of figures 4.7 - 4.10
- in the maps of Δw_σ , for each class of whistlers dispersion coefficient values the signal-to-noise ratio is generally higher than that in the $hcum_{ratio}$ maps
- for both Δw_σ and $hcum_{ratio}$ estimators, a lower noise is observed in the maps of daytime data
- a residual dependence of Δw_σ and $hcum_{ratio}$ geographic distribution from the odd-even whistlers class index is evident. This indicates that the construction of whistler standard score and of normalized cumulative does not erase completely, the effect of the spurious dependence of number of whistlers from the odd-even index class
- the signal-to-noise value is clearly better for data of highest whistler dispersion coefficient classes.

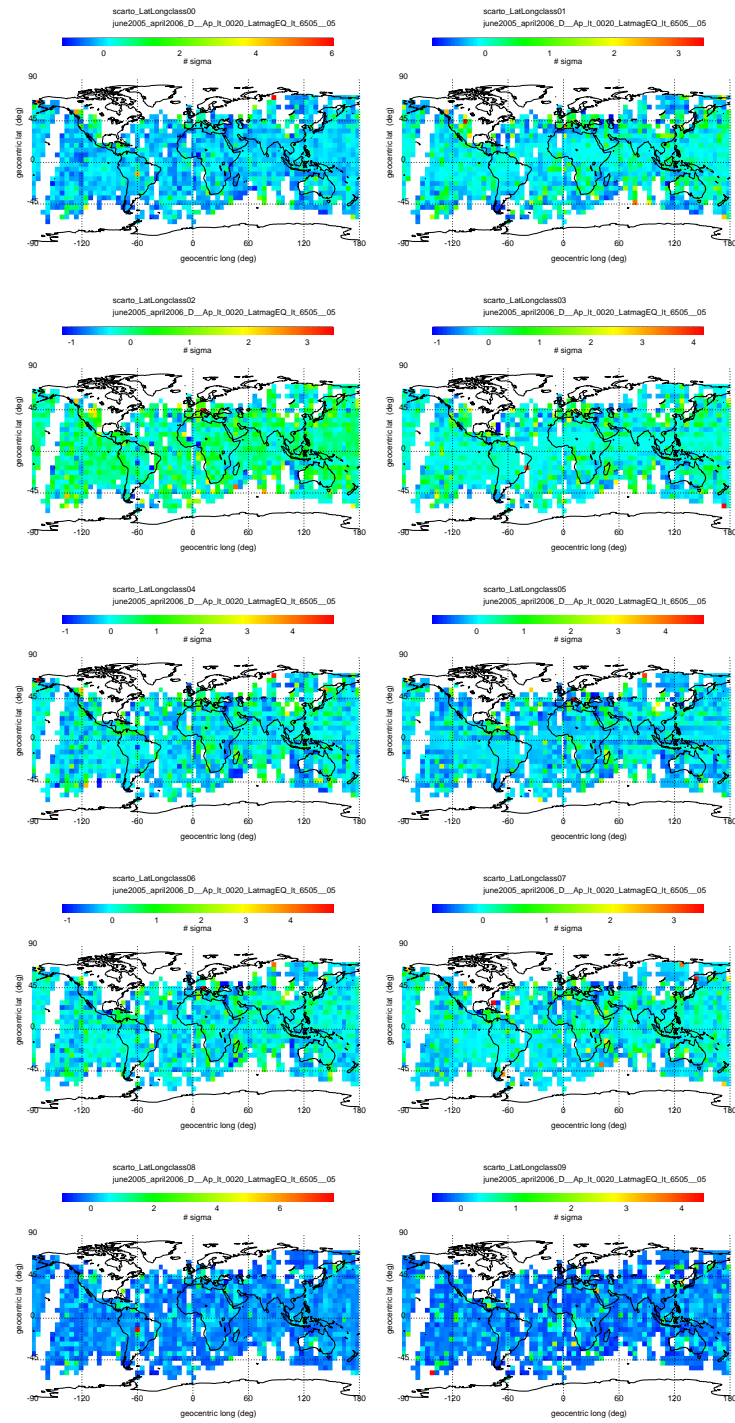


Figure 4.19: Geographic distribution of estimator Δw_σ selected for correlation with EQ for whistler dispersion coefficient classes from 00 to 09 during Daytime. Data have been averaged over the whole time interval.

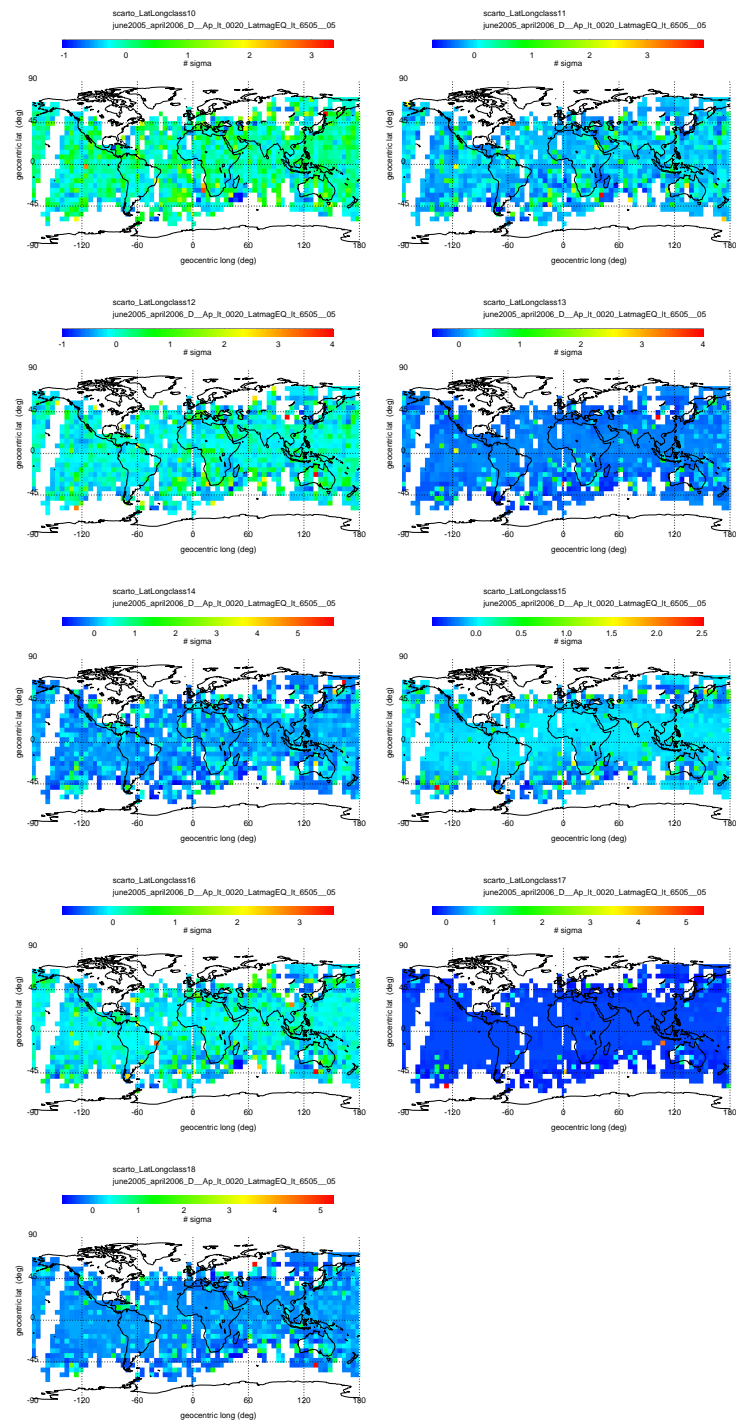


Figure 4.20: Geographic distribution of estimator Δw_σ selected for correlation with EQ for whistler dispersion coefficient classes from 10 to 18 during Daytime. Data have been averaged over the whole time interval.

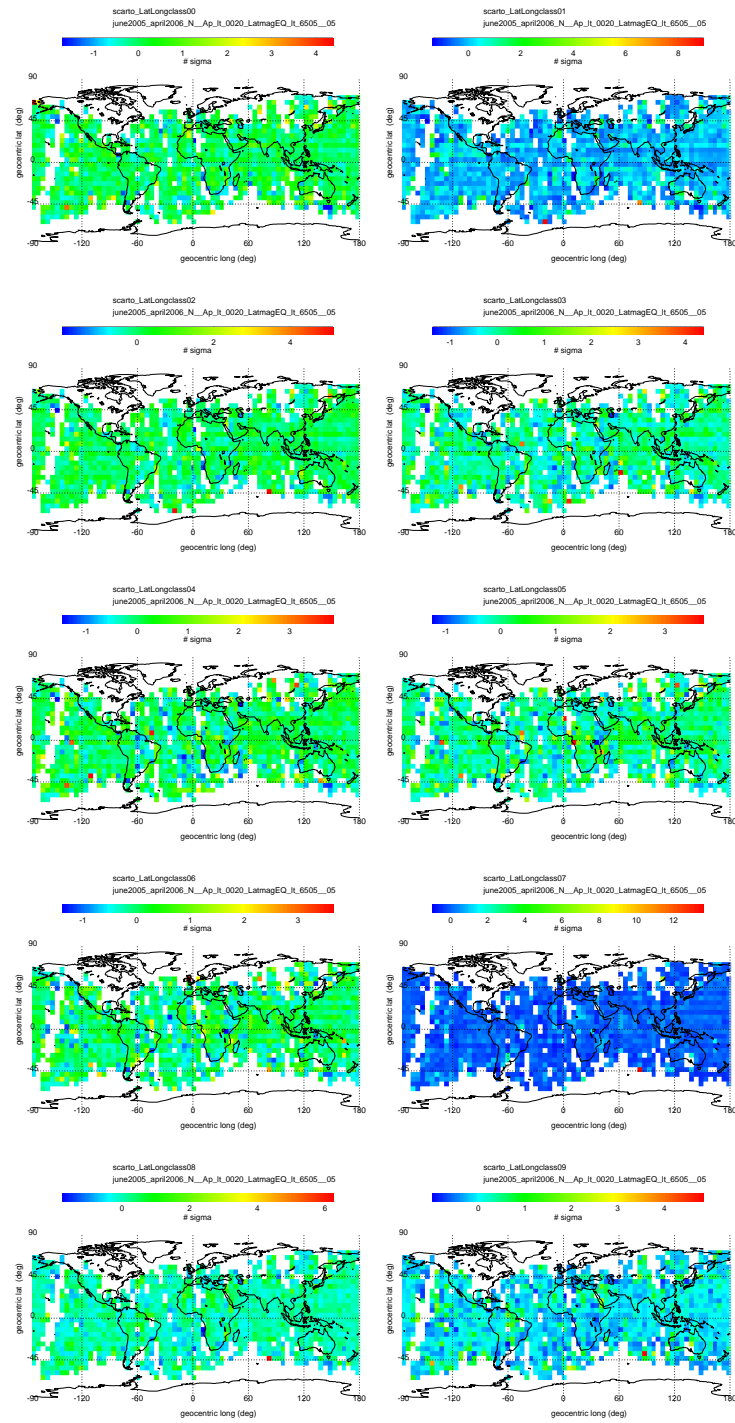


Figure 4.21: Geographic distribution of estimator Δw_{σ} selected for correlation with EQ for whistler dispersion coefficient classes from 00 to 09 during Nighttime. Data have been averaged over the whole time interval.

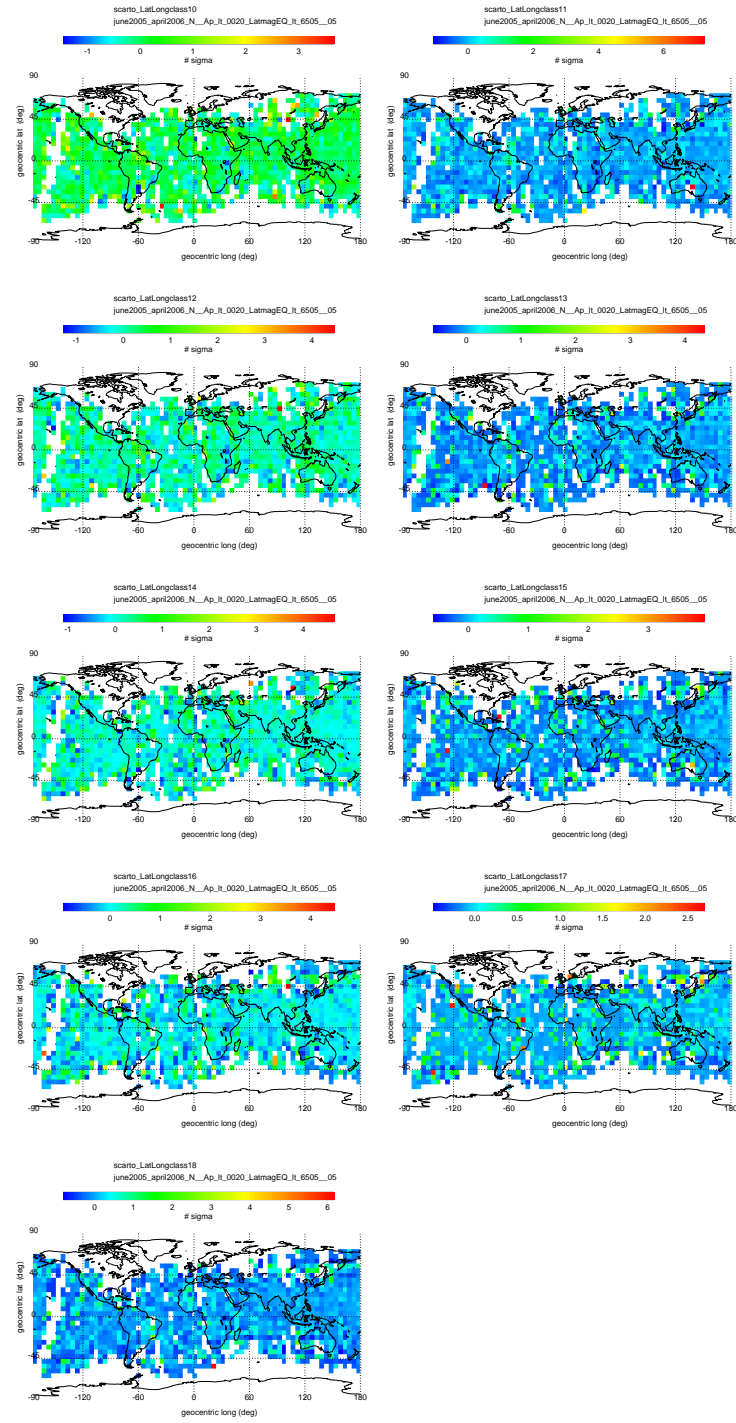


Figure 4.22: Geographic distribution of estimator Δw_{σ} selected for correlation with EQ for whistler dispersion coefficient classes from 10 to 18 during Nighttime. Data have been averaged over the whole time interval analyzed June 2005-April 2006.

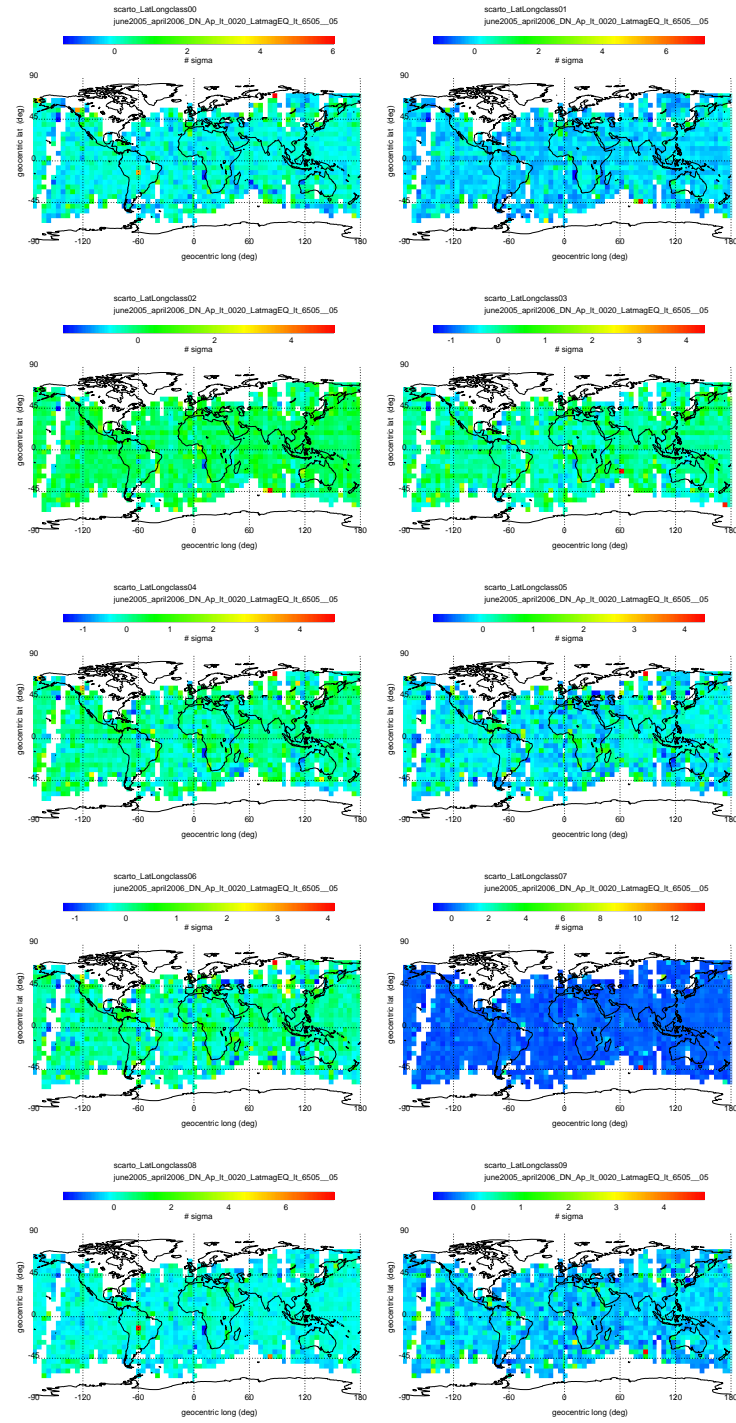


Figure 4.23: Geographic distribution of estimator Δw_σ selected for correlation with EQ for whistler dispersion coefficient classes from 00 to 09 during Nighttime+Daytime. Data have been averaged over the whole time interval.

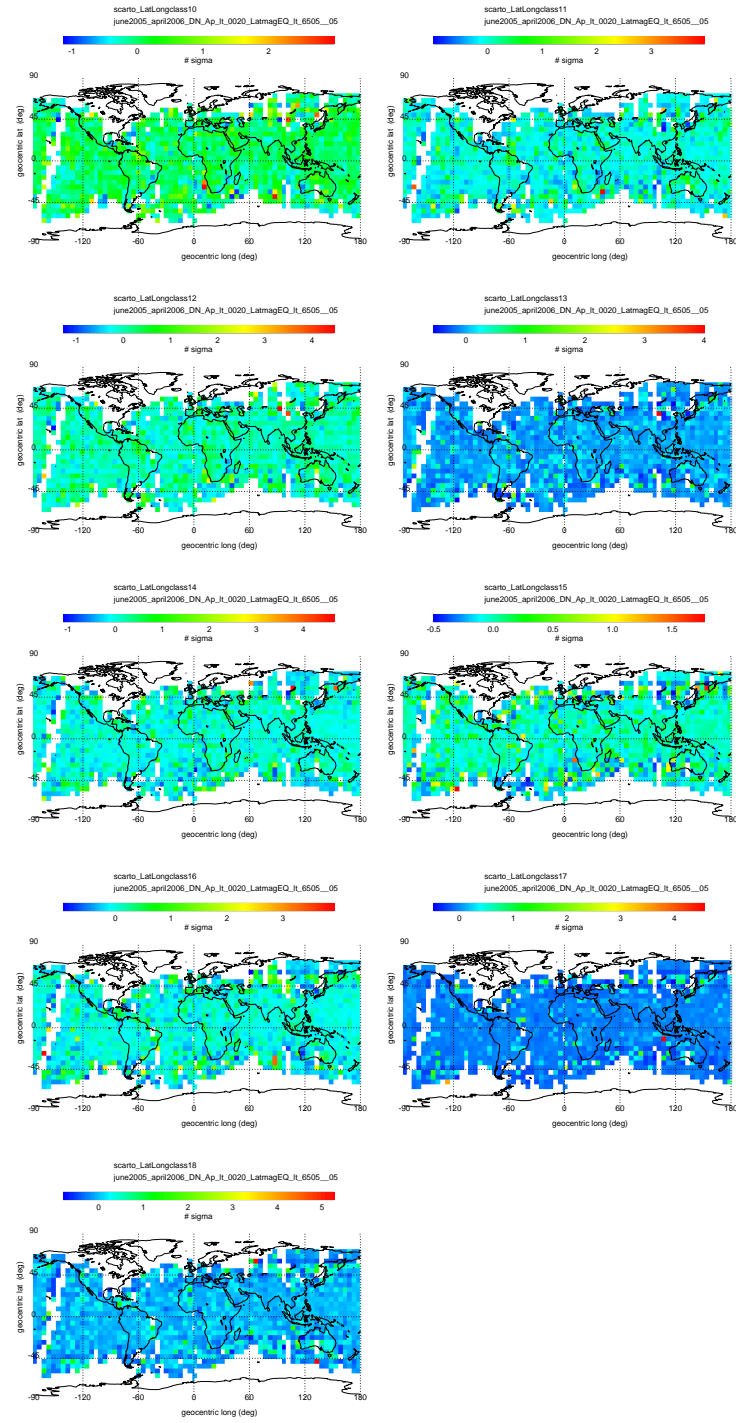


Figure 4.24: Geographic distribution of estimator Δw_{σ} selected for correlation with EQ for whistler dispersion coefficient classes from 10 to 18 during Nighttime+Daytime. Data have been averaged over the whole time interval.

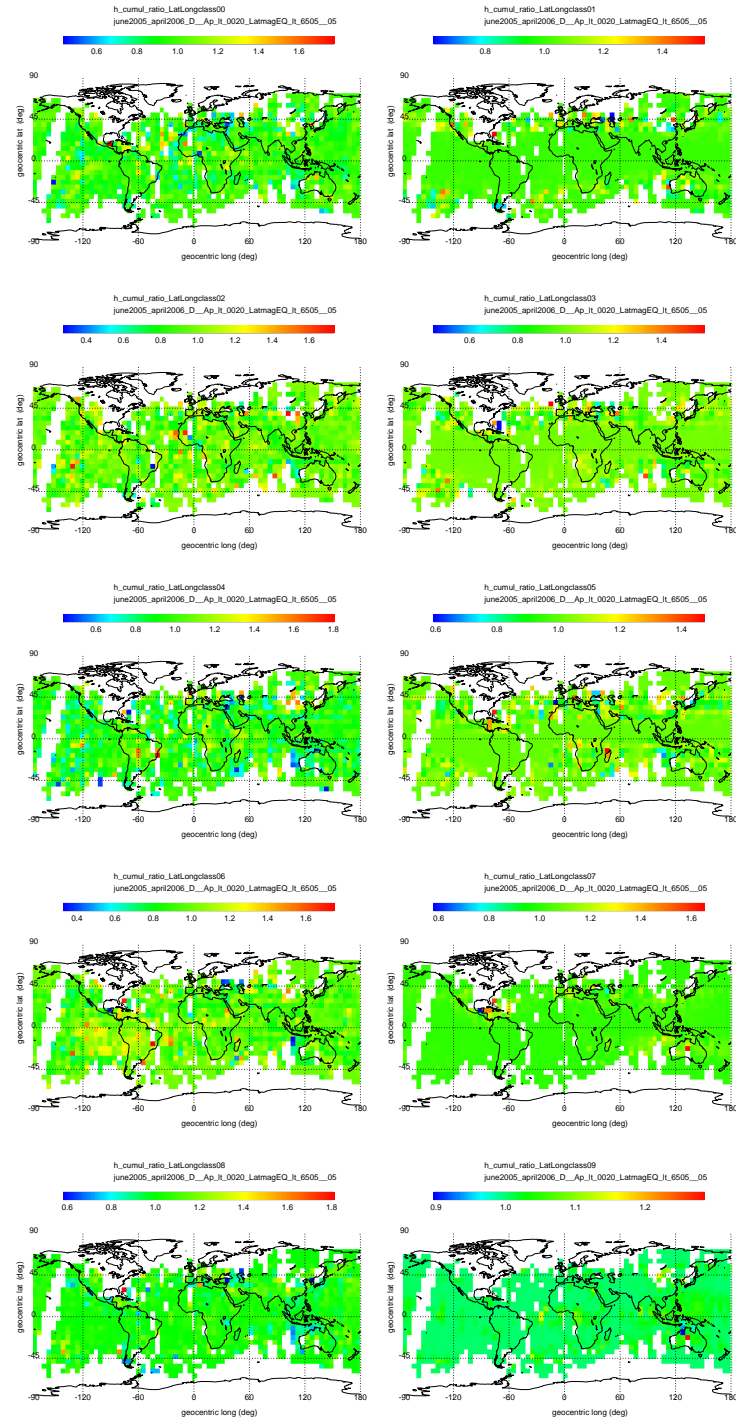


Figure 4.25: Geographic distribution of estimator h_{cum_ratio} selected for correlation with EQ for whistler dispersion coefficient classes from 00 to 09 during Daytime. Data have been averaged over the whole time interval.

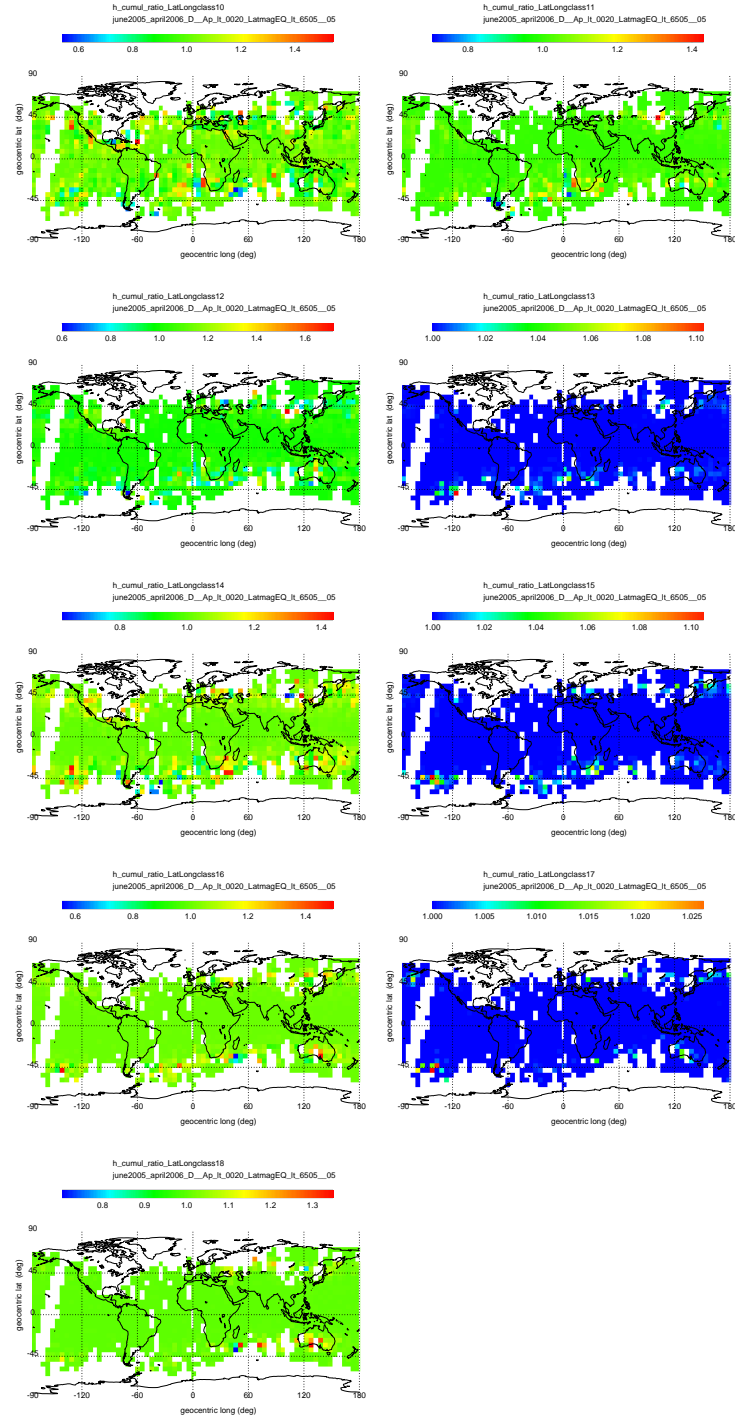


Figure 4.26: Geographic distribution of estimator h_{cum_ratio} selected for correlation with EQ for whistler dispersion coefficient classes from 10 to 18 during Daytime. Data have been averaged over the whole time interval.

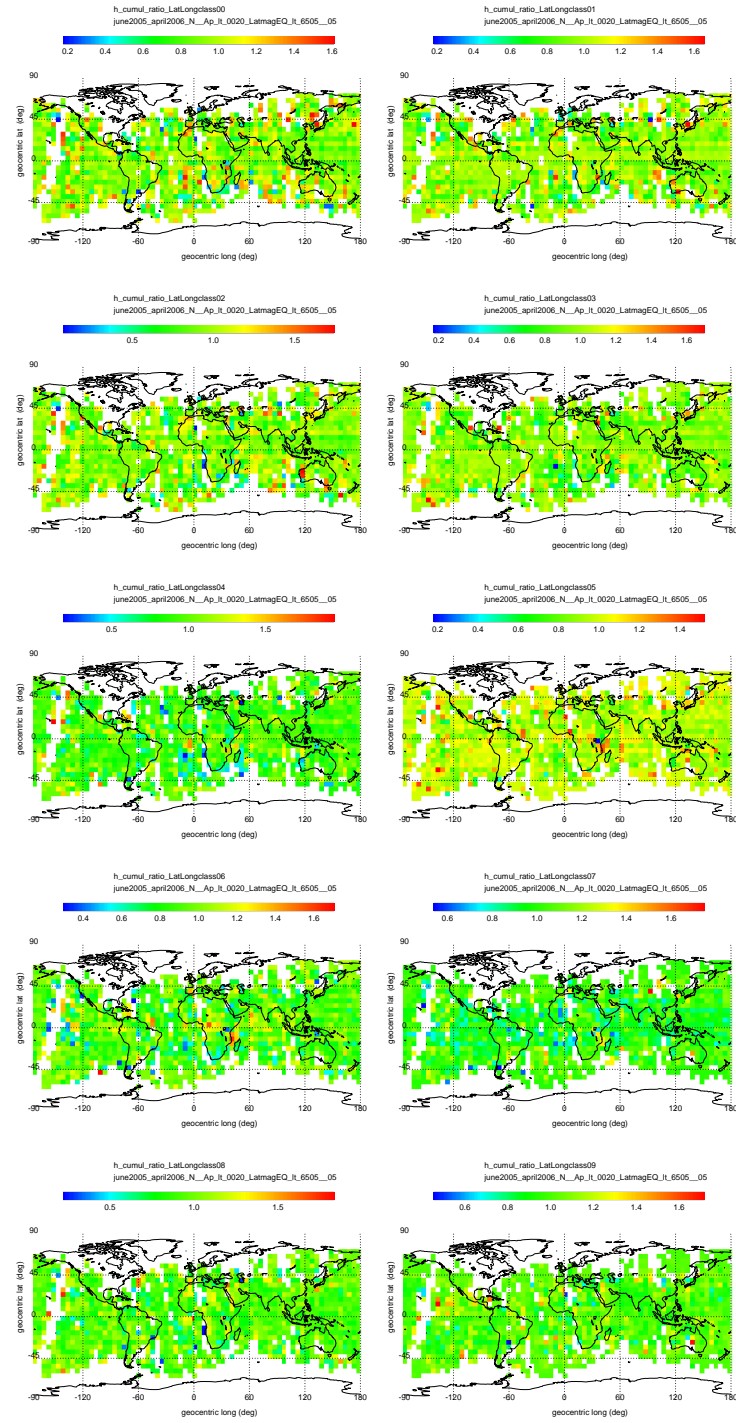


Figure 4.27: Geographic distribution of estimator h_{cum_ratio} selected for correlation with EQ for whistler dispersion coefficient classes from 00 to 09 during Nighttime. Data have been averaged over the whole time interval.

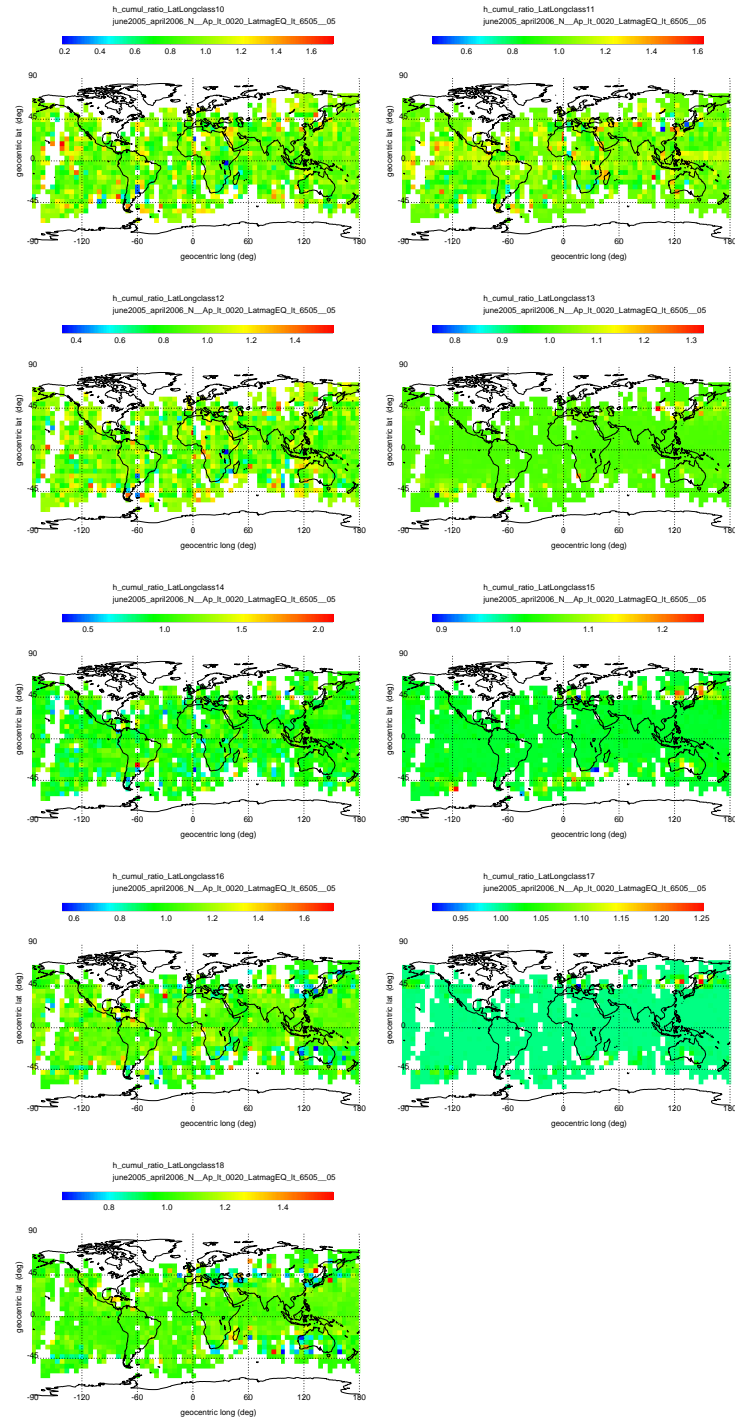


Figure 4.28: Geographic distribution of estimator h_{cum_ratio} selected for correlation with EQ for whistler dispersion coefficient classes from 10 to 18 during Nighttime. Data have been averaged over the whole time interval.

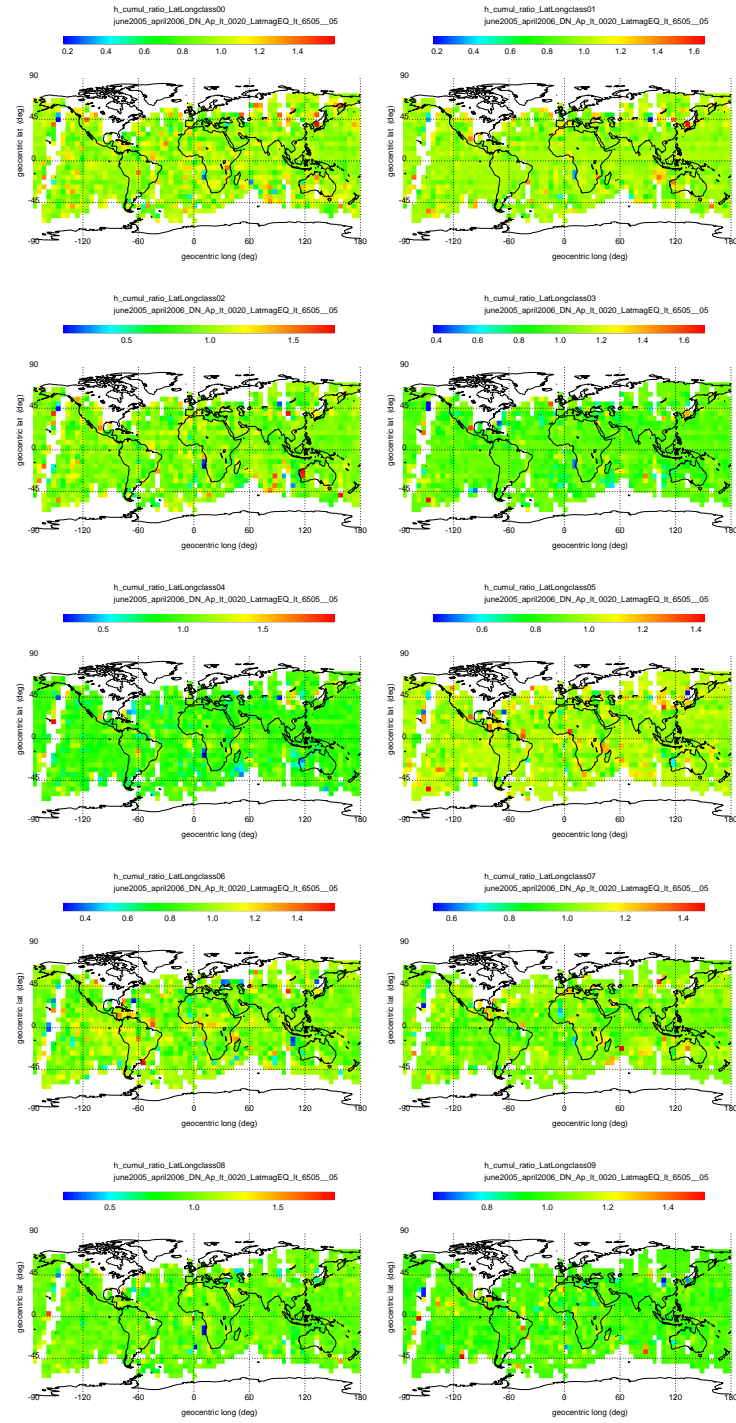


Figure 4.29: Geographic distribution of estimator h_{cum_ratio} selected for correlation with EQ for whistler dispersion coefficient classes from 00 to 09 during Nighttime+Daytime. Data have been averaged over the whole time interval.

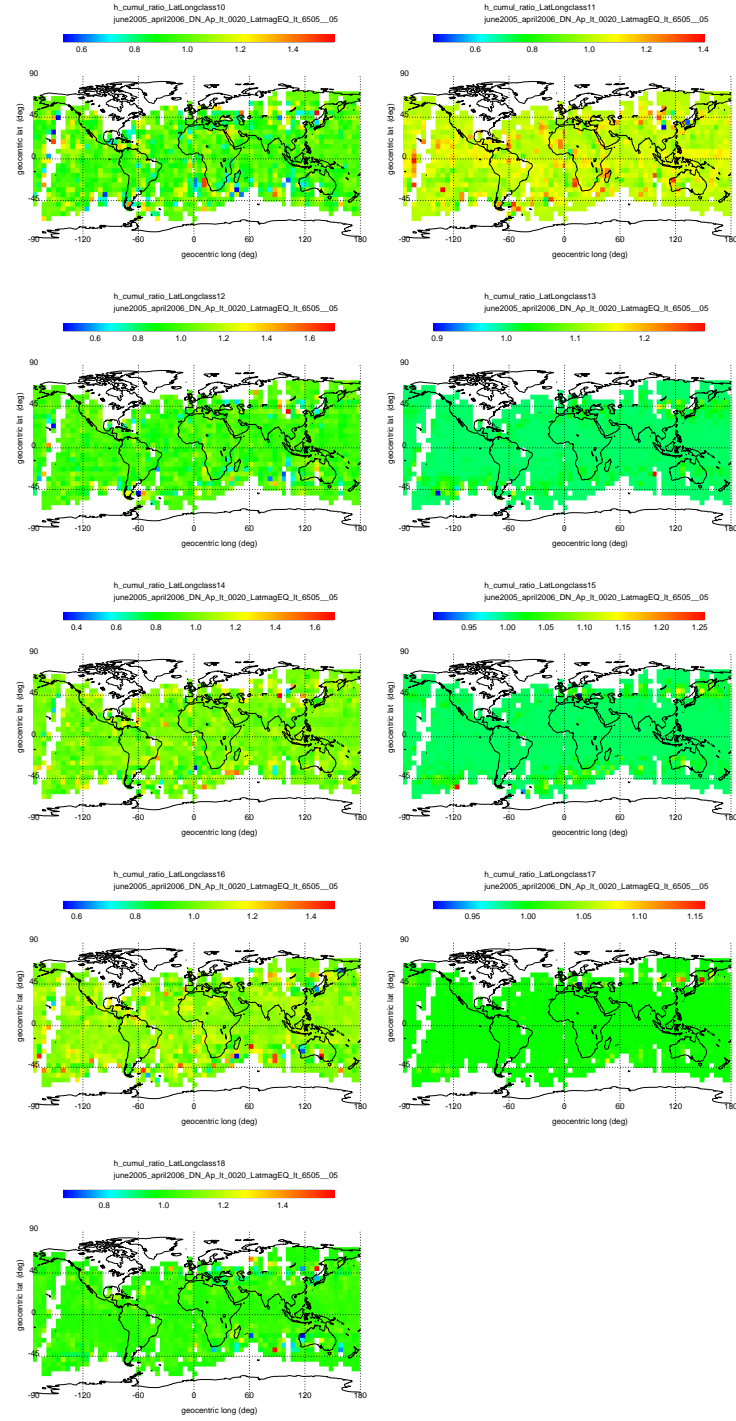


Figure 4.30: Geographic distribution of estimator h_{cum_ratio} selected for correlation with EQ for whistler dispersion coefficient classes from 10 to 18 during Nighttime+Daytime. Data have been averaged over the whole time interval.

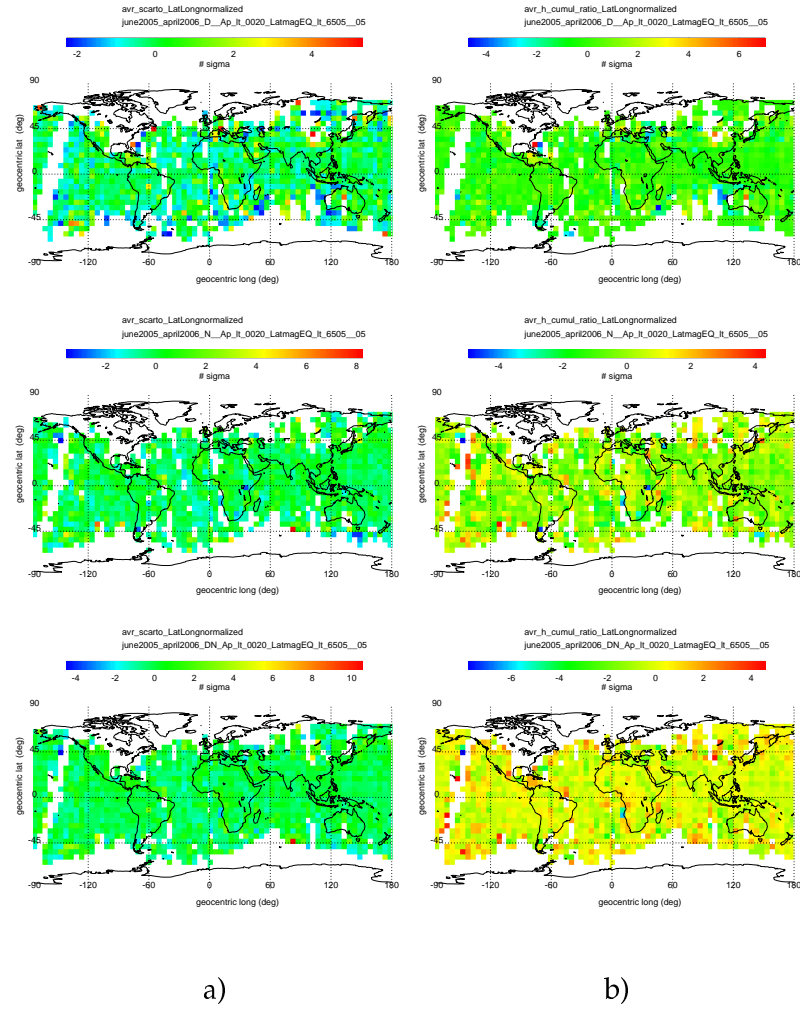


Figure 4.31: Geographic distribution of Δw_σ selected for correlation with EQ (a) and $hcumratio$ (b) averaged over whistler dispersion classes from 00 to 18, during Daytime(top), Nighttime (center), Nighttime+Daytime (bottom). Data have been averaged over the whole time interval.

4.9 Analysis of EQ-whistler correlation

To determine the EQ-whistler statistical correlation I have used the two Δw_σ and $hcum_{ratio}$ estimators.

The geographic distribution of EQ epicenters selected for the statistical analysis on the basis of above mentioned conditions and cuts, are illustrated in figure 4.32. The total number of EQs selected in this way, for $Ap < 20$ (geomagnetic quiet period) resulted to be 1626, which is less than that (2721) of the USGS database with $M \geq 4.8$ and $|\lambda_{EQ}^m| < 65^\circ$.

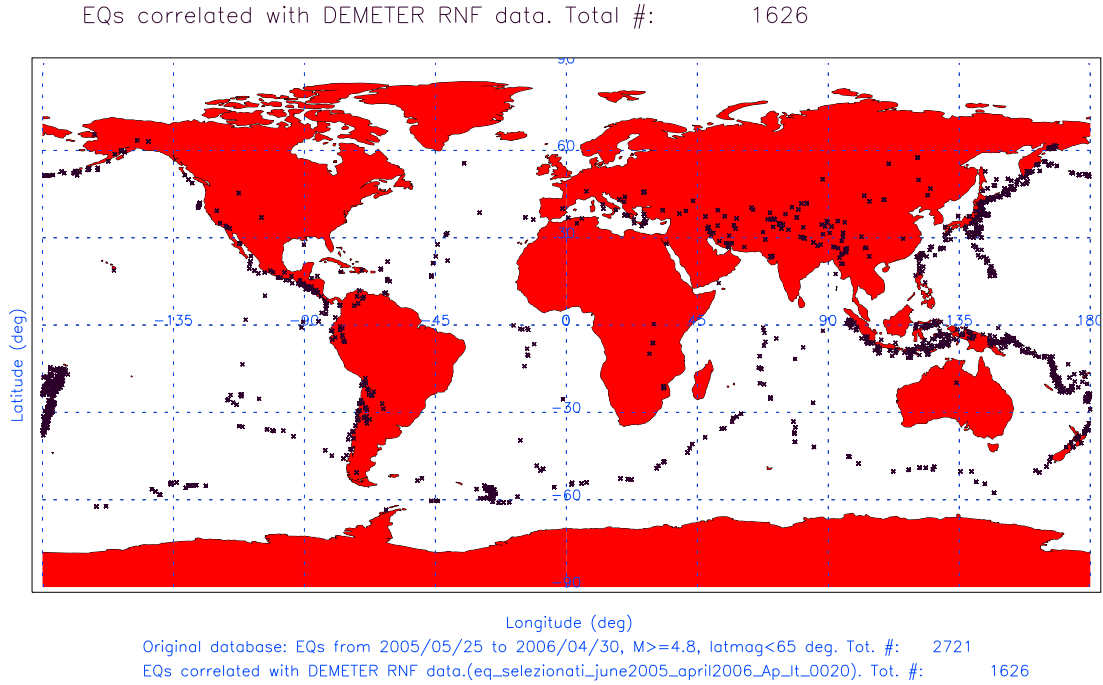


Figure 4.32: Geographic distribution of EQs after cuts have been applied on Δt , $\Delta latmag$ and Ap index for the period May 25, 2005-April 30, 2006.

A more complete information about the representation of Δw_σ and $hcum_{ratio}$ and cuts applied to data is given in table 4.2.

Data set recorded during seismic events are mainly organized as a function of two parameters: Δt , the difference between the time of satellite data and the time of earthquake;

Variables and selection criteria	Values	# of values
Estimators of whistler–EQ correlation	$\Delta w_\sigma, hcum_{ratio}$ (see eq.4.1,eq.4.2)	2
Type of representation	v.s. $(\Delta latmag), \Delta t$, v.s. $(abs(\Delta latmag), \Delta t)$, v.s. (Δt)	3
Average on group of classes	\forall class(01:19) separately, $< (01 : 07) >, < (08 : 13) >, < (14 : 19) >, < (01 : 19) >$	23
Local time selection	Day+Night, Day, Night	3
Demeter data time period	from 2005/06/01 to 2006/04/30	1
Selection on Ap index	no cut Ap, $Ap < 20$	2
Selection of time window	$T_D - T_{EQ} \leq \pm 48 \text{ h}$,	1
Selection on the EQ magnetic latitude	$ latmag_{EQ} \leq 65^\circ, latmag_{EQ} \leq 30^\circ$	2
Selection on the EQ magnitude	$M \geq 4.8$	1
Total number of different representations produced in this analysis	$2 \times 3 \times 23 \times 3 \times 1 \times 2 \times 1 \times 2 \times 1$	1656

Table 4.2: $\Delta w_\sigma, hcum_{ratio}$ estimators of whistler–EQ correlation introduced in the analysis, together with their representation and cuts applied to data for selecting EQ and whistler populations to be correlated. Symbol $< \dots >$ indicate the average on diverse whistler dispersion classes.

$$\Delta t = T_D - T_{EQ} \quad (4.6)$$

and $\Delta latmag$, the difference between magnetic latitude of satellite data and magnetic latitude of earthquakes

$$\Delta latmag = latmag_D - latmag_{EQ} \quad (4.7)$$

Following definition 4.7, and WHIMAP data selection along the EQ field line between the EQ and the CP points, I like to stress that:

$$\Delta latmag \geq 0 \quad (4.8)$$

for EQ occurring in the Southern magnetic Hemisphere and

$$\Delta latmag < 0 \quad (4.9)$$

for EQ occurring in the Northern magnetic Hemisphere.

Consequently in the plots v.s. $(\Delta latmag, \Delta t)$ data correlated with EQs occurring in the Southern ($\Delta latmag > 0$) or in the Northern magnetic Hemisphere ($\Delta latmag < 0$) are separated. In order to try to detect EQ precursory effects, the value of Δw_σ or $hcum_{ratio}$ parameters are reported as a function of Δt with bins of 2 hours and as a function of $\Delta latmag$ with bins of 10 degrees. Aim of this type of maps is to look for significant fluctuations of Δw_σ and $hcum_{ratio}$ parameters near EQ zones. For each dispersion class of whistlers, Ap value, EQ magnetic latitude, etc. have been produced different plots of Δw_σ and $hcum_{ratio}$ parameters.

In figures 4.33-4.36 are shown Δw_σ plots for each one of the (0-18) whistler dispersion classes as a function of $((\Delta latmag), \Delta t)$ (column (a)), as a function of $(abs(\Delta latmag), \Delta t)$ (column (b)), and v.s. Δt after an average on $(\Delta latmag)$. In figures 4.37-4.40 are reported analogous plots but for the $hcum_{ratio}$ variable. In these figures measurements carried out near the EQ epicenter will give $\Delta latmag \simeq 0$, so all the EQs included in the analysis lie on the $\Delta latmag = 0$ axis. Instead the measurement carried out near the CP zones are scattered in different points of the $((\Delta latmag), \Delta t)$ plots. Consequently it is not possible to identify a defined region where to localize measurements carried out by Demeter near the CP of each EQ. This is due to the type of selection applied to the WHIMAP–EQ databases. In fact, us consider two EQs occurring at different latitudes with magnetic field lines of different lengths. If two WHIMAP measurements occur and one each of them is associated with a different EQ but at the same $(\Delta latmag)$ distance, these two WHIMAP data will be put on the same bin in the $((\Delta latmag), \Delta t)$ plot.

Plots of Δw_σ and $hcum_{ratio}$ v.s. $(\Delta latmag, \Delta t)$ point out a difference in the space distributions of these two parameters between the two Earth Hemispheres. It is interesting to note that a check carried out on seismicity revealed an analogous trend in the geographic distribution of selected EQs (figure 4.3(a) and top panel of figure 4.3(f)). In fact, a greater number of EQs is observed in the southern geomagnetic hemisphere than in the northern ones. Δw_σ and $hcum_{ratio}$ v.s. $(\Delta latmag, \Delta t)$ do not show any significant correlation between WHIMAP and EQ data. The existence of scattered bins observed at highest and lowest $\Delta latmag$ values is a consequence of several facts:

- The lengths of EQ field lines are different for EQ occurring at different latitudes. Then, data collected in very different conditions from the point of view of the whistler propagation are merged together.
- Demeter measurements are not homogeneous in $\Delta latmag$ and Δt space phase. It implies an higher statistics is for low $\Delta latmag$ values and a very poor statistics for high $\Delta latmag$ values.
- The well known spatial distribution of EQs at low latitudes, which implies that WHIMAP data satisfying the applied cuts are concentrated near $\Delta latmag \simeq 0$.
- The maps representation v.s. $(\Delta latmag, \Delta t)$ may distinguish data correlated with EQ occurring at the two different geomagnetic Hemispheres. In particular, this distinction reduces the statistical significance and introduces a spurious effect. To reduce this problem I have produced maps of Δw_σ and $hcum_{ratio}$ as a function of Δt and of the absolute value of $\Delta latmag$.

Plots of Δw_σ and $hcum_{ratio}$ vs. $(abs(\Delta latmag, \Delta t))$, allow statistics to be improved (column(b) of figures 4.33 - 4.36), since data are averaged over the two Earth Hemisphere.

Also if the representation v.s. $(abs(\Delta latmag, \Delta t))$ solve the problem, data are always scattered at highest value of $abs(\Delta latmag)$ and no significant signals is observed in the maps. To overcome the difficulty to represent data gathered at different latitudes and at difference distances from the EQ epicenters I have introduced a new representation of Δw_σ and $hcum_{ratio}$, by an averaging over $\Delta latmag$. At this purpose I have calculated the $\xi(\Delta t)$ standard score as follows:

$$\xi(\Delta t) = \frac{x(\Delta t) - m}{\sigma} \quad (4.10)$$

where, for each assigned Δt value, x is the mean value of Δw_σ or $hcum_{ratio}$ parameter averaged over the whole range of $\Delta latmag$ values; m is the mean value of x averaged over Δt , and σ is the standard deviation of x data. Finally, Δw_σ and $hcum_{ratio}$ vs. (Δt) plots have been produced (column(c) of figures 4.33 - 4.36) as a function of time, disregarding the $\Delta latmag$ distance. A high mean intensity value for fixed Δt

values in plots of Δw_σ and $hcum_{ratio}$ vs. $(\Delta latmag, \Delta t)$ corresponds to a large spike in the $\Delta w_\sigma(\Delta t)$ and $hcum_{ratio}(\Delta t)$ plots (column(c) of figures 4.33 - 4.36). These figures shown a few spikes over 2 standard deviation level associated with data of several classes of whistler dispersion coefficient values. Peaks are more frequent in the $\Delta w_\sigma(\Delta t)$ plots than in the $hcum_{ratio}(\Delta t)$ ones. This effect can indicate that the Δw_σ parameter is more sensitive to little fluctuations and so more noisy that the $hcum_{ratio}$ estimator.

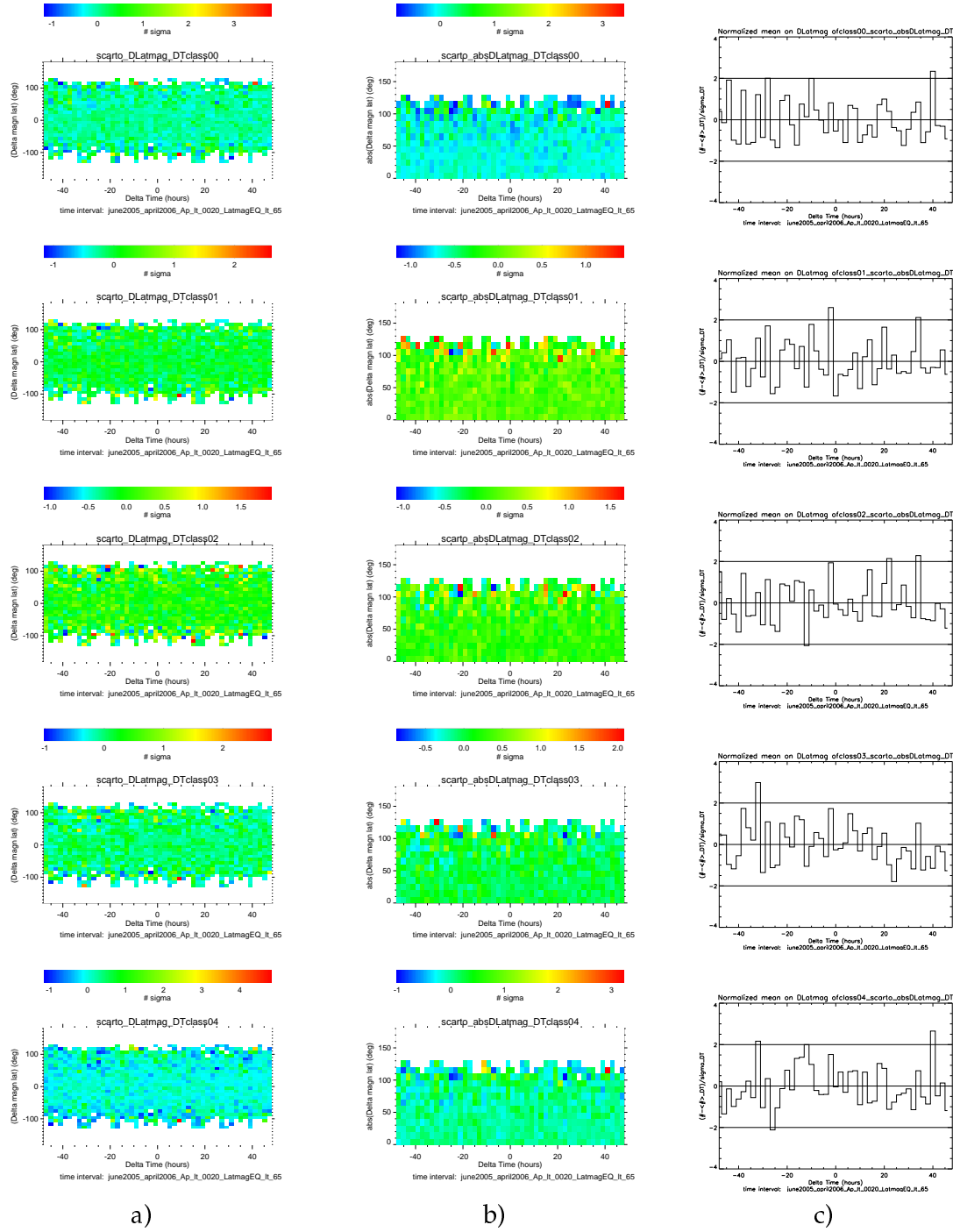


Figure 4.33: Δw_σ distributions from 2005/05/25 to 2006/04/30 for whistler dispersion classes from 00 to 04 v.s. a) $(\Delta latmag, \Delta t)$ b) $abs(\Delta latmag, \Delta t)$ and c) Δt after an averaging over $\Delta latmag$.

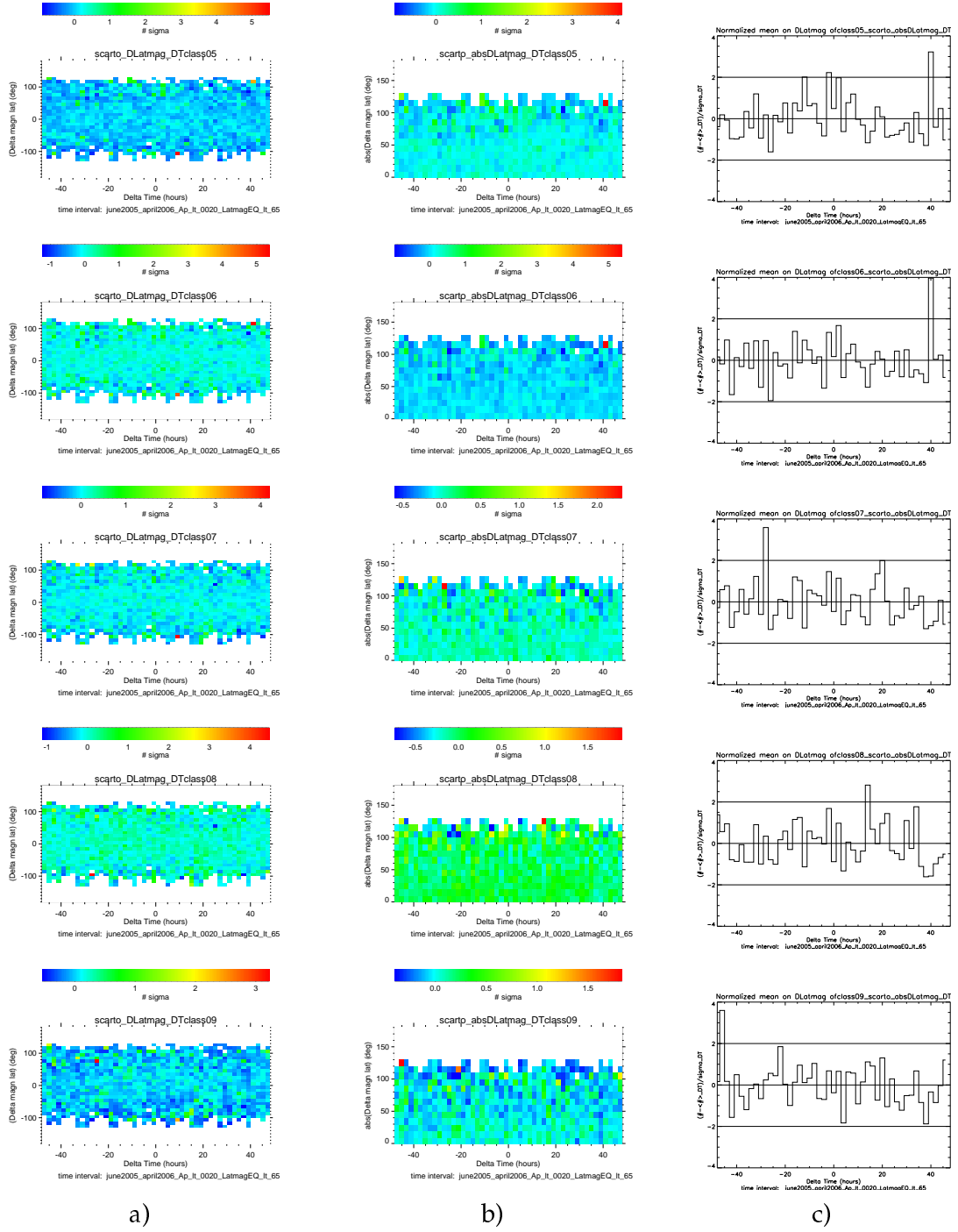


Figure 4.34: Δw_σ distributions from 2005/05/25 to 2006/04/30 for whistler dispersion classes from 05 to 09 a) $(\Delta latmag, \Delta t)$ b) $abs(\Delta latmag, \Delta t)$ and c) Δt after an averaging over $\Delta latmag$.

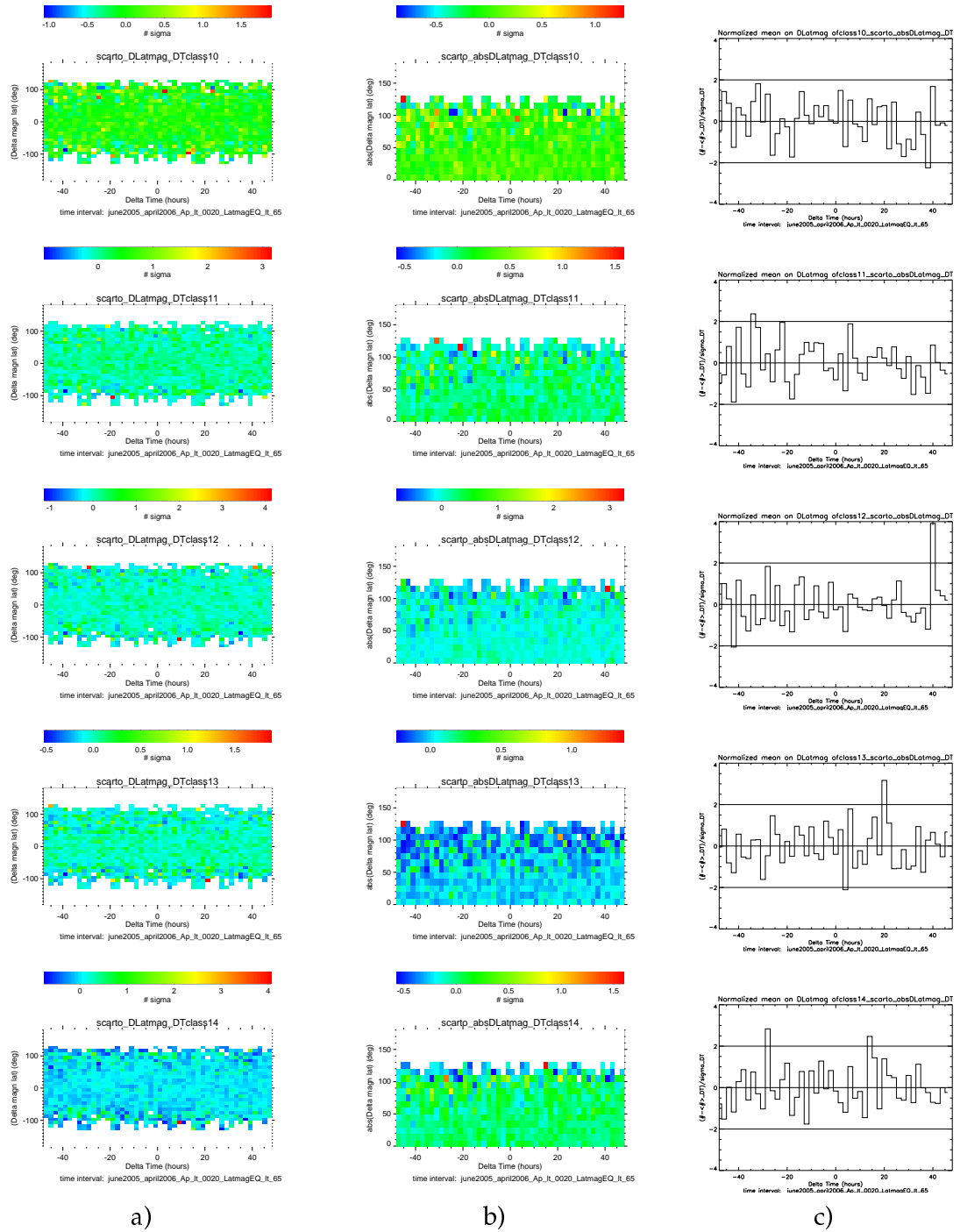


Figure 4.35: Δw_σ distributions from 2005/05/25 to 2006/04/30 for whistler dispersion classes from 10 to 14 a) $(\Delta \text{latmag}, \Delta t)$ b) $\text{abs}(\Delta \text{latmag}, \Delta t)$ and c) Δt after an averaging over Δlatmag .

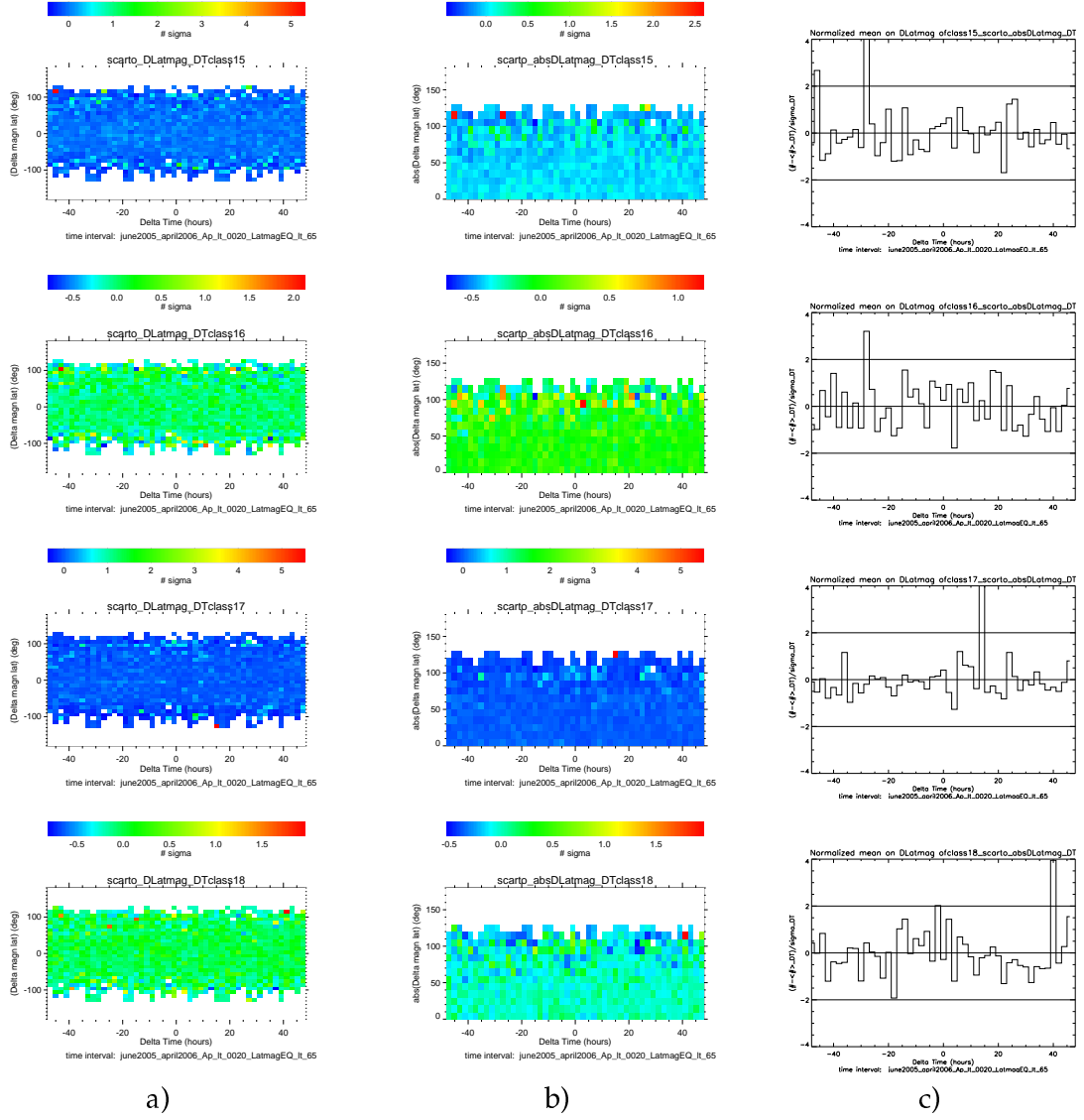


Figure 4.36: Δw_σ distributions from 2005/05/25 to 2006/04/30 for whistler dispersion classes from 15 to 18 a) $(\Delta latmag, \Delta t)$ b) $(abs(\Delta latmag), \Delta t)$ and c) Δt after an averaging over $\Delta latmag$.

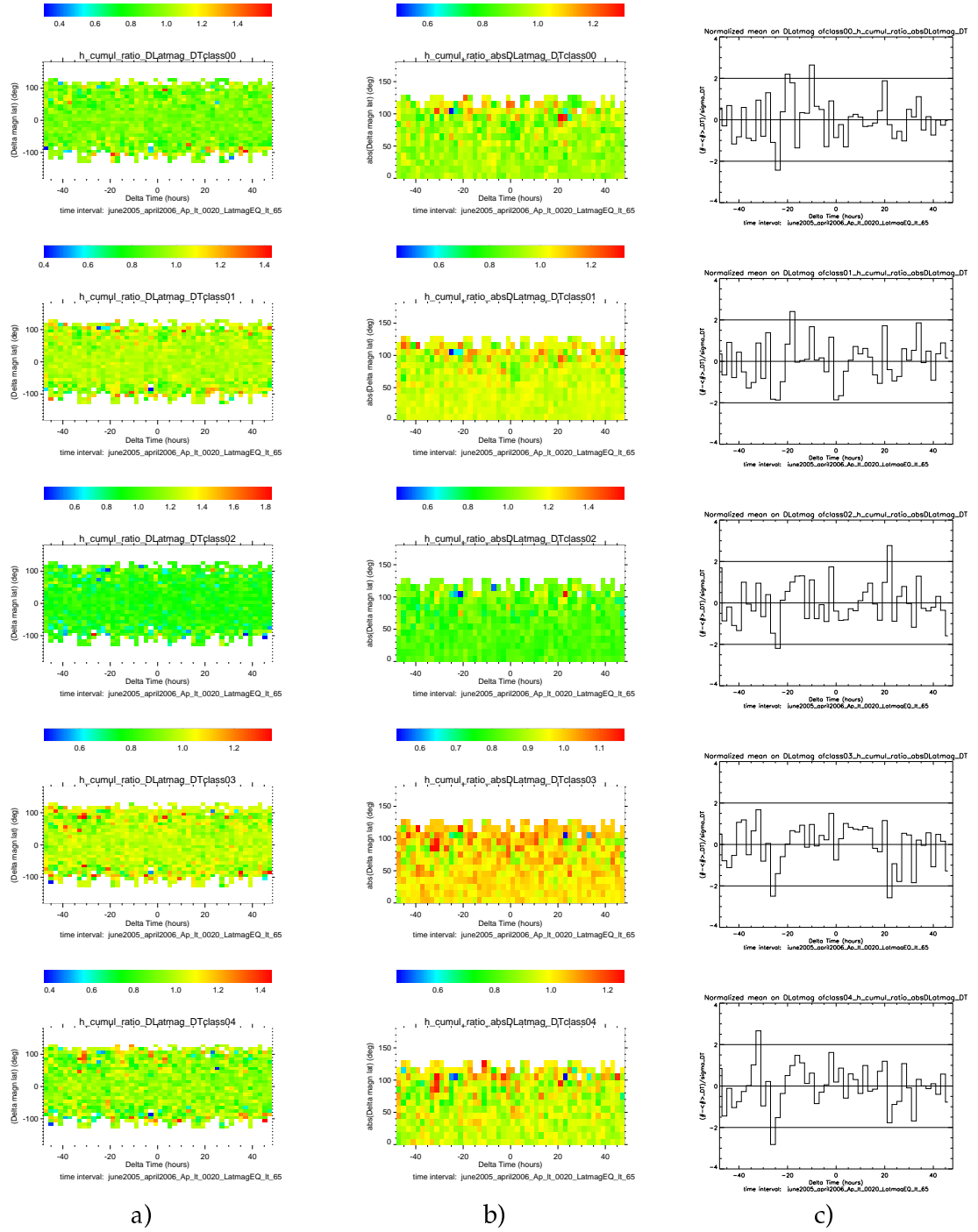


Figure 4.37: h_{cum_ratio} distributions from 2005/05/25 to 2006/04/30 for whistler dispersion classes from 00 to 04 a) $(\Delta latmag, \Delta t)$ b) $abs(\Delta latmag, \Delta t)$ and c) Δt after an averaging over $\Delta latmag$.

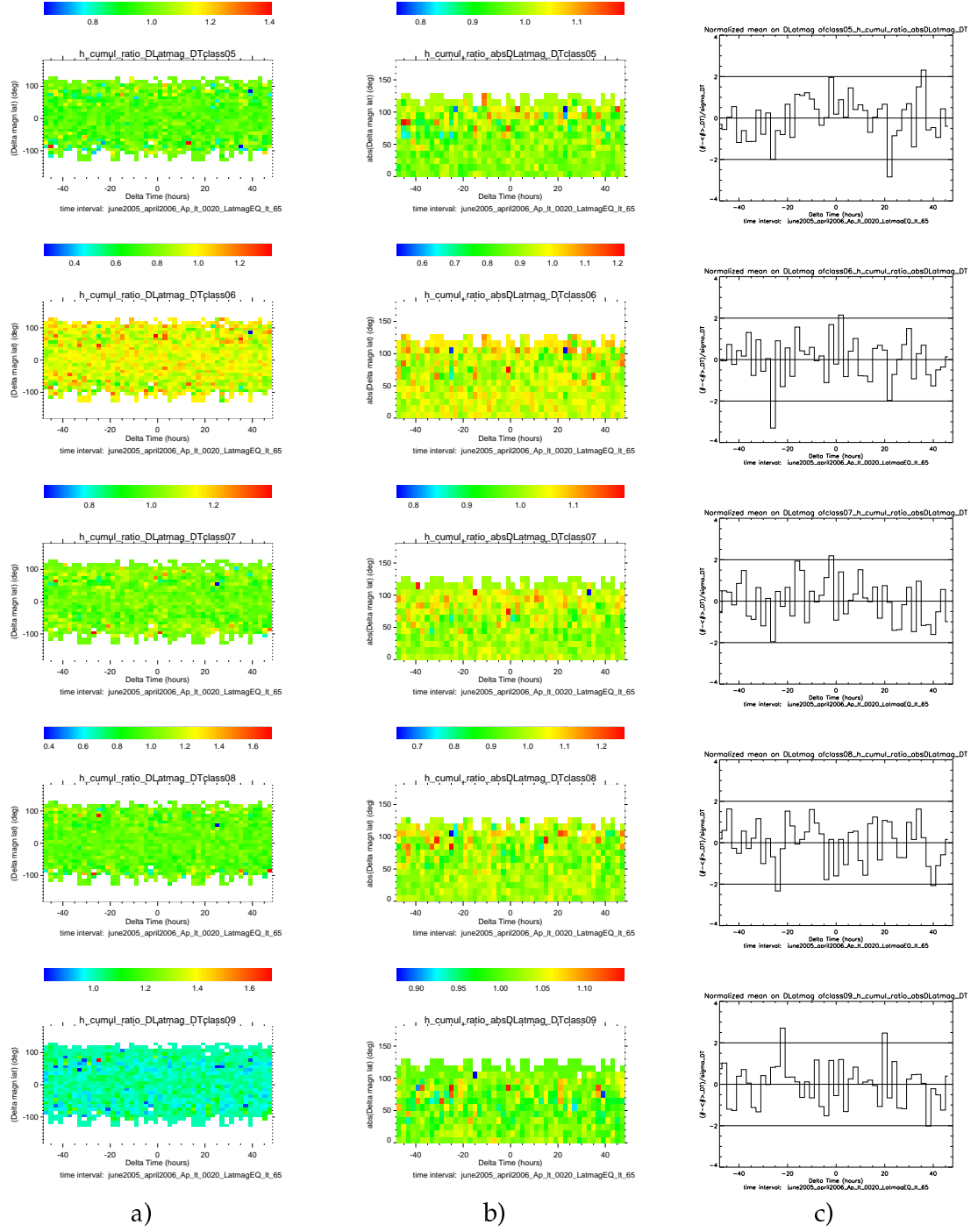


Figure 4.38: h_{cum_ratio} distributions from 2005/05/25 to 2006/04/30 for whistler dispersion classes from 05 to 09 a) $(\Delta latmag, \Delta t)$ b) $abs(\Delta latmag, \Delta t)$ and c) Δt after an averaging over $\Delta latmag$.

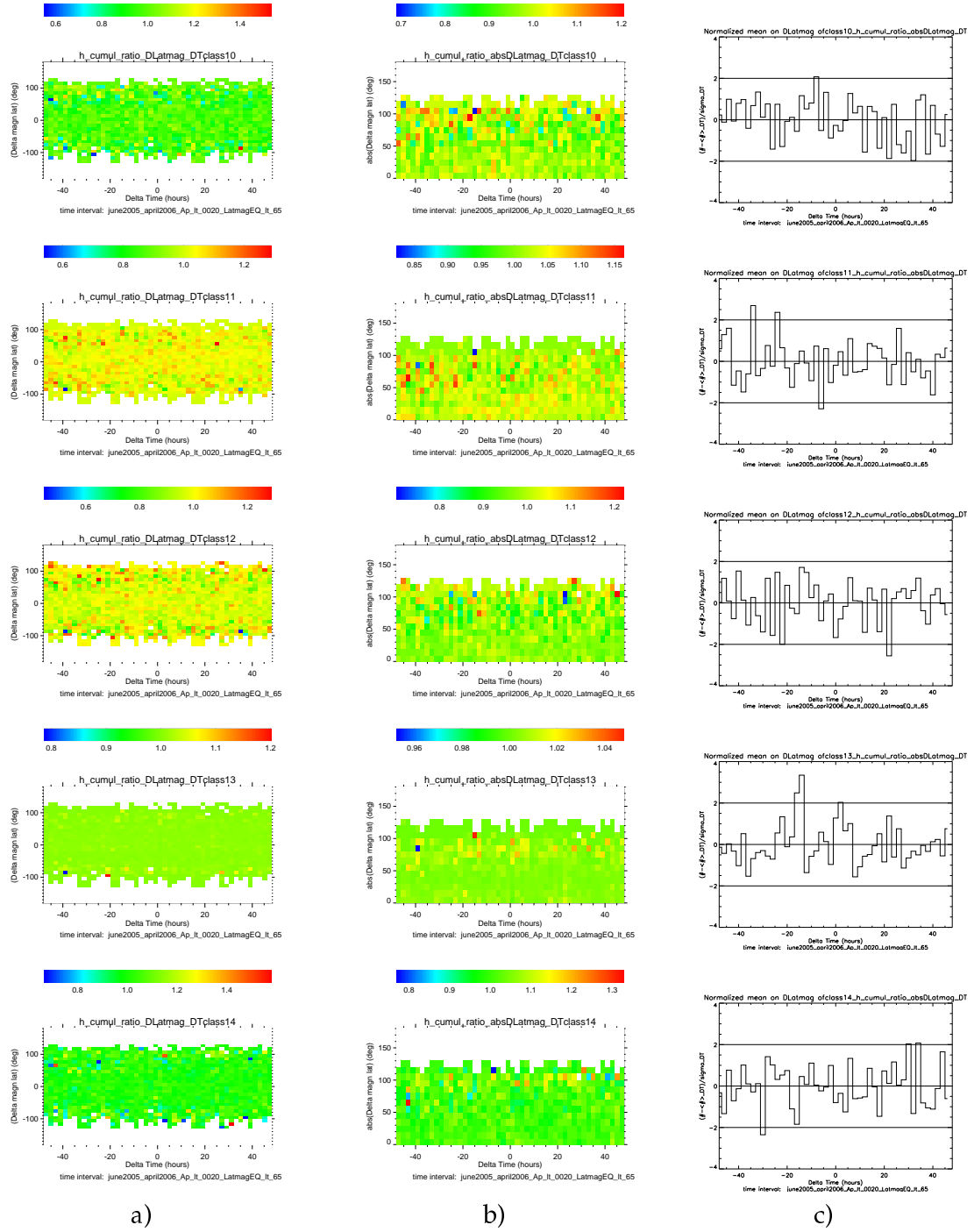


Figure 4.39: h_{cumul_ratio} distributions from 2005/05/25 to 2006/04/30 for whistler dispersion classes from 10 to 14 a) $(\Delta latmag, \Delta t)$ b) $abs(\Delta latmag, \Delta t)$ and c) Δt after an averaging over $\Delta latmag$.

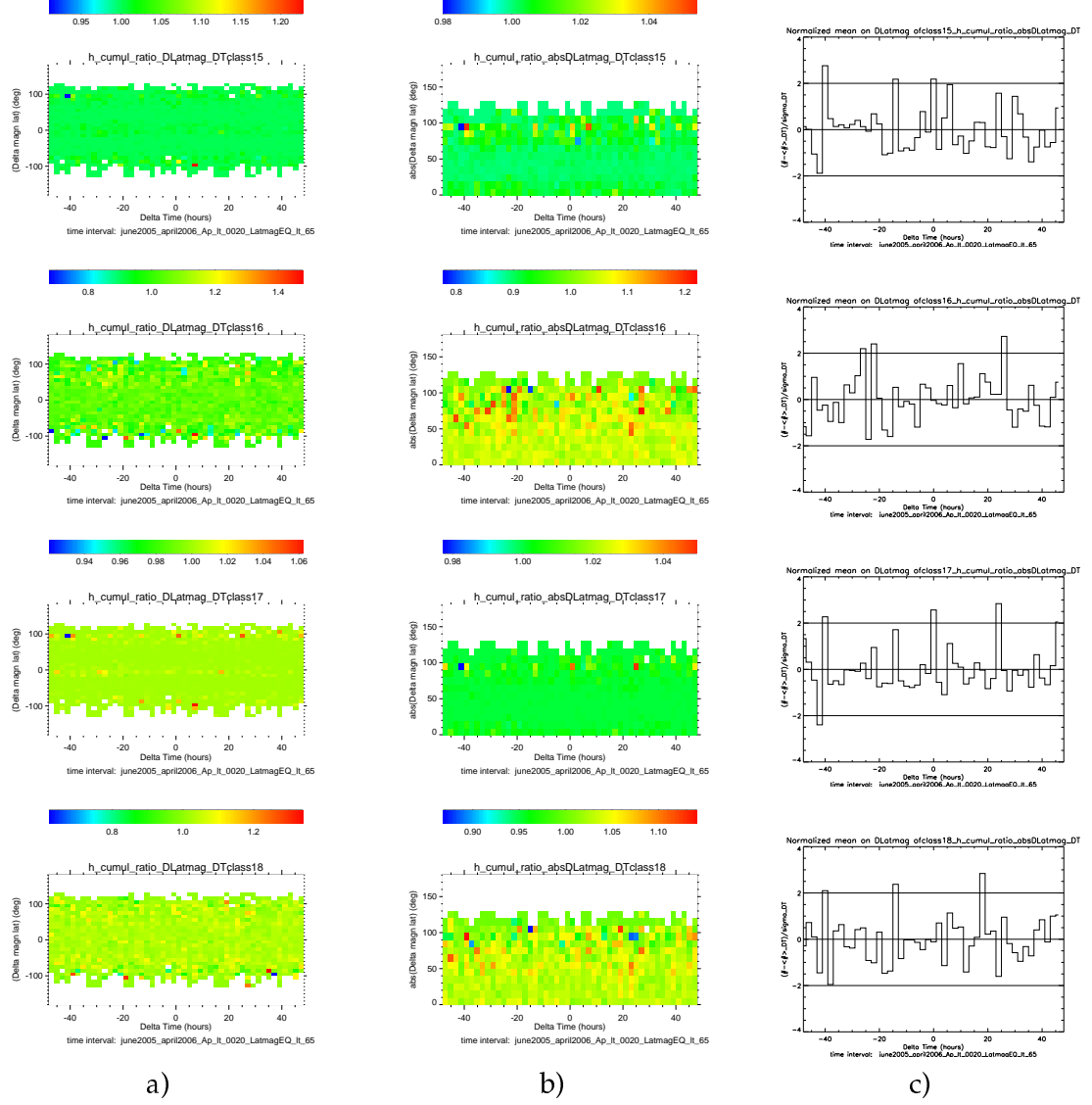


Figure 4.40: h_{cum_ratio} distributions from 2005/05/25 to 2006/04/30 for whistler dispersion classes from 15 to 18 a) $(\Delta latmag, \Delta t)$ b) $abs(\Delta latmag, \Delta t)$ and c) Δt after an averaging over $\Delta latmag$.

In order to try to improve the quality of the above-reported representations, it was also attempted another approach. I have calculated the mean value α of the Δw_σ and $hcum_{ratio}$ distributions over the diverse groups of dispersion classes. In particular, I have performed an averaging over low, medium, high and all whistler dispersion values, corresponding to 0-6, 7-12, 13-18 and 0-18 groups of dispersion classes. Then, I have calculated the quantity χ defined as follows:

$$\chi(\Delta latmag, \Delta t) = \frac{\alpha(\Delta latmag, \Delta t) - A}{\sigma} \quad (4.11)$$

where α is the above averaged value over group of classes (Δw_σ or $hcum_{ratio}$) in each cell ($\Delta latmag, \Delta t$) of figures 4.33 - 4.36, and A is the average of α for all $\Delta latmag$ and Δt values. Denominator of the same relation is the standard deviation of the latter α data values. I also have produced plots of Δw_σ and $hcum_{ratio}$ v.s. Δt by an averaging over groups of dispersion classes, $\Delta latmag$. An example of these types of maps and plots, is given in figure 4.41, where is shown the map of Δw_σ averaged over all the 19 whistler classes v.s. ($abs(\Delta latmag), \Delta t$) (figure 4.41 (a)) and the plot of Δw_σ v.s. Δt (figure 4.41(b)), always averaged over dispersion classes and $\Delta latmag$.

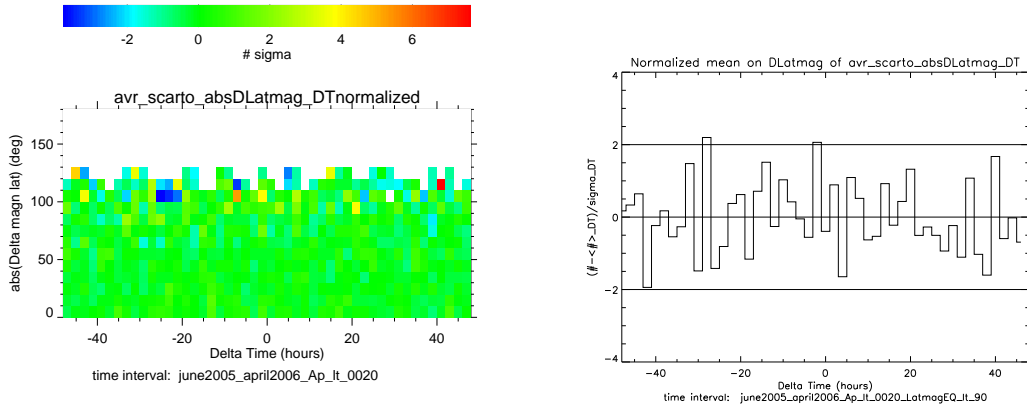


Figure 4.41: Δw_σ averaged over all whistler classes (1-19) (according to eq.(4.11)) v.s. $abs(\Delta latmag)$ and Δt (left panel) and v.s. Δt (after an averaging over $\Delta latmag$) (right panel). Time interval is from 2005/05/25 to 2006/04/30.

Unfortunately, results reported in figure 4.41, as well as the mean on low, medium and high whistler distribution classes, show that the average over groups of classes is not effective to improve the signal to noise ratio. In particular, no significant deviations are observed in coincidence with seismic occurrence (only oscillations within 2 standard deviation level are observed in plot of figure 4.41(right panel).

As discussed above, due to the Demeter and EQ geographic and Δt distribution, the statistical significance of regions at low and high ($\text{abs}(\Delta \text{latmag})$) values is strongly inhomogeneous. It is clearly shown in figure 4.42 where the distribution of WHIMAP observations selected for correlation with EQs is reported as a function of Δlatmag and Δt .

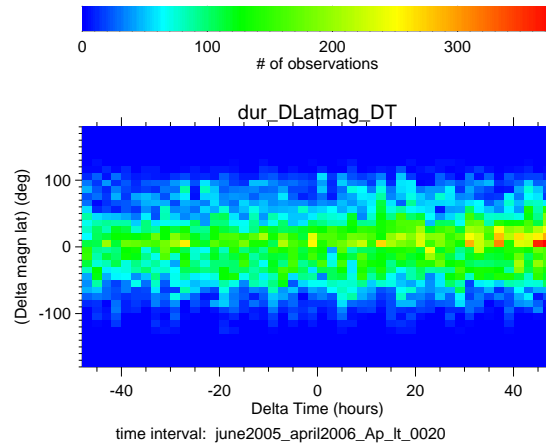


Figure 4.42: Distribution of Demeter whistler observations as a function Δlatmag and Δt , satisfying cuts applied to the whistler–EQ analysis.

Figure 4.42 shows that most of measurements are concentrated within a relative narrow zone of ± 30 degrees around the magnetic equator. Therefore all the analysis was repeated applying to EQs a magnetic latitudinal cut of ± 30 degrees. This will restrict the analysis to EQs near the magnetic field line. Aim of this cut is to construct maps of Δw_σ and $hcum_{ratio}$ v.s. ($\text{abs}(\Delta \text{latmag}), \Delta t$) in which data of each $\text{abs}(\Delta \text{latmag})$ bin have been collected in a more homogeneous geographic region. No significant improvement with respect to the results reported in figure 4.33 - 4.41 are observed.

4.10 Analysis of EQ-whistler correlation using normalized magnetic field line distance

In the previous paragraph we have seen the behavior of Δw_σ and $hcum_{ratio}$ v.s. Δt and $\Delta latmag$ (the magnetic latitudinal distance between EQ and Demeter observations). But the use of $\Delta latmag$ or $abs(\Delta latmag)$ could be not correct because the definition of $\Delta latmag$ is not independent from the hypothesis that the whistler propagation is correlated with the EQ field line. In other words we are assuming that the propagation of whistlers occurs from EQ to CP, roughly in the surface that include the EQ and its magnetic field line. But ducted whistler follow the magnetic field line instead non-ducted whistlers cross in this surface also if they do not propagate along the magnetic field line. In the case of a dipolar geomagnetic field this surface will be the magnetic meridian plane crossing the EQ epicenter. In the real geomagnetic field this surface is not a plane. Since the whistler propagation is governed by the geomagnetic field line, it is important to know not only the magnetic latitude distance between Demeter observation and EQ epicenter but also the EQ - Demeter magnetic latitude distance scaled by the magnetic latitude distance from EQ and CP. In others words we need to weight the $\Delta latmag$ by the $(latmag_{CP} - latmag_{EQ})$ distance. It means that instead of using the absolute magnetic latitude distance $abs(\Delta latmag)$ between the Demeter observation point and the EQ epicenter, we will introduce the relative magnetic distance $nml d$:

$$nml d = \frac{latmag_{Demeter} - latmag_{EQ}}{latmag_{CP} - latmag_{EQ}} \quad (4.12)$$

where, denominator indicates difference in latitude between CP and EQ. We note that it could be possible to weight the $\Delta latmag$ distance by the EQ-CP length magnetic field line projection:

$$nml d' = \frac{latmag_{Demeter} - latmag_{EQ}}{length(EQ - CP)_{fieldline}} \quad (4.13)$$

Since this new definition would be influenced by the shape of EQ-CP magnetic field line projection (including the effects of the longitudinal distortion of the non dipolar geomagnetic field line), I prefer to use definition 4.12. Plots analogous to those reported in figures (4.33) - (4.36) have been constructed, but substituting Δlat_{mag} with n_{mld} . Results for Δw_{σ} and $h_{cum_{ratio}}$ are reported in figures 4.43 - 4.54, for each one of the 0-18 whistler dispersion classes.

Considering that local time can significantly influence the whistler occurrence, I have produced maps for daytime, nighttime and day+night times. In this new plots, n_{mld} values close to 0 indicate whistlers collected close to the EQs. On the contrary, for n_{mld} values close to 1, all whistlers data are collected close to CPs, independently from the EQ geomagnetic latitude and from the length of EQ appropriate field line.

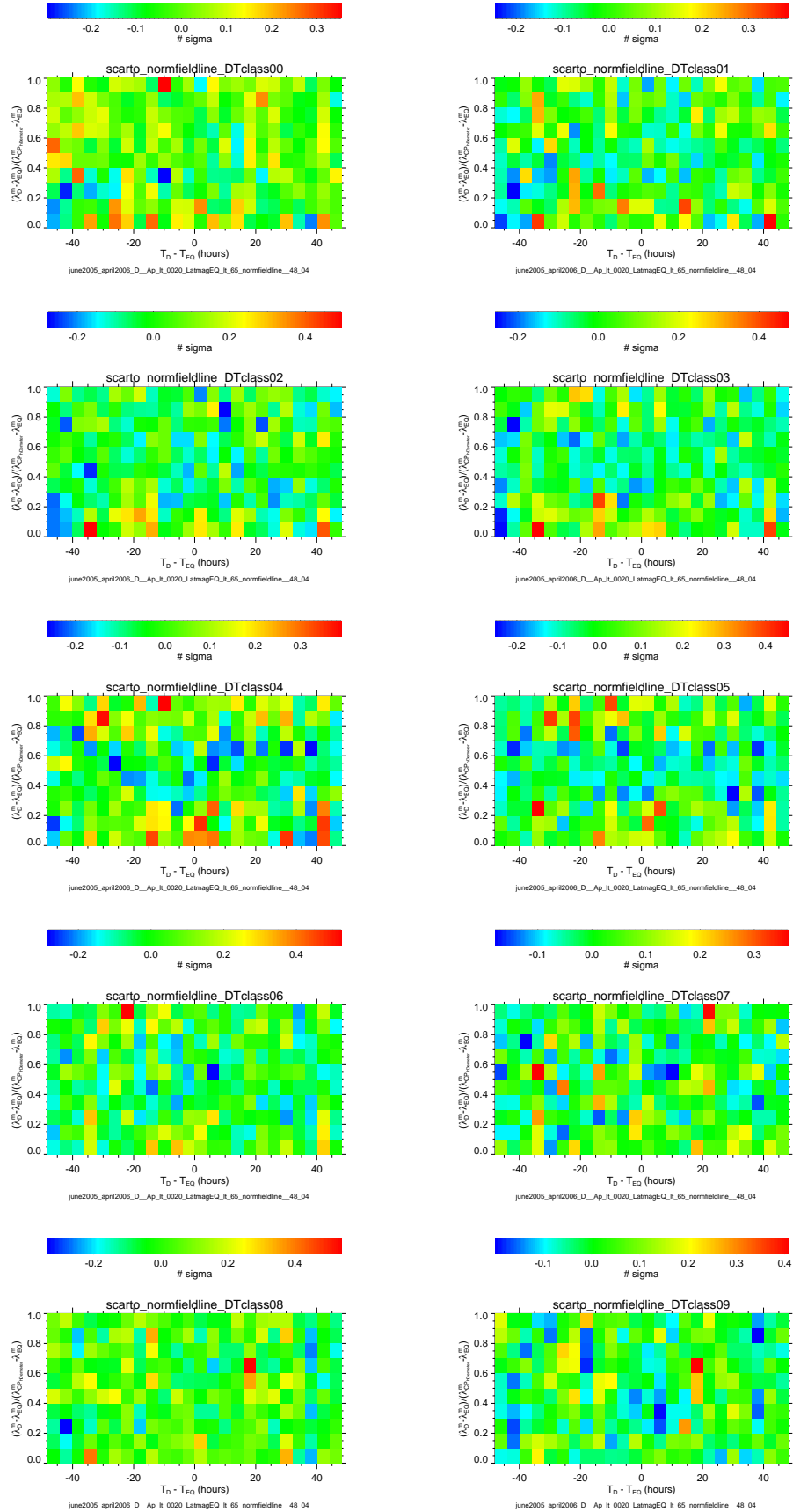


Figure 4.43: Δw_σ v.s nml_d and Δt for whistler dispersion classes from 00 to 09 during Daytime

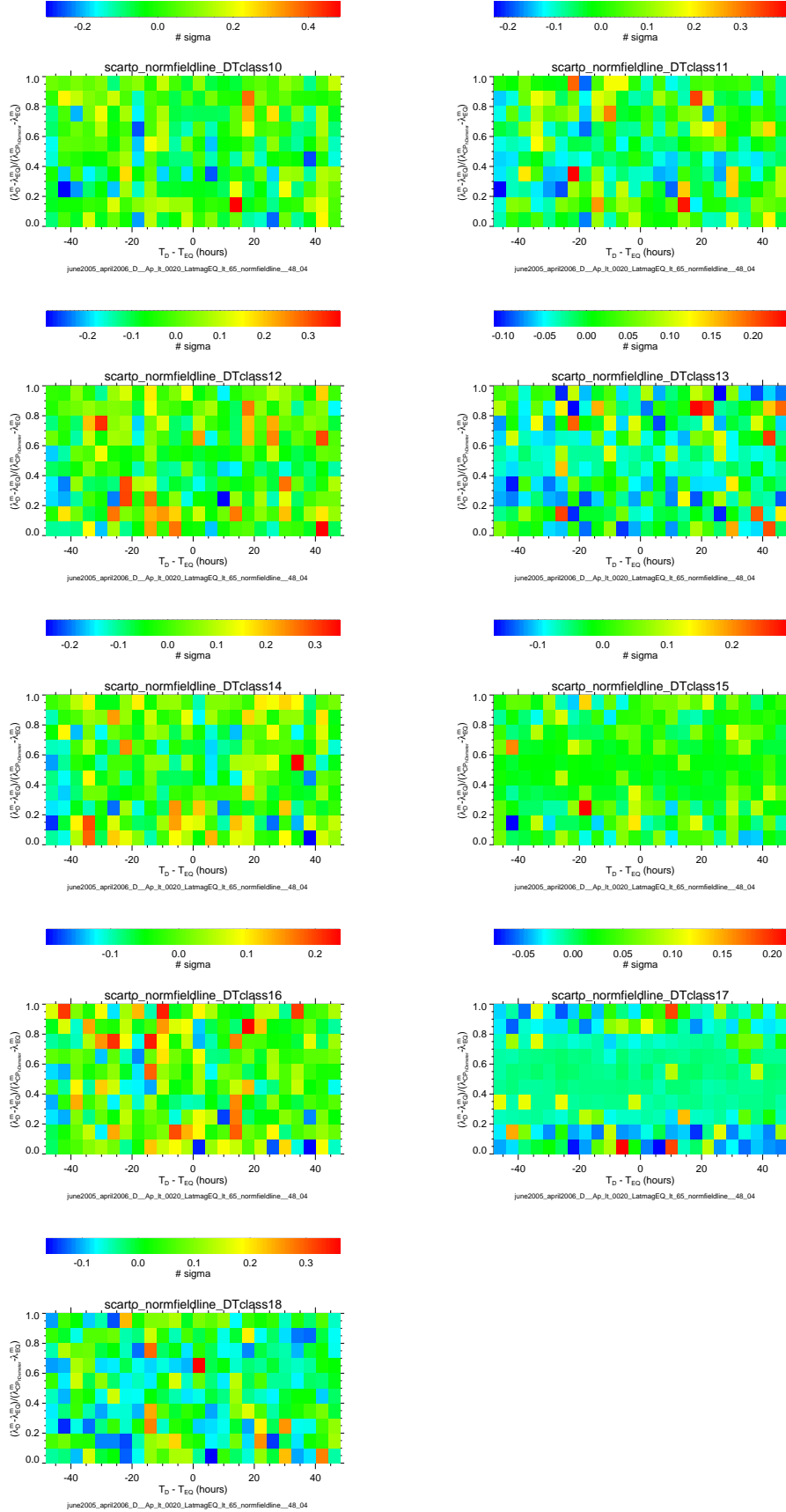


Figure 4.44: $\Delta w_{\sigma} nml d$ and Δt for whistler dispersion classes from 10 to 18 during Daytime.

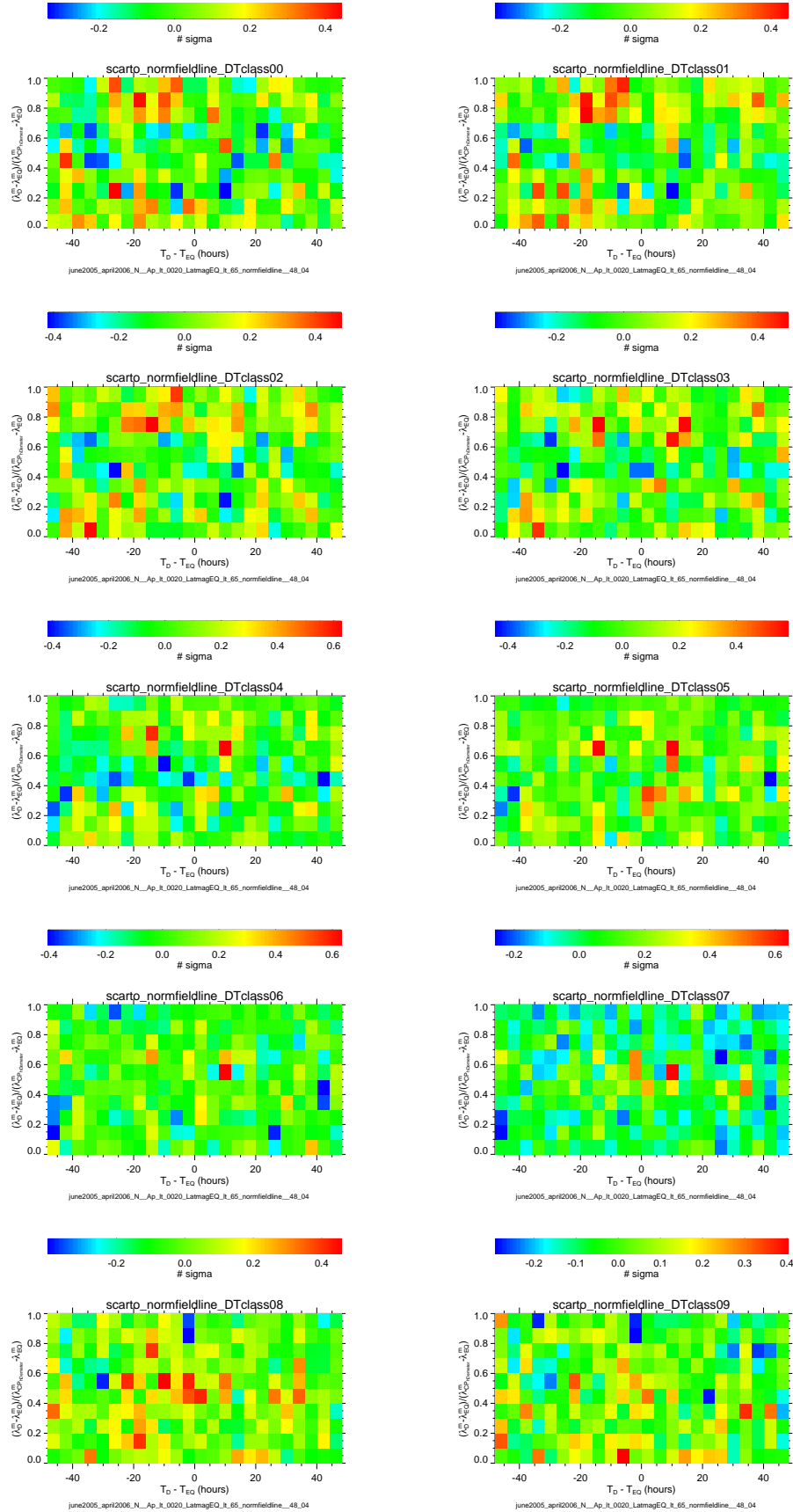


Figure 4.45: Δw_σ *nml*d and Δt for whistler dispersion classes from 00 to 09 during Nighttime.

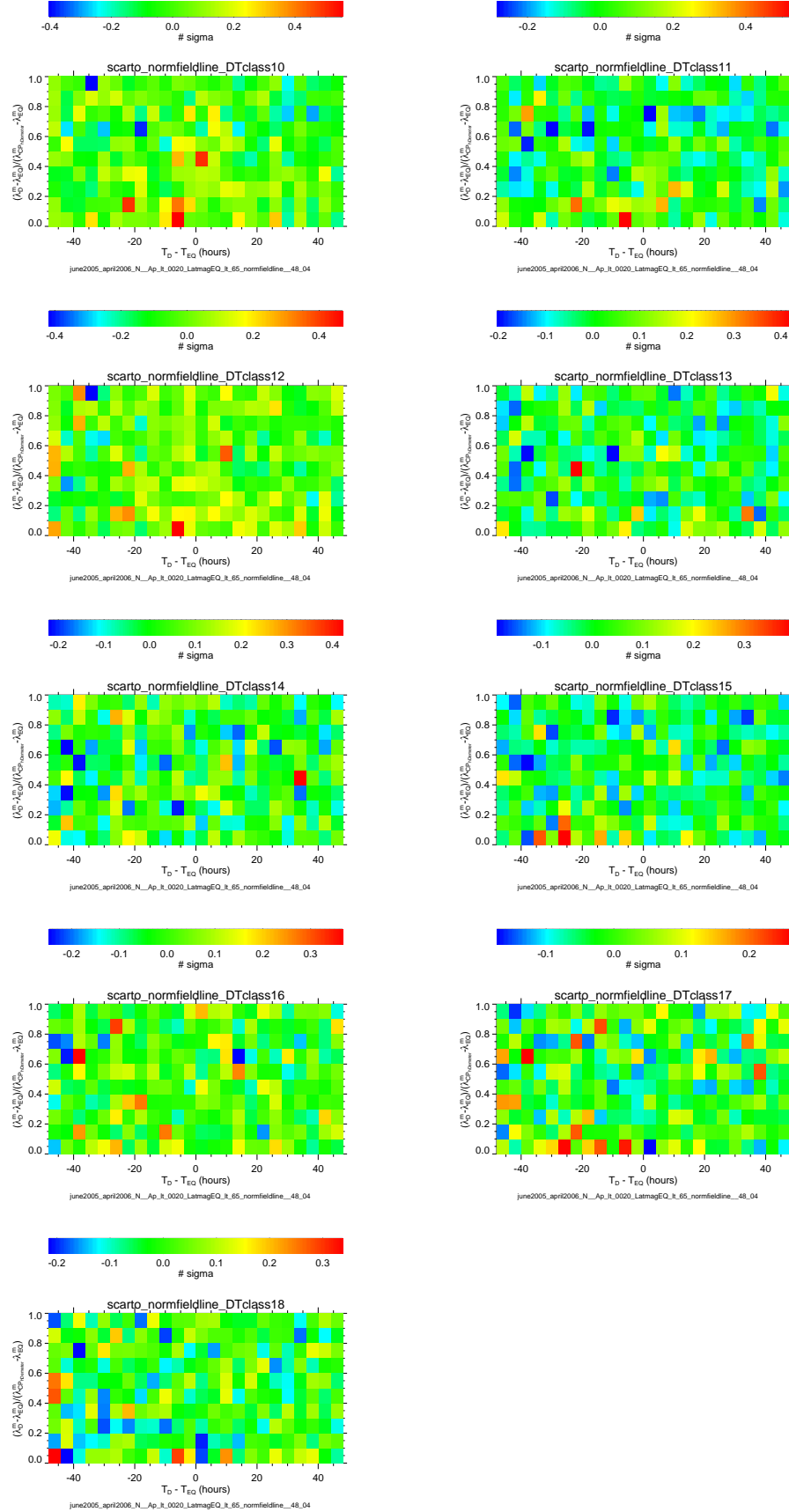


Figure 4.46: $\Delta w_{\sigma} nml d$ and Δt for whistler dispersion classes from 10 to 18 during Nighttime.

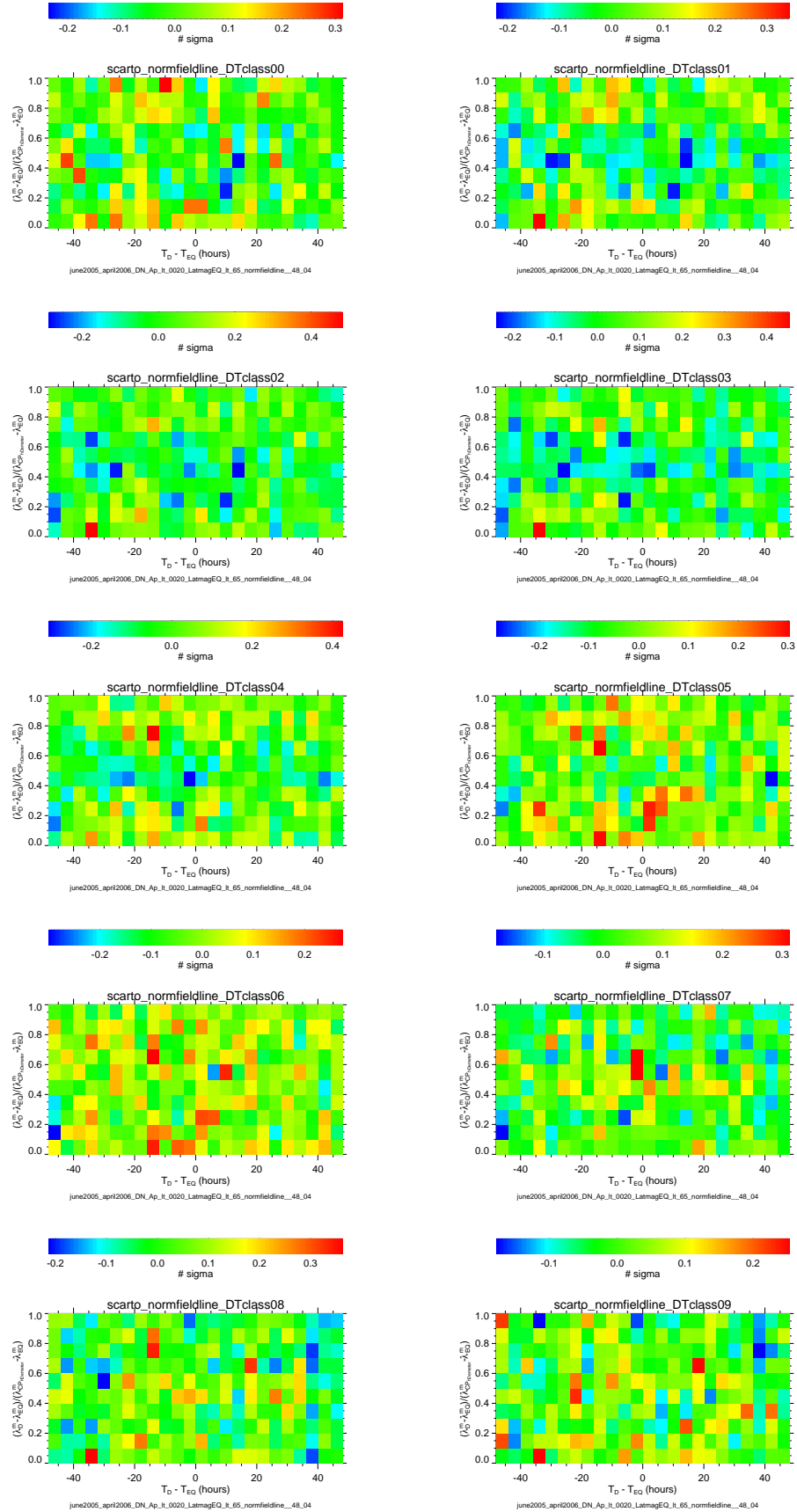


Figure 4.47: Δw_{σ} nml and Δt for whistler dispersion classes from 00 to 09 during Night-time+Daytime.

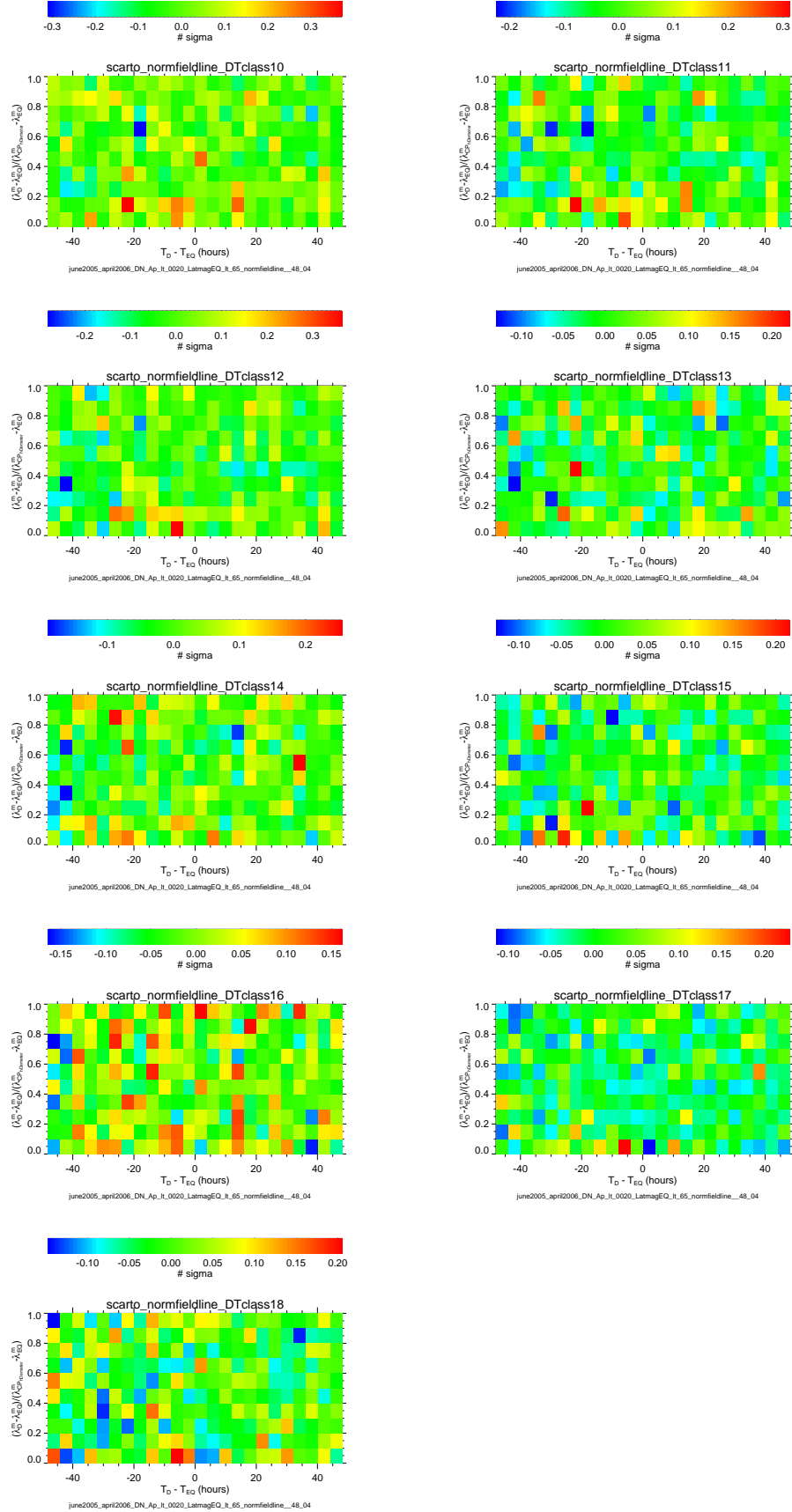


Figure 4.48: Δw_{σ} nml and Δt for whistler dispersion classes from 10 to 18 during Night-time+Daytime.

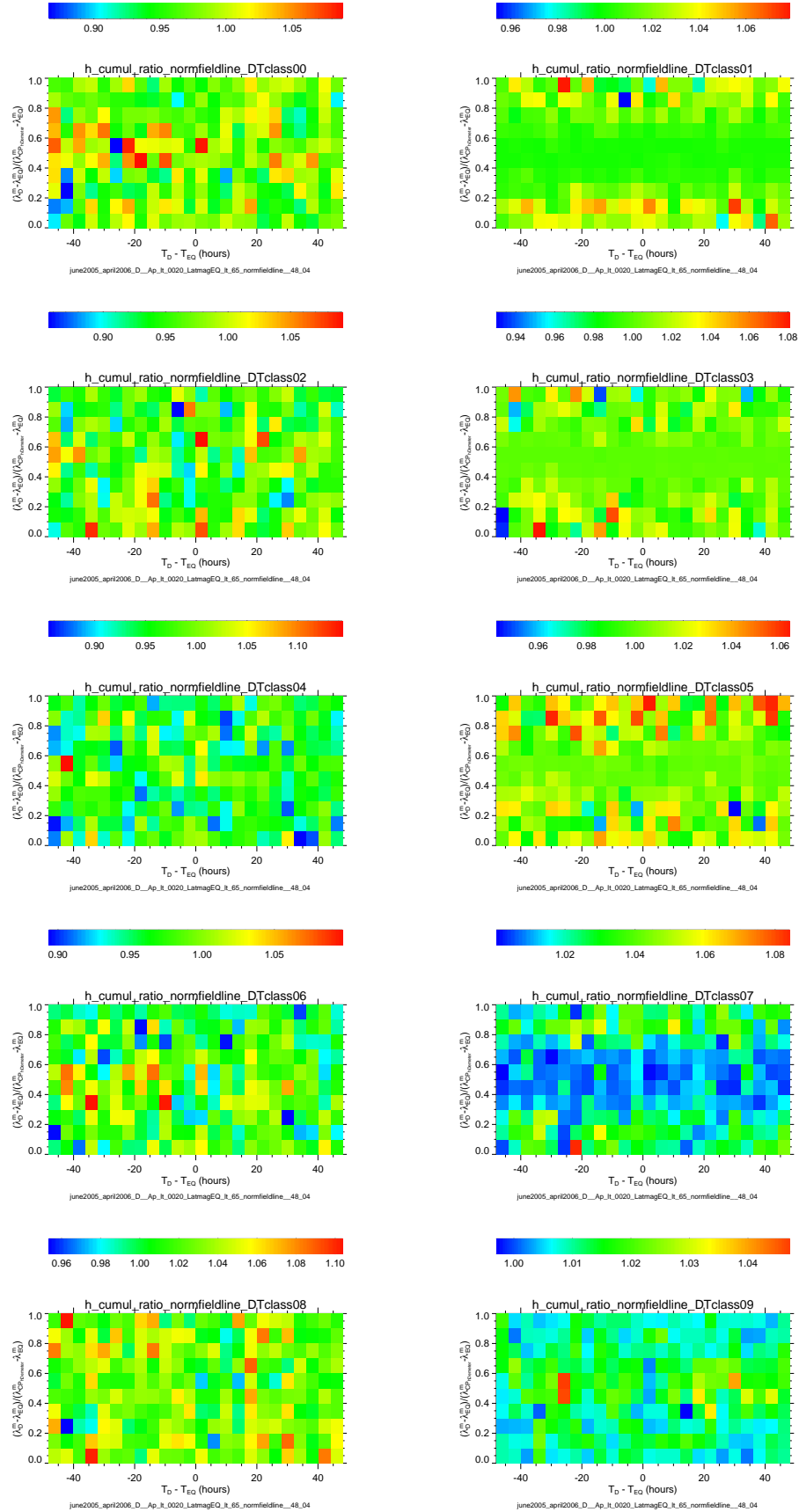


Figure 4.49: h_{cum_ratio} v.s $nmld$ and Δt for whistler dispersion classes from 00 to 09 during Daytime .

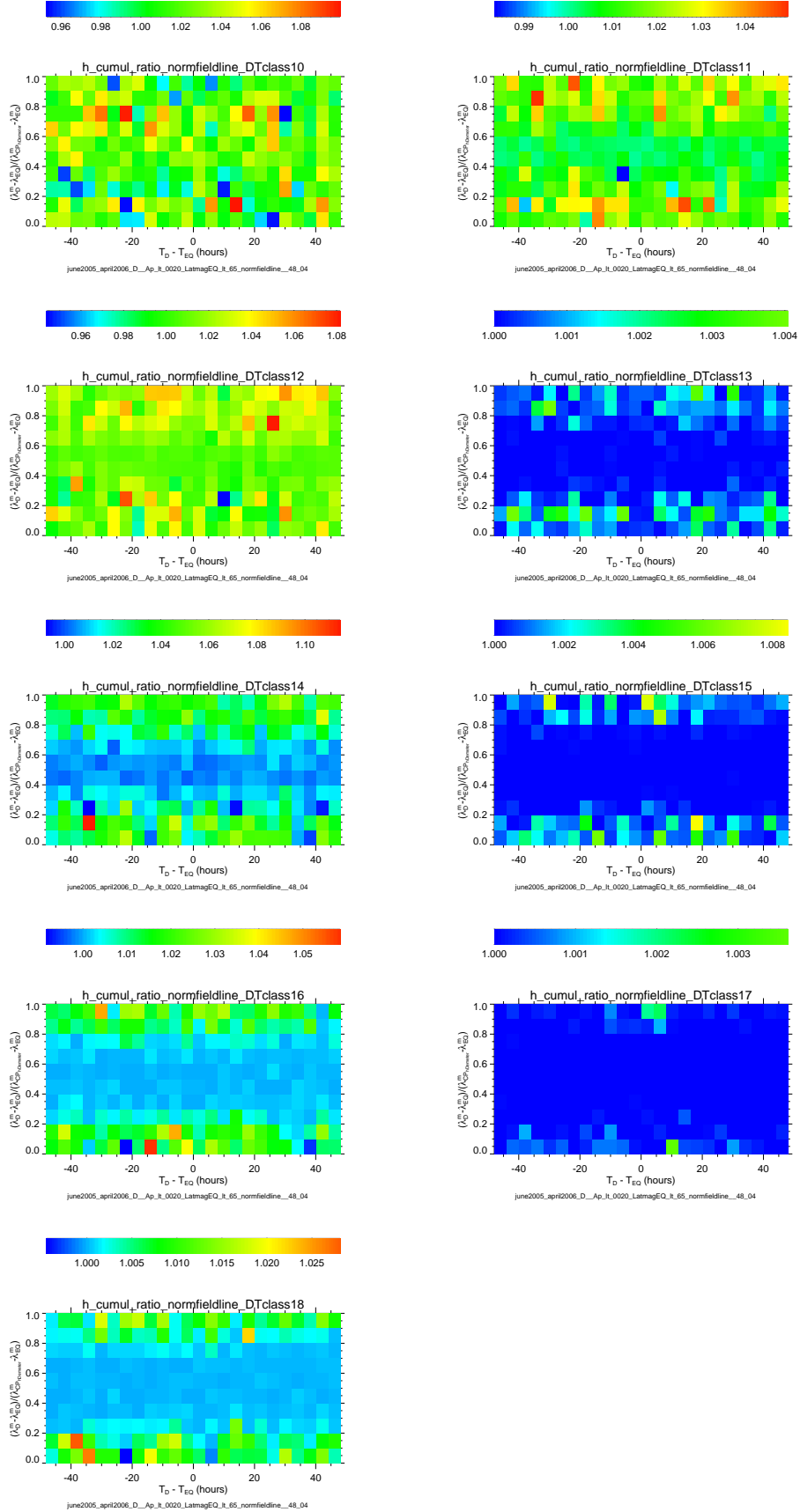


Figure 4.50: h_{cum_ratio} v.s $nmld$ and Δt for whistler dispersion classes from 10 to 18 during Daytime.

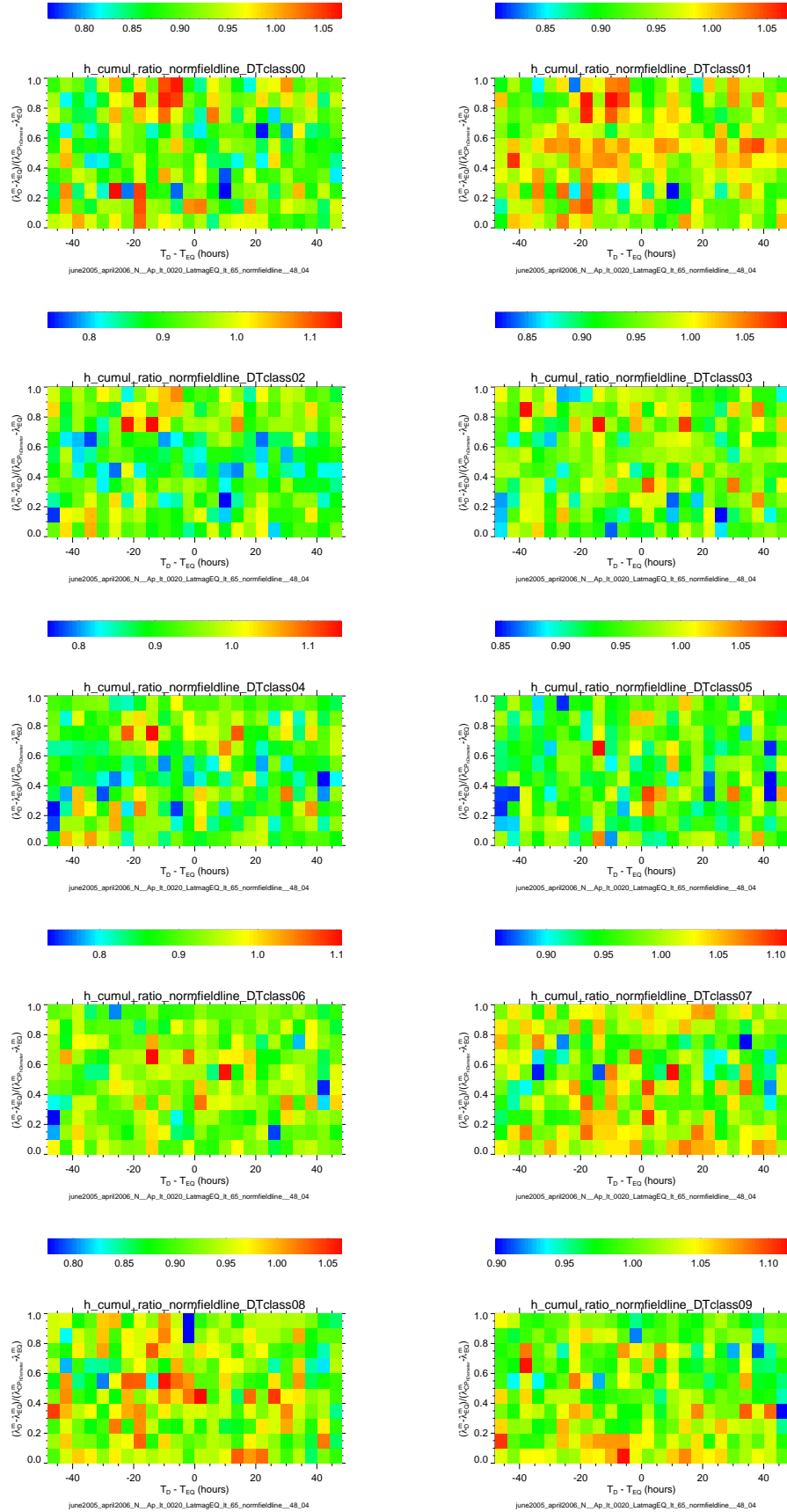


Figure 4.51: h_{cum_ratio} v.s. n_{mld} and Δt for whistler dispersion classes from 00 to 09 during Nighttime.

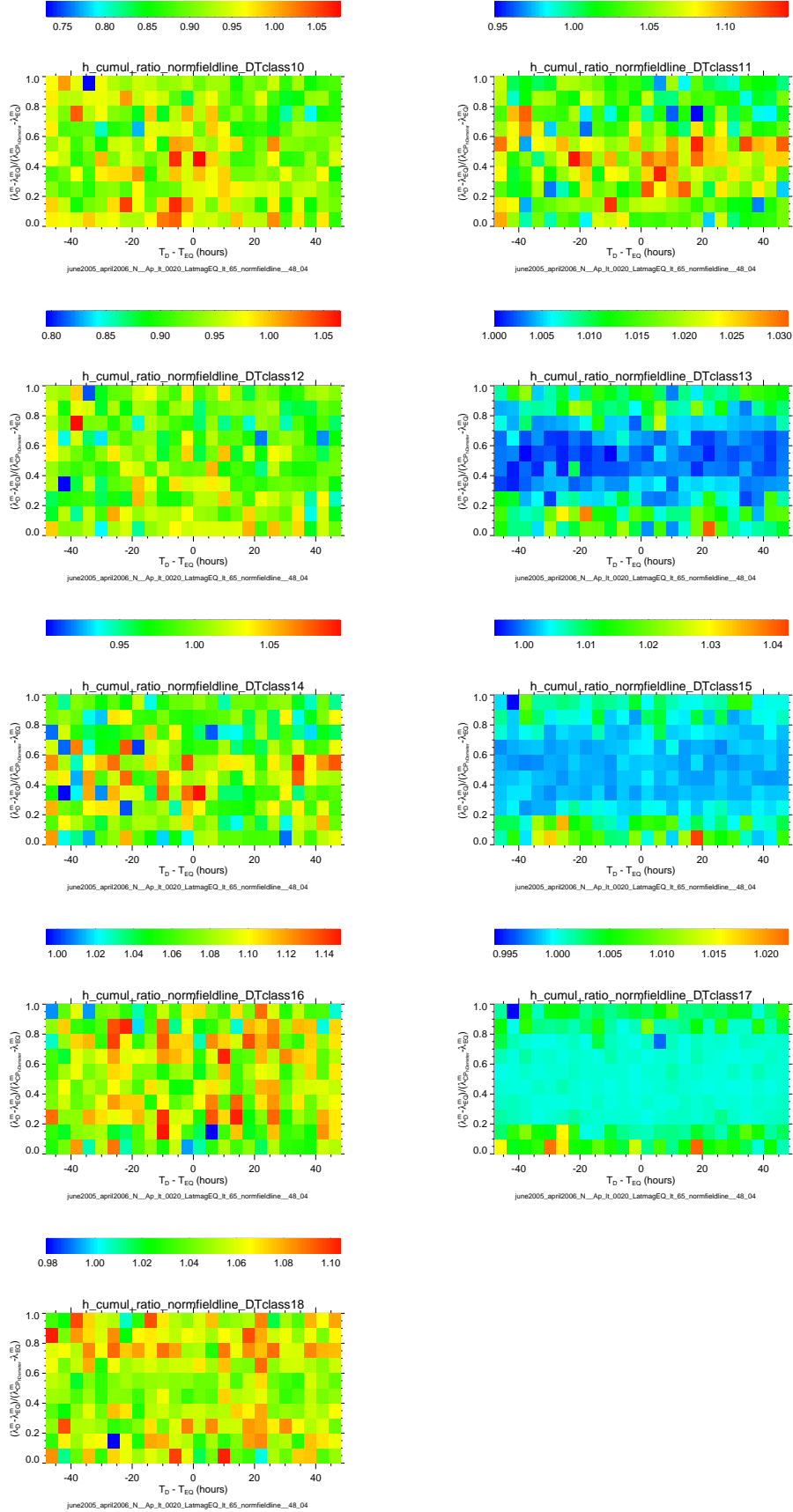


Figure 4.52: h_{cum_ratio} v.s. n_{mld} and Δt for whistler dispersion classes from 10 to 18 during Nighttime..

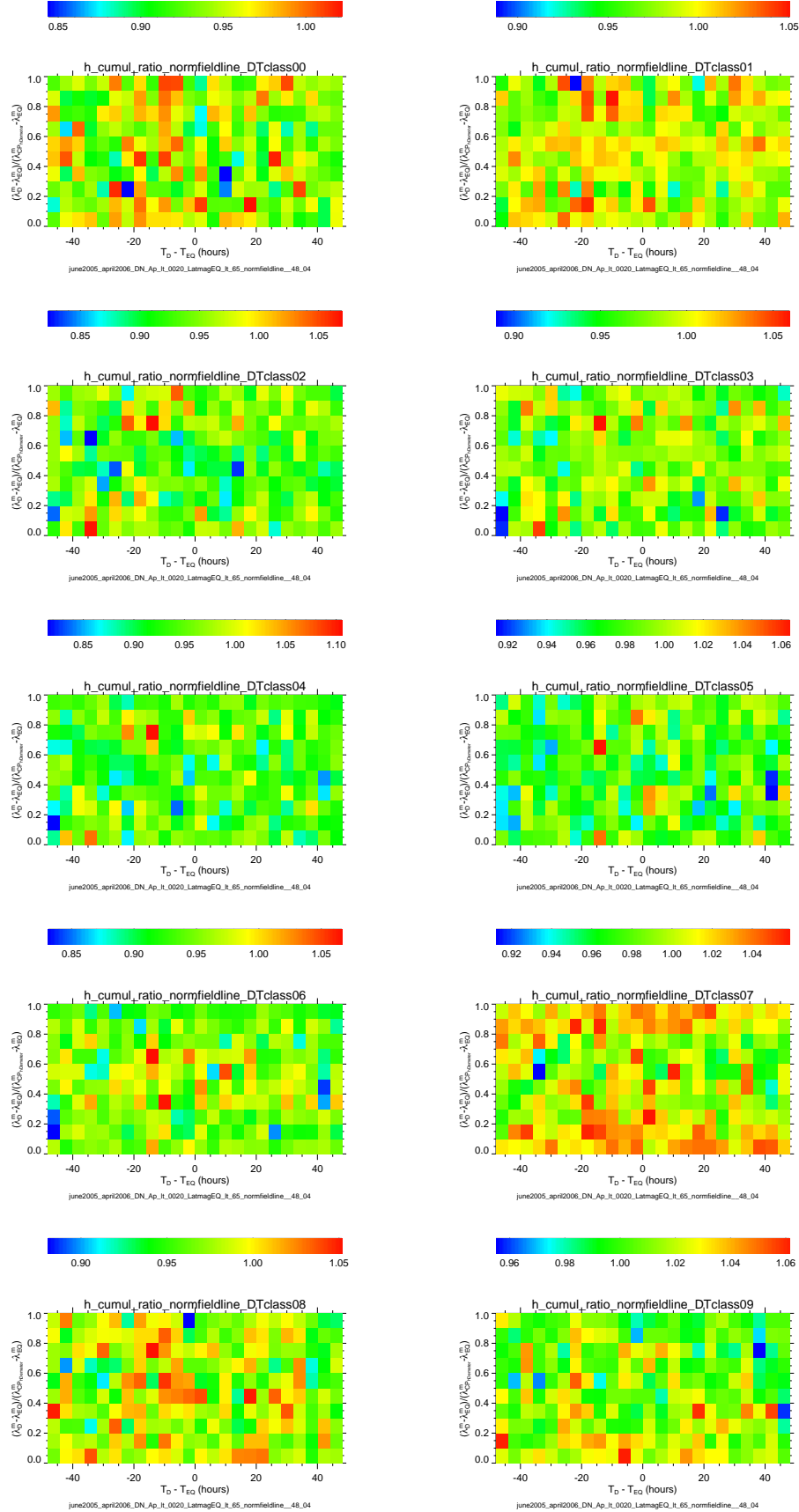


Figure 4.53: h_{cum_ratio} v.s. n_{mld} and Δt for whistler dispersion classes from 00 to 09 during Nighttime+Daytime.

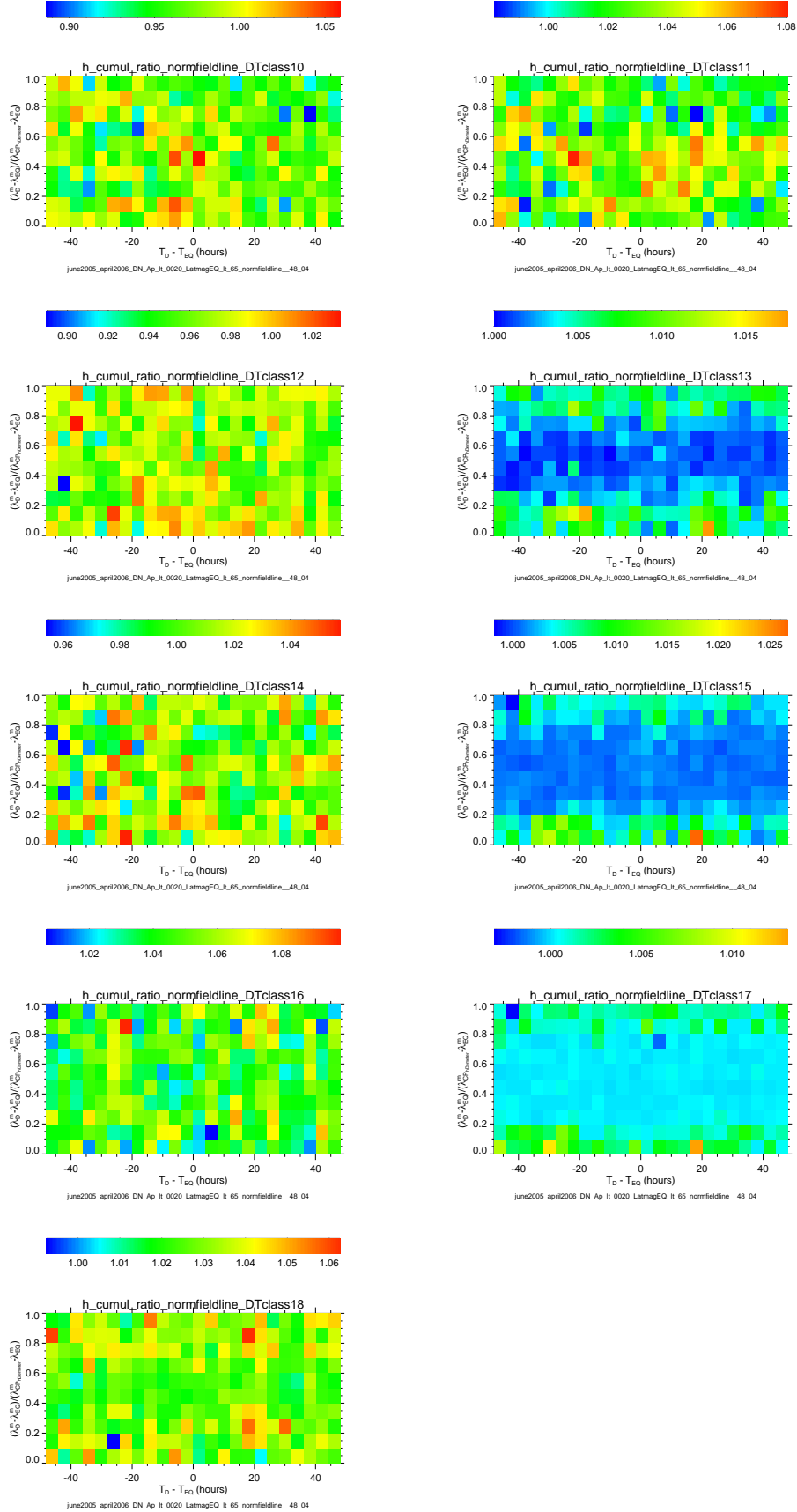


Figure 4.54: h_{cum_ratio} for v.s n_{mld} and Δt for whistler dispersion classes from 10 to 18 during Nighttime+Daytime.

What is observed in figures 4.43 - 4.54 is that:

- $hcum_{ratio}$ versus $nmld$ and Δt for the highest whistler dispersion classes during daytime, exhibit a band of anomalous values for $nmld=0$ and $nmld=1$ (figure 4.49).
- In particular this effect is evident for daytime maps related to data of classes 13-18 (figure 4.50).
- These two bands are independent from the Δt values,
- The same bands of anomalous signals, close to $nmld=0$ and $nmld=1$, are less evident in Nighttime $hcum_{ratio}$ maps (figures 4.51 and 4.52).
- In Nighttimes the bands are evident clear only for dispersion classes 13, 15 and 17.
- The existence of two bands survive when data for daytime and nighttime are averaged together but only for classes 13, 15 and 17 (figures 4.53 and 4.54).
- In general for daytime, nighttime and daytime+nighttime a systematic difference appears between maps related to odd and even classes, but this is due to artifact artifact. This is a know effect due to a problem regarding the algorithm used during the postprocessing of the RNF data³.

The two bands of anomalous signals close to $nmld=0$ and $nmld=1$ can also be seen in the Δw_σ daytime maps (figures 4.43- 4.44) for classes 13, 15, and 17, but with a very low signal to noise ratio. Δw_σ maps of nighttime and daytime+nighttime do not show any anomalous signals.

The existence of the two bands close to the EQ and CP regions could indicate that seismic activity influences the whistler propagation mainly for highest whistler dispersion coefficient values. On the contrary, no dependence is observed versus Δt , indicating that any possible anomalous signal associated with EQs can not be catalogued as pre-seismic, co-seismic, or post-seismic one, but only associated with a time window around a seismic event as a whole.

³J.L. Pinçon Personal Communication

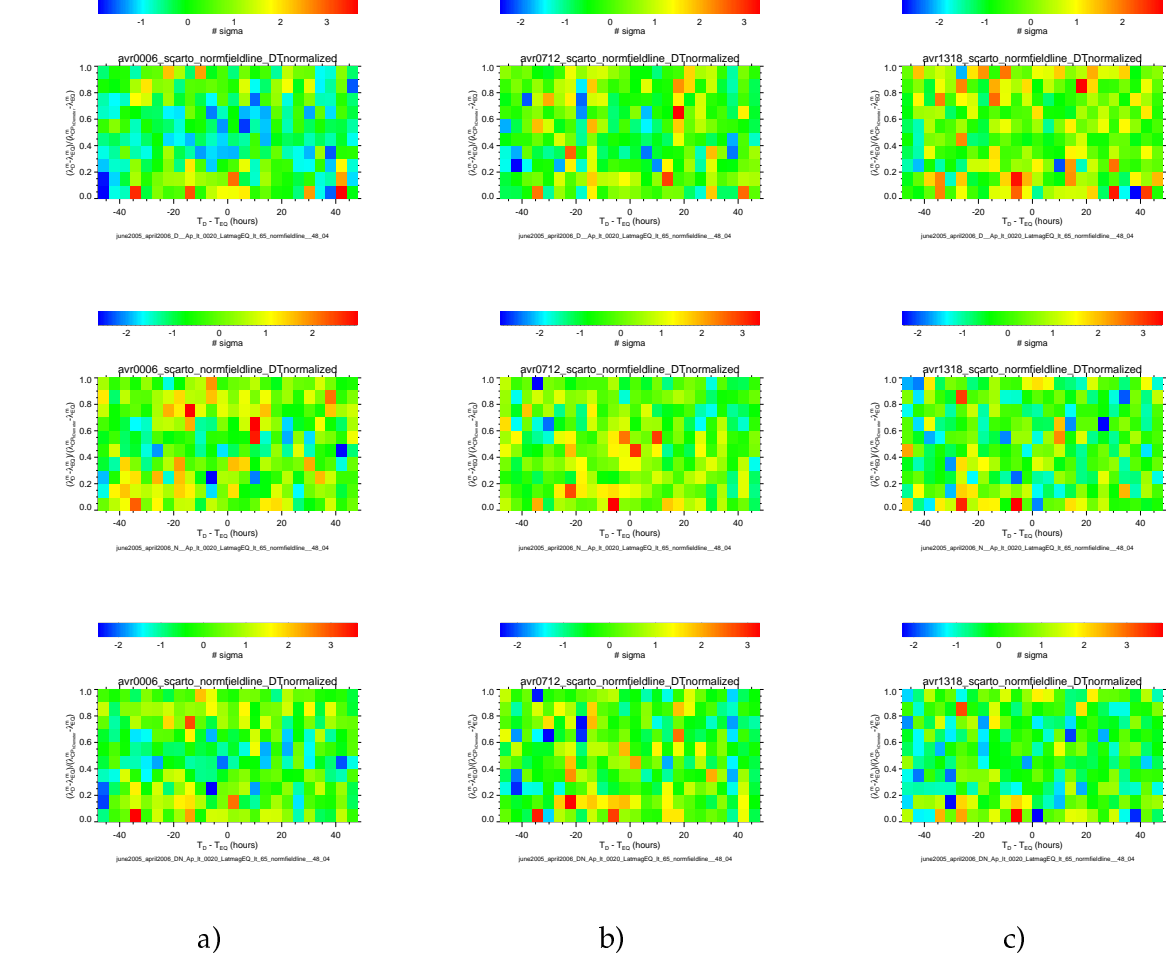


Figure 4.55: Δw_{σ} v.s $nml d$ and Δt averaged over dispersion classes from 00 to 06 a), from 07 to 12 b), from 13 to 18 c) during Daytime (top), Nighttime(center), Nighttime+Daytime (bottom).

Taking into account that $h cum_{ratio}$ for classes of whistlers with high D values show a better signal-to-noise ratio, the analysis has been repeated by gathering whistlers data into three different classes, as follows: low D (0-6), medium D (7-12), or high D (13-18) classes, respectively. Plots for Δw_{σ} and $h cum_{ratio}$ averaged over classes in these three intervals are reported in figures 4.55 and 4.56. Plots of $h cum_{ratio}$ for classes (13-18) show two high density bands during daytime.

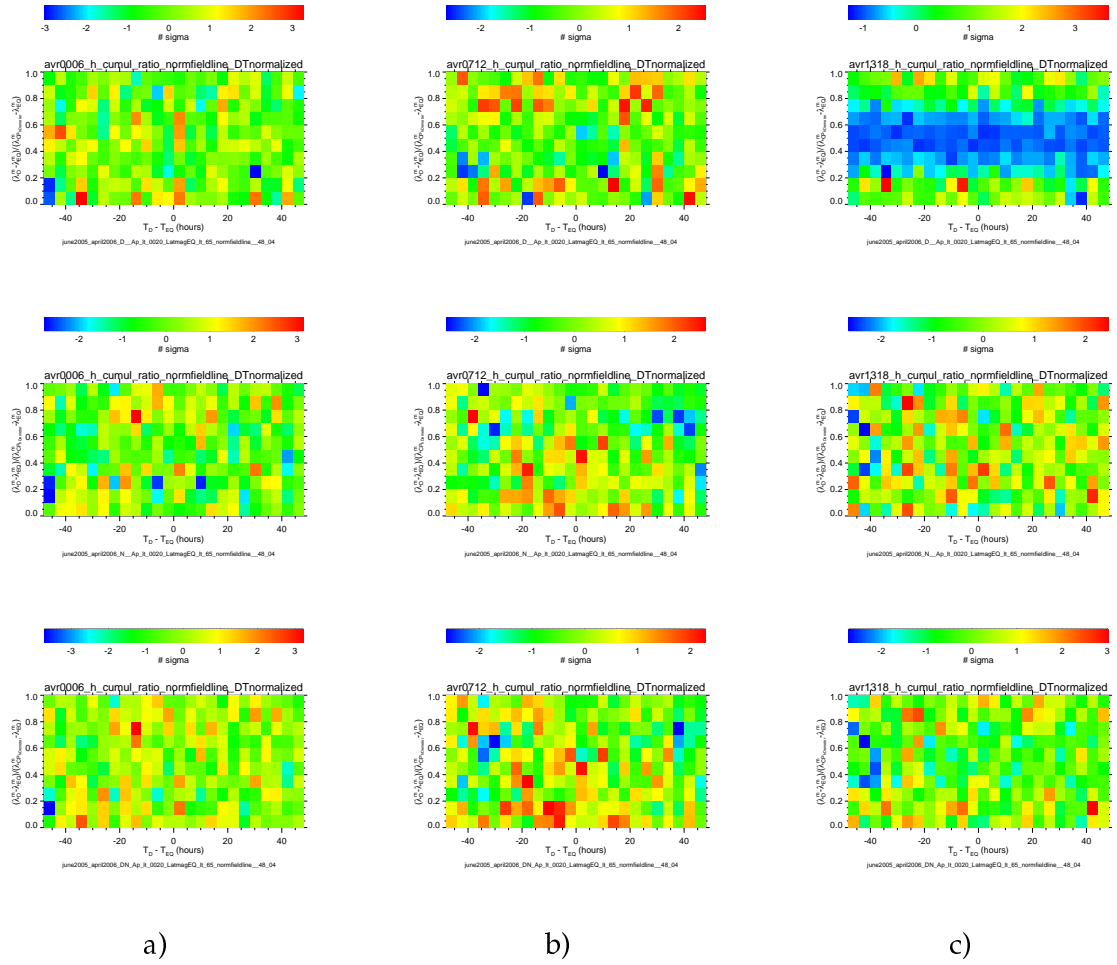


Figure 4.56: $hcum_{ratio}$ v.s nml d and Δt averaged over dispersion classes from 00 to 06 a), from 07 to 12 b), from 13 to 18 c) during Daytime (top), Nighttime(center), Nighttime+Daytime (bottom).

Apparently artifact of the effect of the dependence of the Δw_σ and $hcum_{ratio}$ from odd and even class index mask the existence of the two bands in the maps related to even classes. Maps of Δw_σ and $hcum_{ratio}$ (always for day, night and day+night) averaged on several groups of odd and even classes are shown in figures (4.57)- (4.60). Averaging only over the 13, 15 and 17 dispersion classes the two bands in the maps of $hcum_{ratio}$ are clearly very improved for both day, night and day + night data, whereas for the averaged value over classes 14-16-18 the band appear only in daytime.

Considering that:

- Δw_σ maps are more noisy than the $hcum_{ratio}$ ones
- the two bands of anomalous signals appear for highest classes

we can consider that the existence of the two bands of anomalous signals in the $hcum_{ratio}$ maps is in agreement with the Hayakawa *et al.*, [1993] result concerning the existence of anomalous increment of whistler of high dispersion value in coincidence with earthquake occurrence.

Also if this study is very preliminary the existence of two bands could indicate the existence of a fluctuation of the number of whistler with high D value induced by seismic activity near the EQ epicenter and its CP.

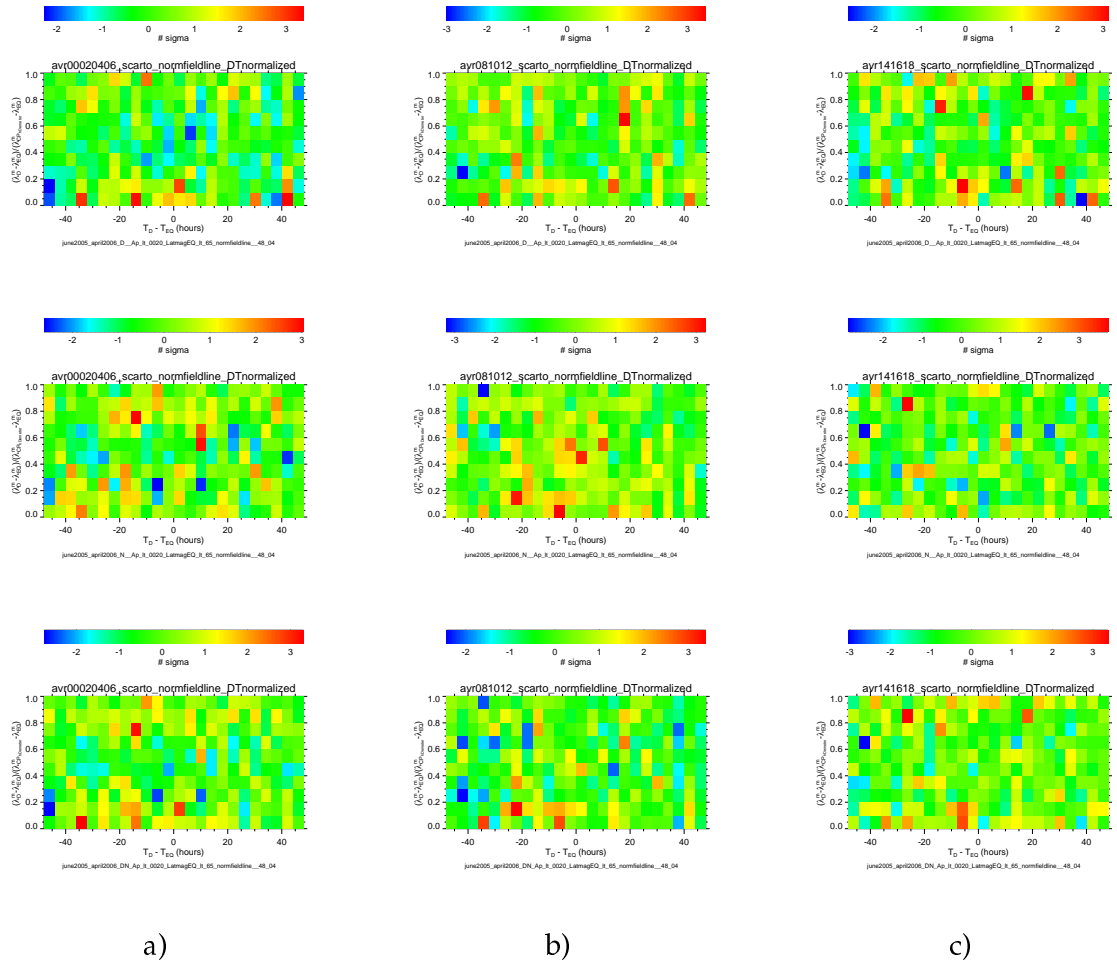


Figure 4.57: Δw_σ v.s $nml d$ and Δt averaged over dispersion classes from classes 00+02+04+06 a), 08+10+12 b), 14+16+18 c) during Daytime (top), Nighttime(center), Nighttime+Daytime(bottom).

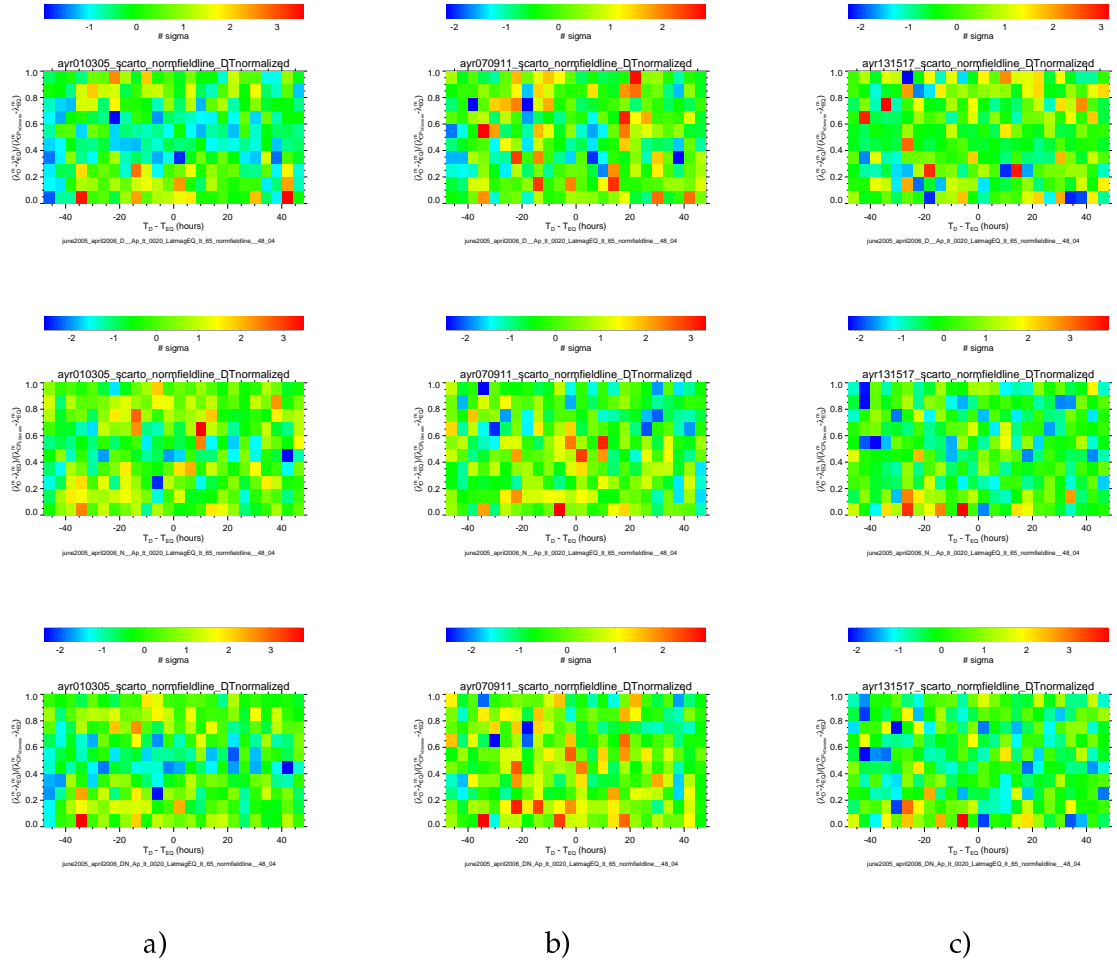


Figure 4.58: Δw_σ v.s $nml\Delta t$ averaged over dispersion classes from classes 01+03+05 a), 07+09+11 b), 13+15+17 c) during Daytime (top), Nighttime(center), Night-time+Daytime(bottom).

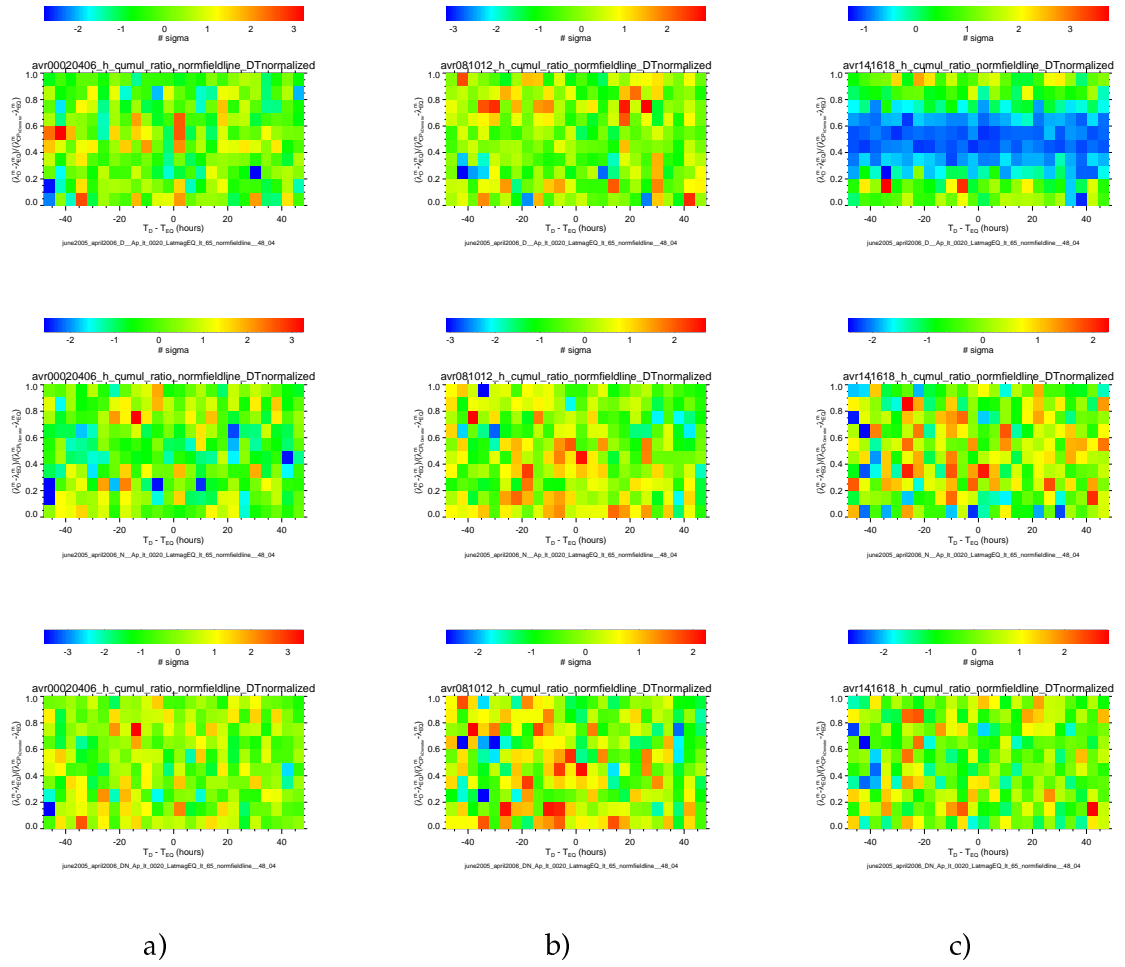


Figure 4.59: h_{cum_ratio} v.s n_{mld} and Δt averaged over dispersion classes from classes 00+02+04+06 a), 08+10+12 b), 14+16+18 c) during Daytime (top), Nighttime(center), Nighttime+Daytime(bottom).

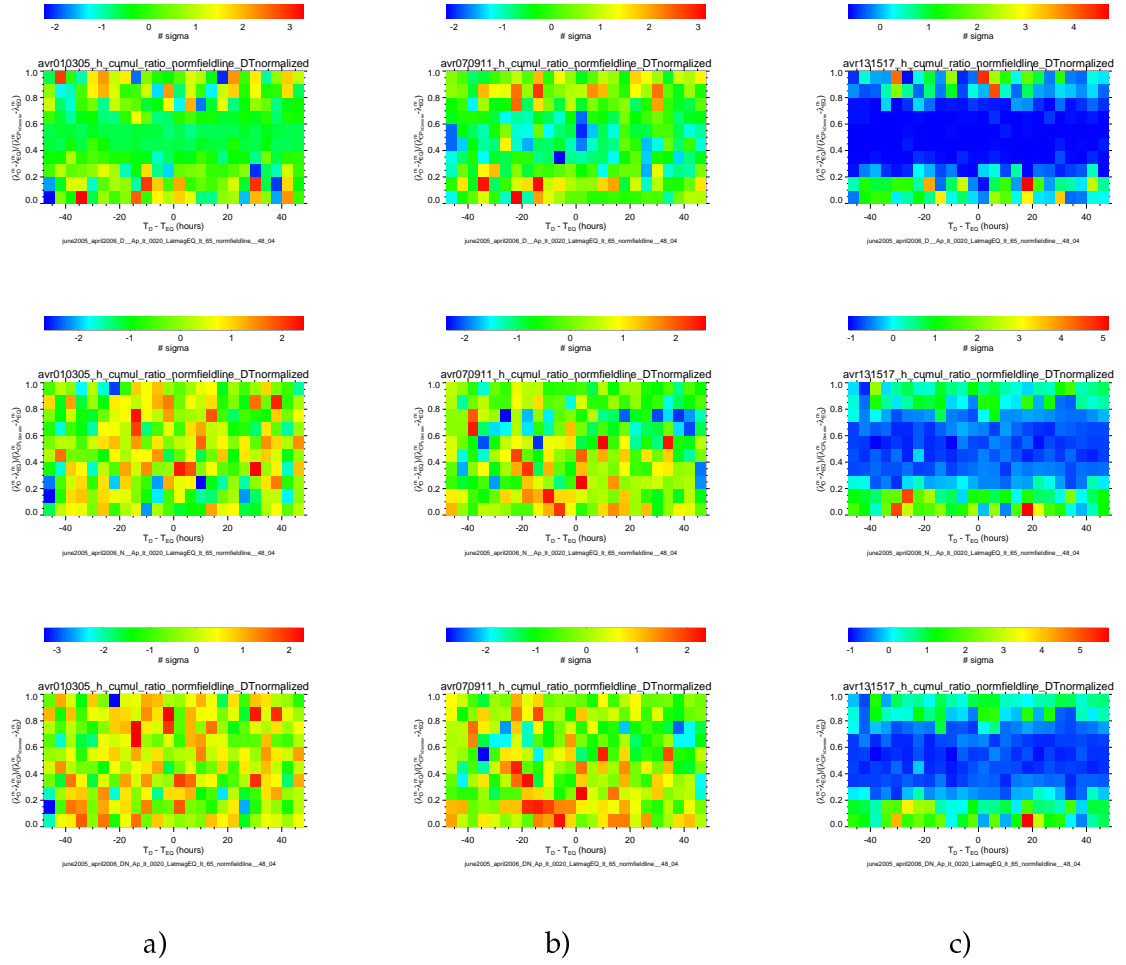


Figure 4.60: h_{cum_ratio} v.s n_{mld} and Δt averaged over dispersion classes from classes 01+03+05 a), 07+09+11 b), 13+15+17 c) during Daytime (top), Nighttime(center), Nighttime+Daytime(bottom).

Chapter 5

Testing temporal correlations between earthquakes and IDP anomalous particle bursts

Some recent studies (Sgrigna et al. (2005)) have pointed out that satellite observations of electron and proton anomalous count rates statistically precede of several hours earthquakes of medium-strong magnitude. It has been supposed that pre-seismic electromagnetic emissions could perturb trapped particles in the inner Van Allen radiation belts inducing particle bursts precipitation which may be detected by satellites. Within the framework of this model, in the second part of the thesis we have tried to apply the Sgrigna et al. (2005) procedure to analyze the existence of a possible correlation between DEMETER IDP particle data and seismic events. In this chapter will be discussed a few preliminary step in this direction: the analysis is still in progress and will be continued even after this thesis work.

5.1 Seismo induced particle precipitation

Several works has been published concerning flux disturbances of Van-Allen trapped particles detected by satellite and statistically correlated with EQs. Fluxes of high energy electrons and protons, detected near the South Atlantic Anomaly (SAA) have

shown a significant increase in coincidence of some seismic events (Sgrigna et al. (2005)). Analysis of particles precipitation suggests that it could be induced by the interaction of electromagnetic disturbances, generated during the preparation phase of an earthquake, with high-energy particles trapped in the inner radiation belt. This interaction could change the particle pitch angle and consequently to cause particles precipitation. The latter may be detected by particle telescopes on board of satellites. Lifetime of these particle fluxes is determined by the rate of particle loss during their interaction with residual atmosphere of the Earth. The particle longitudinal drift allows the observation of particle precipitation in regions not necessarily located over hypocenter areas. As shown in Sgrigna et al., (2005) particle precipitation demonstrated to occur several hours ($\Delta T \sim 4 \div 5$) before moderate or strong earthquakes these phenomena can be classified as “short-term seismic precursors”.

Aim of this analysis is to verify if the statistical time correlation occurs also using the IDP particle data. To carry out the analysis I subdivided the study into the following main steps: construction of the PARMAP database with IDP observations, definition of the “particle bursts” (PBs) events and identification of possible PB into PARMAP database; rejection of PBs whose origin can be reconciled with magnetospheric disturbances of non seismic origin; selection of an EQ population from the USGS catalogue; search of a temporal correlation between selected PBs and EQs.

5.2 IDP-PARMAP database

In this thesis the IDP data collected during burst mode and survey mode have been merged and telemetry information interpolated to build the common particle PARMAP database with sampling rate of 0,25 Hz. The PARMAP database includes information only on the 128 IDP energy channels homogenous between survey and burst mode. Geomagnetic activity is one of the main source of particle precipitation and generates a large background with respect to a possible precipitation induced by seismo-electromagnetic effects. Therefore in the PARMAP database the Ap and DST indexes¹

¹Ap and DST index values have been selected by NOAA through the web addresses <ftp://ftp.ngdc.noaa.gov/STP/GEOMAGNETIC-DATA/INDICES/DST/>, and <http://swdcwww.kugi.kyoto-u.ac.jp/cgi-bin/kp> respectively.

have been included to select IDP data collected in geomagnetically quiet conditions. The details of PARMAP database format are reported in table (5.1),

IDP-detector	Implanted Si, $S = 490 \text{ mm}^2$ ($\Phi = 25\text{mm}$)
External shielding	2 mm Al
Mass	525 g
Power	895 mW
Energy range	0.07-2.4 MeV
Energy resolution	256 channels
Maximum geometrical factor	$1.2 \text{ cm}^2 \text{ ster}$

Table 5.1: IDP characteristics

Figure (5.2) shows the geographic distribution of the DEMETER data acquisition mode. Blue areas correspond to regions of burst acquisition mode, red zones indicates areas of survey acquisition mode. Burst locations could be changed during the mission.

Because IDP does not measure the true particles pitch angle, PARMAP pitch angle is defined as the angle between IDP detector axis and geomagnetic field. the geographic distribution of IDP pitch angle is reported in figure 5.3(a).

The IDP orientation strongly influences the analysis. Since IDP is mainly orthogonal to the magnetic field lines, data collected by this detector are mainly constituted by trapped particles, that are not easy to precipitate and this is a negative factor for the study. Observations are carried out in the narrow range from $\sim 55^\circ$ up to $\sim 120^\circ$ (figure 5.3)(b)). I like to stress that the good temporal correlation between earthquakes and particle burst was obtained by Sgrigna et al., (2005) using the SAMPEX-PET data with pitch angle α_{PET} in the $\sim 20^\circ \div \sim 160^\circ$ range (ORR pointing mode). Moreover in Sgrigna et al., (2005) the statistical significance of the temporal EQs-PBs correlation was improved when anomalous particle burst detected at $70^\circ < \alpha_{PET} < 110^\circ$ was excluded from the study and the analysis was restricted to PBs close to loss cone, excluding trapped particles. In our case, IDP orientation does not allow to carry out a similar analysis.

In figure 5.4 are shown the geographic distribution (a) and the histogram (b) of the DEMETER L-shell values. We can observe that the main part of the observations are carried out at low L-shell values.

IDP_<halforbit>_<start_date>_<end_date>.DAT					
<ul style="list-style-type: none"> - <halforbit>: orbit number as "nnnnns"; - <start_date>: date of the first data sample as "yyyymmdd_hhmnss"; - <end_date>: date of the last data sample as "yyyymmdd_hhmnss". 					
Field number	Type	Array dim.	Size (bytes)	Unit	Description
1	I*2	7	14		UT time of the first point of the data array as: year, month, day, hour, minute, second, millisecond (year as 20xx)
2	R*8	1	8	s	Number of seconds since 01/01/1970 00:00:00
3	I*2	1	2		Orbit number
4	I*2	1	2		Sub-orbit number
5	I*1	1	1		Version (edition number) of the processing software: from 0 to 9
6	I*1	1	1		Sub-version (revision number) of the processing software: from 0 to 9
7	I*2	1	2		Mode 1 : Burst 2 : Survey
8	R*4	1	4	degree	Geocentric latitude (-90°, +90°)
9	R*4	1	4	degree	Geocentric longitude (0°, 360°)
10	R*4	1	4	km	Altitude
11	R*4	1	4	hour	Local time (0, 24h)
12	R*4	1	4	degree	Geomagnetic latitude (-90°, +90°)
13	R*4	1	4	degree	Geomagnetic longitude (0°, +360°)
14	R*4	1	4	hour	Magnetic local time
15	R*4	1	4	degree	Invariant latitude (-90°, +90°)
16	R*4	1	4		Mc Ilwain parameter L (0, 999)
17	R*4	3	12	nT	Components of the magnetic field model at the satellite point (geographic coordinate system)
18	R*4	1	4	nT	Modulus of the magnetic field model
19	R*4	1	4	Hz	Proton gyrofrequency at satellite point
20	R*4	128	512	elec/cm ² /s/ster/keV	Data array of the spectrum
21	R*4	1	4	elec/cm ² /s/ster/keV	Total of the data array of the spectrum
22	R*4	1	4	degree	Pitch angle (from 0 to 180°)
23	R*4	1	4	nT	Dst index
24	R*4	1	4	nT	Ap index
Total			614		

Figure 5.1: PARMAP database.

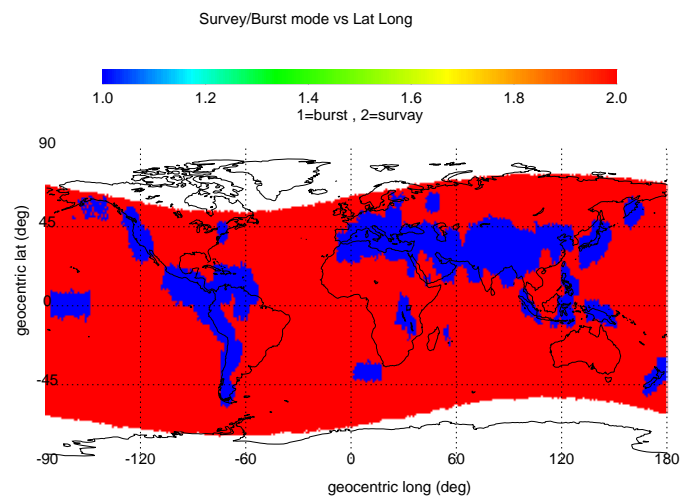


Figure 5.2: Geographic distribution of the survey (red) and burst (blue).

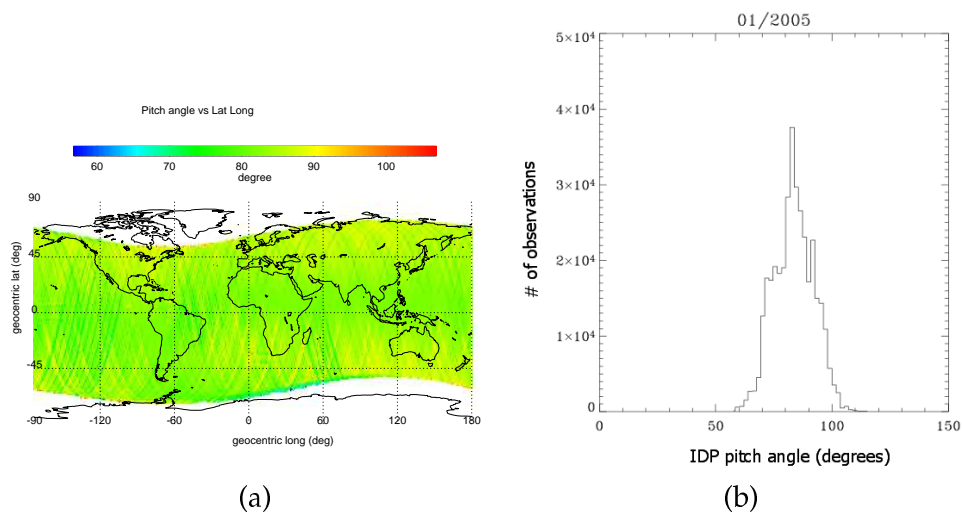


Figure 5.3: Geographic distribution (a) and histogram (b) of the IDP pitch angle during January 2005. Observations are centered near 90° with a narrow range from $\sim 55^\circ$ up to $\sim 120^\circ$.

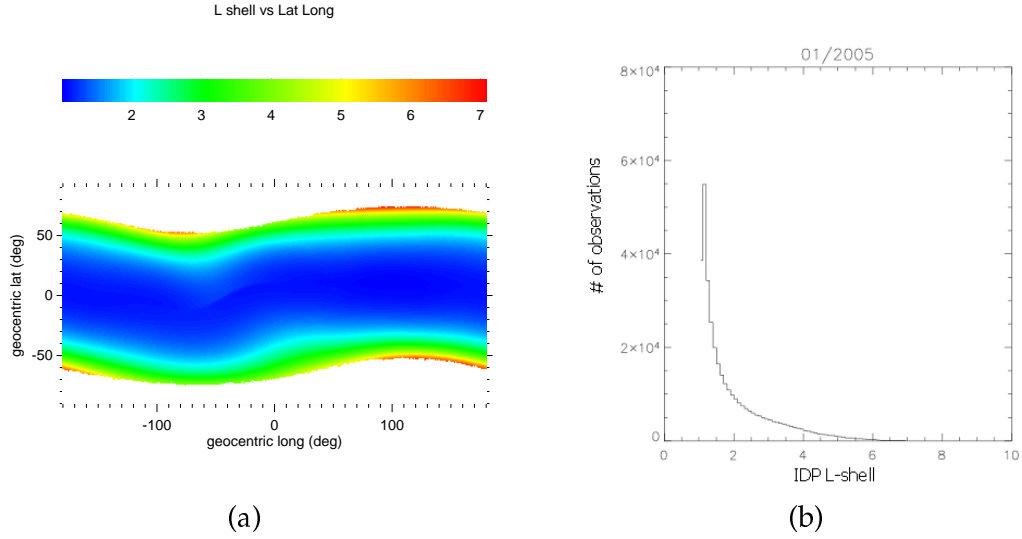


Figure 5.4: Geographic distribution (a) and histogram (b) of DEMETER L-shell values in 1 month of observations (January 2005).

Distributions of the IDP particle fluxes for 16 of the 128 PARMAP energy channels v.s. α_{IDP} pitch angle and L-shell are shown in figures 5.5-5.6. As an example data collected in 1 month of observations are reported in the figure. Energy channel increases from top left panel to bottom right. We can observe that:

- precipitation is higher for low energy channels due to the higher number of counting-ratesCRs detected at these energies.
- particle precipitation is huge at high L-shell values, due to magnetosphere dynamics, and is strongly reduced at low L-shell values.
- particle precipitation at low L-shell values is observed only at lowest and highest values of the IDP pitch angle range. This phenomena is independent from the energy value. Due to the IDP orientation (orthogonal to the magnetic field line), detected particles are mainly trapped. Therefore, number of IDP observations in the pitch angle loss cone is strongly reduced and for low L-shell values, precipitation is restricted to lowest and highest values of the IDP pitch angle range (red points).
- the coverage at high L-shell value is reduced due to the DEMETER altitude and

inclination parameters.

- there are some characteristic "structures" in the maps. These "curves" of higher number of observation are function of (α_{IDP}) and L-shell. This characteristic seems to be independent from the energy channels and is probably due to the representation vs. α_{IDP} and L-shell variables. The effect is under study and must be better understood.

In figures 5.7- 5.8 are shown geographic distributions of IDP-PARMAP particle fluxes for 16 of the 128 PARMAP energy channels. As an example, data collected from July to December 2004 are reported. Energy channel increases from the top left panel to bottom right one. The area of the SAA region is larger for lower energy channels and is reduced for higher energy channels. Due to low statistics, subauroral belts are clearly visible only for lowest energy channels. In the top left panel, corresponding to data with $E \sim 72.90$ keV, are clearly visible two regions, close to Chile and to Cape of Good Hope, where the particle fluxes are unexpectedly higher than those of the nearest homogenous areas. As discussed in the following, I believe that this increase be due to the burst mode acquisition that is active in these two regions in particular period of time.

In figure 5.9 (a) is reported the geographic distribution of the IDP total flux . All 128 PARMAP energy channels have been added.

From the figure one can recognize the SAA region and the subauroral belts where the particle flux is particularly high. Moreover, several regions with unexpected high particle fluxes can be seen over the Mediterranean sea, the Hawaii islands, the Himalaya region, the far east zone, etc.. These anomalous data are under study, but I suppose that it is an effect of the higher rate in the data acquisition (burst mode). In figure 5.9 (b) I have superimposed the geographic distribution of the IDP total flux with the contour plot of the regions where IDP data have been collected in burst mode.

Disregarding a little spurious shift on the right (due to graphical reasons) of the whole burst mode contour plot, it is evident that the unexpected IDP high fluxes observed in some regions corresponds to the zones where the burst mode is operative. Moreover, comparing fluxes of the low (0-42), medium (43-85) and high (86-127) IDP

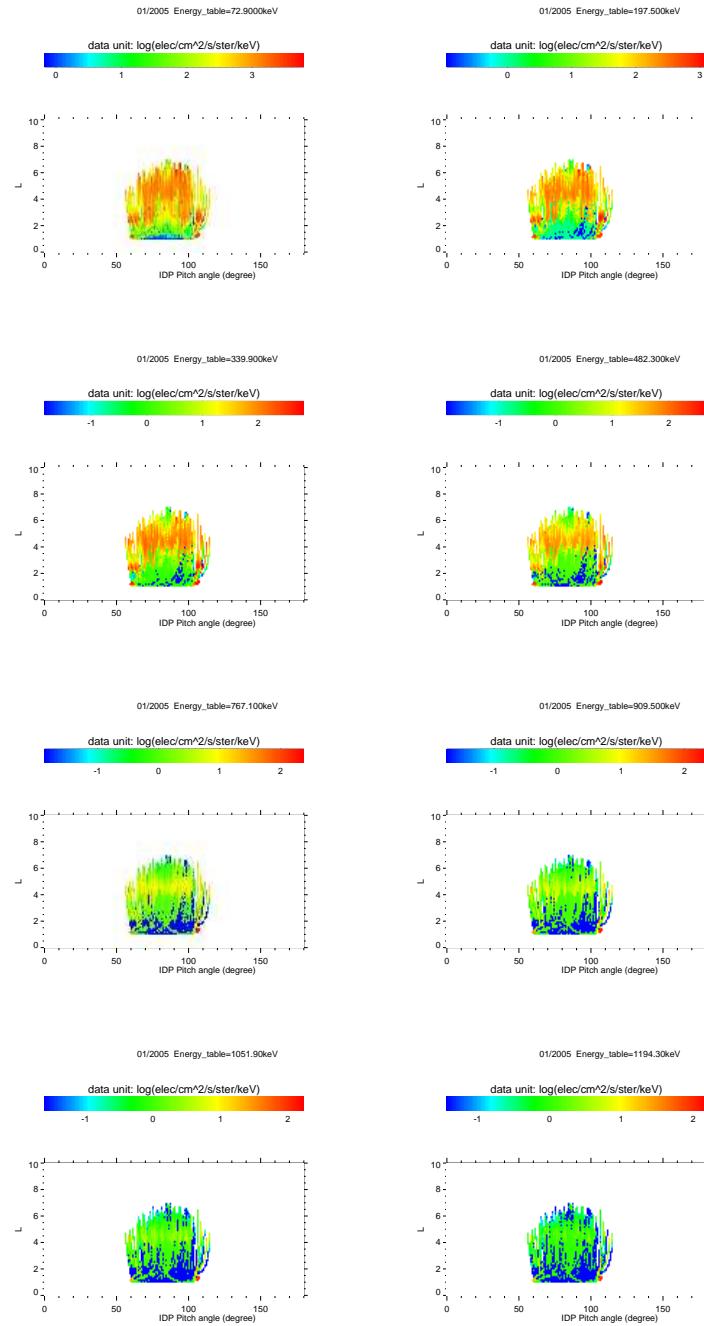


Figure 5.5: Distributions of IDP particle fluxes for 8 of the 128 PARMAP energy channels, as a function of α_{IDP} pitch angle (degrees) and L-shell. As an example, data collected in 1 month are reported. Energy channel increases from the top left panel to the bottom right one.

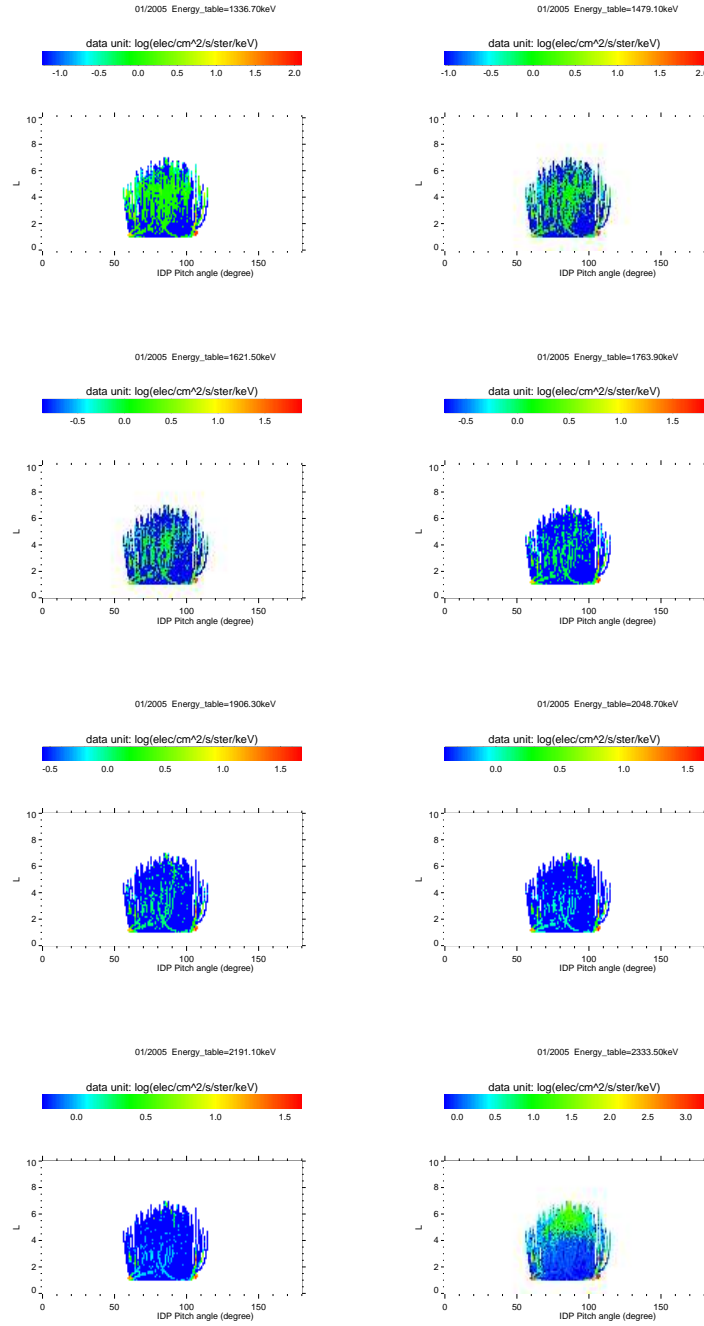


Figure 5.6: Distributions of IDP particle fluxes for 8 of the 128 PARMAP energy channels, as a function of α_{IDP} pitch angle (degrees) and L-shell. As an example, data collected in 1 month are reported. Energy channel increases from the top left panel to the bottom right one.

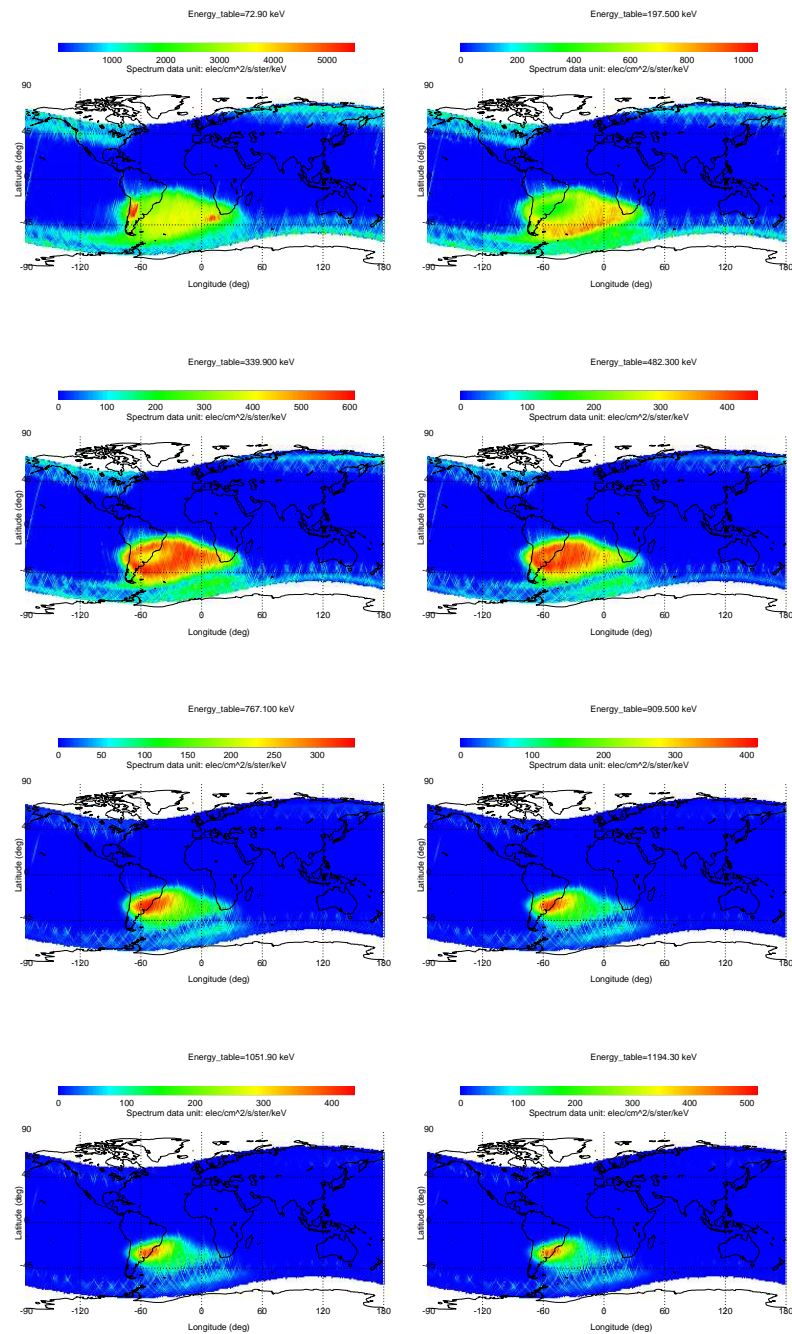


Figure 5.7: Geographic distributions of IDP-PARMAP particle fluxes for 8 of the 128 PARMAP energy channels. As an example, are reported data collected from July to December 2004 . Energy channel increases from the top left panel to the bottom right one.

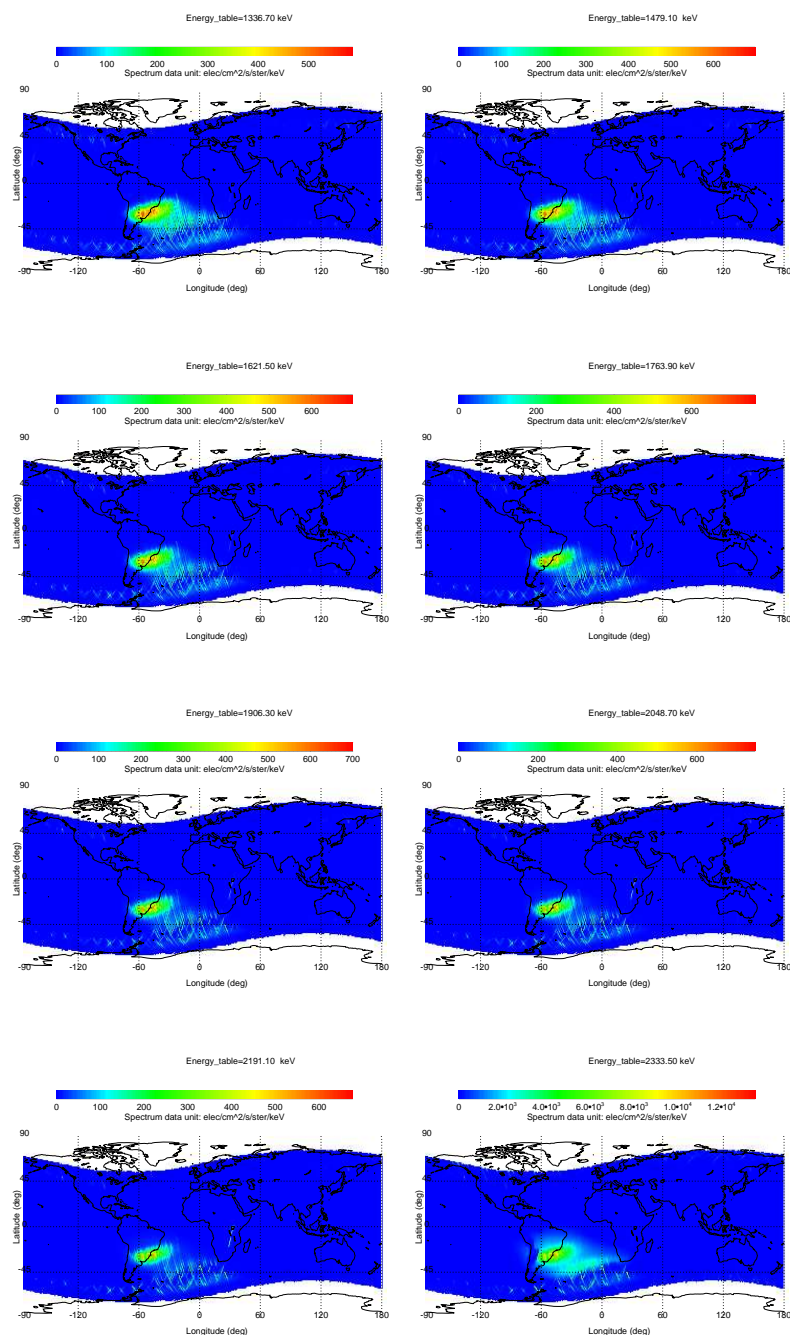


Figure 5.8: Geographic distributions of IDP-PARMAP particle fluxes for 8 of the 128 PARMAP energy channels. As an example, are reported data collected from July to December 2004. Energy channel increases from the top left panel to the bottom right one.

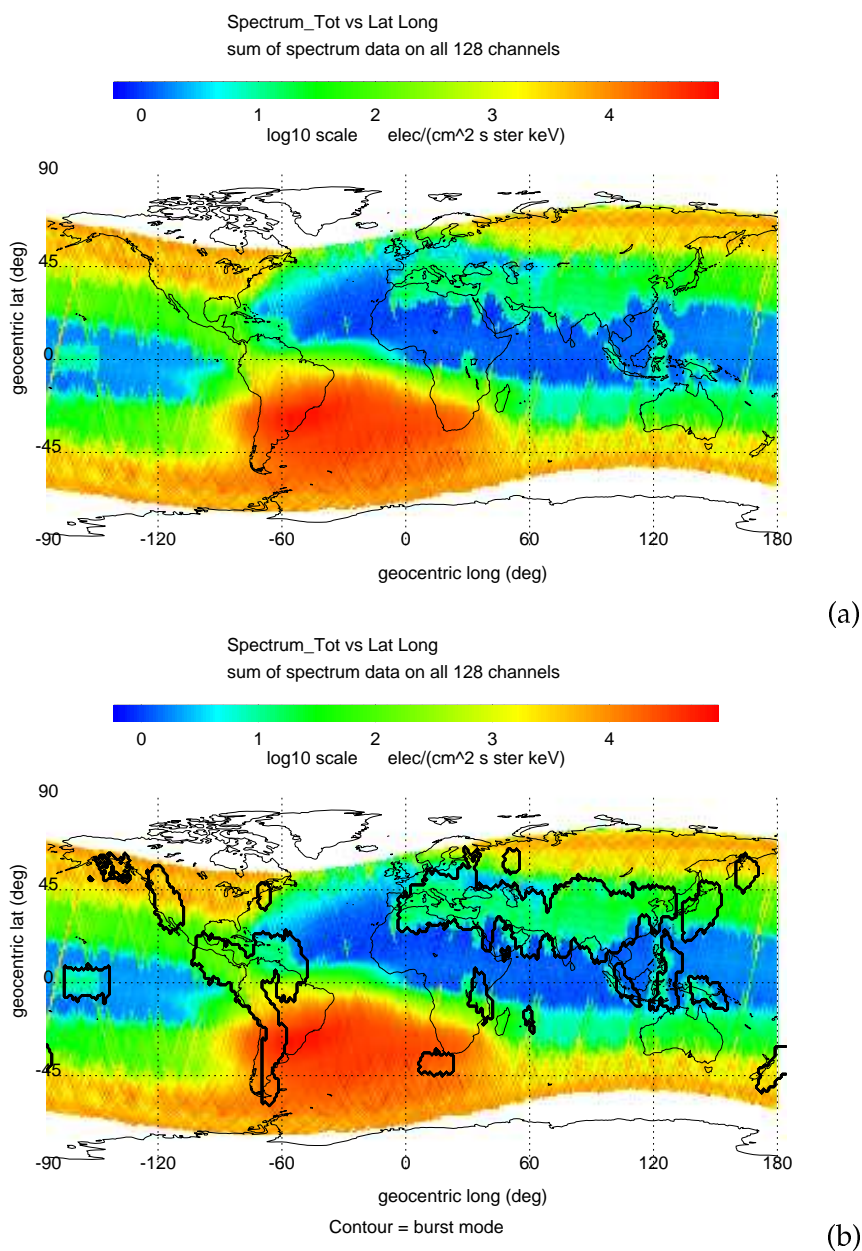


Figure 5.9: (a) geographic distribution of the IDP total particle flux, (b) geographic distribution of the IDP total flux and contour plot of the regions where IDP data have been collected in the burst mode. The spurious little shift of the whole burst mode contour plot on the right is due to graphical reasons. In both (a) and (b) panels, all 128 PARMAP energy channels have been added during time until July 2004 to December 2004.

energy channels (figure 5.10) one can observe that:

- in the low (0-42) IDP energy channels there is an increase of the particle fluxes over the region where the burst mode is active (fig. 5.10 (a));
- some gaps appear in the geographic distribution of the medium (43-85) IDP energy channels (fig. 5.10 (b)) corresponding to the burst mode regions. This effect is due to the logarithmic scale used to represent the IDP flux. It means that where the burst mode is operative there is a decrease of the fluxes in the medium (43-85) IDP energy channels.
- in the high (86-127) IDP energy channels there are large gaps in the data over the burst mode region (fig. 5.10 (c)). It means that where the burst mode is operative there is a strong decrease of the fluxes in the high (86-127) IDP energy channels.

This could be an unexpected systematic effect induced by the burst acquisition mode and could be due to a reduced capability of IDP to distinguish energy channels in burst mode configuration. Consequently, for this preliminary study I have used only fluxes obtained adding data over all the IDP energy channels.

To avoid to include CRs near subauroral zones, regions with an L-shell value > 1.8 and SAA region are excluded because of the high CRs related to the radiation belt lowering (figures 5.5-5.6). In figures 5.7- 5.8 the area of SAA region is a function of the particle energy range. Therefore, in the analysis of the total IDP flux, I define the SAA contour with a cut on the magnetic field value. I have tested several cuts starting from $B < 0.185$ G.

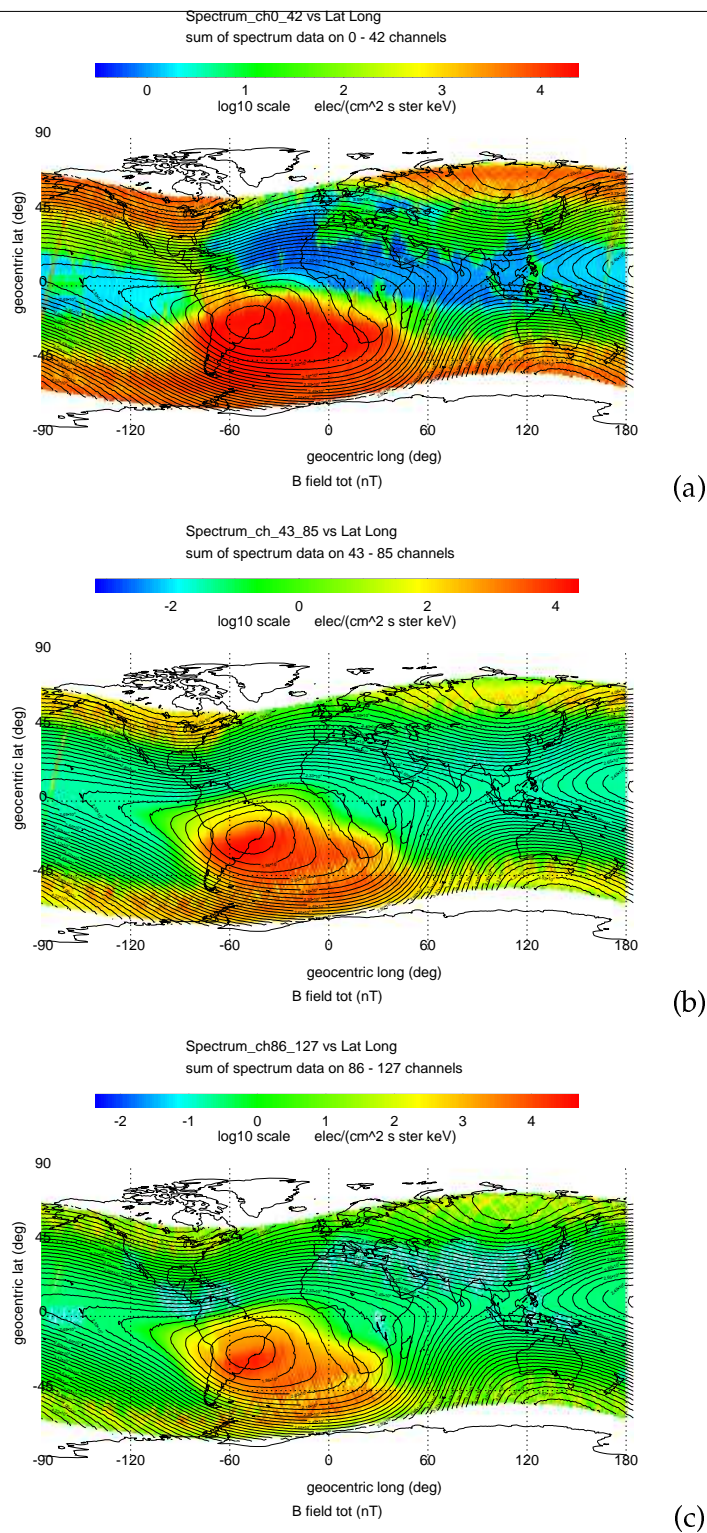


Figure 5.10: Geographic distribution of low (channels 0-42) (a), medium (channels 43-85) (b) and high (channels 86-127) (c) energy IDP particle fluxes.

5.3 Anomalous counting-rate events: PBs selection

In this analysis I have used the PARMAP particle data for the period August 2004 - April 2006. Anomalous count-rate events (PBs) are defined starting from IDP-PARMAP charged particle CRs. Counting rates depend from the L-shell of the DEMETER position and from the instrument pitch angle. Unfortunately IDP is not able to distinguish particle pitch angle, so I assume that particle pitch angle coincides with the angle of IDP axis (α_{IDP}). L-shell the B values in the detection position are calculated via IGRF 2005.

I divided the α_{IDP} range ($0^\circ \div 180^\circ$) in steps of 15° and the L-shell range ($1.0 \div 1.8$) in steps of 0.1. For each cell of the $\{L, \alpha_{IDP}\}$ matrix, I evaluated the daily counting rate distribution in order to define a reference background value. The L and α_{IDP} steps width are defined taking into account the particles fluxes variation and the low number of measurements available in a day. Reducing the number of bins I do not take into account the particles fluxes variation, introducing a systematic error; increasing it I rarely have a sufficient number of measurements in each cell. Statistical tests suggest a Poisson-like distribution of CRs for each $\{L, \alpha_{IDP}\}$ matrix cell. By assuming this hypothesis, I define as PB only the CR whose probability to be a poissonian fluctuation of this background value is lower than a tunable threshold. Applying a 0.1 probability cut, I have selected the PBs events.

In figure 5.11 is shown an example of the background $\{L, \alpha_{IDP}\}$ matrix analysis. Total IDP flux (black line) and poissonian fit (red line) for $1.7 < L < 1.8$ and $60^\circ < \alpha_{IDP} < 75^\circ$ cell are shown. Cyan line is the cumulative number of DEMETER measurements (in the given $\{L, \alpha_{IDP}\}$ cell) normalized to the total number of days with observations. This acquisition rate (scale on the right) is plotted as a function of number of days (scale on the top) for 4 months of data. This acquisition rate shows large fluctuation due to gaps in data acquisition and to not uniform temporal sampling of the given $\{L, \alpha_{IDP}\}$ cell. Apparently 4 months of data acquisition are necessary to stabilize this index. This effect could suggest that the evaluation of the background matrix on a daily basis could be not efficient for the IDP data analysis. For high particle fluxes there is a clear discrepancy between the IDP total flux and the poissonian distri-

bution. This is due to observations carried out in the SAA region due to natural particle precipitation. When the SAA region is excluded from the analysis, this natural noise is significantly reduced. The residual difference between total IDP flux and poissonian distribution is constituted by possible PBs.

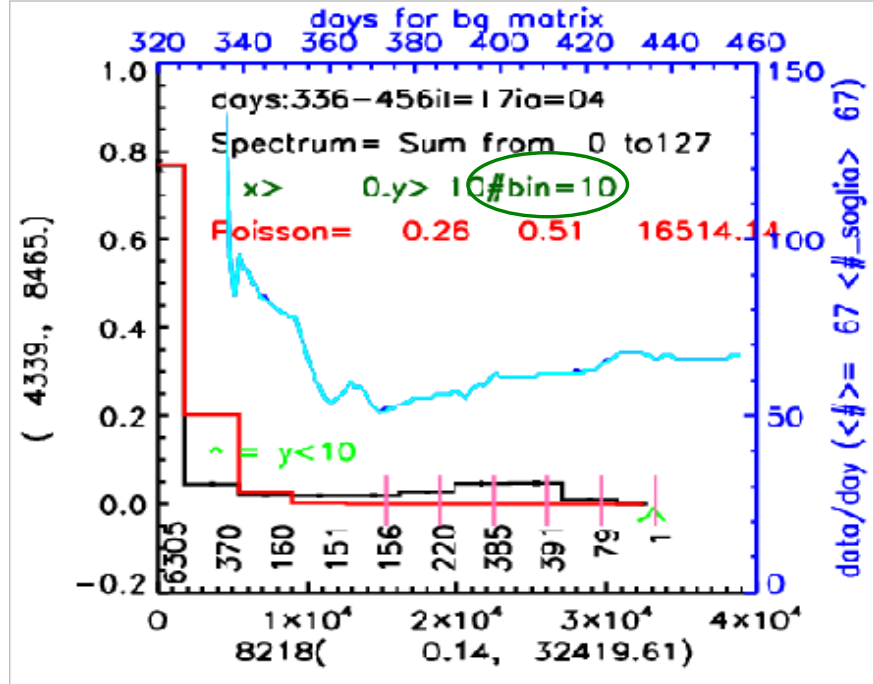


Figure 5.11: Example of background $\{L, \alpha_{IDP}\}$ matrix analysis. Total IDP flux (black line) and poissonian fit (red line) for $1.7 < L < 1.8$ and $60^\circ < \alpha_{IDP} < 75^\circ$ cell. Cyan line is the cumulative number of DEMETER measurements in the given $\{L, \alpha_{IDP}\}$ cell normalized to the total number of days with observations. This acquisition rate (scale on the right) is plotted as a function of number of days (scale on the top) for 4 months of data.

5.4 Earthquake database

Earthquakes events analyzed in this study have been selected from the USGS catalogue for the period August 2004 - April 2006. The intensity of the seismo-electromagnetic emissions depends on the hypocentral zone dimension (Molchanov et al., 1998; Surkov, 1999) that is connected to the earthquake magnitude. It also depends on the hypocen-

tral depth because when propagating in the lithosphere, seismic EM emissions are strongly attenuated (Molchanov et al., 1995). Moreover, most of the seismo-electromagnetic observations are concerned with moderate and strong seismic events (Hayakawa and Molchanov, 1993), generally located in the upper Earth lithosphere. For these reasons, following Sgrigna et al. (2005), in this analysis I have selected earthquakes with magnitude $M > 5.0$ and hypocentral depth $< 100 \text{ km}$.

The altitude at which the seismo electromagnetic emissions interact with trapped charged particles is not yet exactly predicted by theory. According to Kim et al. (1998), Parrot et al (1993) and Voronov et al. (1990), I have assumed that the interaction occurs at altitudes between $\simeq 100 \text{ km}$ and $\simeq 1200 \text{ km}$. We have calculated for each earthquake, an L-shell value (L_{EQ}) projecting the epicentral zone at the altitude where the seismic EM emission interact with particle. The L_{EQ} value is a model- dependent tunable parameter and I have estimated it at a reference altitude of 400 km .

The L_{EQ} histogram has a profile which is similar to that of the DEMETER L-shell measurements. According with Sgrigna et al. (2005), I have restricted the analysis to the $L < 1.8$ zone that could be mostly affected by pre-seismic electromagnetic perturbations. As are can see in figure 5.4, the well-known earthquake distribution at low latitude is fully covered with this cut on L-shell values.

5.5 Analysis of temporal correlation between PBs and EQs

The particles L-shell is not modified by the interaction with seismo-electromagnetic emissions and along the longitudinal drift, so it coincides with the L_{PB} value of the detected PBs.

For the spatial correlation between PBs and selected earthquakes I used the $\Delta L = L_{EQ} - L_{PB}$ difference as a tuneable parameter to take into account the indetermination on the L_{EQ} definition.

I calculated $\Delta T = T_{EQ} - T_{PB}$ and ΔL for each $EQ - PB$ couple, where T_{EQ} e T_{PB} are the universal times of the EQ and PS events. According to Sgrigna et al. (2005), $EQ - PB$ couples with $\Delta L < -0.08$ and $\Delta L > 0.03$ have been excluded. The ΔL cut allows to correlate PBs and EQs assuming that the seismo electromagnetic perturbation

can extends up to 1200 *km*. I looked for a temporal correlation between the PB's and EQ's population by studying the temporal differences ΔT in a time window of ± 3 days before and after each PB to have a statistically reliable analysis. Several cuts have been applied to select the PB catalogue as described in the following. Finally, the histogram of the ΔT frequency distributions for the selected *EQ – PB* couples is composed and I looked for the existence of a peak in the $\Delta T > 0$ region (e.g. PBs occurring before EQs).

Looking for possible correlation between earthquakes and PBs measured by satellites inside the magnetosphere a careful monitoring of the dynamical behavior and temporal variations of the near Earth charged particle environment is needed. In our analysis some filtering procedures have been implemented to better distinguish the PBs of seismo-electromagnetic origin from other ones (background rejection). The geomagnetic *Ap* and *Dst* indices have been used to monitor the occurrence of geomagnetic storms. Because of the global nature of the geomagnetic and solar disturbances I did not apply any cut on geographic position and L-shell values. I have rejected PB detected in periods with $A_p > 20$ to exclude geomagnetically perturbed days (magnetic storms).

In figure 5.12 is shown the ΔT histogram. I have chosen a ΔT bin step of 1 hour because I am looking for particle precursors that happen some hours before earthquakes. The histograms are shown in the ± 18 hours interval to evidence the correlations nearest T_{EQ} ($\Delta T \sim 0$).

There are no significant peak at any ΔT values neither positive nor negative. The absence of correlation could be explained by the IDP orientation. Particle perturbed by seismo-electromagnetic emission should have pitch angle far from 90° and near to the loss cone limit. Consequently, the IDP pointing mode, that is mainly orthogonal to magnetic field line, is not suitable to our study. Moreover, due to the low IDP geometrical factor, the daily PBs number is too low.

I do not expect to find out a temporal correlation for PBs at the IDP energy, because their longitudinal drift is inefficient and the possibility to detect them far from the precipitation zone is strongly reduced. In principle it can be required that the longitudinal distance between EQs and PBs is less than a given value (i.e. $\sim 30^\circ$). Anyway, also applying this cut, the ΔT distribution show does not any peak. This confirms that in

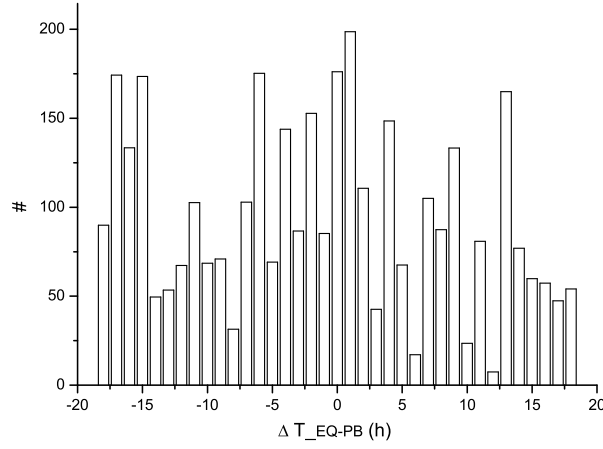


Figure 5.12: Histogram of temporal correlations between PBs and EQs versus ΔT_{EQ-PB} . The bin step is 1 hour, the temporal window is 18 hours. There are no significant peak at any ΔT values neither positive nor negative.

order to observe electron PBs of seismic origin exploiting the longitudinal drift, I need to detect electrons with high energy.

5.6 Results of the EQ-PB analysis

In this chapter I have presented a preliminary study on the possible spatial and temporal correlation between the seismic activity and charged particle bursts precipitating from the lower boundary of the inner Van Allen radiation belt. Results by Sgrigna et al., (2005), based on PET/SAMPEX data, suggested the existence of a such statistical correlation. The authors have found a maximum in the temporal correlation distribution relative to high energy electrons (EHI: $E \sim 4-15$ MeV) channel, located at $\Delta T \sim 4 \div 5$ hours. On the contrary the analysis of the PBs from the SAMPEX-PET low energy electron channel (ELO: $E \sim 2-6$ MeV) shows no peak due to low statistic and to the low efficiency of the longitudinal drift motion that does not allow to detect ELO PBs far from the precipitating zone. The presence of a peak at $\Delta T > 0$ for EHI data means that statistically particle precipitation seems to precede of some hours the occurrence

of seismic events.

In this study of IDP data I have not yet found any significant peak in the ΔT distribution. This is probably due to:

- a not suitable IDP orientation;
- the low energy range of particle detected by IDP;
- the poor statistics due to the low IDP geometric factor.

These results are compatible with those reported by Sgrigna et al., (2005) related to low energy ELO PET/SAMPEX channels for which no correlation with seismicity was also found.

Chapter 6

A comparative study of particle measurements by Demeter and model of wave-particle interaction during a magnetic storm .

The aim of this chapter is to study processes involved in energetic electron precipitation during magnetospheric storms. In particular, some aspects of interactions between waves and particles have been investigated, focusing mainly their effects on energetic electron precipitation. I will start with giving a short introduction to the Sun-Earth system and the different regions of the Earth's magnetosphere together with some elements of the basic magnetospheric plasma physics that are relevant to the studies presented in this thesis.

6.1 Magnetospheric plasma interactions through waves

Three kinds of plasma wave will be discussed: electromagnetic ion cyclotron (EMIC) waves, whistler mode chorus, and plasmaspheric hiss. These waves are generated in the inner magnetosphere and serve as channels for transferring energy from one plasma population to the others. They are important in plasmasphere heating, ring

current-radiation belt loss and buildup.

6.1.1 EMIC Waves

EMIC waves are left-hand polarized with frequencies near ion cyclotron frequencies. EMIC waves propagate along magnetic field lines, reflecting at the ionosphere and bouncing between conjugate ionospheric points. Ion cyclotron modes grow when the ring current ion pitch-angle distribution is sufficiently anisotropic, with more energy perpendicular than parallel to the magnetic field [Kennel and Petschek, 1966]. Magnetospheric processes such as convection, Coulomb and charge exchange interactions tend to reduce the field-parallel flux of ring current ions, providing the free energy for EMIC wave excitations. The amplification of EMIC waves also depends on the cold plasma density. Near the plasmapause where the density gradient is steep, EMIC waves bounce several times across the equator and thus experience multiple wave gains [Thorne and Horne, 1992]. EMIC waves have been observed in the inner magnetosphere, especially in the vicinity of the plasmapause [Anderson et al., 1992; Fraser et al., 1992]. The occurrence and intensity of EMIC waves are much higher during storms than quiet times. The active wave regions move to lower latitudes as storm develops [Braysy et al., 1998], along with the storm time plasmas. EMIC waves cause pitch-angle diffusions and eventually precipitation losses of ring current ions. Jordanova et al., [2001] simulated the ring current ion fluxes during the 14-16 May 1997 storm, including losses due to wave-particle interactions. They found the global patterns of proton precipitation moved to lower L shells during storm main phase and receded back toward larger L shells in storm recovery, consistent with the EMIC wave observations mentioned above [Braysy et al., 1998]. Radiation belt electrons also interact with EMIC waves through cyclotron resonance. Using balloon-borne X-ray detectors, Lorentzen et al., [2000] found intense X-ray event associated with atmospheric bremsstrahlung from 1 MeV precipitation electrons during a storm. They interpreted the event as electron pitch-angle scattering and precipitation caused by resonance with EMIC waves. Based on quasi-linear theory, Summers and Thorne, [2003] calculated the electron pitch-angle diffusion coefficients for cyclotron resonance with EMIC waves. They found, under typical storm condition in the duskside plasmasphere, only electrons with energy above 1

MeV to be resonant with EMIC waves. The time scale for removing these energetic electrons by EMIC wave scattering during magnetic storms is as short as several hours to one day. The location of the calculated precipitation is consistent with the observation by *Lorentzen et al.*, [2000]. EMIC waves resonant with ring current ions and radiation belt electrons cause precipitation losses of energetic particles.

6.1.2 Whistler mode wave

Whistler mode waves are right-hand polarized with frequencies less than the electron gyro-frequency. They travel along magnetic field lines or are refracted across field lines. Whistler mode chorus is identified as quasi-periodic, series of overlapping rising and falling tones [*Shawhan*, 1979]. Two separated chorus emissions were observed in two distinct regions: high-latitude and low-latitude magnetosphere [*Tsurutani and Smith*, 1977; *Meredith et al.*, 2001]. Both studies found the high-latitude chorus is principally on the dayside. The low-latitude chorus was observed mostly outside the plasmasphere at all local times but predominantly in the post-midnight to dayside magnetosphere. A close relationship between storm activities and the low-latitude chorus is found and it is suggested that these chorus emissions are generated by injection of 10-100 keV electrons [*Tsurutani and Smith*, 1977; *Meredith et al.*, 2001]. As storm ring current electrons are injected on the nightside, they gradient-curvature drift to the dayside through dawn. During their earthward transport, the electrons are energized preferentially in the perpendicular direction. The resulting anisotropy in perpendicular and parallel electron temperatures generates instability or excitation of whistler mode chorus. Whistler mode chorus cause energy and pitch-angle diffusion of radiation belt electrons. During the recovery phases of magnetic storms, the fluxes of outer belt electrons are often seen to increase, exceeding the pre-storm level [*Reeves*, 2003]. Two types of mechanism are suggested to be responsible for this storm-time enhancement: earthward diffusion of injected particles from the plasma sheet and internal energization processes. *Summers and Ma*, [2000], developed a kinetic (Fokker-Planck) model of relativistic electrons, considering energy diffusion based on gyroresonance electron-whistler mode waves and precipitation due to pitch-angle scattering by EMIC and whistler mode waves. They assumed a constant background plasma density and

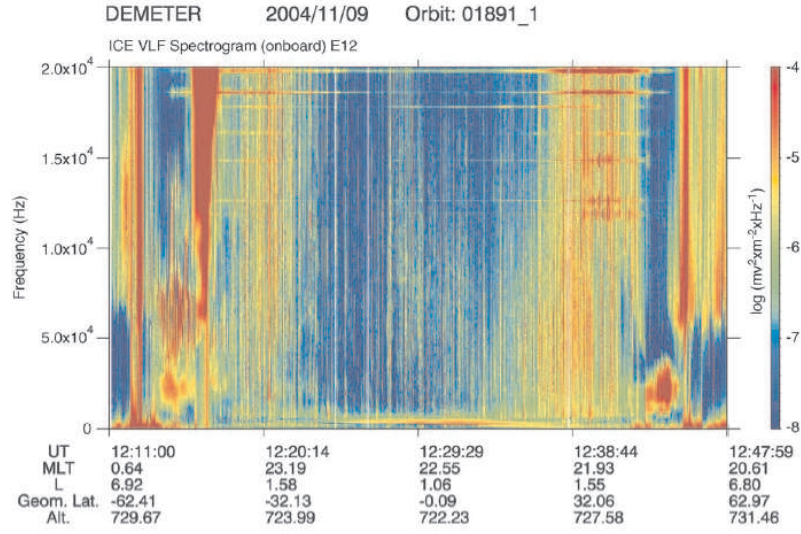


Figure 6.1: Example of a nighttime pass of orbit 1891 on 9 November 2004, provides an overview of typical night time ELF and VLF electric fields measurements. Plasmaspheric hiss is clearly visible in the low latitude part of the orbit with a sharp cut-off which follows the H^+ gyrofrequency. At higher latitudes, structured VLF emissions dominate in two frequency ranges, from 2 to 3 kHz and above 6 kHz, extending above 20 kHz, the frequency limit of the VLF channel. At mid-latitudes the most intense and regular sources are the lightning generated whistler emissions clearly visible on the figure in particular around 12 : 38 UT at a latitude of $\sim 30^\circ$

whistler amplitudes on the order of 100 pT. Their model is able to generate the observable increases in relativistic electrons during storm recovery phases. On the other hand, MeV electrons experience pitchangle scattering when interact with the whistler mode chorus and precipitate into the atmosphere. This diffusion loss is evident in the collocation of observed chorus emissions and MeV electron microburst precipitation [O'Brien *et al.*, 2003].

6.1.3 Plasmaspheric hiss

Another type of whistler mode turbulence propagates in the magnetosphere is the plasmaspheric hiss. These waves have the same frequency range (100 Hz-5 kHz) as the chorus. However, plasmasphere hiss emissions are mostly seen inside the plasmapause and for this reason they are named. Plasmaspheric hiss is relatively steady, persistently seen throughout the plasmasphere. It is proposed that plasmaspheric hiss is generated

through cyclotron resonant instability with 10-100 keV electrons that diffuse inward to the plasmasphere from the outer belt [Thorne *et al.*, 1973; Shawhan, 1979]. The generation region is presumed to lie in the outer plasmasphere. From the source, waves propagate to fill the plasmasphere [Lyons *et al.*, 1972]. Whistler mode plasmaspheric hiss is believed to be the source of the slot region that separates the inner and outer radiation belts during quiet periods. Plasmaspheric hiss interacts with radiation belt electrons through gyroresonance, causing pitch-angle diffusion and subsequent precipitation loss of these energetic electrons. The slot region is located at L shells $\approx 2 - 3.5$, where precipitation decay rates are comparatively high and radial diffusion is weak to balance the loss. Lyons *et al.*, [1972] computed the pitchangle diffusion coefficients of energetic electrons due to interaction with plasmaspheric hiss and solve the diffusion equation of electron distribution function. In their calculation, they considered cyclotron-harmonic and Landau resonances, as well as oblique propagation of waves. Their calculated pitch-angle distribution and precipitation lifetimes are in good agreement with satellite observations.

6.2 Wave-particle interaction

The importance of waves in relation to particle precipitation and influence on particle distributions is extensively proved in the literature dating back to the start of modern space physics [Kennel and Petschek, 1966]. In a plasma the magnetic and electric field control over particles lead to a wide variety of possible wave modes. In a collision-less plasma electrostatic and electromagnetic waves will influence the individual charged particles, but only the part of the particle distribution that is in near resonance with the waves will change in a systematic way. In this part of the thesis we will focus on the waves known to be relevant for energetic electron precipitation, namely electromagnetic waves in whistler mode, typically measured in the ELF (3-3000 Hz) or VLF (3-30 kHz) frequency band. Note that in the following, non-relativistic and relativistic equations will be presented.

6.2.1 L-dependent peaks in the energy spectra of electron precipitating from the inner belt

The loss of radiation belt particles is likely due to interactions with whistler mode waves but the origin of some of these waves is uncertain as well as the relative contributions of each wave type. Possible types of ELF/VLF whistler mode waves observed in the inner magnetosphere are plasmaspheric hiss, lightning generated whistler waves (ducted and nonducted), VLF transmitter signals, as well as power line harmonic radiation (PLHR). A more recent study performed by *Abel and Thorne* [1998 a ; b] examined the relative contributions to the loss of radiation-belt electrons of coulomb interactions and three different wave types: plasmaspheric hiss (occupying the frequency band $f = 1 \pm 0, 5kHz$), whistler wave originating in lightning discharges ($f = 4, 5 \pm 2kHz$), and VLF transmitters ($f = 17, 1kHz \pm 50Hz$ and $22.3kHz \pm 50Hz$).

It is generally agreed that Doppler-shifted cyclotron resonance interaction between particle and whistler mode waves in the magnetosphere result in the amplification of the waves, triggering of discrete emissions, and various wave-particle interactions. During these interactions the electron scattered in energy and pitch-angle, and their trapped adiabatic motion is perturbed. As results of such scattering some energetic electrons are precipitated out of the radiation belts and into atmosphere [*Inan et al.*, 1978].

For interaction in low L shell, the inner radiation belt, and for cases when the wave frequency and/or the cold plasma density is low, such gyrofrequency interactions involve quasi-relativistic electrons with energies in the range of several tens up to several hundreds of keV. Precipitation of electrons in this energy range in one-to-one correspondence with and therefore believed to be induced by natural VLF/ELF/ULF waves (whistlers, chorus emission, etc) has been reported by several authors [*Helliwell et al.*, 1973; *Parrot and Zaslavski*, 1996].

Satellite measurements show that electrons in the drift loss cone precipitate from the slot region between the inner and outer radiation zones ($L \sim 2$ to ~ 3.5) and from the outer edge ($L \sim 1.5$ to 1.8) of the inner radiation zone. This observed characteristic suggests that the precipitation may be due to first-order cyclotron resonance interaction of the trapped electrons with waves near magnetic equator. Electrons are precipitated

from the slot region of the radiation belts by ELF-VLF waves originating from various sources and spanning a broad range of frequencies. The curves shown in the (fig. 6.2.1) represent the electron energies as plotted as function of L and calculated for first-order cyclotron resonance at the equator with waves traveling parallel to magnetic field lines.

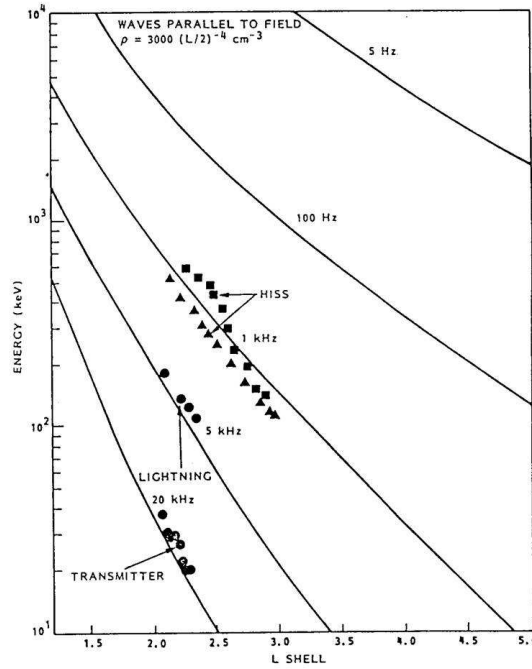


Figure 6.2: The electron energies calculated for first-order cyclotron resonant interactions near the equator for waves traveling parallel to the magnetic field lines. The central energies of observed peaks are plotted for selected cases identified as being due to waves associated with VLF transmitters, or lightning or plasmaspheric hiss [Imhof *et al.*, 1996].

Equatorial plasma densities of $3000 (L/2)^{-4} \text{ cm}^{-3}$ have been assumed [Chappell *et al.*, 1970]. For comparison the central energies of peaks observed in the energy spectra of electrons at various L values and mirroring at low altitudes are plotted for representative passes of satellite when the interaction were identified as being due to VLF waves from transmitters [Imhof *et al.*, 1983], to waves associated with lightning [Voss *et al.*, 1984], or plasmaspheric hiss [Imhof *et al.*, 1982]. The curves are calculated under the assumption that the particle scattering occurs primarily at the equator with field-aligned waves. The energies of the observed precipitating electrons in these experiments are generally in the quasi-relativistic range of 10 to 500 keV. Detailed study of spectral

characteristics of the precipitating electrons has suggest that these electrons were precipitated by first-order cyclotron resonance interactions with nearly monochromatic waves, possibly from ground-based VLF transmitters. In most of these studies the nonrelativistic equations of motion of the particles were used. The relativistic formulations are necessary in order (1) to more directly compare theoretical and experimental results and (2) to begin to properly assess the effects of man-made VLF waves on the inner radiation belt particle population. In the following we compare our theoretical predictions, rederiving the equations of motion for the cyclotron resonance interaction between whistler mode waves and energetic particles (with relativistic effect included), with observed peaks in the precipitated energy spectra on board the satellite Demeter.

6.2.2 Physics of nonrelativistic and relativistic wave-particle interaction

The basic of energy diffusion of relativistic electrons resulting from resonant interactions with whistler mode waves in the magnetosphere was originally discussed by *Li et al.*, [1997]. *Horne and Thorne*, [1998] identified potential wave modes that are capable of being in resonance with the important electron energy range of few keV to few MeV. The principal waves are L mode electromagnetic ion cyclotron (EMIC) waves and R mode whistlers. *Summers et al.*, [1998], on the basis of diffusion curves for particles in primary ($n=1$ and $n=-1$) resonance with parallel propagating waves, proposed that pitch angle scattering of electrons by enhanced EMIC waves near the plasmapause, in conjunction with heating by cyclotron resonant whistler waves, could account for the enhancement of energetic outer zone electrons accompanying magnetic storms. Enhanced convection electric fields provide the principal mechanism for the intensification of ring current (10-100 keV) flux during geomagnetic storms *Lyons and Williams*, [1980]. Inward convection also leads to an anisotropic distribution of the ring current ions and electrons which provides a source of free energy for the excitation of both EMIC waves and whistler mode waves respectively. Figure. 6.2.2 provides a schematic description of the spatial region where enhanced levels of both EMIC and whistler mode waves occur during a storm.

This part of thesis is related to the electromagnetic harmonic emission observed by the microsatellite Demeter. These emission are detected in the range 500Hz-2kHz in the

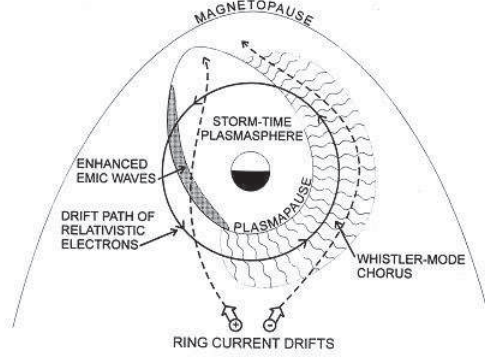


Figure 6.3: Schematic diagram showing spatial distribution of whistler mode waves and EMIC waves during magnetic storms. This map is taken from [Summers *et al.*, 1998]; the regions of wave activity are determined empirically from published data.

upper ionosphere during large magnetic storm, and they could be related to the EMIC waves. Electron flux at particular energies can be observed by Demeter in association with these emission. The purpose of this paper is to examine whether the observation are consistent with the fact that the dominant precipitation mechanism is cyclotron resonance.

Inan *et al.*, [1984] studied the electron precipitation induced by E.M. signals from ground-based VLF transmitters. The involved mechanism is the well-known cyclotron resonance, this interaction can only occur if the following condition is satisfied:

$$\omega - kv_{\parallel} \simeq n\omega_{ge} \quad (6.1)$$

where ω is the angular wave frequency, v_{\parallel} is the electron's parallel velocity, $\omega_{ge} = \frac{eB}{mc}$ is the angular electron gyrofrequency, n is the order of the resonance and k is the wave number. Landau resonance is described by $n=0$ while other values of n gives cyclotron harmonic resonances. It is important to note that this equation is only valid for waves and particles of the same sense, that is, right hand waves resonating with negatively charged particles or left hand waves with positively charged particles. Resonance between waves and particles of opposite sense can also be possible for particles of higher v_{\parallel} than the phase velocity ($v_{phase} = \omega/k$) of the waves, but this requires high energies [Parks, 1991]. In general one considers the resonance mode requiring the least

particle velocity ($n = -1$ or $n = 1$) to be most important as the phase space density F ($F = \frac{J}{p^2}$ where p is particle momentum and J is the particle flux measured in the $(cm^2 s sr keV)^{-1}$) typically decreases rapidly towards higher velocities and the resonance is also more effective at these principal harmonics. In the case of resonance between the right hand whistler mode waves and electrons performing bounce and gyration motion in the magnetosphere the resonance mode of least particle velocity is for $n = 1$. Resonance modes for $n < 0$ are nonexistent as the whistler mode waves exist when upper frequency cutoff is either the local electron plasma frequency f_{pe} or gyrofrequency f_{ge} , whichever is less [Stix, 1992]. Effectively this means that the particle must move in the opposite direction of the wave phase velocity to obtain resonance in the reference frame of the particle bounce motion. This is also mentioned as resonance at the Doppler shifted frequency of the particle. The wave and the particles interact when the Doppler-shifted wave frequency seen by the particles is close to the electron gyrofrequency f_{ge} . Here is used the convention that both k and v are positive, although waves and particles must travel in opposite directions for whistler-mode waves to resonate with electrons having small pitch angles. If this condition is satisfied, waves and particles can exchange energy, causing pitch angle scattering and precipitation. Considering a circularly polarized monochromatic whistler mode signal propagating longitudinally along the static magnetic field B_0 in a cold magnetoplasma, the dispersion relation for whistler mode wave [Helliwell et al., 1965] is given by :

$$k = \frac{\omega_{pe}}{c} \sqrt{\frac{\omega}{\omega_{ge} \cos \theta - \omega}} \quad (6.2)$$

where $\omega_{pe} = \sqrt{\frac{e^2 N}{\epsilon_0 m}}$ is the angular electron plasma frequency and θ is angle between B_0 and k . This dispersion relation is valid if plasma frequency is much greater than the electron gyrofrequency, for frequencies $f < f_{ge}$ and propagation angles $\theta \simeq 0$. Combining Equation (6.1) and (6.2) one can obtain Equation (6.3) for E_{res} , the parallel energy of an electron to be in resonance with a whistler mode wave at a given wave frequency, magnetic field strength, and cold plasma density N . This equation is only valid for waves propagating at small angles relative to the background magnetic field and for non-relativistic electrons.

$$E_{res} = -\frac{1}{2} \frac{mc^2(\omega - \omega_{ge})^3}{\omega_{pe}^2 \omega} \quad (6.3)$$

In the following the relativistic kinetic energy will be presented. The whistler dispersion relation in relativistic case when including the angle of propagation and $\omega < \omega_{ge}$ [Baumjohann and Treumann, 1996] is given by :

$$\frac{k^2 c^2}{\omega^2} = 1 + \frac{\omega_{pe}^2}{\omega(\omega_{ge} \cos \theta - \omega)} \quad (6.4)$$

The kinetic energy of the particle is :

$$E = mc^2(\gamma - 1) \quad (6.5)$$

where mc^2 is the rest energy of the particle, being 511 keV for electrons and $\gamma = (1 - \frac{v^2}{c^2})^{-1/2}$ is the relativistic Lorentz factor, for non relativistic case $\gamma = 1$. When $v \ll c$ the relativistic kinetic energy expression can be written as nonrelativistic kinetic energy expression, in particular for the square root expression then expanded by use of the binomial theorem and the relativistic kinetic energy expression can be written by:

$$E = \frac{1}{2}mv^2 + \frac{3}{8} \frac{mv^4}{c^2} + \dots$$

and for low velocities ($v \ll c$) this expression approaches the non-relativistic kinetic energy expression

$$E \simeq \frac{1}{2}mv^2$$

The relativistic cyclotron resonance condition can be written as :

$$\omega - kv_{||} \simeq \omega_{ge}/\gamma \quad (6.6)$$

Combining Equation (6.4), (6.5) and (6.6) one can obtain Equation (6.7) $E_{res-rel}$, the parallel relativist kinetic energy of an electron in resonance with a whistler mode wave at a given wave frequency, magnetic field strength, and cold plasma density N.

$$E_{res-rel} = \frac{-\delta - \sqrt{\delta^2 - 4\eta\xi}}{2\eta} \quad (6.7)$$

where the parameter used in this equation are show in table 1.1

$$\begin{aligned} \chi &= 1 + \frac{\omega_{pe}^2}{\omega(\omega_{ge} - \omega)} \\ \eta &= \omega^2 - \omega^2\chi \\ \delta &= 2mc^2\omega^2 - 2mc^2\omega\omega_{ge} - 2mc^2\omega^2\chi \\ \xi &= \omega_{ge}^2 m^2 c^4 - 2m^2 c^4 \omega\omega_{ge} + m^2 c^4 \omega^2 \end{aligned}$$

Table 6.1: Parameters used to calculate energy kinetic in the relativistic case.

6.3 New observations of ELF emissions by the Demeter satellite during large magnetic storms and interaction with the electron populations

In this section I present some measurements we have made on board of Demeter about energy spectra of electrons precipitating from the slot region and inner belt. The scope is to examine whether the observation are consistent with the fact that the dominant precipitation mechanism is cyclotron resonance. At this purpose it is relevant to note that the scattering by EMIC waves near the duskside plasmopause(fig. 6.2.2) could be important since it would maintain an electron distribution which is more isotropic than that associated with resonant diffusion during electron-whistler interactions [Summers *et al.*, 1998]. Strong precipitation of electrons is seen mostly in substorm and storm time periods when enhanced fluxes of electrons are observed in the inner radiation belts, through impulsive injections or strong convection. Following such storm time injections the fluxes decay over several day period, and the quiet time slot is reformed. The removal of electrons to levels near zero throughout the slot has been accounted for by pitch-angle diffusion resulting from resonant interactions with the existing VLF band [Imhof *et al.*, 1973]. On board the satellite Demeter were measured (by the instrument ICE) the electrical field components in the frequency range from DC to 3.25 MHz, the three magnetic field components in the frequency range from a few Hz to 17.4 kHz (by

the instrument IMSC) and the fluxes of energetic electrons in the energy range: 30 keV - 2 MeV (by the instrument IDP).

Data recorded during three different magnetic storms will be shown in chronological order. The first severe storm after the launch occurred on November 8-10, 2004 (maximum Dst = -373 nT and Kp = 9 on November 8th). The other two ones have been seen on January 21-22, 2005 (maximum Dst = -105 nT and Kp = 8) and on May 15, 2005 (maximum Dst = -256 nT and Kp = 8). The Dst index for the period of magnetic storm occurred on November 2004, January and May 2005 are reported in figures 6.4, 6.5, 6.6, respectively. Let us now compare peaks of energy measured during the November 2004, January and May 2005 magnetic storms with kinetic energy calculated for first-order cyclotron resonance near the equator with waves traveling parallel to the Earth's magnetic field lines.

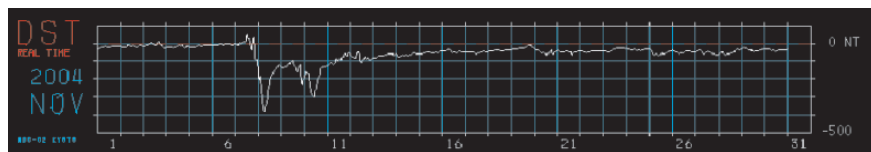


Figure 6.4: Dst for the magnetic storm of November 2004.

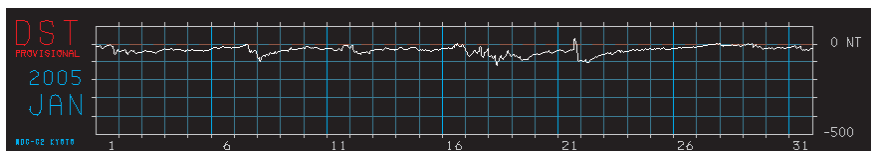


Figure 6.5: Dst for the magnetic storm of January 2005.

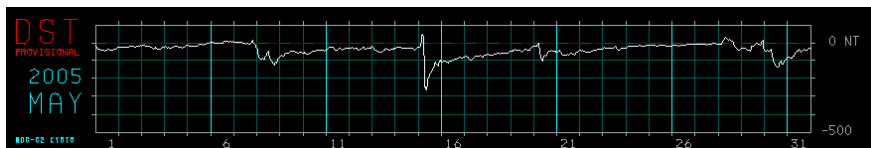


Figure 6.6: Dst for the magnetic storm of May 2005.

Top panels of figures 6.7, 6.8, 6.9, 6.10, and 6.11 report the electric and magnetic fields measured by ICE and IMSC experiments respectively. Bottom panels of the same figures show spectra of particle measured by IDP experiment. From top to bottom, the first and second panels display the spectrograms between 0 and 2 kHz of one electric and magnetic component, respectively while the bottom panel represents an energy spectrogram (30 keV - 2352 keV) of the locally mirroring electrons.

Figures 6.7, 6.8, 6.9 show clear anomalies in the electric and magnetic fields and in the spectrum of energy associated with the magnetic storm of November 2004 (see Dst plot in figure 6.4). Figure 6.10 shows analogous anomalies in the electric and magnetic fields and in the spectrum of energy associated with the magnetic storm of January 2005 (see Dst plot in figure 6.5). Finally, figure 6.11 shows anomalies of the electric and magnetic fields and of the energy spectrum associated with the magnetic storm of May 2005 (see Dst plot in figure 6.6) [Parrot *et al.*, 2006].

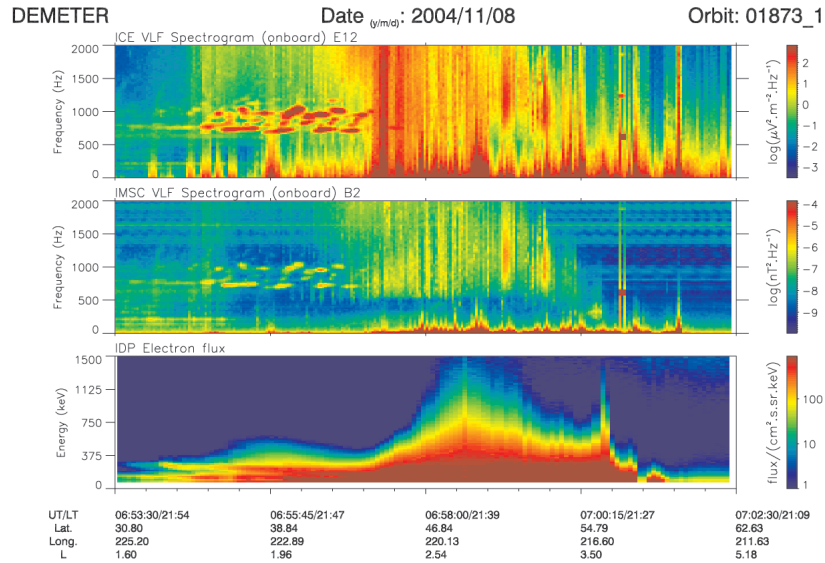


Figure 6.7: Electric, magnetic and particle data, recorded during a complete half-orbit on November 8, 2004 between 06:53:30 and 07:02:30 UT (night time).

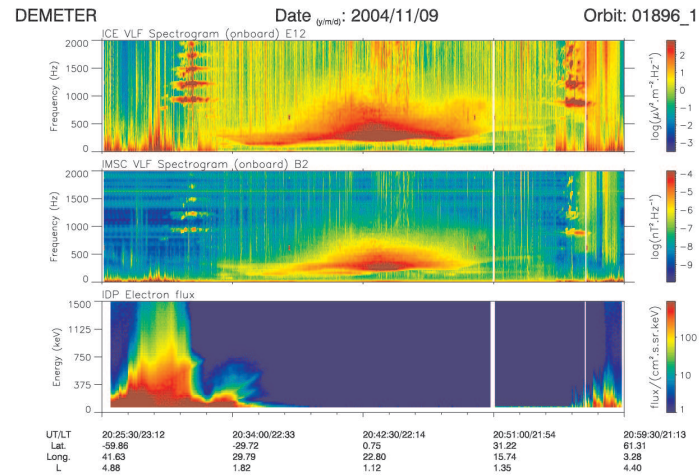


Figure 6.8: Electric, magnetic and particle data, recorded during a complete half-orbit on November 9, 2004 between 20:25:30 and 20:59:30 UT (night time).

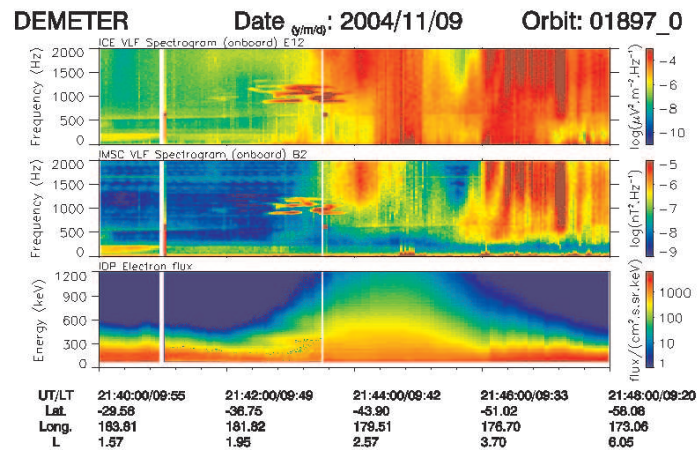


Figure 6.9: Electric, magnetic and particle data, recorded during a complete half-orbit on November 9, 2004 between 21:40:00 and 21:48:00 UT (night time).

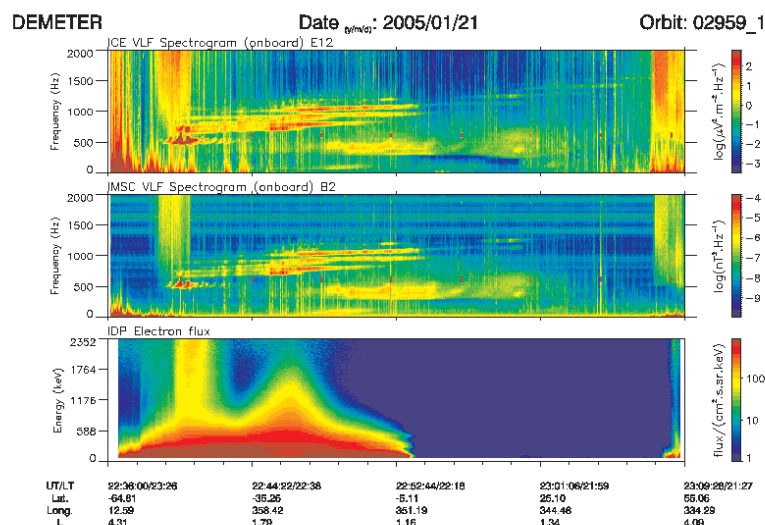


Figure 6.10: Electric, magnetic and particle data, recorded during a complete half-orbit on January 21, 2004 between 22:36:00 and 23:09:28 UT (night time).

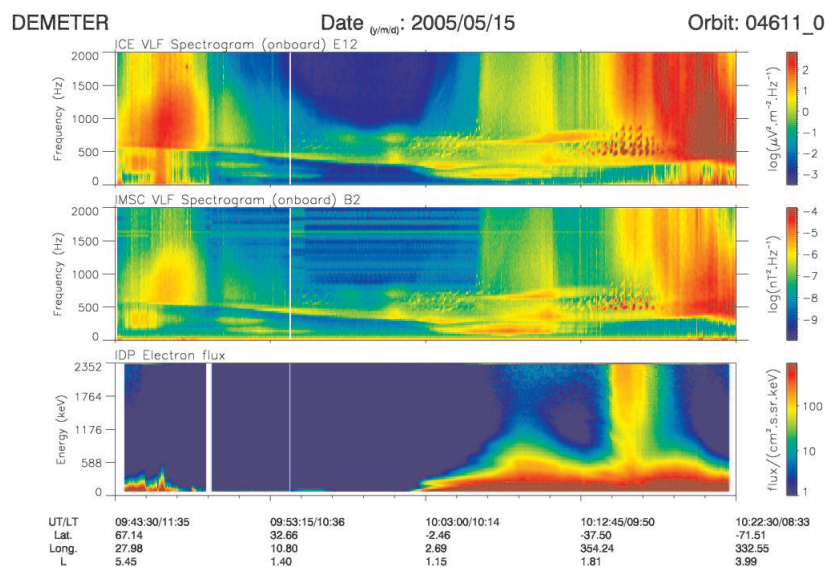


Figure 6.11: Electric, magnetic and particle data, recorded during a complete half-orbit on May 15, 2004 between 09:43:30 and 10:22:30 UT (day time).

It is important to note that during magnetic storm density values in the slot region can be higher than those assumed in the calculations. Several authors have considered for the equatorial plasma density a value around $3000 (L/2)^{-4} \text{cm}^{-3}$ [Imhof *et al.*, 1983; Voss *et al.*, 1984; Imhof *et al.*, 1982]. On the contrary, it has been shown that during a magnetic storm this density value can increase by at least a factor 5 [Chappell *et al.*, 1970]. A study of electron precipitation during a magnetic storm is reported in Imhof *et al.*, [1982]. In this case electron densities were assumed to follow the typical R^{-4} curve normalized to a value of $3 \times 10^3 \text{cm}^{-3}$ at $L=2$. The peak energies measured by Imhof *et al.*, [1982] are not consistent with those expected for cyclotron resonance with waves traveling parallel to the Earth's magnetic field lines. This because during magnetic storm the plasma density model is different from that observed during quiet time. Results reported by Imhof *et al.*, [1982] show that density at $L=2.5$ increased from $1.23 \times 10^3 \text{cm}^{-3}$ to $2.46 \times 10^3 \text{cm}^{-3}$, and resonance energy for a 500 Hz electromagnetic wave decreased from 583 to 345 keV. In this analysis I assume a plasma density value of $5 \cdot 3000 (L/2)^{-4} \text{cm}^{-3}$ because Demeter data used for the study were collected during a great magnetic storm.

Parameter values I used to calculate the kinetic relativistic energy are given in table 1.2, where $f_{pe} = 8,98 \cdot 10^3 \sqrt{N}$. According with Baumjohann and Treumann, [1996] we assume a centered dipole model for the Earth's magnetic field, which is represented by the lowest order term in Gauss's multipole expansion. After taking the gradient of the magnetic potential field and using the equatorial magnetic field B_T on the Earth's surface, the intensity of the field B can be written as $B = B_T/L^3 = 3,11 \cdot 10^4/L^3 [\text{nT}]$ and $f_{ge} = 28 \cdot B$. The geomagnetic field described in this way is a good approximation to the real field. In fact, our region of interest is far enough away from the Earth's surface for the rapidly decaying higher order terms to become insignificant, and yet sufficiently close to remain unaltered by solar wind deformation, and other external current systems (e.g., the ring current, magnetopause current).

Orbits selected to compare particle energies calculated for the first order cyclotron resonance near equator with energies of near $\sim 1 \text{kHz}$ waves measured on board Demeter are reported in table 6.2.

$$\begin{aligned} c &= 2.99 \times 10^8 [m/s] \\ m &= 9.1 \times 10^{-31} [kg] \\ f_{pe} &= 4394 \times 10^3 / L^2 [Hz] \\ B &= 3.11 \times 10^{-5} / L^3 [T] \\ f_{ge} &= 8.71 \times 10^5 / L^3 [Hz] \end{aligned}$$

Table 6.2: Parameters used to calculate the energy kinetic in the relativistic case .

Orbit selected	U T	L and f	E _{model}	E _{Demeter}
1873 – 1	6:55:52	$L = 1.98; f = 956.97Hz$	$E = 231.4keV$	$E = 197.5keV$
1896 – 1	20:32:08	$L = 2.14; f = 1230.39Hz$	$E = 118.3keV$	$E = 90.7keV$
1897 – 0	21:42:49	$L = 2.16; f = 917.91Hz$	$E = 164.7keV$	$E = 170.8keV$
2959 – 1	22:46:50	$L = 1.52; f = 800.730Hz$	$E = 751.7keV$	$E = 784.9keV$
2959 – 1	22:46:50	$L = 1.52; f = 937.440Hz$	$E = 671.3keV$	$E = 749.3keV$
2959 – 1	22:46:50	$L = 1.52; f = 1035.09Hz$	$E = 624.4keV$	$E = 713.7keV$
4611 – 0	10:14:35	$L = 2.02; f = 722.61Hz$	$E = 268.9keV$	$E = 215.3keV$

Table 6.3: Orbit, UT, values of L frequency, electron kinetic energy calculated in the relativistic case and electron energy spectra measured on board of Demeter along selected orbits.

Figures, 6.12, 6.13, 6.14, 6.15, 6.16, 6.17 and 6.18 show curves representing the electron energies calculated for cyclotron resonance at equator with waves of assigned frequency, propagating parallel to the Earth's magnetic field using the relationship 6.7. Curves in blue, red and black color reported in the above mentioned figures correspond to frequencies near $\sim 1kHz$, $5kHz$ and $20kHz$, respectively. In particular frequencies of the e.m. field along all orbits used in this analysis, and reported in table 6.3, are measured by ICE and IMSC experiment. These frequencies are associated with anomalies of electric and magnetic field during the storm of November 2004, of the January and May 2005. We will compare in the following theoretical energy model with waves of near 1 kHz associated with the increase of IDP data caused by the November 2004, January and May 2005 magnetic storm. Energies of peaks corresponding to the different orbits of table 6.3 plotted in figures 6.12, 6.13, 6.14, 6.15, 6.16, 6.17 and 6.18 as a function of L. For comparison in the same figures , peak measured by Demeter are also shown. Square in the figures are energies calculated using Demeter particle data reported in table 6.3.

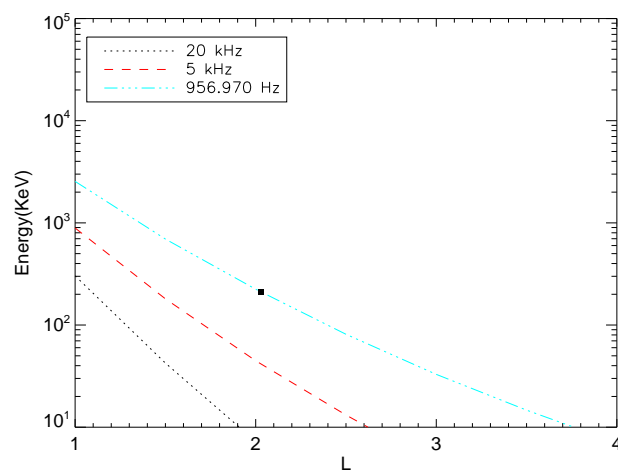


Figure 6.12: Curves resonant energy for different frequencies v.s. L calculated resonant energies for different frequencies. The square represents experimental value energy from Demeter data along the for orbit 1873 – 1.

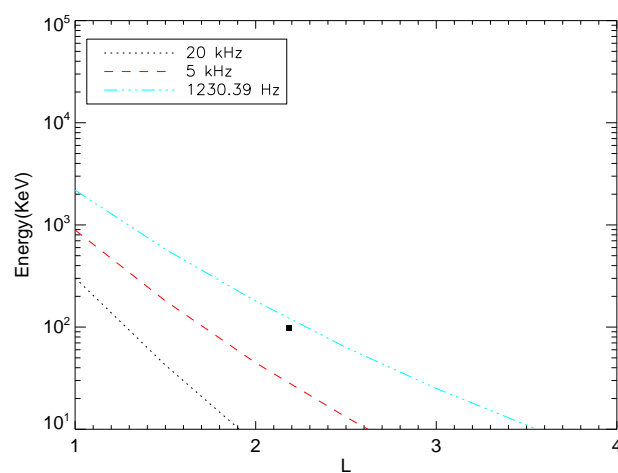


Figure 6.13: Curves resonant energy for different frequencies v.s. L calculated resonant energies for different frequencies. The square represents experimental value energy from Demeter data along the for orbit 1896 – 1.

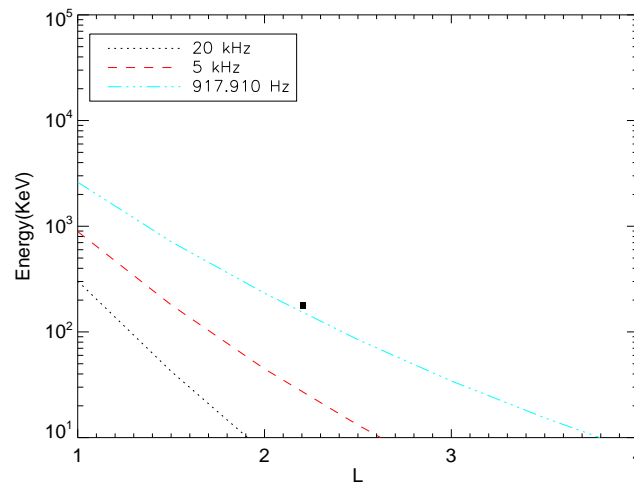


Figure 6.14: Curves resonant energy for different frequencies v.s. L calculated resonant energies for different frequencies. The square represents experimental value energy from Demeter data along the for orbit 1897 - 0.

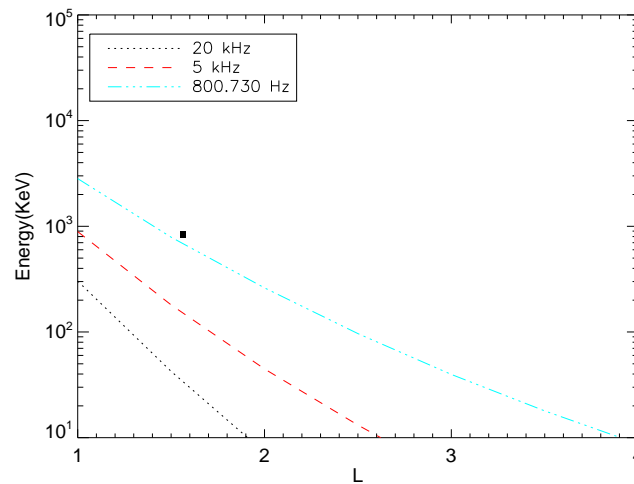


Figure 6.15: Curves resonant energy for different frequencies v.s. L calculated resonant energies for different frequencies. The square represents experimental value energy from Demeter data along the for orbit 2959 - 1.

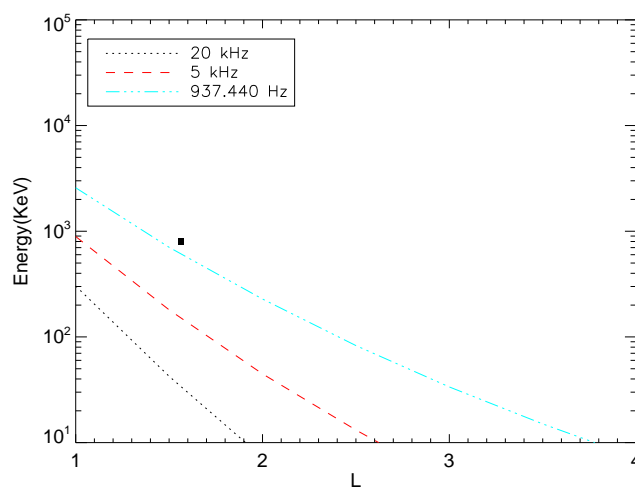


Figure 6.16: Curves resonant energy for different frequencies v.s. L calculated resonant energies for different frequencies. The square represents experimental value energy from Demeter data along the for orbit 2959 – 1.

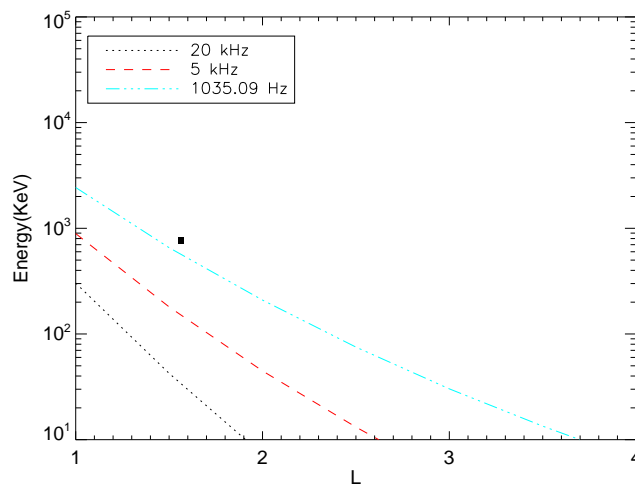


Figure 6.17: Curves resonant energy for different frequencies v.s. L calculated resonant energies for different frequencies. The square represents experimental value energy from Demeter data along the for orbit 2959 – 1.

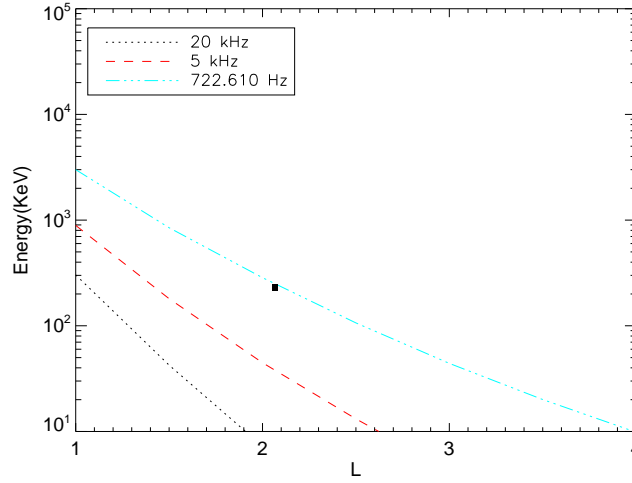


Figure 6.18: Curves resonant energy for different frequencies v.s. L calculated resonant energies for different frequencies. The square represents experimental value energy from Demeter data along the for orbit 4611 – 0.

Observations presented here have show interesting spectra for electrons precipitating from slot region between the inner and outer radiation zones and from the the outer edge of the inner radiation zone. Here the spectra of energetic electrons are known to decrease abruptly with increasing L-values [*Mihalov and White, 1962*], forming the slot region and our observation confirm this trend.

We also suggest that an important loss mechanism for few keV electrons in the slot region could be the pitch angle diffusion due to a resonant wave-particle interaction in the few hundred Hertz frequency range. Finally, the energy peaks from orbits 1873-1, 1896-1, 1897-0, 2959-1 and 4611-0 are consistent with those expected for a cyclotron resonance between particles and waves traveling parallel to the geomagnetic field lines.

Conclusions and Outlook

Whistler-waves and radiation belt particles detected by Demeter LEO micro-satellite have been investigated in order to look for iono-magnetospheric perturbations and related sources. In particular, time and space correlations of earthquakes with anomalous whistler-waves and radiation particle bursts have been attempted as well as the effect of magnetic storms on whistler-wave propagation. Results demonstrated to be interesting. They are summarized in the following. Concerning whistlers, at beginning on the basis of original data from the Demeter neural network (RNF), a special software WHIMAP has been developed to construct the whistlers database used in the study. Then, it has also been constructed the earthquakes database to be correlated with whistlers. From the analysis of EM data concerning whistlers, it has been developed an ad hoc method to investigate the influence of seismic activity on whistlers propagation. By applying to data this method it has been observed that for high whistler dispersion values, number of whistlers over seismic zones and their geomagnetically conjugates is significantly perturbed respect to that detected in average in the same zones. This result is particularly evident for a few classes of whistlers (specifically, the 13th, 14th, and 17th) where it is possible to note an influence of seismicity on the whistlers propagation. On the contrary, in the same analysis has not yet possible to distinguish between anomalous fluctuations observed in different time intervals around an EQ pre-seismic, co-seismic, and post-seismic ones.

This is the first study of EQ-whistler correlation carried out using satellite data. A manuscript is in preparation, describing results, to be submitted in an International Journal of the field.

In the second part of this thesis has been carried out a study of radiation belt particle fluxes. For this analysis a special software (PARMAP) has been developed to construct a database on the basis of original data from the Demeter IDP particle counter. PARMAP allows to read particle data detected by IDP both in burst mode and in survey mode by avoiding the problem connected with the different sampling rate of the two modes. The study has been carried out to look for a possible correlation between anomalous bursts of particles precipitating from the inner Van Allen radiation belt and selected earthquake of moderate and large magnitude. This attempt has been carried out according to a previous work based on particle data collected by the SAMPEX-PET mission (Sgrigna et al., 2005). Contrary to this case, results obtained up to now with IDP data do not show any significant correlation between the two populations. Several reasons can be at the basis of such results. In fact, energy range of particles detected by IDP is significantly lower than that of the SAMPEX-PET detector, due to the orientation of IDP, data collected by this detector are mainly constituted by trapped particles, the IDP detector its capability in discriminating low-, medium-, and high-energy particles, or its behavior during the burst mode-survey mode transition must be better investigated. Therefore, the analysis is still in progress and in this first step of the study the main goal is to better understand the IDP behavior and, then, the physical mechanisms of the phenomenology. Up to now results confirm those obtained in the previous SAMPEX-PET study using low energy particles.

In third part of this thesis has been dedicated to analyze effects of magnetic storms on radiation belt particles. According to a model proposed by a few authors, it has been verified that during most great magnetic storms, precipitation of charged particle fluxes was mainly caused by the cyclotron-resonance mechanism. In particular, particle energy spikes observed by the Demeter IDP during several orbits (namely, 1873-1, 1896-1, 1897-0, 2959-1, and 4611-0) are consistent with those expected for a cyclotron-resonance coupling mechanism between waves and particles moving parallel to the magnetic field lines. This result has been presented to two international congresses (Buzzi et al., 2006; Parrot et al., 2006), and published in an international Journal (Parrot et al., 2006). During this thesis work the candidate has produced as co-author five papers on the subject and participated to eleven congresses and workshops (see reference

list).

Summarizing all information reported above, results pointed out by this thesis work seem to be interesting and promising for further applications. The study is still in progress in order to confirm and improve quality of results obtained up to now. In particular, concerning EQs-whistlers correlation I am going to extend the time window around EQs up to a few days, to repeat the study using EQs randomly distributed, and to extend the analysis to the whole Demeter time period up to December 2006 (Ap and Dst data are still unavailable). More in general, further and deeper analysis are requested for a more complete understanding of the phenomena detected by DEMETER. Therefore, results of the study have to be considered as a first and preliminary contribution to the understanding of this very complicated matter.

Papers in international journals with referees

1. Sgrigna, V., A. Buzzi, L. Conti, A.V. Guglielmi, O.A. Pokhotelov, 2004. Electromagnetic Signals Produced by Elastic Waves in the Earth's Crust, *Nuovo Cimento*, 27C, 115-132.
2. Sgrigna, V., Buzzi, A., Conti, L., Picozza, P., Stagni, C., Zilpimiani, D., 2006. Seismo-induced Effects in the Near-Earth Space: Combined Ground and Space Investigations as a contribution to Earthquake Prediction, *Tectonophys.*, accepted, in press, 2006.
3. Sgrigna, V., A. Buzzi, L. Conti, P. Picozza, C. Stagni, D. Zilpimiani. The ESPERIA satellite project for detecting seismic-associated effects in the topside ionosphere. First instrumental tests in space, *Earth Planet. and Space*, submitted, 2006.
4. Sgrigna, V., Battiston, R., Buzzi, A., Casolino, M., Conti, L., Picozza, P., Stagni, C., Zilpimiani. The EGLE space experiment onboard the ISS, *Microgravity and Sci. Technology*, accepted, in press, 2006.
5. Parrot, M., A. Buzzi, O. Santolk, J. J. Berthelier, J. A. Sauvaud, J. P. Lebreton, New observations of electromagnetic harmonic ELF emissions in the ionosphere by the

DEMETER satellite during large magnetic storms, *J. Geophys. Res.*, 111, A08301, doi:10.1029/2005JA011583, 2006.

Participation to Congresses

1. Conti, L., A. Buzzi, A.M. Galper, S.V. Koldashov, V. Malvezzi, A.M. Murashov, P. Picozza, R. Scrimaglio, V. Sgrigna, L. Stagni, 2003. A possibile correlation between seismic events and trapped particles precipitation, ISEC 2003 Radiation Belt Science Meeting, September 2-5, 2003, Toulouse, France, Poster P19, Abstract pag. 45.
2. Sgrigna, V., Console, R., Buzzi, A., Conti, L., Galper, A.M., Malvezzi, V., Parrot, M., Picozza, P., Scrimaglio, R., Spillantini, P., Zilpimiani, D., 2004. ESPERIA: an equatorial magnetic, plasma and particle mission for monitoring perturbations in the topside ionosphere and for defining the near-Earth magnetic environment, *EOS Trans., AGU*, vol. 85, GP13A-03, n.17, JA162, 2004 (INVITED).
3. Sgrigna V., Buzzi, A.; Conti, L.; Picozza, P.; Stagni, C.; Zilpimiani, D 2005. Ground rock deformation events and their possible effects in the near-Earth space. General Assembly of the European Geosciences Union, Vienna, Austria, 24-29 April, 2005. Session Natural Hazards, NH 4.02: Deformation processes accompanying mechanical and electromagnetic phenomena, for rocks and other materials, from laboratory to geophysical scale, EGU05-A-06210, NH4.02-1FR3P-0043, p. 450 (INVITED and Co-Convener of the Session).
4. Conti, L., A. Buzzi, V. Sgrigna, C. Stagni, D. Zilpimiani, 2005 et al., The EGLE experiment. (within the LAZIO-SIRAD-EGLE Collaboration). 10th Scientific Assembly of the International Association of Geomagnetism and Aeronomy (IAGA 2005), Toulouse, France, July 18-29, 2005, Session Division II, C085: Low Latitude atmosphere-ionosphere-magnetosphere coupling, dynamics and energetics; IAGA2005-A-01522, p.83.
5. Conti, L., A. Buzzi, A. M. Galper, S. V. Koldashov, A. M. Murashov, P. Picozza, R. Scrimaglio, V. Sgrigna, L. Stagni, 2005. Influence of the seismic activity on the in-

ner Van Allen radiation belt. 10th Scientific Assembly of the International Association of Geomagnetism and Aeronomy (IAGA 2005), Toulouse, France, July 18-29, 2005, Session Division I, GA101: Monitoring earthquakes and volcanic activity by magnetic, electric and electromagnetic methods; IAGA2005-A-01518, p.46.

6. Bencardino, R., F.Altamura, V.Bidoli, M.Casolino, M.P. De Pascale, P.Picozza, A. Alvino, S.Ascani, P.Azzarello, R.Battiston, S.Bizzaglia, M.Bizzarri, S.Blasko, G. Chiocci, D.Cosson, L.Di Masso, G.Esposito, L.M.Farnesini, M.Ionica, S.Lucidi, A.Papi, V.Postolache, S.Rossi, G.Scolieri, L.Bongiorno, S.Dell'Agnello, A. Franceschi, M. Ricci, C. Falcone, S. Tassa, A. Abramov, A. Ivanova, A.M. Galper, A. Kalmikov, M.C. Korotkov, A.V.Popov, A. Buzzi, L. Conti, V. Sgrigna, C. Stagni, D. Zilpimiani, A. Pontetti, L. Valentini. Response of the LAZIO-SiRad detector to low energy electrons, in: Proc. ICRC 2005, Pune(India), vol. 2, p. 449-452, (2005).
7. Altamura, F., R. Bencardino, V. Bidoli, L. Bongiorno, M. Casolino, M.P. De Pascale, M. Minori, P. Picozza, D. Aisa, A. Alvino, S. Ascani, P. Azzarello, R. Battiston, S. Bizzaglia, M. Bizzarri, S. Blasko, L. Di Masso, G. Chiocci, D. Cosson, G. Esposito, S. Lucidi, A. Papi, V. Postolache, S. Rossi, G. Scolieri, M. Ionica, A. Franceschi, S. Dell'Agnello, M. Ricci, C. Falcone, S. Tassa, A. Kalmikov, A.V. Popov, A. Abramov, M.C. Korotkov, A.M. Galper, A. Ivanova, L.Conti, V.Sgrigna, C.Stagni, A.Buzzi, D. Zilpimiani, A.Pontetti, L.Valentini. Preliminary results from the LAZIO-Sirad experiment on board of the International Space Station. Proc.ICRC 2005, Pune (India) vol. 2, 343-344.
8. Conti, L., Buzzi, A., Picozza, P., Ronchetti, S., Sgrigna, V., Stagni, C., Zilpimiani, D., 2006. Seismo-induced electromagnetic and particle perturbations in space, International Symposium DEMETER, Toulouse, France, June 14-16, 2006.
9. Buzzi, A., Parrot M., Sauvaud J.A., Precipitation of particles by intense electromagnetic harmonic waves during magnetic storms, Communication to the Conference "Symposium International Demeter" (Toulouse, France, 14 - 16 Giugno 2006).

10. Parrot, M., Buzzi, A., Santolik, O., Berthelier, J.J., Sauvaud, J.A., Lebreton, J.P.
New observations of electromagnetic harmonic ELF emissions in the ionosphere
by the DEMETER satellite during large magnetic storms (solicited), European
Geosciences Union General Assembly 2006, Vienna, Austria, 02 - 07 April 2006,
Geophysical Research Abstracts, Vol. 8, 01643, 2006.
11. Buzzi, A., Conti, L., Galper, A. M., Koldashov, S.V., Malvezzi, V., Murashov, A.M.,
Picozza, P., Scrimaglio, R., Sgrigna, V., Stagni, L., 2006. Sismo-electromagnetic
emissions, Proc. NATO Adv. Study Institute on "Sprites, Elves and Intense
Lightning Discharges", Edited by M. Fullekrug, E.A. Mareev and M.J. Rycroft,
Published by Springer, vol. 225, pp. 388-389, 2006. (NATO Science Series II:
Mathematics, Physics and Chemistry- vol.225. ISBN-10 1-4020-4628-6 (PB)).

Bibliography

- [1] Abel, B., and R.M. Thorne, Electron scattering loss in Earth's inner magnetosphere - 1. Dominant physical processes, *J. Geophys. Res.*, 103 (A2), 2385, 1998a
- [2] Abel, B., and R.M. Thorne, Electron scattering loss in Earth's inner magnetosphere - 2. Sensitivity to model parameters, *J. Geophys. Res.*, 103 (A2), 2397, 1998b.
- [3] Akasofu, S.-I., The development of the auroral substorm, *Planet. Space Sci.*, 12, 273282, 1964.
- [4] Akasofu, S.-I., S.-I., Several controversial issues on substorms, *Space Sci. Rev.*, 113(1-2), 140, doi: 10.1023/B:SPAC.0000042938.57710.fb, 2004.
- [5] Aleshina, M.E., Voronov, S.A., Galper, A.M., Koldashov, S.V., Maslennikov, L.V., 1992. *Correlation between Earthquake Epicenters and Regions of High-Energy Particle Precipitations from the Radiation Belt*, *Cosmic Res.*, **30**, n.1, pp. 79-83; n.6, pp. 79-81.
- [6] Aleksandrin, S.Yu., A.M. Galper, L.A. Grishantzeva, S.V. Koldashov, L.V. Maslennikov, A.M. Murashov, P. Picozza, V. Sgrigna, S.A. Voronov, 2003. *High-Energy Charged Particle Bursts in the near-Earth space as earthquake Precursors*, *Annales Geophysicae*, **21**, pp. 597-602.
- [7] Alfven, H., 1942. *On the existence of electromagnetic hydromagnetic waves*, *Ark. Mat. Astron. Fys.*, **29B**(2), n.2 (7pp).
- [8] Areshidze, G., Bella, F., Biagi, P.F., Caputo, M., Chkuaseli, V., Della Monica, G., Ermini, A., Manjgaladze, P., Melikadze, G., Sgrigna, V., Slavina, L., Zilpimiani, D., 1992. *Anomalies in geophysical and geochemical parameters revealed in the occasion of the Paravani (M=5.6) and Spitak (M=6.9) earthquakes (Caucasus)*, *Tectonophysics*, **202**, pp. 23-41.

- [9] Baumjohann W. and Treumann R.A., Basics Space Plasma Physics, 329 p., Imperial College Press, 1997.
- [10] Baker, D. N., T. I. Pulkkinen, M. Hesse, and R. L. McPherron, A quantitative assessment of energy storage and release in the Earth's magnetotail, *J. Geophys. Res.*, **102**, 71597168, 1997.
- [11] Bell, T.F., 1985. *High-Amplitude VLF Transmitter Signals and Associated Sidebands Observed near the Magnetic Equatorial Plane on the ISEE 1 Satellite*, *J. Geophys. Res.*, **90**, pp. 2792-2806.
- [12] Bell, T.F., Luethe, J.P., and U.S. Inan, 1982. *ISEE 1 Observations of VLF Line Radiation in the Earth's Magnetosphere*, *J. Geophys. Res.*, **87**, pp. 3530-3536.
- [13] Bella, F., Biagi, P.F., Caputo, M., Cozzi, Della Monica, G., Ermini, A., Plastino, W., Sgrigna, V., 1995. *Helium content in thermal waters revealed in the Caucasus from 1985 to 1991 and their correlations with the seismic activity*, *Tectonophysics*, **246**, pp. 263-278.
- [14] Bella, F., Biagi, P.F., Caputo, M., Cozzi, E., Della Monica, G., Ermini, A., Plastino, W., Sgrigna, V., 1998. *Field strength variations of LF radio waves prior to earthquakes in Central Italy*, *Phys. Earth Planet. Int.*, **105**, 279-286.
- [15] Bernabé, Y., 1998. *Streaming potential in heterogeneous network*, *J. Geophys. Res.*, **103**, pp. 20827-20841.
- [16] Berthelier, J.J., Godefroy, M., Leblanc, F., Malingre, M., Menvielle, M., Lagoutte, D., Brochot, J.Y., Colin, F., Elie, F., Legendre, C., Zamora, P., Benoist, D., Chapuis, Y., Artru, J., ICE, the electric field experiment on DEMETER, *Planet. Space Sci.*, this issue, doi:10.1016/j.pss.2005.10.016, 2006a
- [17] Berthelier, J.J., Godefroy, M., Leblanc, F., Seran, E., Peschard, D., Gilbert, P. Artru, J., 2006b. IAP, the thermal plasma analyzer on DEMETER, *Planet. Space Sci.*, this issue, doi:10.1016/j.pss.2005.10.018, 2006b.
- [18] Bilichenko, S.V., Iljin, F.S., Kim, E.F., Pokhotelov, O.A., Puschaev, P.P., Stanev, G.A., Streltsov, A.V., Chmyrev, V.M., 1990. *ULF response of the ionosphere for earthquake preparation processes*, *Dokl. Acad. Nauk, USSR*, **311**, pp. 1077-1080.
- [19] Bishop, J.R., 1981. *Piezoelectric effects in quartz-rich rocks*, *Tectonophysics*, **77**, pp. 297-321.
- [20] M. Boezio, V. Bonvicini, E. Mocchiutti, P. Schiavon, A. Vacchi, G. Zampa, N. Zampa, A. Bakaldin, A. M. Galper, S. V. Koldashov, M. G. Korotkov, V. V. Mikhailov, S. A. Voronov, Y.

- Yurkin, A.Basilic, R.Bencardino, L. Bongiorno, M. Casolino, M.P. De Pascale, G.Furano, A. Menicucci, M.Minori, A.Morselli, P. Picozza, R.Sparvoli, R.Wischnewski, O.Adriani, L.Bonechi, M.Bongi, F.Giambi, P.Papini, S.B. Ricciarini, P. Spillantini, S.Straulino, F. Taccetti, E. Vannuccini, G. Castellini, P. Carlson , J. Lund , J.Lundquist, S.Orsi, M.Pearce, G.C. Barbarino, D.Campana, G.Osteria, G.Rossi, S.Russo, M.Boscherini, W.Menn, M. Simon, M.Ricci, M.Ambriola, R.Bellotti, F.Cafagna, M. Circella, C.DeMarzo, N. Giglietto, N. Mirizzi, M.Romita, P. Spinelli, E. Bogomolov, S.Krutkov, G.Vasiljev, G.Bazilevskaja, A.Grigorjeva I, R. Mukhametshin, Y.Stozhkov, J.W. Mitchell, R.E. Streitmatter, S.J.Stochaj, The Space Experiment PAMELA, *JNuclear Physics B (Proc. Suppl.)* 134 ,pp 39-46, 2004.
- [21] Brautigam,D.H., M.S.Gaussenhoven, and D.A.Hardy, 1991. *A statistical study of IMF B_z and solar wind speed on auroral ion and electron precipitation*, *J. Geophys. Res.*, **96**, pp. 5525-5538.
- [22] Braysy, T., Mursula, K. and Marklund, G., Ion cyclotron waves during a great magnetic storm observed by Freja double-probe electric field instrument, *J. Geophys. Res.*, 103 4145-4155, 1998.
- [23] Burgess W.C., and U.S. Inan, 1993. *The role of ducted whistlers in the precipitation loss and equilibrium flux of radiation belt electrons*, *J. Geophys. Res.*, **98**, pp. 15643-15665.
- [24] M. Caputo, 2003. *Notes based on: Evidence for electromagnetic emission during rock loading and fracture: a way towards an earthquake precursor*, Seventh Workshop on Non-Linear Dynamics and Earthquake Prediction.
- [25] Chappell,C.R., K.K.Harris, and G.W.Sharp, The morphology of the bulge region of the plasmasphere, *J. Geophys. Res.*, 75, 3848, 1970.
- [26] Chmyrev, V.M., Isaev, N.V., Serebryakova, O.N., Sorokin, V.M., Sobolev, Ya.P., 1997. *Small-scale plasma inhomogeneities and correlated ELF emissions in the ionosphere over an earthquake region*, *J. Atm. Solar-Terr. Phys.*, **59**, pp. 967-974.
- [27] Church, S.R., and R.M., Thorne, 1983. *J. Geophys. Res.*, **88**, p. 7941.
- [28] Thibery Cussac, Marie-Anne Clair, Pascale Ultré -Guerard, François Buisson, Gérard Lassalle-Balier, Michel Ledu, Christian Elisabelar, Xavier Passot, Nelly Rey, *The Deme-ter microsatellite and ground segment*, *Planet. Space Sci.*, 54, 413427, 2006

- [29] Dobrovolsky, I.P., Gershenzon, N.I., Gokhberg, M.B., 1989. *Theory of electrokinetic effects occurring at the final stage in the preparation of a tectonic earthquake*, Phys. Earth Planet. Int., **57**, pp. 144-156.
- [30] Draganov, A.B., Inan, U.S., Taranenko, Y.N., 1991. *ULF magnetic signatures at the Earth surface due to the ground water flow: a possible precursor to earthquakes*, Geophys. Res. Lett., **18**, pp. 1127-1130.
- [31] Eftaxias, K., Kaporis, P., Polygiannakis, J., Peratzakis, A., Kopanas, J., Antonopoulos, G., Rigas, D., 2003. *Experience of short term earthquake precursors with VLF-VHF electromagnetic emissions*, Nat. Hazard Earth Syst. Sci., **3**, pp. 217-228.
- [32] F. Elie, Hayakawa M., Parrot M., Pinon J.L., Lefevre F., Neural Network System for the Analysis of transient Phenomena on board the Demeter micro-satellite, *IEICE TRANS. FUNDAMENTALS, E82-A, NO 8*, 1999.
- [33] Fenoglio, M.A., Johnston, M.J.S., Byerlee, J.D., 1995. *Magnetic and electric fields associated with changes in high pore pressure in fault zones: application to the Loma Prieta ULF emissions*, J. Geophys. Res., **100**, pp. 12951-12958.
- [34] D.V. Fitterman, 1979. *Theory of electrokinetic-magnetic anomalies in a faulted half space*, J. Geophys. Res., **84**, pp. 6031-6040.
- [35] Fraser-Smith A.C., A. Bernardi, P.R. McGill, M.E. Ladd, R.A. Helliwell, and O.G. Villard, Jr, 1994. *Low frequency magnetic field measurement near the epicenter of the Ms 7.1 Loma Prieta earthquake*, Geophys. Res. Lett., **17**, 1465-1468.
- [36] Fraser, B. J., Samson, J.C., Hu, Y.D., McPherron, R.L. and Russell, C.T., *Electromagnetic ion cyclotron waves observed near the oxygen cyclotron frequency by ISEE 1 and 2*, J. Geophys. Res., **97** 3063-3074, 1992.
- [37] Freund, F., 2002. *Charge generation and propagation in igneous rocks*, J. Geodyn., **33**, pp. 543-570.
- [38] Freund, F., 2003. *On the electrical conductivity structure of the stable continental crust*, J. Geodyn., **35**, pp. 353-388.
- [39] Fujinawa, Y., Takahashi, K., Matsumoto, T., 2002. *Modeling confined pressure changes inducing anomalous electromagnetic fields related with earthquakes*, J. Appl. Geophys., **49**, pp. 101-110.

- [40] Fukunishi, H., Y., Takahashi, M., Kubota, K., Sakanoi, U.S., Inan, and W. A., Lyons , 1996. *Elves: lightning-induced transient luminous events in the lower ionosphere*, Geophys. Res. Lett., **23**, pp. 2157-2160.
- [41] Galper, A.M., Dimitrenko, V.B., Nikitina, N.V., Grachev, V.M., Ulin, S.E., 1989. *Interrelation between High-Energy Charged Particle Fluxes in the Radiation Belt and Seismicity of the Earth*, Cosmic Res., **27**, p. 789.
- [42] Galper, A.M., Koldashov, S.V., Voronov, S.A., 1995. *High energy particle flux variations as earthquake predictors*, Adv. Space Res., **15**, pp. 131-134.
- [43] Galperin, Yu.I., Gladyshev, V.A., Jordjio, N.V., Larkina, V.I., 1992. *Precipitation of High-Energy Captured Particles in the Magnetosphere Above the Epicenter of an Incipient Earthquake*, Cosmic Res., **30**, pp. 89-106.
- [44] Geller, R.J., 1996. *Debate on VAN*, Geophys. Res. Lett., **23**, whole issue 11.
- [45] Gershenzon, N., Bambakidis, G., 2001. *Modeling of seismo-electromagnetic phenomena*, Russian J. Earth Sci., **3**, 247-275.
- [46] Ginzburg, E.A., Malishev, A.B., Proshkina, I.P., Pustovetov, V.P., 1994. *Correlation of strong earthquakes with radiation belt particle flux variations*, Geomagn. Aeron. (Engl. Transl.), **34**, pp. 315-320.
- [47] Gokhberg, M. B., Gufeld, I. L., Rozhnoy, A. A., Marenko, V. F., Yampolsky, V. S., Ponomarev, E. A., 1989. *Study of seismic influence on the ionosphere by super long-wave probing of the Earth-ionosphere waveguide*, Phys. Earth and Planet. Int., **57**, pp. 64-67.
- [48] M.B.Gokhberg , I.L.Gufeld , N.I.Gershenzon , and V.A.Pilipenko ,1985 . *Electromagnetic Effects during Rupture of the Earth's Crust*,Izvestiya Earth Physics,**21**,pp. 52–63 .
- [49] Grimalsky, V.V., Kremenetsky, I.A., Rapoport, Yu.G., 1999. *Excitation of EMW in the Lithosphere and Propagation into Magnetosphere*, M.Hayakawa, Ed., TERRAPUB, Tokyo, pp. 777-787.
- [50] Grunberg, L., 1958. *A survey of exo-electron emission phenomena*, British J. Applied Physics, **9**, pp. 85-93.
- [51] Gurnett, D.A., and B.J., O'Brien, 1964. *High-latitude geophysical studies with spacecraft Injun 3, 5, Very-low-frequency electromagnetic radiation*, J. Geophys. Res., **69**, pp. 65- 89.

- [52] Guo, Z., Liu, B., Wang, Y., 1994. *Mechanism of electromagnetic emissions associated with microscopic and macroscopic cracking in rocks*, M. Hayakawa, Ed., TERRAPUB, Tokyo, pp. 523-529.
- [53] Hayakawa M., T. Yoshino, and V.A. Morgounov, 1993. *On the possible influence of seismic activity on the propagation of magnetospheric whistlers at low latitudes*, Phys. Earth Planet. Int., **77**, pp. 97-108.
- [54] Hayakawa, M., Kopytenko, Yu., Smirnova, N., Troyan, V., Peterson, Th., 2000. *Monitoring ULF Magnetic Disturbances and Schemes for Recognizing Earthquake Precursors*, Phys. Chem. Earth (A), **25**, pp. 263-269.
- [55] Hayakawa, M., F. Lefeuvre, and J.L. Rauch, On the system of Aureol-3 satellite direction finding for ionospheric and magnetospheric ELF waves, *Trans. Inst. Electr. Inform. Comm. Eng. E*, **73**, 942-951, 1990.
- [56] Helliwell R.A., *Whistlers and Related Phenomena*, Stanford University Press, Stanford, 1965.
- [57] Horne, R.B., R.M. Thorne, Potential waves for relativistic electron scattering and stochastic acceleration during magnetic storm. *Geophys. Res. Lett.*, **25**, 3011, 1998.
- [58] Imhof, W.L., E.E. Gaines, and J.B. Reagan, Evidence for the resonance precipitation of electrons from the slot region of the radiation belt, *J. Geophys. Res.*, **79**, 3141, 1974.
- [59] Imhof, W.L., R.R. Anderson, J.B. Reagan, and E.E. Gaines, Coordinated measurement of slot region electron precipitation by plasmaspheric wave bands, *J. Geophys. Res.*, **87**, 4418, 1982.
- [60] Imhof, W.L., J.B. Reagan, E.E. Gaines, H.D. Voss, D.W. Datlowe, J. Mobilia, R.A. Helliwell, U.S. Inan, J.P. Katsufakis, and R.G. Joiner, Direct observation of radiation belt electrons precipitated by the controlled injection of VLF signals from a ground-based transmitter, *J. Geophys. Res. Lett.*, **10**, 361, 1983.
- [61] Imhof, W.L., E.E. Gaines, and J.B. Reagan, Dynamic variations in intensity and energy spectra of electrons in the inner radiation belt, *J. Geophys. Res.*, **78**, 4568, 1973.
- [62] Inan, U.S., T.F. Bell, and R.A. Helliwell, Nonlinear pitch angle scattering of energetic electrons by coherent VLF waves in the magnetosphere, *J. Geophys. Res.*, **83**, 3235, 1978.

- [63] Ismaguilov, V.S., Kopytenko, Yu.A., Hattori, K., Voronov, P.M., Molchanov, O.A., Hayakawa, M., 2001. *ULF magnetic emissions connected with under sea bottom earthquakes*, Nat. Hazard Earth Syst. Sci., **1**, pp. 23-31.
- [64] Johnston, M.J.S., Mueller, R.J., 1987. *Seismomagnetic observations during the 8 July 1986 magnitude 5.9 North Palm Springs earthquake*, Science, **237**, pp. 1201-1203.
- [65] Johnston, M.J.S., 1997. *Review of electric and magnetic fields accompanying seismic and volcanic activity*, Surv. Geophys., **18**, pp. 441-475.
- [66] Jordan, T.H., 1990. *Observation of Slow deformation Events and Speculation on their Relationship to Fast Seismic Rupture*, I.C.T.P. Lectures, H4.SMR/480-19, pp. 1-30.
- [67] Jordanova, V.K., Farrugia, C. J., Thorne, R.M., Khazanov, G.V., Reeves, G.D. and Thomsen, M.F. , Modeling ring current proton precipitation by electromagnetic ion cyclotron waves during the May 14-16, 1997, storm, *J. Geophys. Res.*, **106** 7-22, 2001.
- [68] Kan J.R., et al. *Magnetospheric substorm*, Geophysical Monograph, **64**, American Geophys. Union, Washington, D.C., 1991.
- [69] Kaufman A.A., and P. Hoekstra, 2001. *Electromagnetic Sounding*, Elsevier, Amsterdam.
- [70] Kennel C.F. and Petschek, H.E., Limit on stably trapped particle fluxes, *J. Geophys. Res.*, **71**, 1-28, 1966.
- [71] Kivelson M.G., and C.J. Russel. *Introduction to space physics*, Cambridge Univ. Press, Cambridge, 1995.
- [72] O. Koefoed, 1979. *Geosounding Principles*, **1**, Elsevier, Amsterdam.
- [73] Kopytenko, Yu.A., Matiashvili, T.G., Voronov, P.M., Kopytenko, E.A., Molchanov, O.A., 1993. *Detection of ultra-low-frequency emissions connected with the Spitak earthquake and its aftershock activity, based on geomagnetic pulsations data at Dusheti and Vardzia observatories*, Phys. Earth Planet. Int., **77**, pp. 85-95.
- [74] Krechetov, V.V., 1996. *Cerenkov radiation of protons in the magnetosphere as a source of VLF waves preceding an earthquake*, Geomag. and Aeron. (Engl Transl.), **35**, pp. 688-691.
- [75] Langel, R.A., T.J. Sabaka, R.T. Baldwin, and J.A. Conrad, 1996. *The near-earth magnetic field from magnetospheric and quiet-day ionospheric sources and how it is modeled*, Phys. Earth Planet. Int., **98**, pp. 235-267.

- [76] Larkina, V.I., Migulin, V.V., Molchanov, O.A., Kharkov, I.P., Inchin, A.S., Schvetsova, V.V., 1989. *Some statistical results on very low frequency radiowave emissions in the upper ionosphere over earthquake zones*, Phys. Earth Planet. Inter., **57**, pp. 100-109.
- [77] Lee, C.C., Liu, J.Y., Pan, C.J., 2000. *The height of sporadic-E layer simultaneously observed by the VHF radar and ionosondes in Chung-Li*, Geophys. Res. Lett., **27**, pp. 641-644.
- [78] Lebreton, J.P., Stverak, S., Travnicek, P., Maksimovic, M., Klinge, D., Merikallio, S., Lagoutte, D., Poirier, B., Kozacek, Z., Salaquarda, M., The ISL Langmuir Probe experiment and its data processing onboard DEMETER: scientific objectives, description and first results, *Planet. Space Sci., this issue*, doi:10.1016/j.pss.2005.10.017, 2006
- [79] Li, X., D.N. Baker, M. Temerin, T.E. Cayton, E.D.G. Reeves, R.A. Christensen, J.B. Blake, R. Nakamura, S.G. Kanekal, Multisatellite observations of outer zone electron variation during the November 3-4, 1993, magnetic storm. *J. Geophys. Res.*, **102**, 14123, 1997.
- [80] Lorentzen, K.R., McCarthy, M.P., Parks, G.K., Foat, J.E., Millan, R.M., Smith, D.M., Lin, R.P. and Treilhou, J.P., Precipitation of relativistic electrons by interaction with electromagnetic ion cyclotron waves, *J. Geophys. Res.*, **105** 5382-5389, 2000.
- [81] Lyons, L.R., Thorne, R.M. and Kennel, C.F., Pitch-angle diffusion of radiation belt electrons with the plasmasphere, *J. Geophys. Res.*, **77** 3455-3474, 1972.
- [82] Lyons, L.R., and D.J. Williams, A source for geomagnetic storm main phase ring current, *J. Geophys. Res.*, **85**, 523, 1980.
- [83] Malvezzi, V., Sgrigna, V., Yanovskaya, T.B., 2002. *Observation and Modeling of Preseismic Fault Creep Events. Correlation with the 1997 Umbria-Marche earthquake Sequence (central Italy)*, EOS Trans., AGU, **83**, T31A-08, n.19, S358.
- [84] Meng, C.-I., and K. Liou, Substorm timings and timescales: A new aspect, *Space Sci. Rev.*, **113**(1-2), 4175, doi: 10.1023/B:SPAC.0000042939.88548.68, 2004.
- [85] Meredith P.N., Horne, R.B. and Anderson, R.R., Substorm dependence of chorus amplitudes: Implications for the acceleration of electrons to relativistic energy, *J. Geophys. Res.*, **106** 13165-13178, 2001.
- [86] Merzer, M., Klemperer, S.L., 1997. *Modeling low-frequency magnetic-field precursors to the Loma Prieta earthquake with a precursory increase in fault-zone conductivity*, Pure Appl. Geophys., **150**, pp. 217-248.

- [87] Mihalov, J.D., and R.S. White, Energetic electron spectra in the radiation belts, *J. Geophys. Res.*, **71**, 2217, 1966.
- [88] X. Miniere, Pinon J.L., Lefevre F., A Neural Network approach to the classification of electron and proton whistler, *Journal of Atmospheric and Solar-Terrestrial Physics*, **58**, No.7 911-924, 1996.
- [89] Molchanov, O.A., Mazhaeva, O.A., Golyavin, A.N., Hayakawa, M., 1993. *Observation by the Intercosmos-24 satellite of ELF-VLF electromagnetic emissions associated with earthquakes*, *Ann. Geophysicae*, **11**, pp. 431-440.
- [90] Molchanov, O.A., Hayakawa, M., Rafalsky, V.A., 1995. *Penetration Characteristics of Electromagnetic Emissions from an Underground Seismic Source into the Atmosphere, Ionosphere and Magnetosphere*, *J. Geophys. Res.*, **100**, pp. 1691-1712.
- [91] Molchanov, O.A., Hayakawa, M., 1998. *On the Generation Mechanism of ULF seismogenic Electromagnetic Emissions*, *Phys. Earth Planet. Inter.*, **105**, pp. 201-210.
- [92] O.A.Molchanov, A.V.Shvets, and M.Hayakawa, 1999. *Analysis of lightning-induced ionization from VLF Trimp events*, in *Atmospheric and Ionospheric Electromagnetic Phenomena Associated with Earthquakes*, Ed. M.Hayakawa, pp. 959-988, Terra Scientific Publishing Company (TERRAPUB), Tokyo, 1999.
- [93] Myachkin, V.I., Brace, W.F., Sobolev, G.A., Dieterich J.H., 1975. *Two models for earthquake forerunners*, *Pure Appl. Geophys.*, **113**, pp. 169-181.
- [94] Nardi A., M. Caputo, G. De Natale, and G. Scarascia Mugnozza, 2003. *Evidence for electromagnetic emission during rock loading and fracture: a way towards an earthquake precursor*, submitted.
- [95] Nitsan U., 1977. *Electromagnetic emission accompanying fracture of quartz-bearing rocks*, *Geophys. Res. Lett.*, **4**, pp. 333-336.
- [96] Obrien T.P., K.R., Lorentzen, I.R., Mann, N.P., Meredith, J.B., Blake, J.F., Fennell, M.D., Looper, Milling, D.K. and Anderson, R.R. , *Energization of relativistic electrons in the presence of ULF power and MeV microbursts: Evidence for dual ULF and VLF acceleration*, *J. Geophys. Res.*, **108** (A8) 1329, 2003.
- [97] Ondoh, T., et al., 1983. *Plasmaspheric hiss observed in the topside ionosphere at mid- and low-latitudes*, *Planet. Space Sci.* **31**, pp. 411-422.

- [98] Ohta, K., Umeda, K., Watanabe, N., Hayakawa, M., 2001. *ULF/ELF emissions observed in Japan, possibly associated with the Chi-Chi earthquake in Taiwan*, Nat. Hazard Earth Syst. Sci., **1**, pp. 37-42.
- [99] Oike, K., Ogawa, T., 1986. *Electromagnetic radiations from shallow earthquake observed in the LF range*, J. Geomagn. Geoelectr., **38**, pp. 1031-1040.
- [100] Park, S. K., Johnston, M.J.S., Madden, T.R., Morgan, F.D., Morrison, H.F., 1993. *Electromagnetic precursors to earthquakes in the ULF band: a review of observations and mechanisms*, Rev. Geophys., **31**, pp. 117-132.
- [101] Parks, G. K., Physics of space plasmas, 1 ed., Addison-Wesley Publishing Company, 350 Bridge Parkway, Redwood City, 1991.
- [102] Parrot, M. and Y.Zaslavsky, Physical mechanisms of man-made influences on the magnetosphere, *Surveys in Geophysics* , **17**, 67, 1996.
- [103] Parrot, M., Benoist, D., Berthelier, J.J., Blecki, J., Chapuis, Y., Colin, F., Elie, F., Ferreau, P., Lagoutte, D., Lefeuvre, F., Legendre, C., Leveque, M., Pincon, J.L., Poirier, B., Seran, H.C., Zamora, P., The magnetic field experiment IMSC and its data processing onboard DEMETER: scientific objectives, description and first results. *Planet. Space Sci., this issue*, 2006.
- [104] Parrot, M., Mogilevsky, M.M., 1989. *VLF emissions associated with earthquakes and observed in the ionosphere and the magnetosphere*, Phys. Earth and Planet. Inter., **57**, pp. 86-99.
- [105] Parrot, M., Achache, J., Berthelier, J.J., Blanc, E., Deschamps, A., Lefeuvre, F., Menvielle, M., Plantet, J.L., Tarits, P., Villain, J.P., 1993. *High Frequency seismo-electromagnetic effects*, Phys. Earth Planet. Inter., **77**, pp. 65-83.
- [106] Parrot, M., 1994. *Statistical study of ELF/VLF emissions recorded by a low-altitude satellite during seismic events*, J. Geophys. Res., **99**, pp. 23339-23347.
- [107] Parrot, M., 1995. *Handbook of Atmospheric Electrodynamics*, Ed, by Hans Volland (CRC Press), vol II, pp. 95-115.
- [108] Parrot, M., A. Buzzi, O. Santolk, J. J. Berthelier, J. A. Sauvaud, J. P. Lebreton, New observations of electromagnetic harmonic ELF emissions in the ionosphere by the DEMETER satellite during large magnetic storms , J. Geophys. Res., **vol . 111, A08301**, doi:10.1029/2005JA011583, 2006 .

- [109] Patella D., 1977. *Resistivity sounding on a multi-layered Earth with transitional layers. Part 1: theory*, Geophys. Prosp., **25**, pp. 699-729.
- [110] Patella D., A. Tramacere, and R. Di Maio, 1997. *Modelling earth current precursors in earthquake prediction*, Ann. Geofis., **XL**, pp. 495-517.
- [111] Poulsen, W.L., and U.S., Inan, 1988. *Satellite observations of a new type of discrete VLF emission at L₄*, J. Geophys. Res., **93**, pp. 1817-1838.
- [112] Pustovetov, V.P., Malyshev, A.B., 1993. *Space-Time Correlation of Earthquakes and High-Energy Particle Flux Variations in the Inner Radiation Belt*, Cosmic Res., **31**, pp. 84-90.
- [113] Salvati, M.A., U.S., Inan, T.J., Rosenberg, and A.T., Weatherwax, 2000. *Solar wind control of polar chorus*, Geophys. Res. Lett., **27**, pp. 649- 652.
- [114] Sakamoto, K., Y. Kasahara, I. Kimura, K-vector determination of whistler mode signals by using amplitude data obtained by spacecraft borne instrument, *IEEE Trans. Geosci. Remote Sens.*, **33**, 528-534, 1995.
- [115] Sauvaud, J.A., Moreau, T., Maggiolo, R., Treilhou, J.P., Jacquey, C., Cros, A., Coutelier, J., Rouzaud, J., Penou, E., Gangloff, M., High energy electron detection onboard DEMETER: the IDP spectrometer, description and first results on the inner belt, *Planet. Space Sci.*, this issue, doi:10.1016/j.pss.2005.10.019, 2006
- [116] Sazhin, S.S., and M., Hayakawa, 1992. *Magnetospheric chorus emissions: a review*, Planet. Space Sci., **40**, pp. 681-697.
- [117] Serebryakova, O.N., Bilichenko, S.V., Chmyrev, V.M., Parrot, M., Rauch, J.L., Lefeuvre, F., Pokhotelov, O.A., 1992. *Electromagnetic ELF radiation from earthquake regions as observed by low-altitude satellite*, Geophys. Res. Lett., **19**, pp. 91-94.
- [118] Shawhan, S.D., Magnetospheric plasma wave research 1975-1978, *Rev. Geophys. Space Phys.*, **17** 705-724, 1979.
- [119] Sgrigna, V., D'ambrosio, C., Yanovskaya, T.B., 2002a. *Numerical modeling of preseismic slow movements of crustal blocks caused by quasi-horizontal tectonic forces*, Phys Earth. Planet. Int., **129**, pp. 313-324.
- [120] Sgrigna, V., Console, R., Conti, L., Galper, A., Malvezzi, V., Parrot, M., Picozza, P., Scrimaglio, R., Spillantini, P., Zilpimiani, D., 2002b. *Preseismic Natural Emissions from the*

Earth's Surface and their effects in the near Earth Space. A project for monitoring Earthquakes from Space, EOS Trans., AGU, **83**, T22B-10, n.19, S356.

- [121] Sgrigna V., R. Console, L. Conti, A.M. Galper, V. Malvezzi, M. Parrot, P. Picozza, R. Scrimaglio, P. Spillantini, D. Zilpimiani, 2003b. *The ESPERIA space project: a mission for monitoring preseismic emissions and anthropogenic effects in the near-Earth space, and for de-foining the near-Earth magnetic environment*, 2nd CHAMP Science Meeting, September 1-4, 2003, GeoForschungsZentrum, Potsdam, Germany.
- [122] Sgrigna, V., R. Console, L. Conti, A. Galper, V. Malvezzi, M. Parrot, P. Picozza, R. Scrimaglio, P. Spillantini, D. Zilpimiani, 2003c. *The ESPERIA Mission*, EOS Trans., AGU, vol. 84, T52D, n.46, F1462, 2003
- [123] Sgrigna, V., Malvezzi, V., 2003. *Preseismic creep strains revealed by ground tilt measurements in central Italy on the occasion of the 1997 Umbria-Marche Apennines earthquake sequence*, Pure Appl. Geophys., **160**, pp. 1493-1515.
- [124] V. Sgrigna, L. Carota, L. Conti, M. Corsi, A.M. Galper, S.V. Koldashov, A.M. Murashov, P. Picozza, R. Scrimaglio, L. Stagni, *Correlations between earthquakes and anomalous particle bursts from SAMPEX/PET satellite observations*, *Journal of Atmospheric and Solar-Terrestrial Physics*, 67, 14481462, 2005.
- [125] V. Sgrigna, Battiston, R., Buzzi, A., Casolino, M., Conti, L., Picozza, P., Stagni, C., Zilpimiani, , *The EGLE space experiment onboard the ISS*, *Microgravity and Sci. Technology* submitted, 2006.
- [126] Sgrigna, V., (Principal Investigator), 2001. *ESPERIA: Earthquake investigation by Satellite and Physics of the Environment Related to the Ionosphere and Atmosphere*, Phase A Report, Italian Space Agency (ASI), Program for Scientific Missions dedicated to Earth Sciences, Rome, July 2001, pp.194.
- [127] Shalimov S., and M. Gokhberg, 1998. *Litosphere-ionosphere coupling mechanism and its application to the earthquake in Iran on June 20, 1990. A review of ionospheric measurements and basic assumptions*, Phys. Earth and Planet. Inter., **105**, pp. 211-218.
- [128] L. Slifkin, 1993. *Seismic electric signals from displacement of charged dislocations*, Tectonophysics, **224**, pp. 149-152.
- [129] Smith, R.L., *Propagation characteristics of whistlers trapped in field-aligned columns of enhanced ionization*, J. Geophys. Res., 66, 3699-3707, 1961.

- [130] Sonwalkar, V. S., and U. S. Inan (1989), Lightning as an embryonic source of VLF hiss, *J. Geophys. Res.*, **94**, 6986-6994.
- [131] Sorokin, V.M., and V.M., Chmyrev, 1999. *The Physical Model of Electromagnetic and Plasma Response of the Ionosphere on the Pre-Earthquake Processes*, Ed. M.Hayakawa (TERRAPUB), pp. 819-828.
- [132] Sorokin, V.M., Chmyrev, V.M., Yaschenko, A.K., 2001. *Electrodynamic model of the lower atmosphere and the ionosphere coupling*, *J. Atm. Sol. Terr. Phys.*, **63**, pp. 1681-1691.
- [133] Southwood, D.J., 1974. *Some features of field line resonances in the magnetosphere*, *Planet. Space Sci.*, **22**, p. 483.
- [134] Southwood, D.J., and M.G. Kivelson, 1982. *Charged particle behaviour in low-frequency geomagnetic pulsations. 2. Graphical approach*, *J. Geophys. Res.*, **87**, pp. 1707-1710.
- [135] Stern D.P., 1977. *Representation of magnetic fields in space*, *Rev. Geophys. Space Phys.*, **14**, 199 (Ch3).
- [136] Stix, T. H., *Waves in plasmas*, pp.27-28,40v, Am. Inst. of Phys.,College Park,Md, 1992.
- [137] Summers, D. and Ma, C.-Y., A model for generating relativistic electrons in the Earths inner magnetosphere based on gyroresonant wave-particle interactions, *J. Geophys. Res.*, **105** 2625-2639, 2000.
- [138] Summers, D. and Thorne, R.M. , Relativistic electron pitch-angle scattering by electromagnetic ion cyclotron waves during geomagnetic storms, *J. Geophys. Res.*, **108** (A4) 1143, 2003.
- [139] Summers, D., R.M. Thorne, and Fuliang X., Relativistic theory of wave-particle resonant diffusion with application to electron acceleration in the magnetosphere, *J. Geophys. Res.*, **103**, 20487, 1998.
- [140] Surkov, V., 1999. *ULF Electromagnetic Perturbations Resulting from the Fracture and Dilatancy in the Earthquake Preparation Zone*, M.Hayakawa, Ed., TERRAPUB, Tokyo, pp. 371-382.
- [141] Taylor, W. W. L., and D. A. Gurnett 1968, The morphology of VLF emissions observed with the Injun 3 satellite, *J. Geophys. Res.*, **73**, 5615- 5626.
- [142] Teisseyre, R., 1997. *Generation of electric field in an earthquake preparation zone*, *Ann. Geofis.*, **40**, pp. 297-304.

- [143] Telford W.M., L.P. Geldart, and R.E. Sheriff, 1990. *Applied Geophysics*, Cambridge University Press.
- [144] Thorne, R.M., et al., 1973. *Plasmaspheric hiss*, J. Geophys. Res., **78**, p. 1581.
- [145] Thorne, R.M. and Horne, R.B. , The contribution of ion-cyclotron waves to electron heating and SAR-arc excitation near the storm time plasmapause, *Geophys. Res. Lett.*, **19**, 417-420, 1992.
- [146] Thorne, R.M., Smith, E. J., Burton, R.K. and Holzer, R.E. , Plasmaspheric hiss, *J. Geophys. Res.*, **78** 1581-1596, 1973.
- [147] Trakhtengerts, V.Y., and M.J., Rycroft, 2000. *Whistler-electron interactions in the magnetosphere: new results and novel approaches*, J. Atmos. Solar-Terr. Phys., **62**, pp. 1719-1733.
- [148] Treumann R.A., and W. Baumjohann. *Basic Space Plasma Physics*, Imperial College Press, London, 1997.
- [149] Tsurutani, B.T. and Smith, E. J., Two types of magnetospheric ELF chorus and their sub-storm dependences, *J. Geophys. Res.*, **82** 5112-5128, 1977.
- [150] Uyeda, S., Sulaiman Al-Damegh, K., Dologlou, E., Nagao, T., 1999. *Some relationship between VAN seismic electric signals (SES) and earthquake parameters*, Tectonophysics, **304**, pp. 41-55.
- [151] F. Vallianatos, and A. Tzanis, 1999. *On possible scaling laws between electric earthquake precursors (EEP) and earthquake magnitude*, Geophys. Res. Lett., **26**, pp. 2013-2016.
- [152] Varotsos, P., Alexopoulos, K., Lazaridou, M., Nagao, 1993. *Earthquake predictions issued in Greece by seismic electric signals since February 6, 1990*, Tectonophysics, **224**, pp. 269-288.
- [153] Varotsos, P., Sarlis, N., Lazaridou, M., Kaperis, P., 1997. *Transmission of stress induced electric signals in dielectric media*, J. Appl. Phys., **83**, pp. 60-70.
- [154] Voronov, S.A., Galper, A.M., Koldashov, S.V., Maslennikov, L.V., Mikhailov, V.V., Nikitina, N.V., Popov, A.V., 1990. *Increases in High Energy Charged Particle Fluxes near the South Atlantic Magnetic Anomaly and the Seismicity of the Earth*, Cosmic Res., **28**, pp. 789-791.
- [155] Voss H.D., W.L. Imhof, M. Walt, J. Mobilia, E.E. Gaines, U.S. Inan, J.B. Reagan, R.A. Helliwell, J.P. Katsufakis, D.L. Carpenter, and H.C. Chang, Lightning-induced electron precipitation, *Nature*, **312**, 740, 1984.

- [156] Warwick, J.W., Stoker, C., Meyer, T.R., 1982. *Radio emission associated with rock fracture: possible application to the great Chilean earthquake of May 22, 1960*, J. Geophys. Res., **87**, pp. 2851-2859.
- [157] Woch, J., G. Kremser, A. Korth, O. A. Pokhotelov, V. A. Pilipenko, Y. M. Nezlina, and E. Amaty, 1988. *Curvature-driven drift mirror instability in the magnetosphere*, Planet. Space Sci., **36**, pp. 383-393.
- [158] Yoshida, S., Uyeshima, M., Nakatani, M., 1997. *Electric potential changes associated with slip failure of granite: preseismic and coseismic signals*, J. Geophys. Res., **102**, pp. 14883-14897.